The Film Formation and Phase Separation of Spin Coated Polymer Blends

Eleanor Grace Dougherty

MPhys

This thesis is submitted for the degree of

Doctor of Philosophy

The University of Sheffield

Physics and Astronomy

January 2019

This thesis is dedicated to

Edith Nettleton, Eileen Dougherty and Christine Blunden.

Not a day goes by where I don't miss my Grandma, Nana and Auntie Christine and I hope I would have made you proud.

Acknowledgements

I would like to thank Dr Matt Mears for his encouragement, guidance and inspiration in polymer physics since 2012. When disaster struck, he was always there with advice, ideas or even to just to listen.

My supervisor Prof Mark Geoghegan has been a source of good discussions and support during my PhD and his direction has made me a better scientist, for which I am grateful.

Stephanie Burg, Emily Hall, Jamie Blakeman and Tom Kennelly have been much more than wonderful colleagues. I wish to say thank you for their help with my work, but their company has been lovely in both the Hicks Building and at the University Arms. I would also like to thank Mr Richard Webb, Dr Mike Weir and Dr Andy Parnell for their help the past four years.

Everyone that I have met in Sheffield since I moved here in 2010 has changed my life for the better and all deserve a thank you. Joe Langlands, Doris Lowman, Tash Cowley, Sam Fargher and Harry Moss all deserve a special mention for their kindness, humour and friendship these past eight years. I am so happy to have met them and I already miss not living in the same city.

Nicole Rimmer, Jess Flynn and Tara Priestley have been such good friends to me for so long and even though we live hundreds of miles apart now, they deserve thanks for supporting me from so far away and being a respite from work.

My parents Geoff and Pauline Dougherty have always stressed the importance of education and were only a phone call away when I needed them. In the last year of my PhD, they were both so conscientious of the pressure I was under and did everything they could to help.

Ross, the support you have given since we met is not possible to express in words, but I'm going to try. Our road trip adventures, silly in jokes and your words of encouragement have felt like a break in the clouds of a storm. Your support and love helped me through some tough times and I would not have been able to do this without you. Thank you.

I declare that this thesis is the result of my own work except where the work of others is cited, either explicitly or via the list of references. No part of this dissertation has been submitted for in whole or in part for any other degree or qualification at this university or any other institute.

Eleanor Grace Dougherty

January 2019

Abstract

Polymer spin coating is a popular technique in adhering a thin film to a substrate as it can quickly produce a uniform film. The properties of a thin film can generally be controlled but the spin coating of a polymer blend solution induces phase separation, which causes morphological variations. Radial features have been noted many times but to date, a model that quantifies the film thinning away from the film centre does not exist. This could be problematic when using spin coating to make larger films.

This thesis explores the film formation of poly(methyl methacrylate) and polystyrene blends cast from a toluene based solution as a function of time and radius using *in situ* light scattering experiments. The specularly reflected laser light is indicative of the film thickness and the off-specularly reflected light can be used to determine phase separation length scale. This experimental method is known as optospinometry.

Specular data sets from numerous film radii were compared with a spin coating model that assumes no radial dependence, in order to test the validity of its assumptions. The off-specular results were compared with optical microscopy data in order to quantify the phase separation in the blended films.

The results of the experiments indicate that radial variations in film thickness and structure are not always negligible and should be considered when deriving spin coating models. Numerous different effects such as a temperature gradient, varying solution flow, three-dimensional Ekman spirals and the Marangoni effect affect the film in a radial manner. The morphology of high concentration solution films (6% and 8%) clearly changes with radius yet this is not seen in lower concentration solution films (2% and 4%), that exhibit a non-uniform non-monotonic evaporation rate at different radii.

This thesis also explores the interfaces between polymer trilayers after annealing. The boundaries between layered polymer structures have an interfacial width which exhibits a volume fraction gradient. Experimental interfacial widths are larger than theoretically predicted and capillary waves are theorised to contribute to this discrepancy. The disruption caused by capillary waves was investigated in polymer trilayers where the central layer was comparatively very thin. Fully disrupted central layers were observed after long annealing times, supporting the theory of capillary waves effect on the interfacial width.

Contents

1 Introduction

Polymers are extremely versatile materials that have a wide variety of applications from solar cells [1] to bioengineering for medicine [2] due to their ability to be used in the production of organic electronics. Widely used inorganic electronics have expensive composite materials, such as crystalline silicon, and require time consuming and complicated methods of production. In contrast, organic electronics have relatively inexpensive component materials and easier methods of production, both of which reduces their cost. Organic electronics have a lower environmental impact than inorganic electronics, which is another important factor to consider. The additional properties of organic electronics, such as their lower mass and flexibility, makes potential future applications an exciting prospect.

Whilst organic electronics have numerous advantages, there are considerable problems. Not only do organic solar cells degrade when in contact with light, they are much less efficient than inorganic solar cells, which have an efficiency of around 33% that is minimally impacted when the process is scaled up to an industrial level [3]. In comparison, organic solar cells have an efficiency of approximately 16% [4] when in a laboratory environment. If organic solar cells are to be more widely used, their efficiency must be increased or shortcomings in efficiency must be balanced by their inexpense.

The fundamental properties of organic electronics can be studied by producing thin polymer films. Such films are simple homopolymer coatings that have a thickness between 0.1 - 2000nm cast on to a substrate such as glass or silicon.

A simple and inexpensive method with a high level of control over the final film properties are all desirable features of any coating process. Coating involves the polymer of choice to be dissolved in a solvent, forming a polymer solution. If more than one polymer is used, the solution is referred to as a polymer blend solution. The solution can be deposited onto the substrate of choice in numerous ways, which is not limited to the methods indicated by figures 1.1 - 1.4. The concentration of a solution controls the thickness of the film in a relationship dependent on the coating method itself. Thicker films are a result of casting from a higher polymer concentration solution.

In drop coating, the polymer solution is adhered to the substrate directly by equipment as simple as a syringe. The volatile solvent then evaporates and the polymer remains in the form of a thin film. The method can be seen in a diagram in figure 1.1. Drop casting is inexpensive and quick but the final

film thickness is difficult to control.

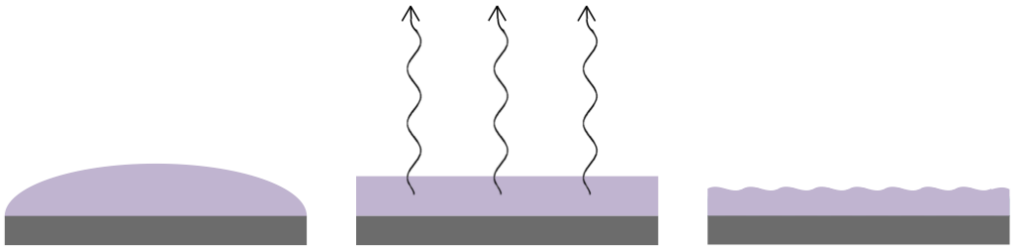

Figure 1.1: Drop coating. (L) The solution is added to the substrate, which is static, using a pipette. (C) The evaporation of the solvent causes the solution to thin. (R) Eventually only the polymer in the solution remains, leaving behind a polymer thin film.

Spray coating utilises a nozzle which sprays the substrate with solution as shown in figure 1.2. The film thickness is varied by using different nozzles and coating times; a larger nozzle used for a longer time will lead to a thicker film. This method can be expensive due to a variety of nozzles necessary for different film thicknesses but the films produced are typically very uniform at large thicknesses [5]. Spray coating is an excellent method by which to make high quality films with a large area, to the extent that this method of coating is primarily used in the photovoltaics industry.

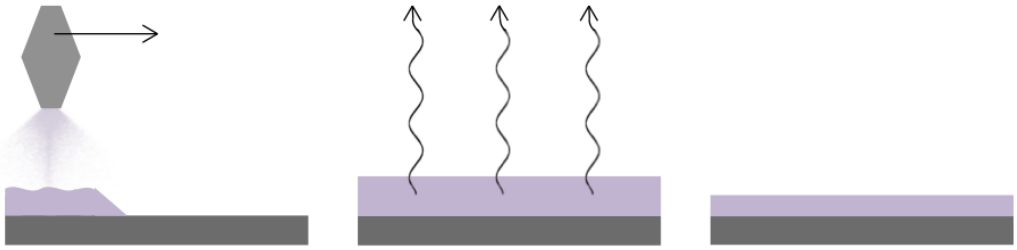

Figure 1.2: Spray coating. (L) The solution is added to the substrate, which is static, using a nozzle to spray the solution. (C) The evaporation of the solvent causes the solution to thin. (R) Eventually only the polymer in the solution remains, leaving behind a polymer thin film.

Dip coating involves a substrate which is immersed in the polymer solution. The substrate is then removed, the solvent evaporates and a dually coated surface remains, as is shown by figure 1.3. The thickness of the resultant film is controlled by the speed at which the substrate is removed from the

solution. The process can be slow and potentially wasteful due to the excess solution required for immersion but the films produced have a good thickness uniformity.

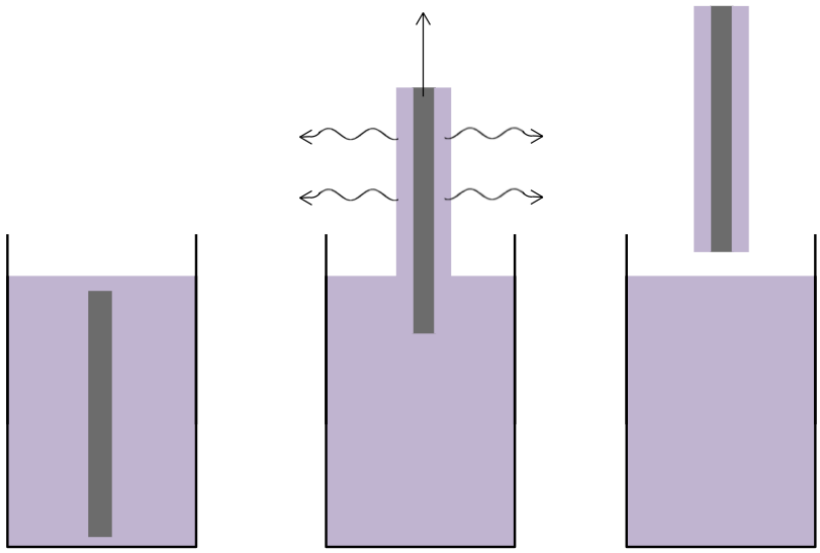

Figure 1.3: Dip coating. (L) The substrate is completely immersed into the solution. (C) The substrate is slowly removed from immersion. As this happens, the solvent in the solution adhered to the substrate begins to evaporate. (R) Eventually only the polymer in the solution remains, leaving behind a polymer thin film.

In spin coating, the substrate is adhered to a platform by means of a vacuum as shown in figure 1.4. The platform and substrate are then spun at an angular velocity ω for a time t. These two variables are the spin parameters and when varied they alter the thickness of the film; a larger ω and t will result in a thinner film.

The solution is added to the substrate either before or during the spin. As the mass of the substrate and solution after the pipette deposition is concentrated in the centre of the film, an inertial force is induced which causes the solution to fully coat the substrate. This effect is often referred to in the literature as the centrifugal force, the pseudo-force which is often used to describe the effect of a lack of inertia on a spinning mass. This is the inertial dominant period of thinning, which can last between a few milliseconds or couple of seconds. After this initial stage occurs, the thinning caused by the solvent in the solution evaporating becomes more significant. This stage is the evaporation dominant period of thinning, which upon completion, leaves

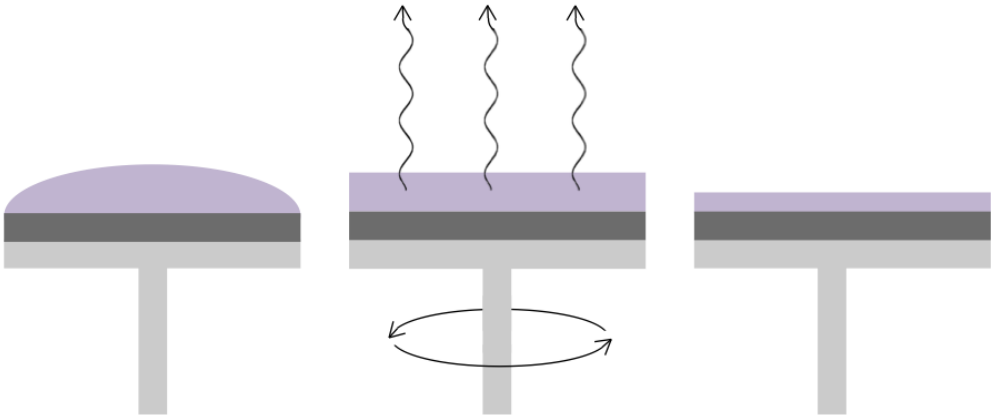

Figure 1.4: Spin coating. (L) The solution is added to the substrate, which is static, using a pipette. It is also possible to deposit the solution onto the substrate when it is already spinning. (C) The platform begins to spin at an angular velocity, ω for a time t. As this occurs, the inertial forces and solvent evaporation cause the film to thin. (R) Eventually only the polymer in the solution remains, leaving behind a polymer thin film.

behind the polymer thin film. The thickness of a film produced by spin coating depends on multiple factors. A solution with a high polymer concentration will be more viscous and therefore result in a thicker film. As mentioned previously, the thickness of the film can be controlled with spin parameters; time t and angular velocity ω.

Table 1 compares three methods of coating. The advantages and limitations of each method determine their suitability to different applications. Spin coating is limited to flat surface coating, whereas spray coating and dip coating can cover complex surfaces and step heights. Films produced by spin coating are typically uniform in thickness but they are prone to imperfections at large radii.

As a result of these factors, spray coating is a preferred industrial method to produce large polymer films however it not suitable for viscous polymer solutions and it is more expensive. Spin coating can coat viscous solutions and is relatively inexpensive, but its radial limitation is significant. If radial non-uniformities in a spin coating can be predicted and mitigated, this could lead to reduced industrial costs in the production of large thin films.

Spin coated films cast with more than one polymer are also subject to phase separation, which is difficult to model on a spin coated thin film [7, 8]. How-

Name	Thickness	Cost	Thickness Uniformity	Misc.
Spray	2nm-20μm	expensive	mixed	Conformal step coverage, suitable for large films but requires a solution with a low viscosity. Film uniformity increases with thickness.
Dip	20nm-50μm	inexpensive	poor	A continuous process but films are susceptible to voids.
Spin	10nm-5μm	inexpensive	good	Good thickness control and reproducibility but limitations in film quality with increased area due to striations.

Table 1: Comparing coating methods. Adapted from *Solution Processing of Inorganic Materials*, D. B. Mitzi, 2009, page 50 [6].

ever numerous research groups have observed how varying experimental conditions have an effect on the final film [9].

Radial striations are film imperfections that originate from random, thermal fluctuations in the initial phase of spin coating and become more prominent with increasing time and radius, as can be seen in figure 1.5. They can also be seen in photoresist films [10] and silica gel films [11]. A higher ambient temperature has been a clear cause of these film imperfections [12–15]. Such non-uniformities have been found to be removed completely when the ambient temperature is reduced; PS-PMMA blend films of 3.5% polymer concentration were found to have negligible imperfections when cast at 15°C or below [16].

The solvent used to make a spin coating solution has an effect on the resultant thin film due to differing evaporation rates. Solvents with high volatilities such as tetrohydrofuran (THF) and methyl ethyl ketone (MEK) have been shown to have more radial striations than thin films cast with toluene, which has a lower evaporation rate. If striations are undesired, a less volatile solvent is recommended [17].

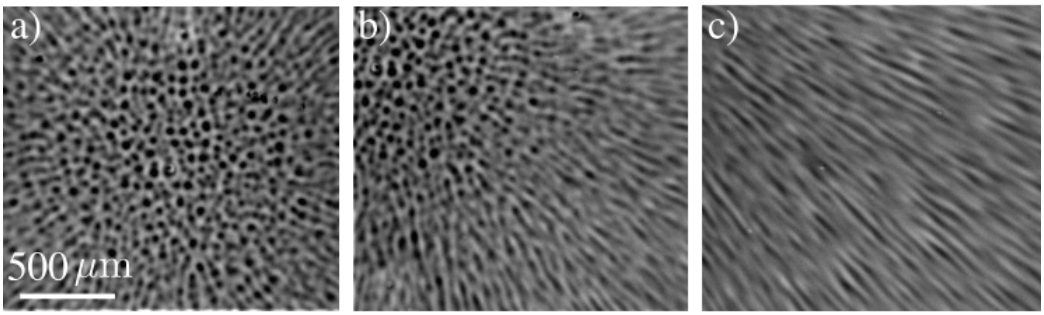

Figure 1.5: Optical microscope images at various radii of a striated film at a) the film centre, b) a small distance away from the centre of the film and c) the edge of the film. The radial striations are noticeable in b and more so c thus indicating greater prominence with radius. From P. D. Fowler et al, 2016 [16].

Numerous research groups have derived models to determine final film thickness and thinning rate of a spin coating. One of the first models to gain the thickness of a spin coated film was that of Emslie, Bonner and Peck (EBP) [18]. In this model, no solvent was considered and so no evaporation parameter was included: the film was assumed to be dry. The substrate was considered infinite in radius and parallel to the film surface in order to disregard edge effects or gravitational effects on film formation. EBP assumed that during a spin coating, the viscous forces balanced the centripetal forces. As a result, the parameters that affected the thinning rate of the film were derived to be either intrinsic to the film itself, such as solution density, viscosity and thickness, or related to the spin parameters, angular velocity and time. Equation 1.1 gives the thinning rate dh/dt obtained by the EBP model in terms of solution density ρ, solution viscosity η and film thickness h, as well as the spin parameters angular velocity ω and time t.

$$\frac{dh}{dt} = -\frac{2\rho\omega^2 h^3}{3\eta} \tag{1.1}$$

A model for the thinning rate of wet films was developed by Meyerhofer [19]. This model includes two terms to represent two regions in spin coating where different physics dominate. In the initial few milliseconds of spin coating the model is similar to that of Emslie, Bonner and Peck and inertial forces dominate the thinning of the film. At this stage, the thinning rate is dominated by the viscous flow of the solution and the solvent evaporative effects are negligible. When the viscous flow reduces, the thinning due to the evaporation of the solvent begins to be the most significant contributor

to film thinning. For simplicity, Meyerhofer assumed that the evaporation rate was constant and that solvent does not evaporate until the viscous flow ends. The thinning rate of the Meyerhofer model is therefore given by

$$\frac{dh}{dt} = -\frac{2\rho\omega^2 h^3}{3\eta} - E, \tag{1.2}$$

in which solution density is ρ, its viscosity is η, the angular velocity is ω and the evaporation rate of the system is E. No overlap between the inertial forces and solvent evaporation is considered in this model. Experiments show that this is not the case and an intermediate transition stage of spin coating, where viscous flow and evaporation rate both significantly contribute to thinning, does occur.

The Reisfield, Bankoff and Davis (RBD) [20] model considers thorough fluid mechanics of spin coating solutions, governed by a set of differential equations known as the Navier-Stokes equations. The assumptions made were that the solution was Newtonian in nature and flow was axisymmetric. To simplify the derivation, Reisfeld, Bankoff and Davis worked with dimensionless parameters but after the full derivation and restoring the dimensions, the thinning rate is given by

$$\frac{\partial h}{\partial t} = -\left(E + \frac{2\omega^2\rho h^3}{3\eta} + \frac{5E\omega^2\rho^2 h^4}{12\eta^2} - \frac{68\omega^4\rho^3 h^7}{315\eta^3}\right), \tag{1.3}$$

in which solution density is ρ, its viscosity is η, the angular velocity is ω and the evaporation rate of the system is E. Evaporation rate is typically given in units of $\mathrm{kg.m^{-2}.s^{-1}}$ but as the Meyerhofer and RBD models only consider the film thinning in one dimension, the evaporation rate is given in thickness per unit time [19, 21].

Each of the models discussed make numerous assumptions in order to simplify the derivation but the validity of each assumption is disputable. The Emslie, Bonner and Peck model only concerns dry films which is incorrect as films are cast from volatile solutions. The Meyerhofer model assumes no solvent evaporation at the start of spin coating which is inaccurate for spin coatings done at ambient temperature. Additionally, the assumptions made by Meyerhofer lead to a model that does not produce either analytical or numerical solutions [22]. Despite the Reisfeld, Bankoff and Davis model being more thorough by considering fluid mechanics, assumptions are made for the sake of simplifying the derivation: complicated contributing effects are

deemed negligible with little justification; dimensions are wholly ignored in order to focus on very specific cases; despite a sharp increase in viscosity as solvent evaporates, the solution is always assumed to have Newtonian flow.

The product of these assumptions are three spin coating models that give approximations for both thinning rate and final thickness at the centre of a film but as discussed, spin coated films can vary greatly with radius. All three models ignore radial effects and therefore can be improved by considering a region of film away from the centre.

Previous research had been done at the University of Sheffield which considers these three models. A spin coater called the optospinometer was adapted in order to perform *in situ* light scattering experiments. Laser light is incident to the surface of the film being cast and this light is either refracted or reflected. The refracted light gives information about the thickness of the film as the emergent light intensity oscillates between constructive and destructive interference. Some reflected light is off-specular due to the rough surface of the heterogeneous film. This light can be collected and used to infer a phase separation length scale of the film.

Between January 2005 and July 2014, the effect the evaporation rate of a PS/PMMA/toluene ternary solution had on phase separation in the spinning films was the main focus of optospinometry experiments. The evaporation rate can be controlled using a chamber to control the vapour pressure surrounding the system. Films were cast using PS, PMMA and toluene at a variety of vapour pressures by flooding the chamber with toluene vapour. The films cast in higher vapour pressures indicated these films had a slower evaporation rate [21]. When imaged using optical microscopy, regardless of evaporation rate, the films showed differences between the centre of the film and the edge, as shown in figure 1.6. This work utilised the Meyerhofer model in order to find the solvent evaporation rate.

These results lead to experiments that explored the effect evaporation rate has on the thinning of a PS/PMMA/toluene film. Results were compared to predictions by both the Meyerhofer and RBD models and the latter was found to be the more accurate of the two [23]. These optospinometry experiments focussed on the centre of the film and used theoretical models that ignore radial dependence.

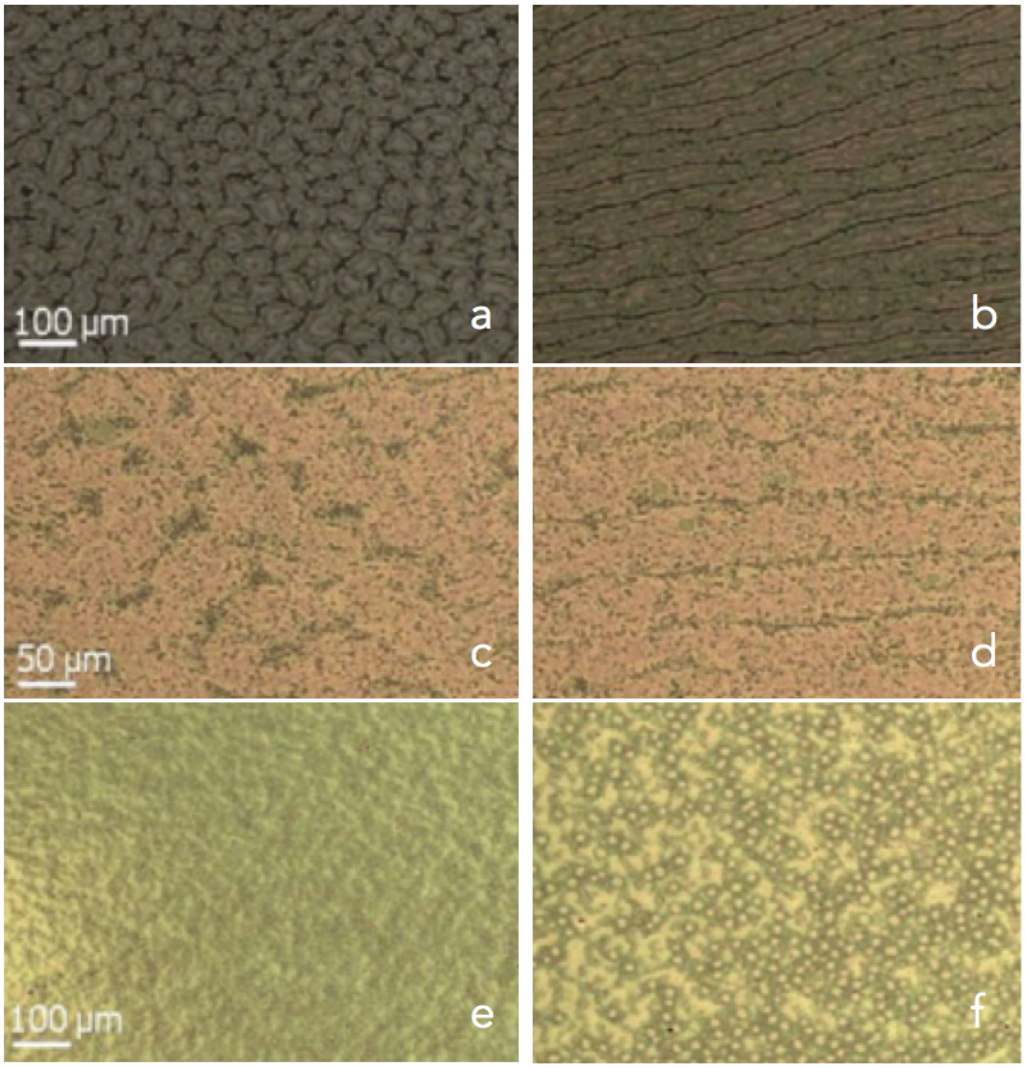

Figure 1.6: Optical microscope images of various films. The film imaged for both figures a) and b) had an evaporation rate of $3.15\mu m.s^{-1}$ but a) is at the centre of the film and b) is at the edge. The film imaged for both figures c) and d) had an evaporation rate of $1.03\mu m.s^{-1}$ but c) is at the centre of the film and d) is at the edge. The film imaged for both figures e) and f) had an evaporation rate of $0.42\mu m.s^{-1}$ but e) is at the centre of the film and f) is at the edge. From P. Mokarian-Tabari et al, 2010 [21].

1.1 Motivations and Aims

The consideration of the industrial applications, spin coating models and experimental results discussed henceforth lead to a hypothesis. Inertial forces are considerable contributors to film thinning and the linear velocity v of a point on a film increases with radius r in the relationship $v = 2\pi r/t$. The primary hypothesis is that a polymer film dries more quickly at regions further away from the film centre and as such, film formation cannot be assumed constant with radius.

The motivation of the work presented in this thesis is to improve theoretical models of spin coating in order to account for predicted radial dependency. If the physics of the spin coating process is fully understood, unwanted radial effects can be mitigated and spin coating can be used to make large organic films. In contrast, if complex structures are desired in a final film, as is often the case for organic electronics, the phase separation of blended films can be manipulated to form these structures without added expense.

The wider implications of this research is improving the methods in which industries produce large, high quality, inexpensive polymer films that can be used as organic solar cells. Solar cells with a low environmental impact are imperative considering the global supply of oil, gas, coal and uranium is estimated to be depleted within the next century [24], in addition to how the consumption of non-renewable energy is irreversibly damaging the planet [25]. This also has importance from a financial perspective, as the photovoltaics industry reported a growth rate of 24% between 2010 and 2017 [26].

The aims of this research is to test the validity of the RBD model for large radius films by comparing its predictions with experimental data from various radii across a polymer film. The thickness as a function of time for the centre of the film in addition to 4mm, 8mm and 12mm from the film centre would be compared to the model. If radial distinctions were present, the possible causes of such a relationship would be proposed by examining the literature and the assumptions made by Reisfeld, Bankoff and Davis. The experimental results could then be used to derive a model for spin coating that depends on radius. Blended PS/PMMA films and homopolymer PS or PMMA films were cast using toluene as a solvent. Whilst PS and PMMA are not usually used in organic electronics, both polymers have been the subject of many experiments in materials science and so any unexpected effects observed in the experiments presented in this thesis would have plethora of results for comparison, in contrast with polymers such as PCDTBT or PEDOT:PSS which are less widely studied. Further to this, both PS and PMMA do not

crystallise, which would add difficulty in analysing any *in situ* spin coating data. Both polymers have similar interaction parameters with toluene ($\chi_{\mathrm{PS/toluene}} = 0.44$ and $\chi_{\mathrm{PMMA/toluene}} = 0.41$) but have distinct refractive indices ($n_{\mathrm{PS}} = 1.5894$ and $n_{\mathrm{PMMA}} = 1.4893$) which is useful in light scattering experiments.

Additionally the interactions between immiscible polymers were explored in a side project done in collaboration with the Free University of Brussels. Multilayered structures are an important aspect of organic electronics although the interfaces between layers are not yet fully understood. The layers do not have discrete interfaces and the boundaries are susceptible to an intrinsic broadening effect called the interfacial width. Experimental measurements of the interfacial width are typically larger than that predicted by theoretical models. The additional broadening of the interface is attributed to thermally induced capillary waves, which have the potential to fully disrupt a thin layer.

Understanding the effect of the capillary waves has important implications in the organic electronics industry. The efficiency of organic solar cells is dependent on their discrete layers and so minimising the effect of capillary waves is beneficial. Organic electronics such as semi-conductors often require intricate micro-scale or nano-scale structures, which are often time-consuming and expensive to produce. If the disruption of a polymer layer due to capillary effects can be harnessed, it can be manipulated to cause desired structures to self-assemble.

With this in mind, a secondary aim of was to detect a fully disrupted layer in a multi-layered polymer structure. Trilayers consisting of PS and deuterated PMMA (d-PMMA) were made by spin coating and film floating. The thickness of the central d-PMMA layer was varied between 6nm and 17nm thick. The foundation and surface PS layers were much thicker in comparison, with estimated thicknesses of 200nm. The trilayers were subject to neutron scattering after various annealing times in order to measure the interfacial widths of the internal boundaries. The neutron beam experiments were done at OFFSPEC, ISIS, Rutherford Appleton Laboratory (RAL) in Didcot, UK and at the Institut Laue-Langevin (ILL) in Grenoble, France.

Chapter 2 will thoroughly explain the necessary theory to undertake this research. The spin coating models and their assumptions shall be discussed in order of publication; EBP, Meyerhofer and RBD. A brief summary of relevant polymer physics shall then be detailed, including polymers and their interactions with solvents, the Flory-Huggins theory, ternary polymer blends and how the viscosity of solutions are calculated. How the polymer physics translates to the morphology of thin films shall then be considered.

Chapter 3 will detail the experimental techniques used. More detail will be given about the primary piece of equipment, the optospinometer: a spin coater with a 633nm laser incident to the surface at an angle of 45°. Once incident to the polymer film and the reflective substrate, the emergent light is either reflected or refracted. The light is then used to infer information about thin film formation during spin coating. How this data output is processed shall be included here. The optospinometer has been used to examine the centre of the film in previous experiments but the focus of this work has been radial differences in the properties of the films. The optospinometer has been adapted in order for this to be done and this shall be addressed. In addition to this, Chapter 3 will contain the properties of the chemicals used in the project, the programs and code used in analysis and the specifications of secondary equipment, such as the optical microscope and ellipsometer.

Chapter 4 discusses the initialisation of the RBD model, including defining its variables and reintroducing its dimensions, which were necessarily removed in the derivation. The results from targeting the laser at the centre of the film compared to data obtained at the various radii are presented. These thicknesses as a function of time for the centre, 4mm, 8mm and 12mm are compared against the RBD model, which does not assume a radial dependence. The validity of the RBD model is tested and discussed.

Chapter 5 presents results regarding the morphology of the produced films using data obtained from off-specular light scattering, optical microscopy and atomic force microscopy. Any differences in the radial variations in film properties are subject to discussion, in addition to probable causes.

Chapter 6 details the theory, experimental methods and final results from the experiment exploring the interfaces between polymer trilayers.

Chapter 7 summarises the conclusions of this thesis and Chapter 8 is an advisory section on the continuation of spin coating experiments exploring the radial effect of immiscible polymer blends.

2 Theory

This chapter shall contain the necessary theory required to complement the experimental work. Section 2.1 shall be on the primary models of interest to spin coating. Firstly the model developed by Emslie, Bonner and Peck (EBP) is derived. EBP modelled a dry film, as it has no evaporation term. The Meyerhofer model is then derived, which considers the evaporation of the solvent as a contributor to thinning. The Reisfeld, Bankoff and Davis (RBD) model introduces complicated fluid mechanics and as such models a wet film in much more detail than the model developed by Meyerhofer. The RBD model does not account for any radial dependence in thickness and assumes complete film uniformity with changing radius. Whether or not this is an accurate assumption will be subject to discussion.

Section 2.2 is a summary of the physics necessary to understand the polymer interactions in a solution used in spin coating. The physics of monomers bonding to form polymers shall be discussed. Polymers are large and complex structures so statistical physics such as the freely jointed chain model are necessary to consider their parameters such as their size and interactions. A solution consisting of a polymer solute is subject to polymer-solvent interactions and an understanding of this is necessary. The consequential phase separation of a immiscible blend is quantified using the Flory-Huggins theory and the physics of ternary polymer blends. In a ternary system, interactions are increased as the two separate polymers both interact with the solvent and each other. Viscosity governs polymer solution physics and so the viscosity of a blend requires a detailed derivation. Newtonian and non-Newtonian solutions shall be considered.

Section 2.3 considers how the polymer physics is affected by interfaces, edge effects and being cast into a thin film. Polymers act differently depending on their position in a structure. The polymer chains at the centre of large structure are in the bulk and are not subject to interface effects. At the boundary of a polymer blend such as one cast in a thin film, interesting effects can occur which are caused by the interface. Surface tension is a primary influence here and causes many structures seen in thin films. Surface tension induces the Marangoni effect, which is accountable for many morphological features. The models considered in section 2.1 assume that films do not vary in morphology or thickness with changing radius. There are numerous examples of radial variance in films, which are then discussed.

2.1 Spin coating models

Numerous models [7, 8, 18–20, 22, 27–49] have been developed over the years in order to quantify the effects of various spin coating variables. The three of primary interest to the work undertaken here are derived in this section. Emslie, Bonner and Peck modelled the thinning of dry spin coated films. Meyerhofer modelled wet films by introducing an evaporation term. Reisfeld, Bankoff and Davis considered detailed fluid dynamics that affect the thinning of a spin coated film.

2.1.1 The Emslie, Bonner & Peck Model

This model [18] was developed in order to test how film thickness and uniformity were affected by differing initial distributions of the material involved in the spin coating. It found that regardless of whether the initial profile was Gaussian or evenly distributed, the final film would have a uniform thickness.

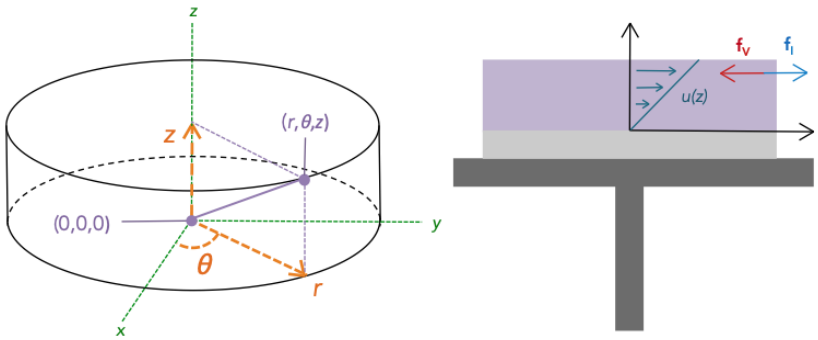

Figure 2.1: A diagram showing the dimensions of the EBP model and the direction of the inertial and viscous forces.

The model assumes that:

1. The rotating plane is infinite, so edge effects are not considered.
2. The rotating plane is horizontal, so gravitational forces do not influence the motion of the solution.
3. The solution is radially symmetrical so there is no variation in gravitational potential.
4. The solution is so thin that shear resistance is negligible in the θ direction and z direction, but not the r direction.

5. The solution is a Newtonian and the fluid is incompressible.
6. Coriolis forces are negligible.
7. The film is dry and no evaporation occurs.

Consider the spinning substrate in polar coordinates (r, θ, z) where the centre and bottom of the film is described by $(0, 0, 0)$ as seen in figure 2.1. A number of vectors are needed for the derivation; angular velocity $\overrightarrow{\omega}$, radial $\overrightarrow{r}$ and velocity of the flow of the liquid film $\overrightarrow{u}$ which are described in equations 2.1, 2.2 and 2.3 respectively.

$$\overrightarrow{\omega} = (0, 0, \omega) \tag{2.1}$$

$$\overrightarrow{r} = (r, 0, 0) \tag{2.2}$$

$$\overrightarrow{u} = (u_{\mathrm{r}}, u_{\theta}, u_{\mathrm{z}}) \tag{2.3}$$

The thinning of the film can be expressed by the balance of two radial forces, given by

$$-\overrightarrow{f_{\mathrm{I}}} = \overrightarrow{f_{\mathrm{V}}}. \tag{2.4}$$

$\overrightarrow{f_{\mathrm{I}}}$ is the centripetal force, which contributes to film thinning. $\overrightarrow{f_{\mathrm{V}}}$ is the viscous force which resists the film thinning. Both $\overrightarrow{f_{\mathrm{I}}}$ and $\overrightarrow{f_{\mathrm{V}}}$ are forces per unit volume and only act in the radial direction. The centripetal force is represented less generally by

$$\overrightarrow{f_{\mathrm{I}}} = \rho\overrightarrow{\omega} \times (\overrightarrow{\omega} \times \overrightarrow{r}) = \left(\rho r\omega^2, 0, 0\right), \tag{2.5}$$

where density of the solution is given by ρ. The viscous force is represented by

$$\overrightarrow{f_{\mathrm{V}}} = \eta \bigtriangledown^2 \overrightarrow{u} \tag{2.6}$$

where the Laplacian of the velocity vector is given by $\bigtriangledown^2\overrightarrow{u}$ and η is the viscosity of the solution. In cylindrical coordinates, the Laplacian of the velocity vector is equal to

$$\bigtriangledown^2 \overrightarrow{u} = \left(\Delta u_r - \frac{u_r}{r^2} - \frac{2}{r^2}\frac{\partial u_r}{\partial r}\right)\overrightarrow{r} + \left(\Delta u_\theta - \frac{u_\theta}{r^2} - \frac{2}{r^2}\frac{\partial u_\theta}{\partial \theta}\right)\overrightarrow{\theta} + (\Delta u_z)\,\overrightarrow{z}, \tag{2.7}$$

in which Δu_r, Δu_θ and Δu_z are the Laplacians of the radial, azimuthal and vertical components of the velocity vector. Emslie, Bonner and Peck simplify the Laplacian by assuming the film is thin enough that shear forces only act in the r direction. As a result of this assumption, θ and z terms are eliminated. The radial component Δu_r is given by

$$\Delta u_r = \frac{1}{r}\frac{\partial}{\partial r}\left(r\frac{\partial u_r}{\partial r}\right) + \frac{1}{r^2}\frac{\partial^2 u_r}{\partial \theta^2} + \frac{\partial^2 u_r}{\partial z^2}, \tag{2.8}$$

meaning that

$$\bigtriangledown^2 \overrightarrow{u} = \frac{1}{r}\frac{\partial}{\partial r}\left(r\frac{\partial u_r}{\partial r}\right) + \frac{1}{r^2}\frac{\partial^2 u_r}{\partial \theta^2} + \frac{\partial^2 u_r}{\partial z^2} - \frac{u_r}{r^2} - \frac{2}{r^2}\frac{\partial u_r}{\partial r} \tag{2.9}$$

Equation 2.4 shows that the viscous forces balance the centripetal force, resulting in no net radial force. Newton's first law dictates that as there is no net force, the speed of the flow must be constant and so $\frac{\partial u}{\partial r}$ is always equal to zero.

As the film is axial symmetric and there is no acceleration in the film, $\frac{\partial u}{\partial \theta}$ is also equal to zero. From these two assumptions, equation 2.8 simplifies to

$$\Delta u_r = \frac{\partial^2 u_r}{\partial z^2} - \frac{u_r}{r^2}. \tag{2.10}$$

Recalling equation 2.6, the viscous force is therefore equal to

$$\overrightarrow{f_{\mathrm{V}}} = \eta\left(\frac{\partial^2 u_r}{\partial z^2} - \frac{u_r}{r^2}\right). \tag{2.11}$$

This equation for the viscous forces must then be equated to the inertial forces as the two opposite forces contribute to the thickness as a function of time: the inertial forces cause thinning and the viscosity of the solution hinders thinning. These forces involve the radial velocity of the solution u_{r}. This case can be represented by

$$\frac{\partial^2 u_\mathrm{r}}{\partial z^2} = -\frac{\rho\omega^2 r}{\eta} + \frac{u_r}{r^2}, \tag{2.12}$$

in which η is the viscosity of the solution, ρ is the density of the solution, ω is the angular velocity and r is the radius. The term $\frac{u_r}{r^2}$ decays rapidly whilst $\frac{\rho\omega^2 r}{\eta}$ increases and so $\frac{u_r}{r^2}$ can be treated as negligible, producing

$$\frac{\partial^2 u_\mathrm{r}}{\partial z^2} = -\frac{\rho\omega^2 r}{\eta}. \tag{2.13}$$

Equation 2.13 is integrated once to get equation 2.14 where c is the constant of integration.

$$\frac{\partial u_\mathrm{r}}{\partial z} = -\frac{\rho\omega^2 r z}{\eta} + c \tag{2.14}$$

The constant can be calculated by applying the boundary condition of $\partial u_\mathrm{r}/\partial z = 0$ when $z = h$ as at the surface of the film, there is no shear stress. This integration gives the value of the constant c as

$$c = \frac{\rho\omega^2 r h}{\eta}. \tag{2.15}$$

Combining equations 2.14 and 2.15 results in the first integration of 2.13, which is given by

$$\frac{\partial u_\mathrm{r}}{\partial z} = \frac{\rho\omega^2 r h}{\eta} - \frac{\rho\omega^2 r z}{\eta}. \tag{2.16}$$

This is then integrated with respect to z between $z = 0$ and $z = h$, for the bottom of the film and the top of the film respectively, to give equation 2.17. The constant of integration is found from the no-slip condition; at $z = 0$, the velocity of the film does not differ to the velocity of the substrate.

$$u_\mathrm{r} = \frac{1}{\eta}\left(\rho\omega^2 r h z - \frac{\rho\omega^2 r z^2}{2}\right) \tag{2.17}$$

The radial flow must also be considered so this is integrated with respect to z to obtain equation 2.18 which defines q_f, the radial flow per unit length of circumference.

$$
\begin{aligned}
q_{\mathrm{f}} &= \int_0^h u_{\mathrm{r}} dz \\
&= \left[\frac{\rho\omega^2 r h z^2}{2\eta} - \frac{\rho\omega^2 r z^3}{6\eta} \right]_0^h \\
&= \frac{6\rho\omega^2 r h^3}{12\eta} - \frac{2\rho\omega^2 r h^3}{12\eta} \\
&= \frac{4\rho\omega^2 r h^3}{12\eta} \\
&= \frac{\rho\omega^2 r h^3}{3\eta}
\end{aligned}
\tag{2.18}
$$

To find an equation for the thinning rate, it is necessary to define the change in thickness with time. A partial differential equation for thickness, h, with respect to time, t is equated to zero, $\partial h/\partial t = 0$, in order to use the continuity equation,

$$
r\frac{\partial h}{\partial t} = -\frac{\partial (r q_{\mathrm{f}})}{\partial r}. \tag{2.19}
$$

Combining equation 2.19 with the integral from equation 2.18 results in

$$
\frac{\partial h}{\partial t} = -\frac{\rho\omega^2}{3\eta}\frac{1}{r}\frac{\partial}{\partial r}\left(r^2 h^3\right). \tag{2.20}
$$

For simplicity the constant κ can be defined as $\kappa = \frac{\rho\omega^2}{3\eta}$ which simplifies to

$$
\frac{\partial h}{\partial t} = -\kappa\frac{1}{r}\frac{\partial}{\partial r}\left(r^2 h^3\right). \tag{2.21}
$$

The expansion of equation 2.21 is

$$
-2\kappa h^3 = \frac{\partial h}{\partial t} + 3\kappa r h^2 \frac{\partial h}{\partial r}. \tag{2.22}
$$

Equation 2.22 has the general form of

$$
\frac{dh}{dt} = \frac{\partial h}{\partial t} + \frac{\partial h}{\partial r}\frac{dr}{dt}. \tag{2.23}
$$

From equations 2.22 and 2.23, two differential identities can be obtained, given by

$$\frac{dh}{dt} = -2\kappa h^3, \tag{2.24}$$

and

$$\frac{dr}{dt} = 3\kappa r h^2. \tag{2.25}$$

Equation 2.24 integrates to

$$h = \frac{h_0}{\sqrt{1 + 4\kappa {h_0}^2 t}}, \tag{2.26}$$

in which h is the thickness variable of the film, $\kappa = \frac{\rho\omega^2}{3\eta}$, t is the time and h_0 is the initial thickness of the film at $t = 0$. Figure 2.2 shows the position of h_0 with respect to the polar coordinate system. Equation 2.26 rearranges to equation 2.27 which gives the thickness as a function of time, as is desired.

To summarise, the time-dependent thickness according to the EBP model is given by

$$h\left(t\right) = h_0 \left(1 + \frac{4{h_0}^2 t\rho\omega^2}{3\eta}\right)^{-\frac{1}{2}}, \tag{2.27}$$

and the thinning rate is given by

$$\frac{dh}{dt} = -\frac{2\rho\omega^2 h^3}{3\eta}. \tag{2.28}$$

This model only regards dry films. Often films cannot be assumed to be dry as they contain a solvent which evaporates during the spin coating. This evaporation also contributes to the film thinning and as a result density, ρ, and viscosity, η, cannot be assumed constant. A model that considers evaporation is required.

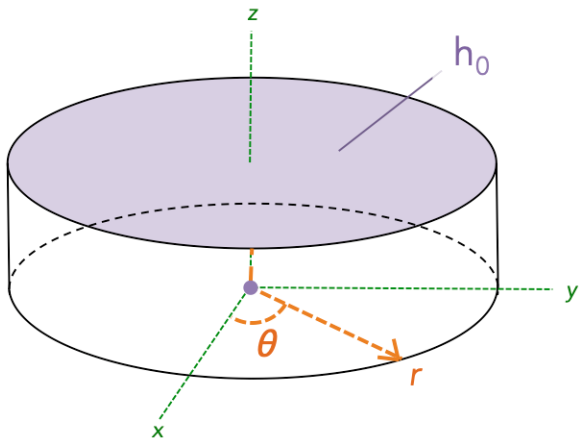

Figure 2.2: A diagram showing h_0 with respect to the polar coordinate system.

2.1.2 The Meyerhofer Model

The model assumes that:

1. The rotating plane is infinite, so edge effects are not considered.
2. The rotating plane is horizontal, so gravitational forces do not influence the motion of the solution.
3. The solution is radially symmetrical so there is no variation in gravitational potential.
4. The solution is so thin that shear resistance is negligible in the θ direction and z direction, but not the r direction.
5. The solution is a Newtonian liquid.
6. Coriolis forces are negligible.

The Meyerhofer model [19] considers the spin coating of a wet film. The model firstly regards how the concentration of the solution varies with time. The solution consists of a solid solute and liquid solvent which are assumed to have the same density and to be mixed uniformly within the solution in equal parts. As with equation 2.28 in the Emslie, Bonner and Peck model, Meyerhofer does not consider film thickness h to be dependent on radius r.

Meyerhofer developed a model that was similar to the EBP model given in equation 2.28 but included an additional term to describe the thinning due to evaporation rate,

$$\frac{\partial h}{\partial t} = -\frac{2\rho\omega^2 h^3}{3\eta} - E \tag{2.29}$$

in which E is the evaporation rate and thus quantifies the film thinning due to evaporative effects. Using equation 2.13 from the Emslie, Bonner Peck model which represents force balance, Meyerhofer was able to solve equation 2.29 using the continuity equation, given by

$$\frac{\partial h}{\partial t} = -\frac{1}{r}\frac{\partial (rq)}{\partial r} - E, \tag{2.30}$$

where r is the radius, E is the evaporation rate and the total radial flow per unit of circumference is defined by q, which is given by

$$q = \frac{\omega^2 r h^3 \rho}{3\eta}. \tag{2.31}$$

Meyerhofer states that to produce a solid film, solvent must evaporate and this is assumed to be constant with radius. As a result, the film concentration rises independently of r. The film thickness h decreases uniformly as it is independent of r. The film is assumed to be thin enough to assume the change in c with z is negligible.

The concentration of the solution is defined by

$$c\,(t) = \frac{X}{X+Y}. \tag{2.32}$$

The concentration varies with time as the solvent evaporates. The volume of the solute is indicated by X and the volume of the solvent is indicated by Y. Both X and Y are given in volume per unit area which leads to the thickness h being represented by

$$h = X + Y. \tag{2.33}$$

As the solvent evaporates, the solution composition changes, becoming increasingly dense and viscous which leads to amendments to density and viscosity. The rate of change of both X and Y due to outflow of material from inertial forces and due to solvent evaporation are given by differential equations, $\frac{dX}{dt}$ and $\frac{dY}{dt}$ which can be calculated for $\frac{dX}{dt}$ by rearranging equations 2.32 and 2.33 for X,

$$X = h(t)c(t), \tag{2.34}$$

then applying the product rule in differentiating,

$$\frac{dX}{dt} = \frac{dh}{dt}c + \frac{dc}{dt}h, \tag{2.35}$$

$$\frac{dX}{dt} = \left(-\frac{1}{r}\frac{\partial(rq)}{\partial r} - E\right)c + \frac{dc}{dt}h, \tag{2.36}$$

and the evaporation rate is equated to $\frac{dc}{dt}h$ and so

$$\frac{dX}{dt} = \left(-\frac{2h^3\omega^2\rho}{3\eta} - E\right)c + E, \tag{2.37}$$

which results in

$$\frac{dX}{dt} = -\frac{2h^3\omega^2\rho c}{3\eta} - Ec + E, \tag{2.38}$$

and

$$\frac{dX}{dt} = -\frac{2h^3\omega^2\rho c}{3\eta} + E\left(1 - c\right). \tag{2.39}$$

Similarly, $\frac{dY}{dt}$ can be found by firstly rearranging equations 2.32 and 2.33 for Y,

$$Y = h(t) - h(t)c(t), \tag{2.40}$$

then differentiating by applying the product rule,

$$\frac{dY}{dt} = \frac{dh}{dt} - \left(\frac{dh}{dt}c + \frac{dc}{dt}h\right). \tag{2.41}$$

Recalling that

$$\frac{dX}{dt} = \frac{dh}{dt}c + \frac{dc}{dt}h, \tag{2.42}$$

$\frac{dX}{dt}$ and the value of $\frac{dh}{dt}$ can be substituted in, giving

$$\frac{dY}{dt} = \left(-\frac{2h^3\omega^2\rho}{3\eta} - E\right) - \left(-\frac{2h^3\omega^2\rho c}{3\eta} + E\,(1-c)\right) \tag{2.43}$$

which simplifies to

$$\frac{dY}{dt} = -\frac{2h^3\omega^2\rho(1-c)}{3\eta} + Ec. \tag{2.44}$$

The equations for $\frac{dX}{dt}$ and $\frac{dY}{dt}$ are integrated numerically, using h_0 and concentration as initialising parameters, until $Y = 0$. This is shown in figure 2.3, where it can be seen that at a relative thickness of 0.3, X/X_0 and Y/Y_0 diverge. This is because inertial effects become a less significant contributor to thinning and the solvent evaporation begins to dominate, eventually reaching 0. Meyerhofer numerically found h_f as a function of ω and this is shown in figure 2.4. This figure shows that at high angular velocities $\omega > 4000$ rpm there is no dependence on the value of h_0. It is at that point that $X_0 = c_0 h_0 > 2h_\mathrm{f}$.

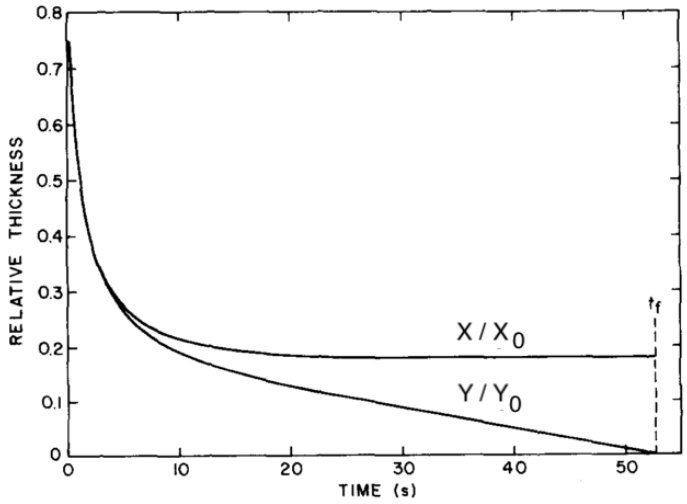

Figure 2.3: The numerical integration of equations 2.39 and 2.44. The parameters input were $h_0 = 30\mu m$, $c_0 = 0.1$, $E = 1 \times 10^{-7}\mathrm{m.s}^{-1}$, $\omega = 4500$rpm and the kinematic viscosity $\nu = \eta/\rho$ was modelled as $\nu = \left(1 \times 10^{-6} + c^4\right)\mathrm{m}^2.\mathrm{s}^{-1}$. From D. Meyerhofer, 1978 [19].

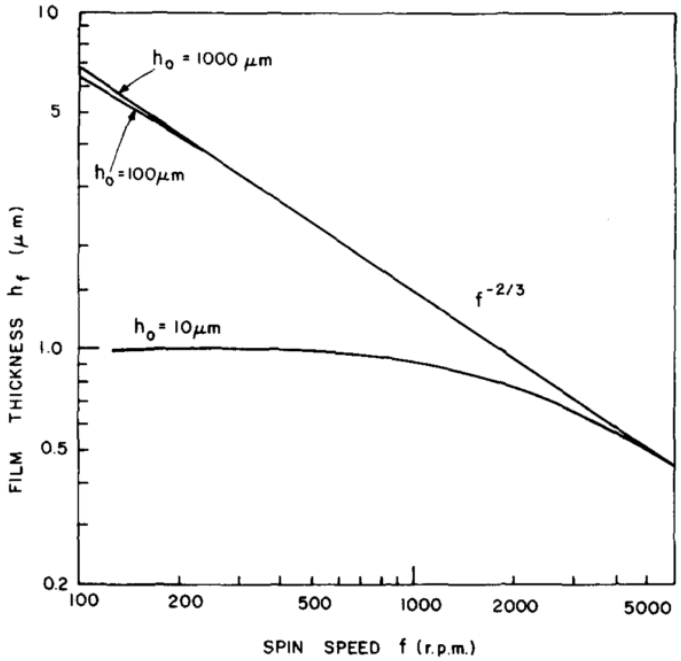

Figure 2.4: The parameters are the same as those in figure 2.3 unless otherwise stated. From D. Meyerhofer, 1978 [19].

As equations 2.39 and 2.44 cannot be solved analytically, the results in figures 2.3 and 2.4 are used to find an approximate value for h_f when the initial concentration of the solute $X_0 > 2h_\mathrm{f}$.

At this point, Meyerhofer simplifies the calculation by assuming that evaporation is negligible at the start of spin coating and that inertial forces are negligible at the end of spin coating. These two regimes are separated by the critical time, t_c which occurs when

$$E = (1 - c_0)\,\frac{2\omega^2 \rho_0 {h_\mathrm{c}}^3}{3\eta_0}, \tag{2.45}$$

in which c_0 is the concentration, ρ_0 the density, and η the viscosity of the initial solution. Recalling that $X = c \times h$ and that after the critical time, inertial thinning is negligible to evaporative thinning, Meyerhofer concludes that the final film thickness is

$$h_\mathrm{f} = X_\mathrm{f} = c_0 h_\mathrm{c} = c_0 \left[\frac{3E\eta_0}{2\,(1 - c_0)\,\omega^2 \rho_0}\right]^{1/3}. \tag{2.46}$$

Meyerhofer concludes that this is a sound solution, but this is not the case. Whilst the model gives a good foundation for the understanding of the two spin coating regimes, inertial and evaporation dominant thinning, they do overlap. Further work on the Meyerhofer model showed that it was incorrectly formulated [22] and no numerical solutions were adequate.

To summarise, the Meyerhofer model is given by

$$\frac{dh}{dt} = -\frac{2\rho\omega^2 h^3}{3\eta} - E. \tag{2.47}$$

2.1.3 The Reisfeld, Bankoff & Davis Model

Most of the assumptions in the Emslie, Bonner and Peck model and the Meyerhofer model do not hold true for the Reisfeld, Bankoff and Davis model. The assumptions are as follows:

1. The rotating plane is not assumed to be infinite and edge effects are considered as a result.
2. Gravity is a contributing factor to certain effects that may be deemed negligible in specific cases.
3. The solution is radially symmetrical so there is no variation in gravitational potential.
4. Shear resistance affects all three directions; r, z and θ.
5. The solution is a Newtonian liquid.
6. Coriolis forces are not negligible.

The derivation [20] is based on a set of differential equations that describe the motion of a fluid: the Navier-Stokes equations, the continuity equation and the boundary conditions. Cylindrical coordinates (r, θ, z) are used.

The vectors necessary for this derivation are the fluid velocity vector,

$$\overrightarrow{u} = (u_r, u_\theta, u_z)\,, \tag{2.48}$$

the angular velocity vector,

$$\overrightarrow{\omega} = (0, 0, \omega)\,, \tag{2.49}$$

and the radial vector,

$$\overrightarrow{r} = (r, 0, 0)\,. \tag{2.50}$$

The unit normal vector is defined as

$$\overrightarrow{n} = \left(-\frac{\partial h}{\partial r}, 0, 1\right)\left[\frac{1}{\sqrt{1+\left(\frac{\partial h}{\partial r}\right)^2}}\right]. \tag{2.51}$$

The unit tangent vectors $\overrightarrow{t_r}$ and $\overrightarrow{t_\theta}$ are defined as

$$\overrightarrow{t_r} = \left(1, 0, \frac{\partial h}{\partial r}\right)\left[\frac{1}{\sqrt{1+\left(\frac{\partial h}{\partial r}\right)^2}}\right] \tag{2.52}$$

and

$$\overrightarrow{t_\theta} = (0, 1, 0)\,. \tag{2.53}$$

An incompressible Newtonian fluid has a Navier-Stokes equation in the form

$$\rho\left[\frac{\partial \overrightarrow{u}}{\partial t} + \overrightarrow{u}.\nabla\overrightarrow{u}\right] = -\nabla P + \rho\overrightarrow{g} + \overrightarrow{f} + \nabla.\mathbb{T} \tag{2.54}$$

in which P is the pressure, ρ is the density, $\overrightarrow{g}$ is the gravitational acceleration vector, $\mathbb{T}$ is the viscous stress tensor and $\overrightarrow{f}$ represents the non-viscous forces exerted on the fluid.

Equation 2.54 has radial r, azimuthal θ and vertical z components. The radial component is

$$\begin{aligned}\rho\left[\frac{\partial u_r}{\partial t} + u_r\frac{\partial u_r}{\partial r} - \frac{u_\theta^2}{r} + u_z\frac{\partial u_r}{\partial z}\right] &= -\frac{\partial P}{\partial r} + \rho g_r + f_r \\ &\quad + \eta\left[\frac{1}{r}\frac{\partial}{\partial r}\left(r\frac{\partial u_r}{\partial r}\right) - \frac{u_r}{r^2} + \frac{\partial^2 u_r}{\partial z^2}\right].\end{aligned} \tag{2.55}$$

The azimuthal component is

$$\rho\left[\frac{\partial u_\theta}{\partial t}+u_r\frac{\partial u_\theta}{\partial r}+\frac{u_r u_\theta}{r}+u_z\frac{\partial u_\theta}{\partial z}\right]=\rho g_\theta+f_\theta \\ +\eta\left[\frac{1}{r}\frac{\partial}{\partial r}\left(r\frac{\partial u_\theta}{\partial r}\right)-\frac{u_\theta}{r^2}+\frac{\partial^2 u_\theta}{\partial z^2}\right]. \tag{2.56}$$

The vertical component is

$$\rho\left[\frac{\partial u_z}{\partial t}+u_r\frac{\partial u_z}{\partial r}+u_z\frac{\partial u_z}{\partial z}\right]=-\frac{\partial P}{\partial z}+\rho g_z+f_z \\ +\eta\left[\frac{1}{r}\frac{\partial}{\partial r}\left(r\frac{\partial u_z}{\partial r}\right)+\frac{\partial^2 u_z}{\partial z^2}\right]. \tag{2.57}$$

The force $\overrightarrow{f}$ must be identified. The RBD model accounts for two forces here, the centripetal force $\overrightarrow{f_{ce}}$ and the Coriolis force $\overrightarrow{f_{co}}$, which are expressed by

$$\overrightarrow{f_{ce}}=\rho\overrightarrow{\omega}\times(\overrightarrow{\omega}\times\overrightarrow{r})=\left(\rho r\omega^2,0,0\right) \tag{2.58}$$

and

$$\overrightarrow{f_{co}}=\rho 2\overrightarrow{\omega}\times\overrightarrow{u}=\left(-2\rho\omega u_\theta,-2\rho\omega u_r,0\right). \tag{2.59}$$

Equations 2.58 and 2.59 are then substituted into equations 2.55 - 2.57 to give the radial, azimuth and vertical components of the Navier-Stokes equations. The radial component of the Navier-Stokes equation is

$$\rho\left[\frac{\partial u_r}{\partial t}+u_r\frac{\partial u_r}{\partial r}-\frac{u_\theta^2}{r}+u_z\frac{\partial u_r}{\partial z}\right]=-\frac{\partial P}{\partial r}+2\rho\omega u_\theta+\rho r\omega^2 \\ +\eta\left[\frac{1}{r}\frac{\partial}{\partial r}\left(r\frac{\partial u_r}{\partial r}\right)-\frac{u_r}{r^2}+\frac{\partial^2 u_r}{\partial z^2}\right], \tag{2.60}$$

in which the gravitational term ρg_r is removed and the term that considers the force $\overrightarrow{f}$ is given in terms of the Coriolis and centripetal force.

The azimuthal component of the Navier-Stokes equation is

$$\rho\left[\frac{\partial u_\theta}{\partial t}+u_r\frac{\partial u_\theta}{\partial r}+\frac{u_r u_\theta}{r}+u_z\frac{\partial u_\theta}{\partial z}\right]=-2\rho\omega u_r + \eta\left[\frac{1}{r}\frac{\partial}{\partial r}\left(r\frac{\partial u_\theta}{\partial r}\right)-\frac{u_\theta}{r^2}+\frac{\partial^2 u_\theta}{\partial z^2}\right], \tag{2.61}$$

in which the gravitational term ρg_θ has also been removed but the force $\overrightarrow{f}$ is only given in terms of the Coriolis force, as the centripetal force has no component in this dimension.

The vertical component of the Navier-Stokes equation is

$$\rho\left[\frac{\partial u_z}{\partial t}+u_r\frac{\partial u_z}{\partial r}+u_z\frac{\partial u_z}{\partial z}\right]=-2\rho\omega u_r + \eta\left[\frac{1}{r}\frac{\partial}{\partial r}\left(r\frac{\partial u_z}{\partial r}\right)+\frac{\partial^2 u_z}{\partial z^2}\right]. \tag{2.62}$$

The gravitational vector does affect the vertical dimension, recalling $\overrightarrow{g} = (0, 0, g)$ but the centripetal and Coriolis forces have no vertical component, so $\overrightarrow{f}$ becomes zero.

The continuity equation is given by

$$\frac{1}{r}\frac{\partial}{\partial r}(ru_r)+\frac{\partial u_z}{\partial z}=0. \tag{2.63}$$

Boundary conditions are then considered to solve these equations in order to describe the thinning of the film. The two boundaries are at the bottom of the film, at the substrate surface, and at the top of the film, where the air begins. These boundaries, and the cylindrical coordinates, are shown in figure 2.5.

The system adheres to the no-slip condition, in which the substrate is impenetrable by the film and the film spins at the same speed as the substrate. This means that the velocity components $u_r(0) = 0$, $u_\theta(0) = 0$ and $u_z(0) = 0$.

At the surface of the film, the boundary conditions are more complicated. Firstly, the 'kinematic boundary condition' is considered, which relates the

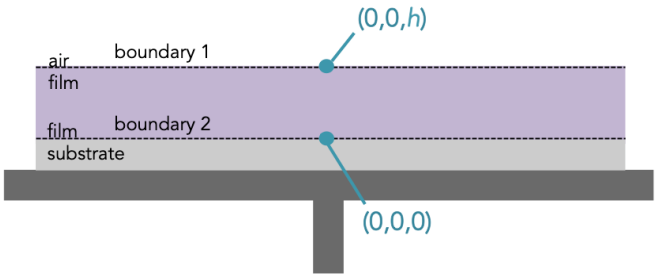

Figure 2.5: A diagram showing the boundaries considered in the RBD model. The centre of the coordinate system $(0, 0, 0)$ is included for clarity, as is the thickness at the centre of the film $(0, 0, h)$.

motion between the film and the air to the fluid velocities at this surface. RBD state that this can be expressed as

$$(\overrightarrow{u} - \overrightarrow{u_{in}}).\overrightarrow{n} = J, \tag{2.64}$$

in which $\overrightarrow{u_{in}}$ is the velocity at the interface, $\overrightarrow{n}$ is the normal vector, defined in equation 2.51 and J is the mass transfer. Substituting the values of all vectors results in an alternative form of J given by

$$J = \left(-\frac{\partial h}{\partial t} - u_r\frac{\partial h}{\partial r} + u_z\right)\left(1 + \left(\frac{\partial h}{\partial r}\right)^2\right)^{-\frac{1}{2}}. \tag{2.65}$$

The 'dynamic boundary condition' describes the forces exerted on the interface, and is composed of three differential equations that quantify the stress at the interface. The normal stress at the free surface equates to the mean curvature $\nabla\dot{\overrightarrow{n}}$ yielding the first defining differential equation

$$\overrightarrow{n}.\mathbb{T}.\overrightarrow{n} = \sigma\nabla.\overrightarrow{n}, \tag{2.66}$$

in which σ is the surface tension. The viscous stress tensor $\mathbb{T}$ for the flow of an axisymmetric incompressible Newtonian liquid is

$$\mathbb{T} = \begin{bmatrix} -P + 2\eta\frac{\partial u_r}{\partial r} & \eta\frac{\partial u_\theta}{\partial r} & \eta\left(\frac{\partial u_r}{\partial z} + \frac{\partial u_z}{\partial r}\right) \\ \eta\frac{\partial u_\theta}{\partial r} & -P & \eta\frac{\partial u_\theta}{\partial z} \\ \eta\left(\frac{\partial u_r}{\partial z} + \frac{\partial u_z}{\partial r}\right) & \eta\frac{\partial u_\theta}{\partial z} & -P + 2\eta\frac{\partial u_z}{\partial z} \end{bmatrix}. \tag{2.67}$$

The two other defining differential equations are simply

$$\overrightarrow{n}.\mathbb{T}.\overrightarrow{t_r} = 0 \tag{2.68}$$

and

$$\overrightarrow{n}.\mathbb{T}.\overrightarrow{t_\theta} = 0, \tag{2.69}$$

as there are no shear forces at the film surface.

Analytically solving the Navier-Stokes equations can then be done in two steps. Firstly lubrication theory is applied, which describes the flow of a fluid where one dimension is much smaller than the other two. In this case, z is much smaller than both r and θ. To apply lubrication theory for this case, the dimensions must be removed from all variables, the continuity equation, the radial, azimuthal and vertical Navier-Stokes components and the boundary conditions.

Secondly, perturbation theory is applied to predict the flow with increasing time. The perturbation considers $t = 0$, the start of the spin coating when the film is static, as the original case which is simpler to solve.

The full derivation that removes the dimensions and utilises both lubrication and perturbation theory is considered fully in the literature [20].

In the full RBD derivation, equations 2.70-2.74 are defined which are useful in redimensionalising the thinning rate obtained. Equations 2.70-2.74 only consider the initial conditions of the solution and as such the terms such as viscosity and thickness are denoted by a 0 subscript. They can be adapted to time-dependent cases by using the equivalent time-dependent values.

The scale factor ϵ is the ratio of the initial thickness of the film h_0 to the total radius of the film itself R, given by

$$\epsilon = \frac{h_0}{R}. \tag{2.70}$$

The kinematic viscosity ν_0 of the solution is a necessary quantity when considering moving fluids. It depends on the intrinsic viscosity of the solution η_0 and its density ρ, shown by

$$\nu_0 = \frac{\eta_0}{\rho}. \tag{2.71}$$

There is a velocity scale in the radial direction which is represented by U_0. The frequency of the spin coating ω, the initial film thickness h_0, the total film radius R and the dynamic viscosity ν_0 all contribute to this in the relationship defined by

$$U_0 = \frac{\omega^2 h_0^2 R}{\nu_0}. \tag{2.72}$$

The solution acts as a liquid and therefore has a dimensionless Reynold's number $\mathtt{Re}$ defined by

$$\mathtt{Re} = \frac{U_0 h_0}{\eta_0}, \tag{2.73}$$

which quantifies the degree of flow. It is given by equation 2.73 in terms of radial velocity scale U_0, the initial thickness of the film h_0 and the viscosity η_0.

Rearranging equations 2.70 - 2.73 can give the Reynold's number in known terms,

$$\mathtt{Re} = \frac{\omega R h_0^3 \rho^2}{\nu^2}. \tag{2.74}$$

The full derivation of RBD results in equation 2.75, where r is evaluated. The thickness is given by h^* which is the dimensionless thickness at time t given by $h\left(t\right)/h_0$ in which h_0 is the initial thickness. The dimensionless evaporation rate is e.

$$\begin{aligned} 0 =& \frac{\partial h^*}{\partial t^*} + \frac{2e}{3} + \frac{r^2 h^{*3}}{3r} + \frac{5\epsilon \mathtt{Re} r h^{*4} e}{36} + \frac{2\epsilon \mathtt{Re} r^2 h^{*6}}{15}\frac{\partial h^*}{\partial r} - \frac{34\epsilon \mathtt{Re} r h^{*7}}{315} \\ & - \frac{\epsilon \mathtt{Re} h^{*3}}{3F^2}\frac{\partial h^*}{\partial r} + \frac{\epsilon h^{*3} T}{3}\frac{\partial h^*}{\partial r} \end{aligned} \tag{2.75}$$

The final two terms in equation 2.75 refer to the Froude effect and the Weber effect respectively. The Froude effect describes how gravity effects the flow of the fluid and is quantified by the Froude number, which is given by

$$F = \frac{\overrightarrow{u}}{\sqrt{\overrightarrow{g}\, d}}, \tag{2.76}$$

in which $\overrightarrow{g}$ is the flow velocity vector of the fluid, $\overrightarrow{g}$ is the gravitational field and d is the characteristic length of the flow field. The Weber effect quantifies the ratio of surface tension to inertial forces and is typically used when considering highly curved surfaces in fluid mechanics, such as droplets and bubbles. The effect is quantified by the Weber number, which is given by

$$T = \frac{\rho u^2 d}{\sigma} \tag{2.77}$$

in which ρ is the fluid density, u is its velocity, d is the characteristic length of the flow field and σ is the surface tension. RBD determine both the Froude and Weber effects as being negligible, yet admitted that their significance may become clear when considering films cast on rough substrates or with larger radii.

$$0 = \frac{\partial h^*}{\partial t^*} + \frac{2e}{3} + \frac{r^2 h^{*3}}{3r} + \frac{5\epsilon \mathtt{Re} r h^{*4} e}{36} + \frac{2\epsilon \mathtt{Re} r^2 h^{*6}}{15}\frac{\partial h^*}{\partial r} - \frac{34\epsilon \mathtt{Re} r h^{*7}}{315}. \tag{2.78}$$

Crucially to the work undertaken in this thesis, at this point Reisfeld, Bankoff and Davis assume that the film does not change with radius and all values of $r = 1$ and $\partial h^*/\partial r = 0$ which results in equation 2.79.

$$0 = \frac{\partial h^*}{\partial t^*} + \frac{2e}{3} + \frac{h^{*3}}{3r} + \frac{5\epsilon \mathtt{Re} h^{*4} e}{36} - \frac{34\epsilon \mathtt{Re} h^{*7}}{315} \tag{2.79}$$

The thinning rate can therefore be expressed as

$$\frac{\partial h^*}{\partial t} = -\frac{2e}{3} - \frac{h^{*3}}{3} - \frac{5\epsilon \mathtt{Re} h^{*4} e}{36} + \frac{34\epsilon \mathtt{Re} h^{*7}}{315}, \tag{2.80}$$

in which e is the dimensionless evaporation rate, ϵ is the scale factor and $\mathtt{Re}$ is the Reynold's number. Equation 2.80 is the dimensionless version of the RBD model, which must be modified in order to be used to analyse experimental results.

2.2 Polymer Physics

This subsection shall focus on the the structure of a polymer as a chain of bonded monomers and how this structure can impact their behaviour.

In a typical polymer blended film-formation process, two polymers are dissolved in a common solvent and as the film is cast, the solvent evaporates leaving a thin polymer film. Polymers are rarely miscible [50–52] so such a solution will often phase separate. Self-assembly consists of disordered systems arranging into structures that are energetically favourable in order to reduce the free energy [53–57]. In spin coating these effects are often seen as film imperfections. However system conditions can be manipulated in order to produce a structure that proves useful [55, 56] which can reduce costs in industrial processes that require nanometre-scale structures.

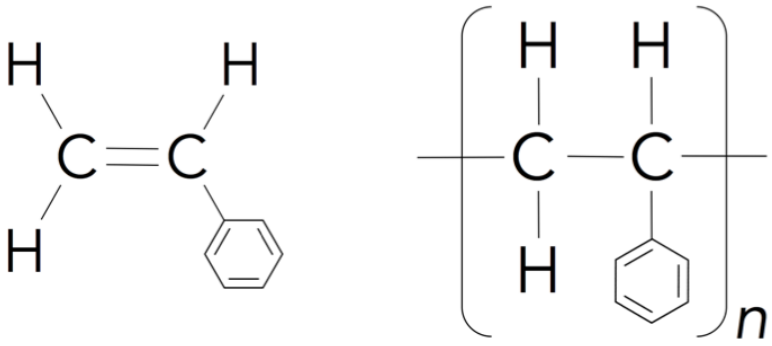

Figure 2.6: The chemical structures of styrene (L) and poly(styrene), PS (R). Styrene contains a double bond which is broken when the monomer units covalently bond to one another to form PS.

2.2.1 Polymer Bonds

Polymers form via the covalent bonding of subsequent monomer units. In the case of homopolymers, these monomers are identical. In figure 2.6, the double bond between the two carbon atoms in the styrene molecule breaks and a bond is formed between another styrene molecule. The degree of polymerisation is given by N and the system is described as a dimer, as $N = 2$. Similarly when three styrene monomers bond in the same process, the degree of polymerisation $N = 3$ and a trimer is formed. As the degree of polymerisation increases to $N \geq 7$, the macromolecule is typically considered as an oligomer. Many more monomer units are bonded together in this way

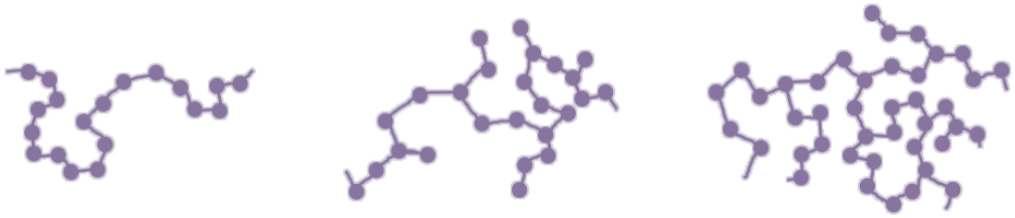

Figure 2.7: This diagram shows how the structure differs between linear polymers (L), branched polymers (M) and crosslinked polymers (R). Branched polymers and crosslinked polymers have more complicated structures than linear chains.

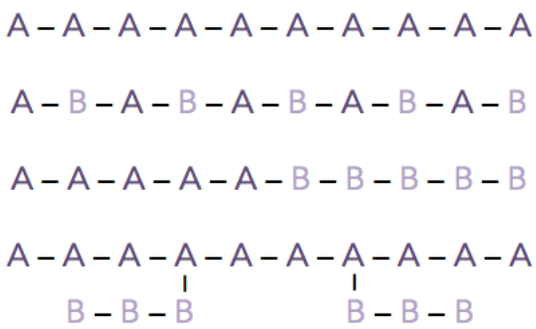

Figure 2.8: Monomers A and B can be arranged in a variety of configurations. The top is a homopolymer composed of A monomers. The second example is an alternating copolymer consisting of A and B monomers. The third polymer is a diblock copolymer as polymer blocks of A and B monomers are bonded together. The final example is a branched copolymer or a graft copolymer and B polymers have bonded to a linear polymer chain of A monomers.

to form polystyrene. It is not uncommon to have $N \geq 10^4$ as a polymer often consists of thousands of monomer units.

Double bonds are more rigid but single bonds have a torsional degree of freedom. As a result of this, polymer chains are often flexible and able to contort in a variety of shapes.

It is possible for the base chain to also be branched. The end of such a branch can bond to a different chain or another point on the same chain. Such a polymer is described as crosslinked. The differences in the architecture of these polymer chains can be seen in figure 2.7. The extra bonds on branched and crosslinked polymers makes it more complex to consider mathematically and as only linear chains are used in these experiments, only these shall be discussed henceforth.

Copolymers contain more than one type of monomer. Monomers A and B can be bonded in a polymer with various structures such as those shown in figure 2.8. The first example in this figure is a simple polymer consisting of monomer A. The second example is a copolymer. A and B do not necessarily alternate in such a copolymer and can be randomly assorted. The third example in figure 2.8 is a diblock copolymer. The two types of monomers are connected to one another and monomer block A and B are joined by a bond. Such a polymer is not limited to only two blocks; triblock copolymers exist if three different monomer blocks are present, such as A, B and C.

Upon considering branching and copolymer architecture, it is clear that a wide array of polymer structures are possible. This thesis will focus on the blending of two distinct, linear homopolymers; PS and PMMA.

2.2.2 The Freely Jointed Chain

As linear homopolymers are molecular chains consisting of repeating monomer units, the polymer can be characterised mathematically by considering each monomer unit to be an individual segment in a larger polymer chain. The freely-jointed chain model is where each monomer connects to its neighbour in a random direction as it has a free bond angle. This is an ideal case as in reality, repulsive forces between the monomers cause limitations to the segment orientation. The freely-rotating chain is a similar model that considers a fixed bond angle.

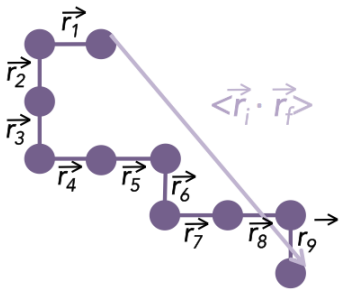

Figure 2.9: The two-dimensional freely jointed chain. The initial monomer is situated at the centre of the grid. The monomers added in sequence have a 25% chance of being added to the chain in each of the four possible directions.

The freely jointed chain can be considered in one, two or three dimensions. For the general case, a polymer is built consisting of N monomers of indi-

vidual size a. Figure 2.9 is a diagram of a polymer constructed by a two-dimensional random walk and confined to a square lattice. The polymer in this example has ten segments, $N = 10$. Each consecutive monomer has an equal possibility of being added to the preceding monomer in any direction, 25%. The contour length of the polymer chain is found simply from the sum of the individual monomer sizes, given by

$$R = \sum_{i=1}^{N} a_i. \tag{2.81}$$

The polymer is coiled somewhat so it could have an effectual size smaller than its length. The end-to-end vector could be used to quantify the chain dimensions. Figure 2.9 shows a two-dimensional chain confined to a square lattice. The end-to-end vector is given by

$$\vec{R} = \sum_{i=1}^{N} \vec{r_{\mathrm{i}}}. \tag{2.82}$$

If this process is repeated for numerous polymer chains of the same type, the mean value of end-to-end vector is calculated to be 0, due to the isotropic nature of the polymers. A Gaussian probability curve can be obtained for the end-to-end distances when x polymers are considered, as seen in figure 2.10. Even when more polymer chains are considered, the highest probability of end-to-end distance for a polymer is still 0.

Numerous polymers such as that in figure 2.9 can be used to find the mean-squared end-to-end distance, which is the simplest non-zero average related to the end-to-end vector and is given by

$$\langle R \rangle^2 = \sum_{i=1}^{N} \sum_{j=1}^{N} \langle \overrightarrow{r_{\mathrm{i}}} \cdot \overrightarrow{r_{\mathrm{j}}} \rangle. \tag{2.83}$$

If all monomers are the same size,

$$\vec{r_i} \cdot \vec{r_f} = a^2 \cos\theta_{ij} \tag{2.84}$$

where θ is the angle between the monomers. The isotropic nature of the polymers leads to

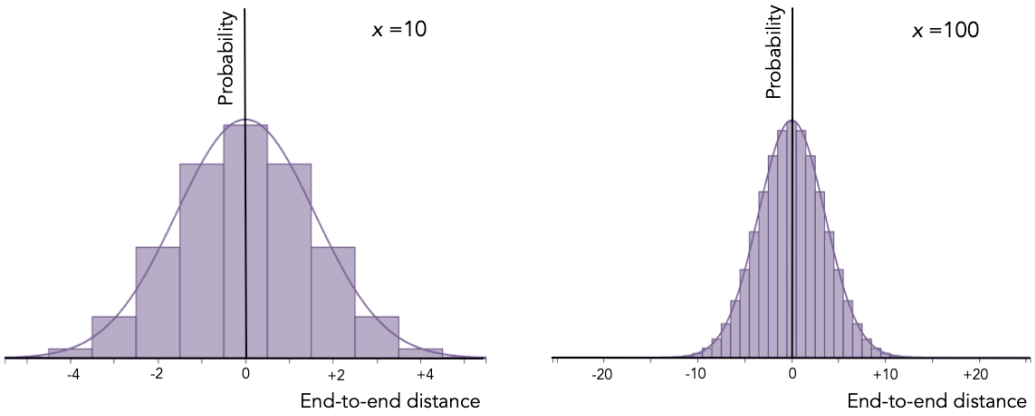

Figure 2.10: The probability distribution for the end-to-end distances of a one-dimensional random walk. The spread changes with increasing x but the most probable value is always 0.

$$\langle R^2 \rangle = Na^2 \tag{2.85}$$

and thus the mean-squared end-to-end distance is given by

$$\sqrt{\langle R^2 \rangle} = \sqrt{N}a. \tag{2.86}$$

The segment size of the polymer chain is not always equal to the monomer size, a. The monomers can act as one segment and the length of such a segment is defined as the Kuhn length, b. The radius of gyration R_{G} is another property of a polymer which relates to its size but considers the centre of mass of the polymer. It is given by

$$\langle R_{\mathrm{G}}^2 \rangle = \frac{\langle R^2 \rangle}{6} = \frac{Nb^2}{6}. \tag{2.87}$$

2.2.3 Flory-Huggins Theory

The calculations for this section concerning the Flory-Huggins Theory are based on the following assumptions:

1. A lattice has no vacant points.
2. Each point is only occupied by one monomer.

3. The monomers have the same volume.
4. There is no repulsion between the monomers to cause extra volume.
5. Each monomer is taken to be equal in size to a single lattice point.
6. There is no concentration fluctuation near the critical point.
7. The polymer is incompressible.

The Gibbs free energy can be used to determine whether a system will phase separate or not. The Gibbs free energy is given by

$$G = U + pV - TS, \tag{2.88}$$

in which U is the internal energy of the system, T is temperature and S is entropy. If the system is at a constant pressure and volume, the free energy can be expressed in terms of the Helmholtz free energy,

$$F = U - TS. \tag{2.89}$$

The terms of this equation must be found in order to understand the phase separation in a mixture. Temperature is characteristic of the system but internal energy and entropy require derivations from first principles. Entropy S can be found using equation 2.90, a variant of the Boltzmann equation.

$$S = -k_{\mathrm{B}} \sum_i P_i \ln P_i \tag{2.90}$$

Here k_{B} is the Boltzmann constant. Each position on the lattice is represented by i and thus this is summed. Each position on the lattice can be occupied by either molecule A or molecule B so P represents this probability. Figure 2.11 shows an ideal, two-dimensional case of how an oligomer consisting of 6 monomers would arrange itself on a square lattice when dissolved in a solvent .

The entropy of the mixture depends on the volume fraction of the two chemicals in the blend, A and B. Volume fraction is represented by the symbol ϕ and is initially given subscripts to distinguish the two. By definition $\phi_{\mathrm{A}} + \phi_{\mathrm{B}} = 1$ and thus $\phi_{\mathrm{A}} = 1 - \phi_{\mathrm{B}}$. The subscripts can be removed at this point and $\phi_{\mathrm{A}} = \phi$ and $\phi_{\mathrm{B}} = 1 - \phi$. Entropy is given by

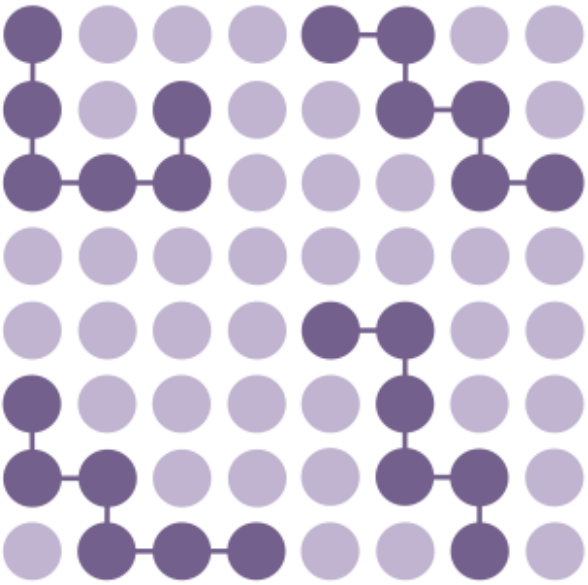

Figure 2.11: A solution of polymer solute and small-molecule solvent on a lattice diagram. The connected dark circles are polymer chains and the light circles are solvent molecules.

$$S_{\text{mix}} = -k_{\text{B}} \left(\phi \ln \phi + (1 - \phi) \ln (1 - \phi) \right). \tag{2.91}$$

Energy U can be found by assuming:

1. The molecules have z_n nearest neighbours which can either be A or B.
2. The interaction energy ϵ varies with the molecules involved.
   (a) ϵ_{AA} is between two A molecules
   (b) ϵ_{BB} is between two B molecules
   (c) ϵ_{AB} is between an A molecule and a B molecule.

An unmixed system has internal energy given by

$$U_{\text{unmix}} = \frac{z_n}{2} \left(\phi_{\text{A}} \epsilon_{\text{AA}} + \phi_{\text{B}} \epsilon_{\text{BB}} \right). \tag{2.92}$$

Equation 2.93 gives the mean field energy in the mixed state for each site on the lattice.

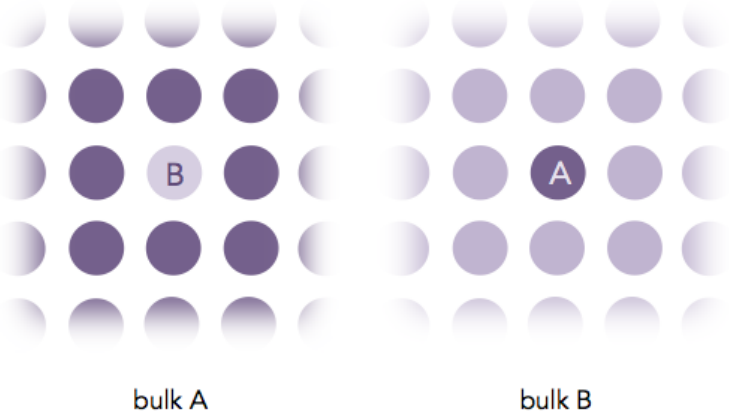

Figure 2.12: A molecule of B is transferred into the bulk of A whilst a molecule of A is transferred into the bulk of B.

$$U_{\text{mix}} = \frac{z_n}{2}\left(\phi_{\text{A}}^2\epsilon_{\text{AA}} + \phi_{\text{B}}^2\epsilon_{\text{BB}} + 2\phi_{\text{A}}\phi_{\text{B}}\epsilon_{\text{AB}}\right) \tag{2.93}$$

Subtracting equation 2.92 from equation 2.93 gives the energy of mixing,

$$\Delta U_{\text{mix}} = \frac{z_n}{2}\left[\left(\phi_{\text{A}}^2 - \phi_{\text{A}}\right)\epsilon_{\text{AA}} + \left(\phi_{\text{B}}^2 - \phi_{\text{B}}\right)\epsilon_{\text{BB}} + 2\phi_{\text{A}}\phi_{\text{B}}\epsilon_{\text{AB}}\right]. \tag{2.94}$$

The dimensionless interaction parameter χ is defined by removing molecules of A and B from their respective bulk liquids and transferring them both to the opposite bulk, as can be seen in figure 2.12.

Consider bulk A, with the B molecule. The interaction energy ϵ_{AB} per pair arises between unalike molecules, to which B and the z_n nearest neighbours contribute. So as not to account twice, this is halved. There are two bulks, so the value is doubled. The contributive interaction energy for both the A and B bulk liquids is therefore

$$\epsilon_{+} = \frac{2z_n\epsilon_{\text{AB}}}{2}. \tag{2.95}$$

Using the same logic, the alike nearest neighbours have a reductive effect on this interaction energy and

$$\epsilon_{A-} = \frac{z_n\epsilon_{\text{AA}}}{2}, \tag{2.96}$$

and

$$\epsilon_{B-} = \frac{z_n \epsilon_{\mathrm{BB}}}{2}. \tag{2.97}$$

Consolidating these interaction energies and dividing by $k_{\mathrm{B}}T$ to create a reduced dimensionless energy, the interaction parameter is defined as

$$\chi = \frac{z_n}{2k_{\mathrm{B}}T}\left(2\epsilon_{\mathrm{AB}} - \epsilon_{\mathrm{AA}} - \epsilon_{\mathrm{BB}}\right). \tag{2.98}$$

χ can be found experimentally [58, 59] and has been found to be inversely proportional to temperature and also depends on concentration [60–66] unless the solvent is a good solvent, where χ is independent of concentration [67,68]. The degree at which χ depends on concentration has been previously been quantified [63, 64].

Substituting equation 2.98 into equation 2.94, the internal energy of mixing is defined by equation 2.99.

$$U_{\mathrm{mix}} = \chi \phi_{\mathrm{A}} \phi_{\mathrm{B}} k_{\mathrm{B}} T \tag{2.99}$$

Equations 2.91 and 2.99 can then be substituted in to $F = U - TS$ to give 2.100; the free energy of mixing.

$$\frac{F_{\mathrm{mix}}}{k_{\mathrm{B}}T} = \phi_{\mathrm{A}} \ln \phi_{\mathrm{A}} + \phi_{\mathrm{B}} \ln \phi_{\mathrm{B}} + \chi \phi_{\mathrm{A}} \phi_{\mathrm{B}} \tag{2.100}$$

As this equation considers monomeric solutions, it must be modified to be used for polymer solutions. The polymers are given a degree of polymerisation N. This polymerisation induces polymer interactions within the solution, which modifies the final term in equation 2.100, giving

$$\frac{F_{\mathrm{poly}}}{k_{\mathrm{B}}T} = \phi_{\mathrm{A}} \ln \phi_{\mathrm{A}} + \phi_{\mathrm{B}} \ln \phi_{\mathrm{B}} + N \chi \phi_{\mathrm{A}} \phi_{\mathrm{B}}. \tag{2.101}$$

χ is independent of degree of polymerisation. The free energy per monomer unit of the polymer rather than the polymer as a whole is given by

$$\frac{F_{\mathrm{site}}}{k_{\mathrm{B}}T} = \frac{\phi_{\mathrm{A}}}{N} \ln \phi_{\mathrm{A}} + \frac{\phi_{\mathrm{B}}}{N} \ln \phi_{\mathrm{B}} + \chi \phi_{\mathrm{A}} \phi_{\mathrm{B}}. \tag{2.102}$$

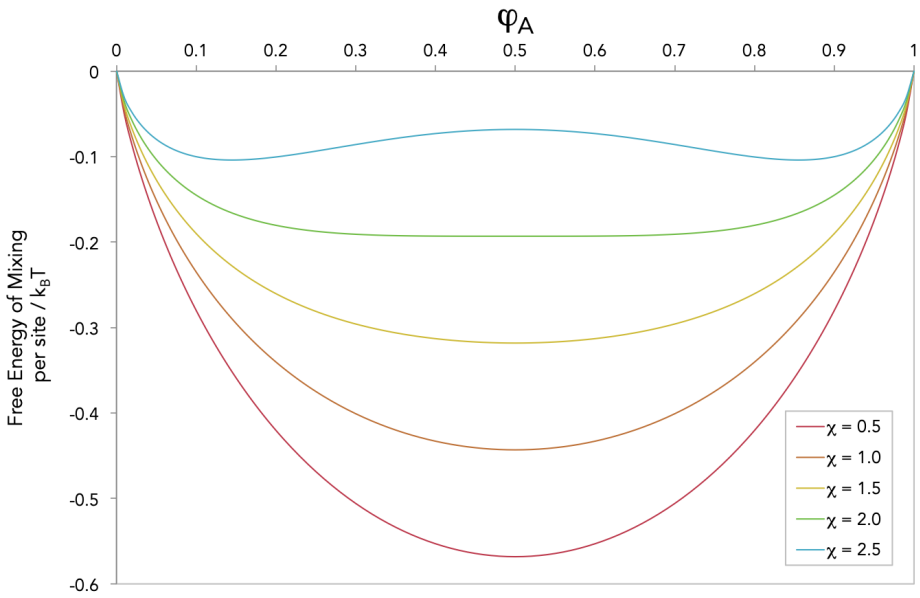

Figure 2.13: The free energy of mixing / $k_{\mathrm{B}}T$ per site as a function of volume fraction ϕ_{A} for solutions of varying interaction parameter χ.

The free energy of mixing can be plotted as a function of volume fraction such as that in figure 2.13. Multiple plots show how a varying interaction parameter χ can affect the mixture. The plots can be used to determine whether a solution will de-mix or not. Consider a mixture with volume V_0 consisting of A and B where A has a volume fraction of ϕ_0. If this mixture separates into two components V_1 and V_2 which have volume fractions of A ϕ_1 and ϕ_2 respectively, due to conservation of volume,

$$\phi_0 V_0 = \phi_1 V_1 + \phi_2 V_2 \tag{2.103}$$

must hold true. Dividing such a sum by the total volume of the mixture V_0 results in

$$\phi_0 = \alpha_1 \phi_1 + \alpha_2 \phi_2, \tag{2.104}$$

where $\alpha_1 = V_1/V_0$ and $\alpha_2 = V_2/V_0$ and thus $\alpha_1 + \alpha_2 = 1$ must be true as volumes V_1 and V_2 must have summed to the original volume V_0.

The total energy of the phase separated system is therefore

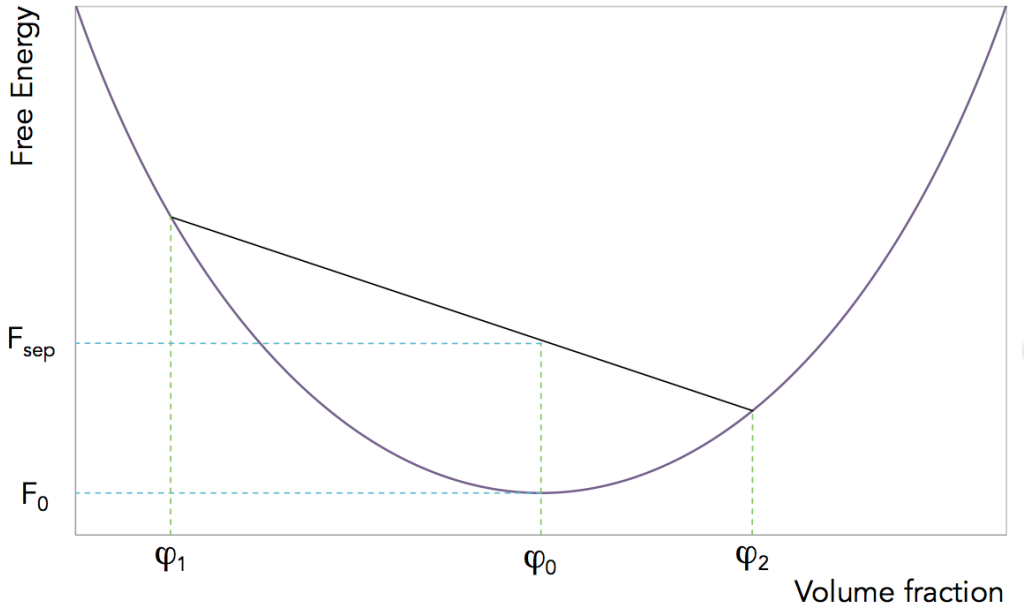

Figure 2.14: The free energy of a solution. The solution consists of A and B which have equal volume fractions, ϕ_0. The solution can phase separate into two mixtures, where A has a volume fraction ϕ_1 and where B has volume fraction ϕ_2. $F_0 < F_{\text{sep}}$ so it is energetically favourable for the system to not separate.

$$F_{\text{sep}} = \alpha_1 F_{\text{mix}}(\phi_1) + \alpha_2 F_{\text{mix}}(\phi_2). \tag{2.105}$$

Equation 2.104 can be used to give the free energy of separation in a different form, such as

$$F_{\text{sep}} = \frac{\phi_0 - \phi_2}{\phi_1 - \phi_2} F_{\text{mix}}(\phi_1) + \frac{\phi_1 - \phi_2}{\phi_1 - \phi_2} F_{\text{mix}}(\phi_2). \tag{2.106}$$

The free energy of separation can be demonstrated more easily with an annotated phase diagram. The figure 2.14 shows a standard phase separation plot with the relevant volume fractions and energies labelled. The energy of separation is found by drawing a line between the two separated volume fractions. F_0 reduces the free energy more than F_{sep} so it is not energetically favourable for the solution to de-mix. The solution is stable.

As the interaction parameter increases to $\chi = 2$ the region where the minima are located becomes extended due to the appearance of an inflection point.

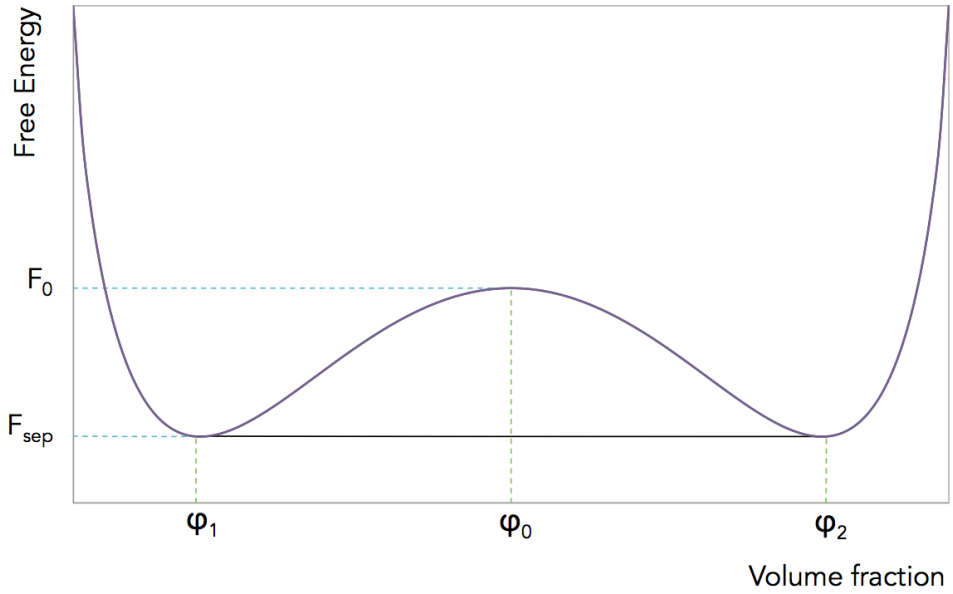

Figure 2.15: Similarly to figure 2.14 the solution can phase separate into two mixtures, where A has a volume fraction ϕ_1 and where A has volume fraction ϕ_2. $F_0 > F_{\text{sep}}$ so it is energetically favourable for the system to phase separate.

As the interaction parameter increases again to $\chi = 2.5$ the inflection has given rise to two separate minima, as is more clearly in figure 2.15.

Using a similar method to that in figure 2.14 for a phase diagram with two minima, it is clear to see from figure 2.15 that in a system where a phase diagram inflection occurs, it is energetically favourable to de-mix in order to reduce the free energy. As a result, the solution will phase separate into two coexisting compositions.

If the free energy follows a similar shape to that in figure 2.15, a phenomenon known as metastability is possible. By differentiating the free energy as a function of volume fraction, the demixing of the system can be understood.

Figure 2.16 shows a plot with two minima and one maximum. These points are located when the gradient of the free energy function is 0. This can be expressed mathematically by equation 2.107.

$$\frac{dF}{d\phi} = F'(\phi) = 0 \tag{2.107}$$

The second derivative of the free energy function is indicative of whether a maximum or minimum is present as at these points, $dF/d\phi = 0$. A maximum

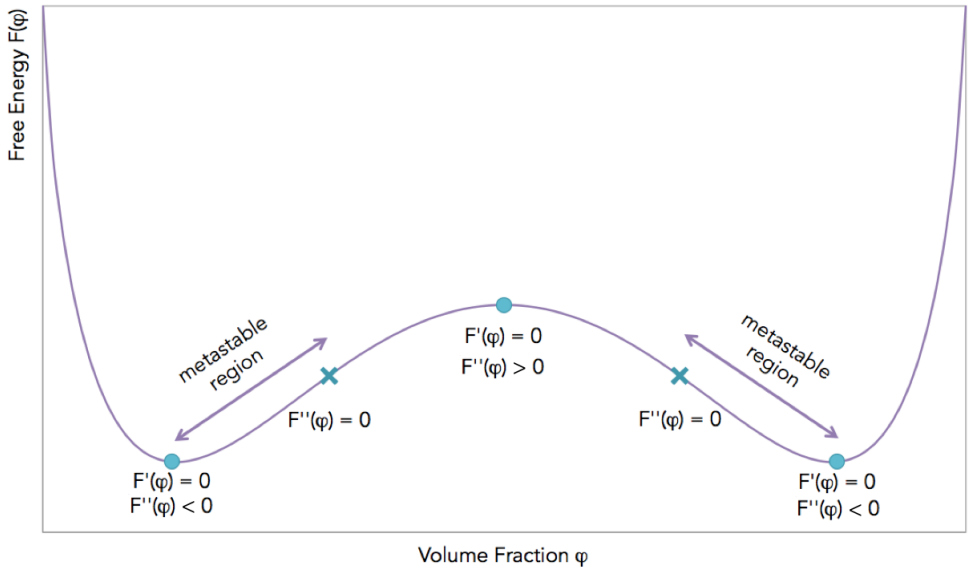

Figure 2.16: A free energy plot showing the derivatives of the free energy function. Minima and maxima occur when $dF/d\phi = 0$. The regions of metastability are labelled.

is present when $d^2F/d\phi^2 < 0$ and a minimum is present when $d^2F/d\phi^2 > 0$.

If the system is globally immiscible but $\frac{d^2F}{d\phi^2} > 0$ then it is metastable. At these points, the curvature of the free energy function changes from positive to negative. The condition is expressed mathematically in equation 2.108.

$$\frac{d^2F}{d\phi^2} = F''(\phi) = 0 \tag{2.108}$$

At true minima, the mixture is stable and small energy fluctuations do not typically cause the mixture to phase separate. However when the volume fraction is close to a point where $d^2F/d\phi^2 < 0$, small energy fluctuations can cause the mixture to phase separate to the limit of local stability.

The third derivative of the free energy function can be used to find the critical point, which meets the condition in equation 2.109.

$$\frac{d^3F}{d\phi^3} = F'''(\phi) = 0 \tag{2.109}$$

The temperature at which this condition is true is at the critical temperature T_c. This point is also where the spinodal line and the coexistance curve meet,

as can be seen in figure 2.17. This example is a lower critical solution temperature (LCST) system, in which below T_c, the mixture is miscible. Conversely an upper critical solution temperature (UCST) system is a miscible mixture above T_c.

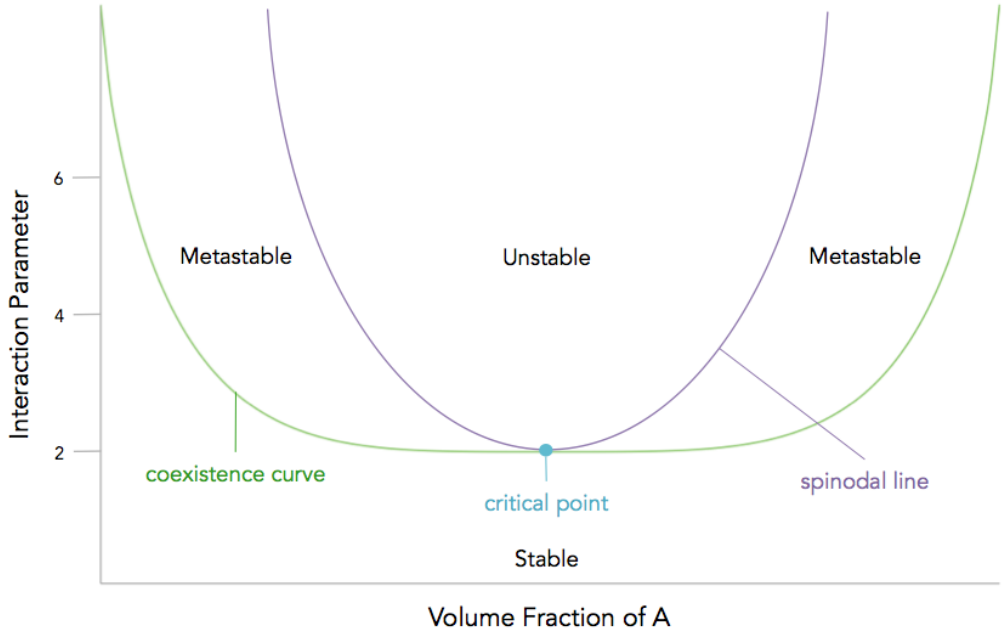

Figure 2.17: The spinodal and the coexistence curve meet at the critical point. The regions of stability, metastability and instability can be seen accordingly.

When the interaction parameter $\chi < 2$, a small molecule mixture is stable for all volume fractions. As the interaction parameter increases beyond 2, when the volume fractions are approximately equal, the mixture becomes unstable. For a mixture where there are large differences between the volume fractions of the chemicals in the mixture, stability remains and intermediate volume fractions cause solutions with metastability to occur.

Depending on its stability, a mixture can segregate into stable structures in order to reduce free energy. Metastable mixtures have the potential to undergo this phase separation by a mechanism called nucleation and growth. An unstable mixture appears uniform at first but will eventually phase separate by either nucleation and growth or spinodal decomposition.

Spinodal decomposition occurs when the system is thermodynamically unstable and any small fluctuations in composition are amplified: it is driven by the diffusion of material in regions of low concentration to regions of higher

concentration in order to phase separate. This uphill diffusion is counter-intuitive as the composition remains non-uniform.

Nucleation and growth occurs when random fluctuations in energy result in a nucleation site, which is a local increase in free energy. As energy fluctuations continue, the demixed state can aggregate in size, which continues until the net formation of the demixed state. There are two methods in which nucleation can occur. Homogeneous nucleation occurs in a bulk mixture. The energy required to cause the nucleation of a spherical particle of size r is defined by equation 2.110 in which σ is the surface tension. ΔF_v is the free energy per unit volume that causes the overall lowering of the free energy of the system as a whole.

$$\Delta F\left(r\right) = \frac{4\pi r^3}{3}\Delta F_v + 4\pi r^2\sigma \tag{2.110}$$

The terms in equation 2.110 represent the volume free energy and the interfacial energy respectively; the first term depends on the volume of a sphere $\frac{4}{3}\pi r^3$ and the second term depends on the surface area of a sphere $4\pi r^2$.

As r increases, these terms are affected differently as shown in figure 2.18. The energy reaches the maximum value when r reaches a critical size r^*. When $r < r^*$, the free energy of the system would increase if more growth were to occur however when $r < r^*$, the free energy of the system decreases with more growth. This is an energy barrier for the metastable system to begin nucleation. The energy required to reach the critical size r^* is given by

$$\Delta F^* = \frac{16\pi\sigma^3}{3\Delta F_v^2}. \tag{2.111}$$

The positive energy contribution of the surface energy causes the energy barrier and so a change in surface area can greatly affect nucleation and growth. Heterogeneous nucleation occurs when the nucleus is at an interface. Due to the interface, the nucleus has a droplet shape dictated by its wetting ability, as can be seen in figure 2.19. The nucleus in heterogeneous nucleation will have a surface area smaller than that of a sphere. This reduced surface area causes a lower energy barrier for nucleation and growth to occur. As a result, heterogeneous nucleation is more common than homogeneous nucleation.

The mutual diffusion D_{mu} of the mixture governs whether it phase separates by spinodal decomposition or nucleation and growth. It is defined by

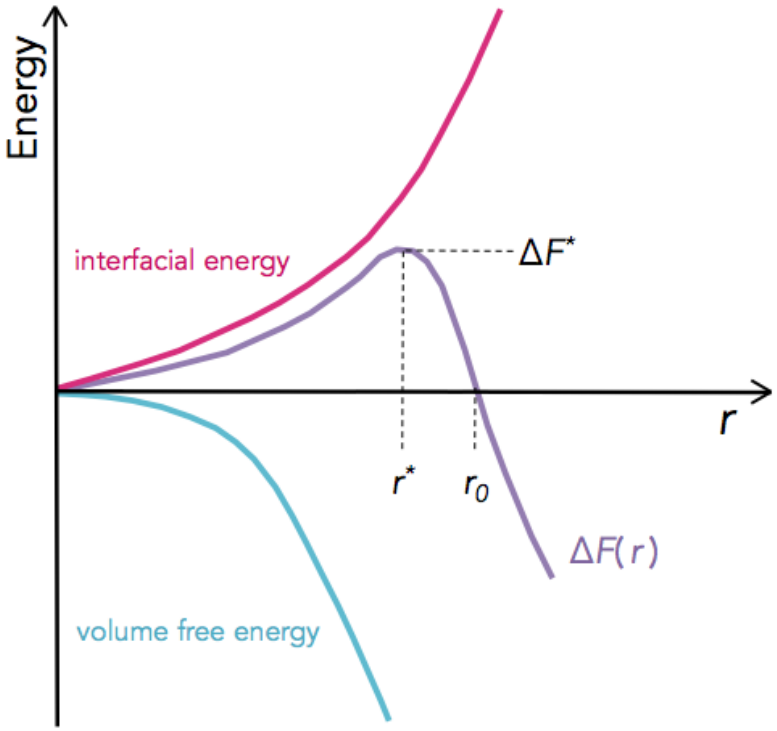

Figure 2.18: The function in equation 2.110 is plotted along with the separate terms.

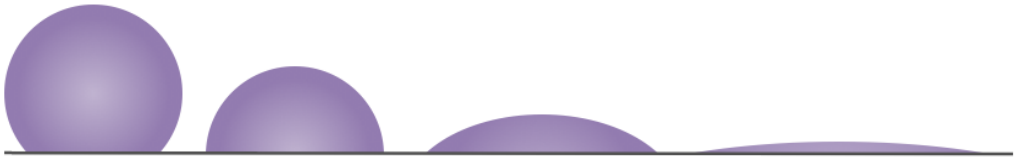

Figure 2.19: The surface area of the nucleus decreases as the contact angle decreases. This causes a smaller energy barrier for nucleation.

$$D_{\text{mu}} = D_0 \left(1 - \phi\right) \frac{d^2 F}{d\phi^2}, \tag{2.112}$$

where the diffusion coefficient D_0 is always positive, the volume fraction ϕ is always less than 1 so the sign of $d^2F/d\phi^2$ controls the sign of D_{mu}. There are two possible consequences:

1. If $d^2F/d\phi^2$ is negative, D_{mu} is negative and material diffuses from low concentration areas to high concentration areas in uphill diffusion. In this case, lower concentration areas have a higher chemical potential. Spinodal decomposition occurs.
2. If $d^2F/d\phi^2$ is positive, D_{mu} is positive material diffuses from high concentration areas to low concentration areas as higher concentration areas have a higher chemical potential. Nucleation and growth occurs.

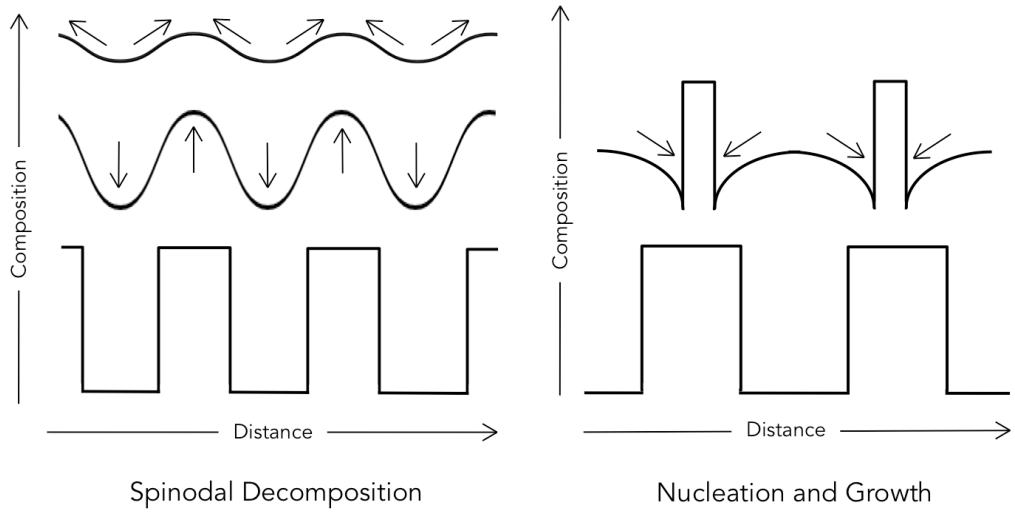

Figure 2.20: In spinodal decomposition, the negative value of D_{mu} causes spontaneous phase separation with a length scale. In nucleation and growth, the positive value of D_{mu} causes domains to grow with constant concentration.

Fick's first law dictates steady state diffusion and is given in equation 2.113. The flux of diffusion is given by J and measures the amount of material flowing through a given region per unit time. Again the diffusion coefficient D_0 is always positive.

$$J = -D_0 \frac{d\phi}{dx} \tag{2.113}$$

In standard diffusion, such as the process of nucleation, $\frac{d\phi}{dx}$ is negative and so the diffusion flux J is positive and Fick's law is obeyed. In uphill diffusion such as that in spinodal decomposition, as $\frac{d\phi}{dx}$ is positive Fick's law is not obeyed as the diffusion flux J is negative.

If the six conditions for Flory-Huggins Theory are not met, the lattice is inhomogeneous and concentration fluctuations can affect the phase boundaries. The free energy of mixing per site is then given by equation 2.114, where ΔF_{mix} is the Flory-Huggins energy of mixing and Ξ is the square gradient term, which is representative of the energy cost for having a variance in the lattice composition. This term is not exclusive to the Flory-Huggins theory and arises due to a change in composition, as is shown in equation 2.139.

$$\Delta F = \int \Delta F_{\text{mix}}(\phi) + \Xi(\phi)(\nabla\phi)^2 \, dV \tag{2.114}$$

2.2.4 Polymers and Solvents

If a polymer is dissolved in a solvent, one of three things will happen to the polymer chain depending on the value of the interaction parameter χ of the system. If $\chi > 0.5$, the monomers in the polymer are more attracted to one another than the surrounding solvent and as a result, the polymer chain will collapse. Such a solvent would be described as poor.

If the system has the precise interaction parameter of $\chi = 0.5$, the polymer chain does not respond to the solvent and behaves as if it were surrounded by identical polymers. Such a solvent is an athermal solvent, or a theta solvent.

A system with an interaction parameter of $\chi < 0.5$ indicates a good solvent; the polymer chain will swell and potentially uncurl due to its preferential interaction with the solvent than itself.

How polymers behave when dissolved in solvent can be examined using a variety of methods including NMR spectroscopy [69], rheometry [70], gas liquid chromatography [68], scanning electron microscopy [51] and dynamic light scattering [70]. Toluene has been found to interact to different degrees with PS and PMMA, which is of note for the consequential experiments. PS is more reactive in toluene and dissolves more readily than PMMA [71]. The

solvent used also affects the film thickness; PMMA films cast from a toluene solution were four times thinner than PMMA films cast from a solution of MEK [72]. By mixing the solvents in a solution, final film morphology can be varied [73]. Casting polymers as bilayers also affects the final morphology of the film [74].

2.2.5 Ternary Polymer Solutions

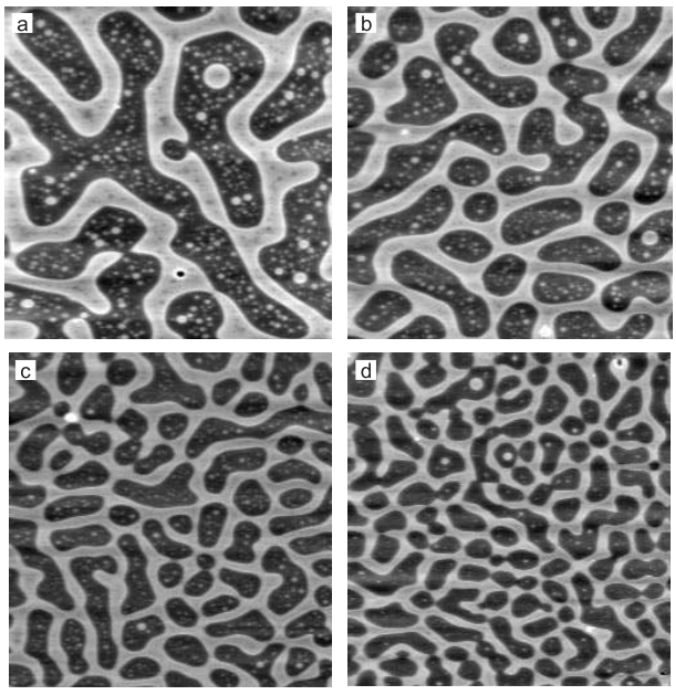

Figure 2.21: Spinodal decomposition of a spin coated film of PS and PMMA represented by the dark and light areas respectively. The scale size of the cells differs due to the varying spin speeds causing different film thicknesses a) 140nm b) 105nm c) 95nm d) 80nm. From S. Walheim et al, 1997 [17].

The demixing from of a solution composed of toluene, PS and PMMA can be seen in figure 2.21. The separation is dictated by solubility of the individual polymers in the solvent, how each polymer interacts with the substrate and how the polymers interact with one another. Toluene is a better solvent for PS than it is for PMMA, as is THF. For both solvents, PS dissolves much more easily, giving rise to segregated phase separation in the form of PS troughs, as shown in figure 2.22a. However if MEK is used instead of toluene

or THF, the PS solidifies much more quickly than the PMMA does, leading to PS islands, shown in figure 2.22b.

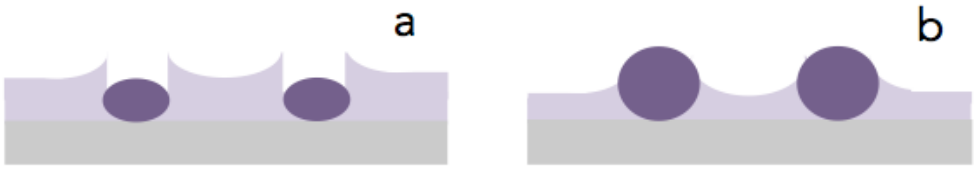

Figure 2.22: The structure of the film varies depending on the solvent used. PS is dark and PMMA is light. a) PS forms troughs when toluene or THF is used in the solution. b) PS forms islands when the polymers are dissolved in MEK.

Spin coating a film from a ternary blend of immiscible polymers often results in lateral domains. The shape of the lateral structures is determined by the polymer solubilities and substrate preferences. If the polymer with the lower surface tension is most soluble, the lateral structures have sharp edges. If the polymer with the larger surface tension is most soluble, the lateral structures have rounded edges instead [17].

The phase behaviour of ternary mixtures can be shown on a ternary plot such as that in figure 2.23. Each point of the triangle represents a mixture that is 100% composed of the respective chemical as volume fractions must sum to 1. A binodal can be plotted on the ternary graph indicating the volume fractions that correspond to a miscible or de-mixing solution. Figure 2.23 shows a binodal line separating the volume fractions that would cause a miscible solution and those that would phase separate. If insufficient solvent is used, the high concentration of polymers is more likely to induce phase separation [71].

When the solvent is represented by S and the polymers in the ternary blend are represented by A and B, the relationship between the interaction parameters χ_{SA}, χ_{SB} and χ_{AB} can be found in the following equation [75].

$$\chi_{AB} - \chi_{SA} - \chi_{SB} = \left[\frac{\frac{S}{r_A} \ln \frac{\phi_A}{\phi'_A} + \frac{S}{r_B} \ln \frac{\phi_B}{\phi'_B} - 2\chi_{SA}\left(\phi_A - \phi'_A\right) - 2\chi_{SB}\left(\phi_B - \phi'_B\right)}{\phi'_B - \phi_B + \phi_A - \phi'_A} \right] \tag{2.115}$$

The volume fractions in the upper and lower phase states are represented by ϕ_i and ϕ'_i respectively, r_i is the number of segments in the chain of polymer

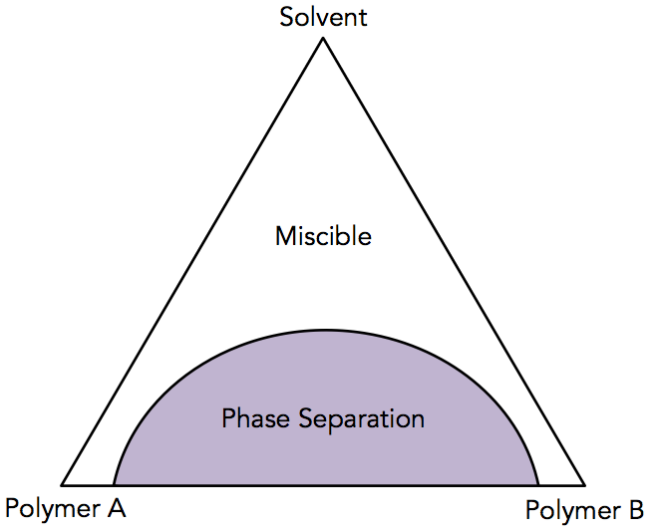

Figure 2.23: A ternary phase diagram for a blend with two polymers dissolved in solvent. The respective volume fractions in the region that are shaded will result in phase separation as there is not enough solvent for the polymers to be fully dissolved.

i. The interaction parameters can be found from techniques such as light scattering [76] and gel permeation chromatography [77].

Difficulty arises when the volume fractions are not the only contributing factor on phase behaviour and de-mixing; pressure and temperature must also be considered if they are varied in the experiment. It is not possible to vary both of these parameters and the chemical volume fractions and consequentially represent the resultant data on a ternary diagram due to such a plot requiring four dimensions. By varying only one of these additional parameters, the diagram is complicated further, as shown in figure 2.24.

The manipulation of ternary blends can be used to give a variety of desired effects in a final film. The polymer with the strongest interaction with the substrate can form a nanometre thick layer at the base of the film, which is done by exploiting the wetting behaviour of an individual polymer in a ternary blend. This has been seen with PS, PMMA and toluene blends [17, 78]. As toluene is a better solvent for PS than PMMA, when the two polymers phase separate, the PS rich phase is more toluene saturated and so the PMMA solidifies first onto the substrate.

The effects of ternary blends should not go unnoticed when considering the results of the experiments in Chapters 4 and 5. In a ternary blend compos-

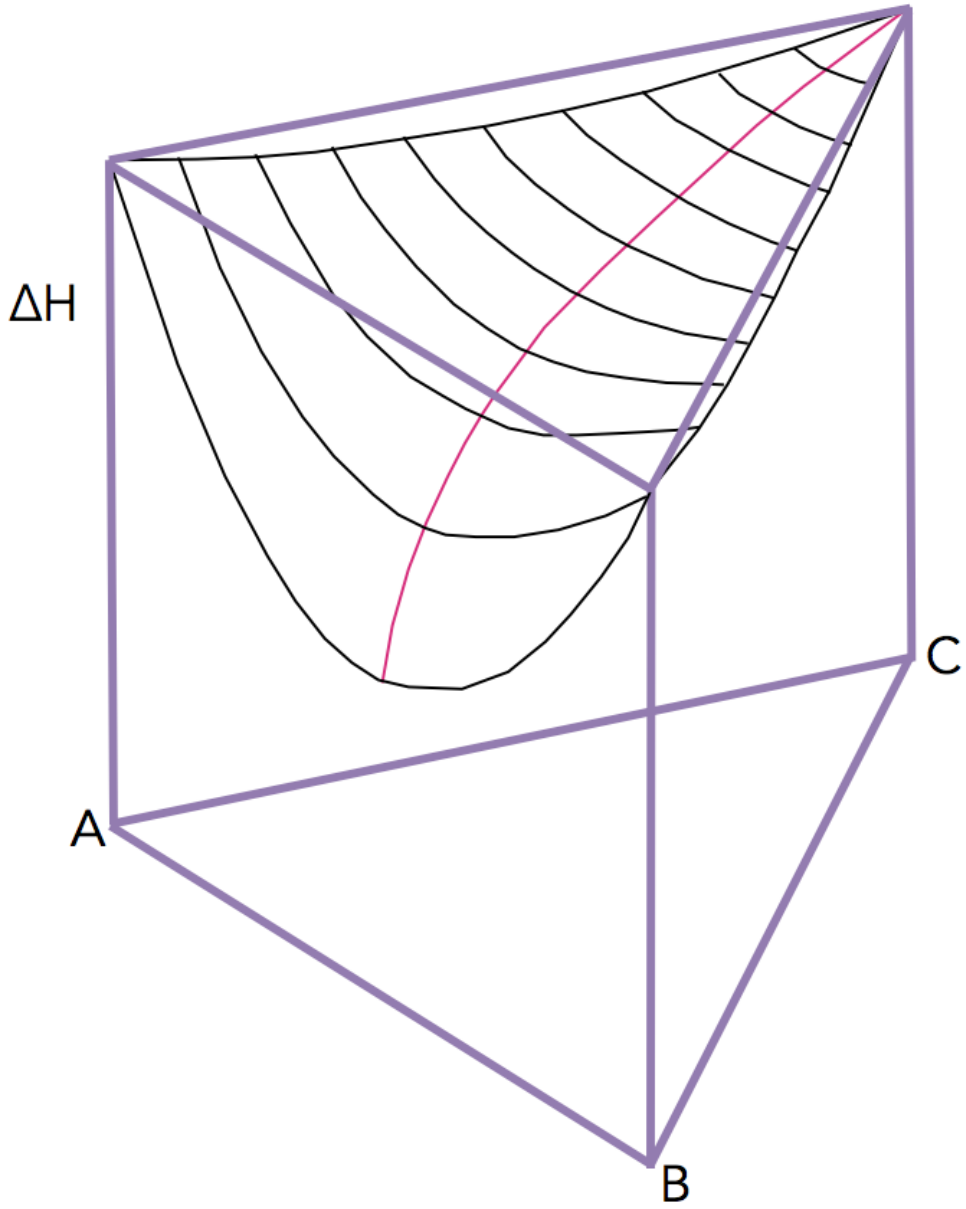

Figure 2.24: The ternary phase diagram for a mixture ABC. The interaction between A and B is much stronger than AC and BC, as indicated by minimum value. The lines are different colours to more clearly illustrate the saddle shape of the phase diagram. Adapted from a figure by G. R. Brannock and D. R. Paul, 1990 [50].

ing of over 90% solvent, there will be far fewer polymer-polymer interactions polymer-solvent interactions and thus these can be neglected. In this solution, the polymers are also highly miscible due to their relatively low concentration. The polymer-polymer interactions become extremely important when the solvent evaporates, increasing the solution polymer concentration.

2.2.6 Viscosity

A solution is governed by the properties of the chemicals within it. The molecular weights, density and volume fraction of the solute and solvent in the blend all have an effect on the solution. External factors such as vapour pressure and temperature also control the final morphology.

Organic solvents are typically less dense than water and any solute added can significantly increase the viscosity of the system, even if the solute accounts for only a small percentage of solution.

When used to describe a fluid, the term viscosity typically refers to the dynamic viscosity which is also known as the absolute viscosity. This viscosity is defined by the shear strain γ on the fluid in question, which is defined by

$$\gamma = \frac{du}{dy}, \tag{2.116}$$

where the displacement in the x direction is u. The strain rate $\dot{\gamma}$ then considers the time dimension and is defined by

$$\dot{\gamma} = \frac{d}{dt}\frac{du}{dy} = \frac{dv_x}{dy}, \tag{2.117}$$

in which the velocity in the x direction is given by v_x. The viscosity η and shear rate $\dot{\gamma}$ can be related when considering the shear stress τ, which is the force per unit area causing the strain.

Numerous viscosities are used to quantify the behaviour of solutions. The relative viscosity η_r is the ratio of the solution viscosity η to the pure solvent viscosity η_solv and is given by

$$\eta_\mathrm{r} = \frac{\eta}{\eta_\mathrm{solv}}. \tag{2.118}$$

The specific viscosity η_{sp} is also used to relate the solution viscosity to the viscosity of the pure solvent. The relationship is defined as

$$\eta_{\text{sp}} = \frac{\eta - \eta_{\text{solv}}}{\eta_{\text{solv}}} = \eta_{\text{r}} - 1. \tag{2.119}$$

The intrinsic viscosity is a measure of the degree of which the solute affects the solution viscosity. It is defined in equation 2.120, in which ϕ is the volume fraction. This relationship holds true for low concentrations.

$$[\eta] = \lim_{\phi \to 0} \frac{\eta_{\text{sp}}}{\phi} = \lim_{\phi \to 0} \frac{\eta - \eta_{\text{solv}}}{\eta_{\text{solv}} \phi} \tag{2.120}$$

The kinematic viscosity ν relates the viscosity of the fluid, whether it be a solution η or a solvent η_{solv}, to the density of the fluid ρ, and is defined as

$$\nu = \frac{\eta}{\rho}. \tag{2.121}$$

In a polymer solution, the chain size and distance between the chains directly affect the viscosity [79]. Large polymer chains increase the viscosity much more so than small polymer chains. [80, 81]. As the distance between the polymer chains decreases with increasing polymer concentration, viscosity and polymer concentration are positively correlated [7, 70, 82].

Einstein proved that, for a dilute solution in which the solute can be treated as hard spheres and the sphere size a_{s} is considered negligible to the inter sphere distance s so that $s >> a_{\text{s}}$, the viscosity of the mixture is defined by

$$\eta_{\text{mix}} \approx \eta \left(1 + \frac{5}{2}\phi\right), \tag{2.122}$$

where η is the viscosity of the liquid without the hard spheres and ϕ is the volume fraction of the hard spheres. This relationship has been proved true in recent years [83] but its application for polymer chains, which cannot necessarily be modelled as hard spheres, is debated.

The intrinsic viscosity can be found from the molecular weight in the Mark-Houwink equation,

$$[\eta] = K M_{\text{w}}^{\alpha}. \tag{2.123}$$

By experimentally finding $[\eta]$ as a function of known molecular weight M_{w} of polymer, the Mark-Houwink parameters K and α can be determined using a model. K is measured in litres per gram ($l.g^{-1}$) and α is dimensionless. Both parameters change with temperature, solvent and molecular weight itself but the more of these experiments that are done, the more true values of K and α can be found.

A variety of values for both K and α have been found experimentally [84–93]. Table 2 shows a particular set of results, in which the Mark-Houwink parameters were found for PMMA when dissolved in toluene [86, 89]. The first row of table 2 [86] concerns a slightly higher molecular weight at a lower temperature and the values of K and α are slightly larger than that in the lower row [89]. Whether these differences are due to the higher temperature or differing molecular weight cannot be determined from these results alone.

$T\,(^{\circ}C)$	M_{w}	K	α
25	$4.1 \times 10^5 - 3.2 \times 10^6$	7.1	0.73
30	$1.9 \times 10^5 - 2.6 \times 10^6$	7.0	0.71

Table 2: The values of K and α for different temperatures and molecular weights. The first row is from S. N. Chinai et al, 1955 [86] and the second row is from E. Cohn-Ginsberg et al, 1962 [89].

Using these values, the effect of a solute on viscosity can be determined as $[\eta]$ is found. As the viscosity of a solvent such as toluene at a given temperature has been experimentally determined, η_0 is known and so equations 2.119 and 2.120 can be arranged to give the viscosity of a solution as

$$\eta = \eta_{\mathrm{solv}} \left(\phi K M_{\mathrm{w}}^{\alpha} + 1\right). \tag{2.124}$$

As the concentration of the solution increases, the distance between the polymer chains decreases and eventually the solution becomes viscous enough that the polymer chains in the solute begin to overlap. This occurs at the overlap concentration c_* which may be given by

$$c_* = \frac{3M_{\mathrm{w}}}{4\pi R_{\mathrm{G}}^3 N_{\mathrm{A}}}. \tag{2.125}$$

N_{A} is Avogadro's number and R_{G} is the radius of gyration of the polymer chain. When the concentration of the solution is lower than c_*, the solution is semi-dilute. The polymers are somewhat free to move, but the density is

high enough that some of the polymer chains penetrate the excluded volume of the other chains.

In this region the specific viscosity defined in equation 2.119 needs a corrective term which is obtained from a Taylor expansion. The specific viscosity is then given in equation 2.126 [82, 94].

$$\eta_{\mathrm{sp}} = [\eta]\phi + k_{\mathrm{H}}[\eta]^2\phi^2 \tag{2.126}$$

The Huggins coefficient is k_{H} and is an indicator of the solvent strength. Strong solvents typically have a value of 0.3 and theta solvents have a value of between 0.5 and 1.

Rheological behaviour, including Mark-Houwink parameters and the relationship between $c - M_{\mathrm{w}} - \eta_{\mathrm{sp}}$, was studied for solutions consisting of toluene and high molecular mass PMMA [95]. This followed from experiments establishing the $M_{\mathrm{w}} - \eta$ relationship [96] and less directly the temperature dependence [97]. For such large molecular weights, equation 2.126 should include an addition term [98], shown in equation 2.127.

$$\eta_{\mathrm{sp}} = [\eta]\phi + k_{\mathrm{H}}[\eta]^2\phi^2 + b_n[\eta]^n\phi^n \tag{2.127}$$

The value of b_n is a constant and n is the power law index, both of which can be found from fitting the model.

Equation 2.124 is true for Newtonian fluids, which have viscosities that are linearly dependent on shear rate. Non-Newtonian fluids are more complicated as viscosity is no longer linearly dependent on the shear rate. The Newtonian fluid assumption is no longer valid as the viscosity of a mixture greatly increases or as external forces become more effective.

Specifically, spin coating consists of inertial forces and solvent evaporation. The inertial forces attribute to a great deal of shear rate and the evaporation of the solvent will cause the solution viscosity to increase for the duration of the spin. Clearly in this case non-Newtonian fluid dynamics will eventually not be negligible but highly diluted fluids do not exhibit non-Newtonian behaviour.

The Ostwald law relates viscosity to shear rate for the general non-Newtonian case. The introduction of a power indicates that viscosity and shear rate have the potential to be no longer linearly related.

$$\eta = K_0 \dot{\gamma}^{\Pi-1} \tag{2.128}$$

K_0 is a constant, $\dot{\gamma}$ is the shear rate and n is the power law index, which indicates the degree to which the shear rate deviates from a linear relationship with η. The flow is Newtonian when $n = 1$. When $n > 1$, shear thickening occurs, which is when the viscosity increases with an increasing shear rate. On the contrary, when $n < 1$, shear thinning occurs, defined as the viscosity increasing with an increasing shear rate.

The Carreau model [99] calculates the viscosity of a fluid using equation 2.129. At low shear rates, it predicts Newtonian behaviour. At high shear rates it predicts non-Newtonian behaviour.

$$\eta = \eta_\infty + (\eta_{00} - \eta_\infty) \left[1 + (\Lambda\dot{\gamma})^2\right]^{\frac{n-1}{2}} \tag{2.129}$$

As the viscosity η depends on the shear rate, the viscosities at an infinite shear rate η_∞ and at a zero shear rate η_{00} must be known as establishing parameters. The relaxation time of the system is Λ, the power index is n and the shear rate is $\dot{\gamma}$. As the shear rate increases, the viscosity decreases [7].

Solution viscosity is thought to be the governing parameter in determining the final thickness h_f of a film [81] so discrepancies between spin coating data and spin coating models for Newtonian fluids could be attributed to this.

The Carreau model can be adapted in order to be applicable to spin coating [100] and the final film thickness as a function of non-Newtonian viscosity is given by equation 2.130.

$$h_\mathrm{f} \approx c_0 \left[\nu_0 D_0 \Omega^{-2\iota} \left(\frac{\dot{\gamma}_\mathrm{c}}{R}\right)^{\iota-1}\right]^{\frac{1}{\iota+3}} \tag{2.130}$$

The subscript 0 represents the value of that respective parameter at a time $t = 0$. The concentration of the solution is c, the kinematic viscosity is ν, the diffusion coefficient is D. The rotation rate is Ω and ι is an inverse power law index. R is the total radius of the disk and $\dot{\gamma}_\mathrm{c}$ is the critical shear rate. The diffusion coefficient in a dilute polymer solution can also be used to quantify the structure of the polymer molecule [101].

Whether a fluid is Newtonian or not can greatly influence the films that can be cast from it during spin coating. Regardless of the initial radial thickness

profile of the solution deposited, a Newtonian fluid will flow to the extent that these irregularities will not be present in the final film [102]. This is not the case in a non-Newtonian fluid, where spin coating will only further propagate earlier induced striations.

For $n > 1$ the film exhibits a uniform thickness for large radii but there is a central dip in thickness [102]. The opposite is true for $n < 1$ and the central region of the film is uniform but at high radii the thickness is deformed [102]. These modelled results were compared with those predicted by the EBP model [18] which does not consider non-Newtonian effects. The discrepancies in these models are evidently caused by the involvement or lack thereof of non-Newtonian effects.

The effect of the initial thickness profile on a film cast from a non-Newtonian fluid has also been modelled to get the final film thickness profile using the Ostwald law and the Carreau model from equations 2.128 and 2.129 [22, 32, 103].

The results that non-uniformities in the initial thickness profiles of films cast from Newtonian fluids yielded uniform films were corroborated. For the non-Newtonian fluids with $n < 1$, the data obtained from the Ostwald law and the Carreau model differed from each other. The Carreau model yielded generally flat films that at times were thicker in the centre. Modelling the Ostwald law resulted in films that were noticeably much thicker in the centre of the film, either displaying a Gaussian curve or for $n = 0.95$ and $n = 0.60$ even an exponentially thick centre [22, 32].

Modelling the rheological behaviour of a solution during spin coating is challenging due to the large shear forces involved. Considering a non-volatile solution in the model simplifies the process but also makes the model unrealistic [28].

Thin films in general are affected by the viscosity in numerous ways. High viscosity solutions can cause a less fluid skin-type structure on the film surface [44]. Solutions can also segregate internally into regions of differing viscosity [104] which has the potential to affect the final film morphology. This effect could be attributable to PMMA solutions having a lower density than an equivalent PS solution [105].

Viscosities of both Newtonian and non-Newtonian solutions consisting of PS and PMMA have been the topic of experiments to assess their dependence on the molecular weight, temperature, shear stresses and how effective the solvent is for the polymer. As the shear stress increases, the dependence of the viscosity on the polymer molecular weight is weaker. For solutions containing

PS specifically, it was found that poor solvents yield higher viscosities and good solvents yield lower viscosities [106].

2.3 Film Morphology

The forces discussed in the models in section 2.1 can be coupled with the discussion of polymer physics from section 2.2 to contextualise the film imperfections often seen in spin coated films. Various features have been observed [107–110] and most are often the product of radial convection and phase separation. Depending on the final use of the film, these effects can be useful or a hindrance. It is also possible to control a film morphology using lab techniques [111] however this section shall discuss the causes of non-uniformities and methods used to minimize or induce their effects.

2.3.1 Surface Tension

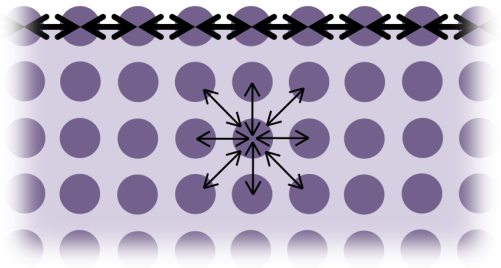

Figure 2.25: A molecule in the bulk bonds to its surrounding neighbours. The molecules at the interface bond tightly to the other surface molecules as there are no adjacent molecules above.

Surface tension is an effect due to the interface of a fluid. Cohesive forces act between a molecule and its neighbouring atoms within the bulk, as shown in figure 2.25. Molecules at the interface bond more strongly to their neighbours due to having no neighbouring molecules beyond the interface; this induces a tension.

Surface tension σ can be quantified by the following equation as the force per unit length

$$\sigma = \frac{F}{L}, \tag{2.131}$$

where F is the force and L is the length of the interface.

The energy in a surface boundary can be found from the energy it takes to increase the surface area. This is shown mathematically in equation 2.132 where W is the work done to increase the surface area by ΔA.

$$\sigma = \frac{W}{\Delta A} \tag{2.132}$$

The effect of surface tension can frequently be seen in the behaviour of liquids. Surface tension governs the shape of the meniscus of a liquid in a vial. If the liquid has a low surface tension, there are strong adhesive forces between the molecules of fluid and container. The effect on the meniscus in this case is producing a concave shape, such as that in figure 2.26a. If the surface tension is high, the cohesive van der Waals forces between the fluid molecules cause the liquid to touch the container minimally, giving rise to a convex meniscus shape, shown in 2.26b.

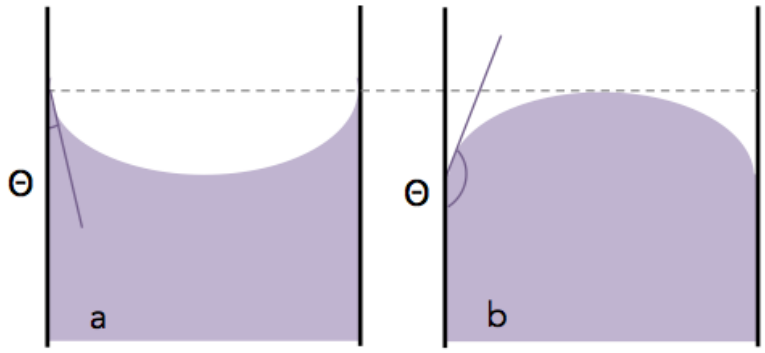

Figure 2.26: The surface tension effects on a meniscus of liquid can cause either a a) concave or b) convex contact with the container.

In figure 2.26 the surface tension is quantified numerically by the value of the contact angle θ. Liquids have a high wetting ability exhibit adhesive forces to dissimilar molecules and have a low surface tension when $\theta < 90°$. However when $\theta > 90°$, the wetting ability is lower, and strong cohesive forces between the liquid molecules are exhibited giving rise to a higher surface tension.

Whilst surface tension can characterise the wetting ability of a liquid, it can also be intrinsic to the hydrophobic or hydrophilic nature of a surface. Figure 2.27 shows a tensiometer image of a water droplet incident to the surface of a 300nm PS film. The small indent either side of the droplet where it is in

contact with the film is caused by the surface tension of the water and the hydrophobic properties of the film. This contact angle has a value of 0° when complete wetting occurs.

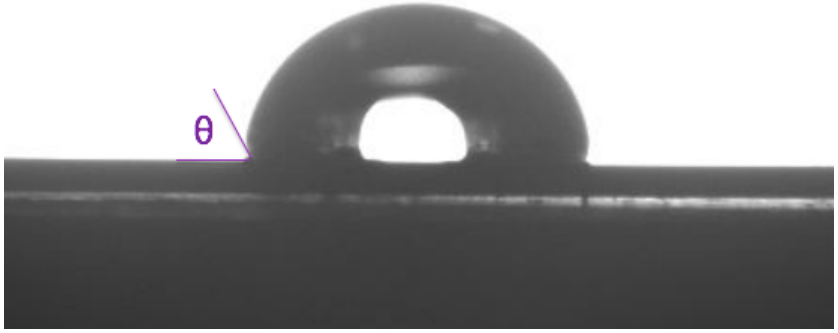

Figure 2.27: A 300nm PS thin film with a water droplet incident to the surface.

Young's equation considers the surface tensions of the solid substrate, liquid droplet and surrounding vapour in order to define the contact angle θ as 2.133 [112]

$$\cos\theta = \frac{\sigma_{\mathrm{SV}} - \sigma_{\mathrm{SL}}}{\sigma_{\mathrm{LV}}}, \tag{2.133}$$

where S, L and V represent the solid, liquid and vapour respectively and σ_{XY} is the surface tension between those interfaces. Equation 2.133 can be adapted to equation 2.134 to consider the wetting ability of an immiscible solution in terms of surface energy. The surface energy is the energy of the surface bonds.

$$\cos\theta = \frac{\zeta_{\mathrm{B}} - \zeta_{\mathrm{AB}}}{\zeta_{\mathrm{A}}} \tag{2.134}$$

ζ_{A} and ζ_{B} represent the surface energy of the separate phases of A and B and ζ_{AB} is the interfacial energy. When perfect wetting occurs, the solution is flat on the surface and the contact angle is $\theta = 0°$.

As a result, if $\theta > 0°$ the inequality of equation 2.135 holds true and only partial wetting occurs.

$$\zeta_{\mathrm{B}} - \zeta_{\mathrm{A}} < \zeta_{\mathrm{AB}} \tag{2.135}$$

At the wetting temperature T_{w}, there is a transition from partial wetting to complete wetting. As the critical point is reached, ζ_{AB} decreases to 0 faster than $\zeta_{\mathrm{B}} - \zeta_{\mathrm{A}}$ causing this transition.

2.3.2 The Marangoni Effect

The Marangoni effect was first detailed in 1855 by James Thomson [113] in the form of 'tears of wine' where the water and alcohol in an alcoholic beverage are seen to separate when spread thinly on the edge of a glass due to their different surface tensions.

Carlo Marangoni studied the effect intensively [114]. The effect was later observed by Henri Bénard, who heated a liquid from the bottom which gave rise to hexagonal shaped cells, such as those in figure 2.28 [115]. He attributed the Marangoni effect to convection, but this was rejected after Lord Rayleigh [116] considered it to be a result of buoyancy. In 1956 the origin of the effect was revisited and found to be due to varying surface tensions in a mixture [117].

The Marangoni effect is often considered to be the cause of certain de-mixing morphological features [118–127]. The effect occurs within a blend of two chemicals with different surface tensions. If A has a higher surface tension than B, the interface between the two share will be acted on more strongly by A. This causes flow in the blend which gives rise to the morphological features. How strongly the Marangoni effect affects the solution is determined by the dimensionless Marangoni number, which is defined as

$$\mathrm{Ma} = \left(\frac{\partial\sigma}{\partial T}\right)\frac{h\Delta T}{\eta\alpha_{\mathrm{T}}}. \tag{2.136}$$

The change in surface tension with temperature is $\partial\sigma/\partial T$, h is the thickness of the solution or film and ∇T is the temperature gradient in the solution from the substrate to the top of the solution. Viscosity of the solution is given by η and α_{T} is the thermal diffusivity.

When $\mathrm{Ma} > 80$ the conditions for the Marangoni effect are met and convection due to surface tension gradients will occur [117]. As Ma increases, the demixing effects increase and more morphological structures are formed. The

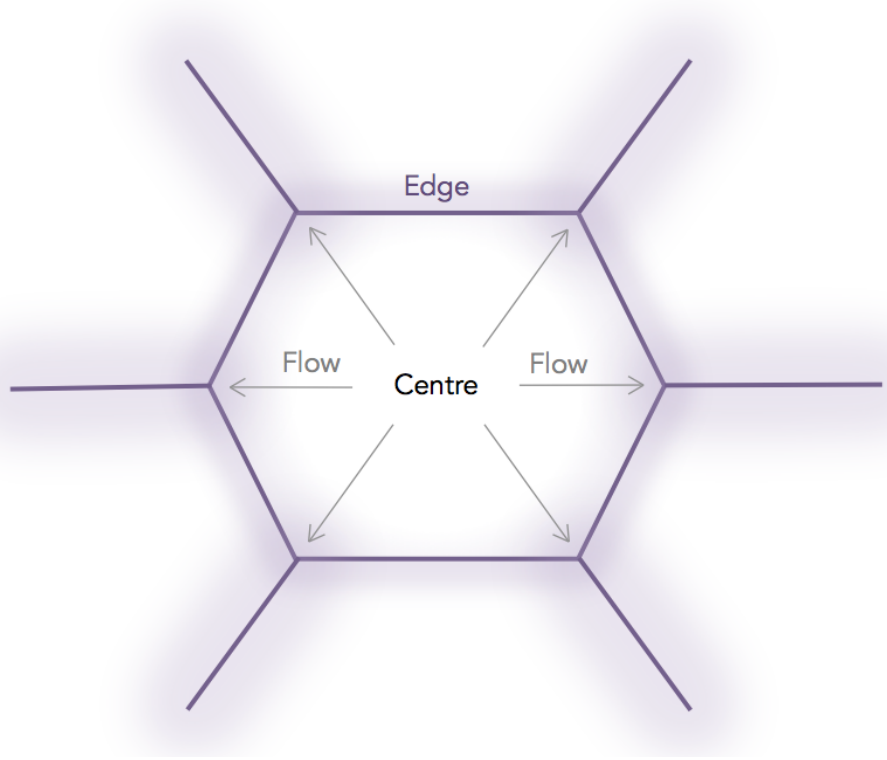

Figure 2.28: An illustration of a Marangoni cell. Adapted from a figure by H. Uchiyama et al, 2012 [56].

Marangoni number can also be expressed in terms of composition gradient which shows how concentration affects mixing rather than temperature as shown in equation 2.137 [128].

$$\mathrm{Ma} = \left(\frac{\partial\sigma}{\partial C}\right)\frac{h^2\nabla C}{\eta D} \tag{2.137}$$

The terms are similar to those in equation 2.136 except the differential term has been replaced by $\partial\sigma/\partial C$, which is the change in surface tension with concentration as the concentration will change as the solvent evaporates. ∇C is the concentration gradient at the surface of the film. The thermal diffusivity α_{T} is replaced by D the diffusion rate of the chemical causing the change in concentration, which is the solvent.

As the Marangoni effect is due to surface tension, the concentration and temperature of a film can vary greatly from the surface of the film to its bottom. This steep gradient drives convection [12, 129]. The penetration

depth of the gradient can be quantified by d and is included in the equations for Ma in the relationship

$$\mathrm{Ma} = \left(\frac{\partial\sigma}{\partial T}\right)\frac{h^2\Delta T}{\eta\alpha_{\mathrm{T}}d}. \tag{2.138}$$

Some degree of control over the Marangoni effect and the resultant morphological features has been shown to be possible. The effect can be reduced by using co-solvents in the polymer solution [130] or by performing the coating at temperatures lower than 15°C [16]. As indicated by equations 2.136 and 2.138, the Marangoni number is highly dependent on temperature [131].

Alternatively, if highly structured and patterned films are desired, this can be obtained by using values in equations 2.136-2.138 that result in a higher Marangoni number [55,56]. These results were all obtained from spin coating but the effect is not exclusive to these films: the Marangoni effect has been observed in dip coated films [132].

2.3.3 Surface Segregation

A system will typically behave differently at its surface compared to within the bulk. This typically affects a multi-component system composed of A and B to separate. There are numerous structures that can be formed from a blend, and some examples are illustrated in figure 2.29.

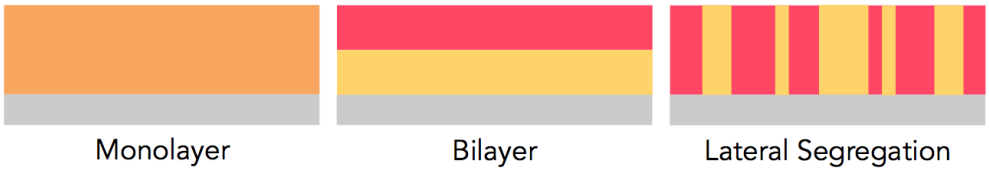

Figure 2.29: Blended single film that has not begun to phase separate. When a blend forms a bilayer, the blend separates and the polymer with the lower surface energy separates to the film surface. A laterally segregated film can occur when a bilayer structure is unstable and breaks down.

A blended single film has not undergone phase separation. A bilayer film has two states due to the film phase separating. A bilayer can only occur when the solution has completely wet the substrate [133]. Lateral segregation may occur when a phase separated bilayer is unstable and breaks down.

The substrate of a polymer blend film affects spinodal decomposition to a noticeable extent. Both polymer-polymer and substrate-polymer interactions have an influence on the phase separation [134]. If A has a lower surface energy than B, A is absorbed to the surface to lower the free energy of the system [135], which is given by

$$\frac{\Delta G}{k_{\mathrm{B}}T} = f_{\mathrm{s}}(\phi) + \int_0^\infty \Delta G_{\mathrm{mix}} - \phi\Delta\mu_\infty + \frac{a^2}{24\phi(1-\phi)}\left[\frac{d\phi}{dz}\right]^2 dz. \qquad (2.139)$$

The effect of the substrate on the demixing can also be seen in spin coated films [17,133]. Substrate-polymer interaction becomes more influential as the film thickness decreases [134].

The energy benefit of having A segregate to the surface is given by $f_{\mathrm{s}}(\phi)$, the Flory-Huggins free energy is ΔG_{mix} and $\Delta\mu_\infty$ is the chemical potential of the bulk system. The final term is the energy cost due to the composition gradient, where a is the scale length of A. The surface excess is defined as the excess amount of polymer segregated at the surface, Z^* defined below in equation 2.140.

$$Z^* = \int \left(\phi\left(z\right) - \phi_\infty\right) dz \qquad (2.140)$$

For a LCST system such as that in figure 2.17, as the temperature is increased to T_{c}, the interaction parameter and the surface excess increases [135]. A blend of PS and d-PS were spin coated and annealed. Only after annealing, thickness profiles showed that d-PS was preferentially segregated at the surface of the film. This effect was due to the difference in surface energy caused by the deuteration. This is experimental evidence of the surface segregation [135]. The nuanced process of surface phase separation is evident from the numerous experimental observations and theoretical models.

The process of surface phase separation can be quantified by equation 2.141, the Cahn-Hilliard equation [136].

$$\frac{\partial c}{\partial t} = D\nabla^2\mu \qquad (2.141)$$

D is the diffusion coefficient and μ is the chemical potential. When solved with boundary conditions, the polymers are seen to exhibit the separation

seen in the d-PS/PS and d-PEP/PEP experiments, where the polymer with the lower surface energy segregates to the top of the film [137].

The effect of a solvent on surface segregation was discussed in section 2.2.5. PS and PMMA films cast using toluene, THF and MEK solvents all laterally segregated [17]. In films cast using toluene or THF, the solvent evaporated slower in PS regions than PMMA regions. This caused differences in film thickness: the PS phase was much thinner than the PMMA phase. The opposite was seen in films cast using MEK and the PS regions were much thicker. This effect was due to PS being more soluble than PMMA in toluene or THF. In MEK, PMMA was more soluble. The solvent used affects the individual surface energies of the polymers [17]. Similarly if a lower solvent concentration is used, phase separation is more pronounced [138].

In polymer blends of PS-PI and PS-PMMA, these PS 'islands' were also seen when using low PS volume fraction ϕ_{PS}. As ϕ_{PS} was increased, eventually a critical PS volume fraction caused the islands to form a continuous layer, resulting in a PS-PI or PS-PMMA bilayer. As ϕ_{PS} was increased further, islands of either PI or PMMA began to form [139]. This can be seen in figure 2.30.

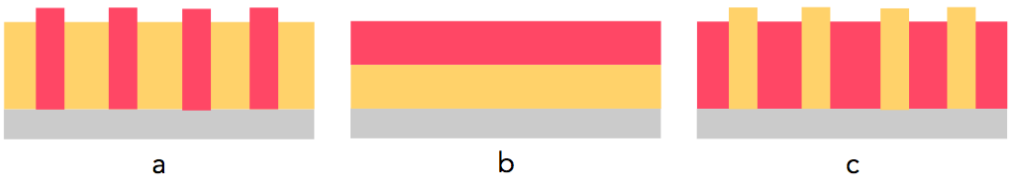

Figure 2.30: a) PS (red) islands in a PI or PMMA (yellow) majority structure. b) The volume fraction of PS has increased to the critical value, causing a bilayer. c) PI or PMMA islands in a PS majority structure.

The solvent evaporation rate E can affect the final morphology of the film. A faster evaporation rate is more likely to cause film imperfections [16, 21]. E can be controlled when spin coating films by the atmosphere and temperature in which the film is cast. If solvent vapour is used to flood the air surrounding the film, E is greatly reduced [21]. Increasing the temperature causes a higher E which can cause film imperfections [16]. By increasing the vapour pressure of the film during spin coating, a system that would typically undergo lateral phase separation did not and instead a bilayer was formed [21].

The surface of a polymer blend essentially breaks the symmetry of the bulk,

inducing a boundary condition on spinodal decomposition. As a result the pattern of phase separation can gradually propagate into the bulk of the polymer blend film [140].

A model of phase separation must combine dewetting and phase separation theory. Dewetting of liquid-liquid [141] and polymer-polymer [142] interfaces have both been explored. When the conjunction of dewetting and phase separation theory was first done, the model was restricted and only concentration fluctuations that were parallel to the substrate caused phase separation [143]. Whether dewetting and phase separation are modelled in consequence or simultaneously affects the theoretical film structure. A percolation path is seen on films modelled by considering dewetting then phase separation. If dewetting and phase separation are modelled as happening simultaneously in a film, this percolation is not seen [144].

Transient wetting layers occur when a polymer blend separates into two distinct layers with a horizontal interface. The transient wetting layer is metastable and therefore can collapse before spin coating is completed, causing lateral segregation [145]. If spin coating is completed before the transient wetting layer collapses, a bilayer film is formed. These two structures are shown in figure 2.31 [146].

The transient wetting layer is caused by a change in surface tension when solvent in the solution evaporates during the spin coating process. The instabilities cause the polymers to separate and in doing so, a concentration gradient is formed. The solution is more concentrated in certain places which causes a surface tension gradient which in turn induces the Maragoni effect [146].

The Marangoni instabilities were modelled for a thin film and confirmed theoretically the bilayer structure of the transient wetting layer. It was theoretically proven that the effect was due to a solvent concentration gradient induced by the solvent evaporating from the film surface [147]. Wetting layers also have the potential to cause crystalline structures in perovskite films [148].

The structure of a polymer blend was also determined theoretically using asymmetric boundary conditions, which represented the different effects on the film at the surface and at the substrate. This model was subjected to concentration changes and various structures were generated, including bilayers and lateral segregation [149].

This model was adapted to account for temperature changes instead of concentration changes. The structures generated in this case were again bilayers and lateral segregation but monolayers were also observed [150].

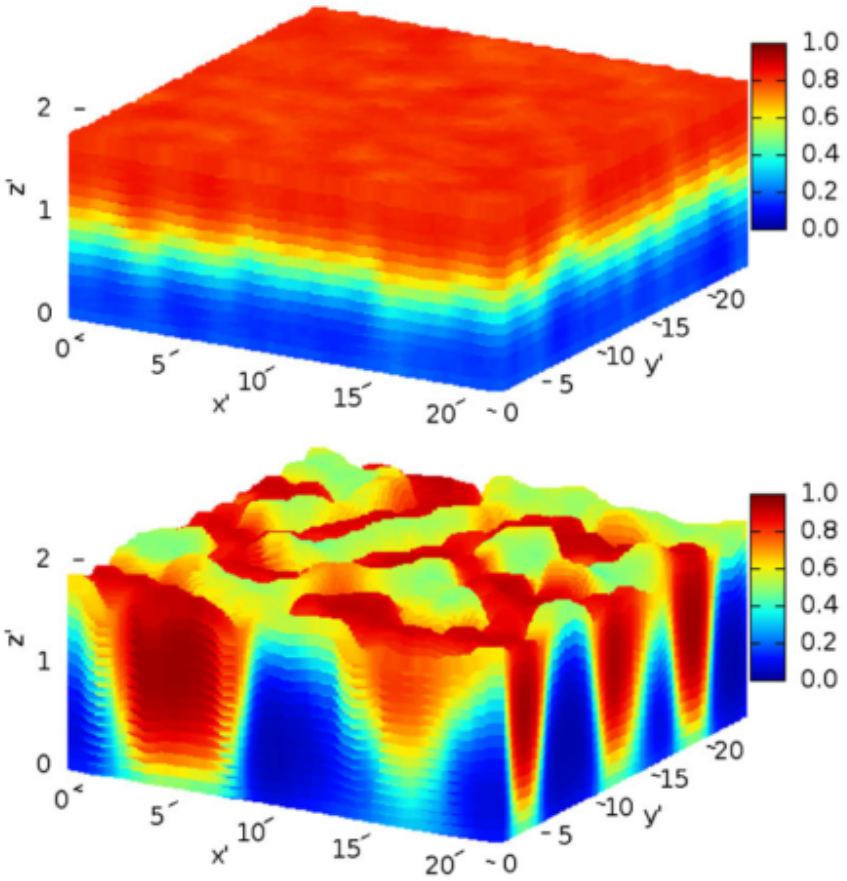

Figure 2.31: The transient wetting layer (top) and the laterally segregated film (bottom) that occurs when the transient wetting layer does collapse before the end of spin coating. From S. Y. Heriot and R. A. L. Jones, 2005 [146].

2.3.4 Radial Effects

The models detailed in section 2.1 do not consider radial effects. Many other models also ignore radial effects [31, 32, 151]. This is not necessarily an accurate assumption. Numerous radial effects have been seen in the film structure.

Bornside et al. [152] developed a model to find the the final film thickness of a spin coated film. Three regions of flow were mathematically determined [152] and are illustrated in figure 2.32. The radial regions themselves vary with the solution in question, but can be found from equations 2.142 and 2.143 in which 1×10^5 and 3×10^5 are the Reynolds numbers and determine the flow of the solution.

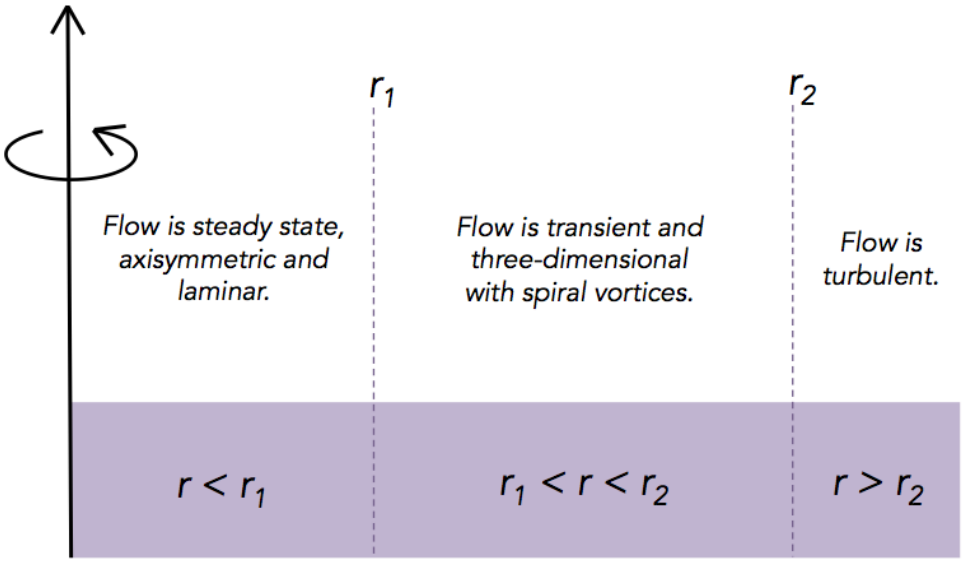

Figure 2.32: The flow of the solution differs in each of the three regions of film. Adapted from a figure by D. E. Bornside et al, 1993 [152].

$$r_1 = \sqrt{\frac{1 \times 10^5 \nu}{\omega}} \tag{2.142}$$

$$r_2 = \sqrt{\frac{3 \times 10^5 \nu}{\omega}} \tag{2.143}$$

For regions of the film where $r < r_1$, the flow is steady state, laminar and axisymmetric as predicted by von Karman [153]. Between $r_1 < r < r_2$, the Coriolis effect becomes a significant influence on the flow of the film and causes the once laminar flow to become disrupted in the form of Ekman spirals. These vortices are three-dimensional and a form of convectional flow which affect the film morphology [29, 107–109, 154, 155] by causing non-uniform drying if the solution has a Reynolds number between 2000-2500 [155]. The convection increases the evaporation rate by replenishing the surface of the film with solvent. Similarly to how hurricanes are large convectional flows spiralling due to the rotation of the Earth, Ekman vortices are convectional flows that occur during spin coating. At larger radii when $r > r_2$, the flow is turbulent and the mass transfer coefficient does increases with radius almost linearly: k has been observed to increase with $r^{0.9}$ [27]. As the edge of the film is approached, material can be lost from the spin coating.

How a film differs with radius is also evident by its thickness profile. The starting thickness of a film has very little effect on the final film thickness [38] as any radial variation present before spin coating has begun is thought to be removed during the process by turbulent forces [18, 32].

A film with non-uniform thickness would be a result of the shear rate changing with radius. If a film were to be thinner at larger radii, a smaller shear rate would be necessary [41]. These effects can be seen when considering the spin coating of non-Newtonian solutions [32,156]. As more solvent in the solution evaporates, non-Newtonian effects become more significant which could give rise to these radial-dependent shear rates which vary the final film thickness profile.

The most noticeable morphological radial effect on spin coated films are radial striations. The striations are primarily visible in two distinct forms. When coupled with phase separation, they can appear as cells that become deformed and stretched with increasing radius, shown in figure 2.33.

Radial striations can also be detected from local variations in thickness [14] in a film with an otherwise uniform thickness, as can be seen in figure 2.34. This can be seen using microscopes but in many cases, striations can be seen with the naked eye.

Figures 2.33 and 2.34 show how the striations are affected radially by the spin speed of the spin coating but the direct cause of the structures are somewhat unclear. They may be attributable to small fluctuations in temperature or solute concentration within a solution at the start of spin coating. The fluctuations are believed to propagate into radial striations in the final film

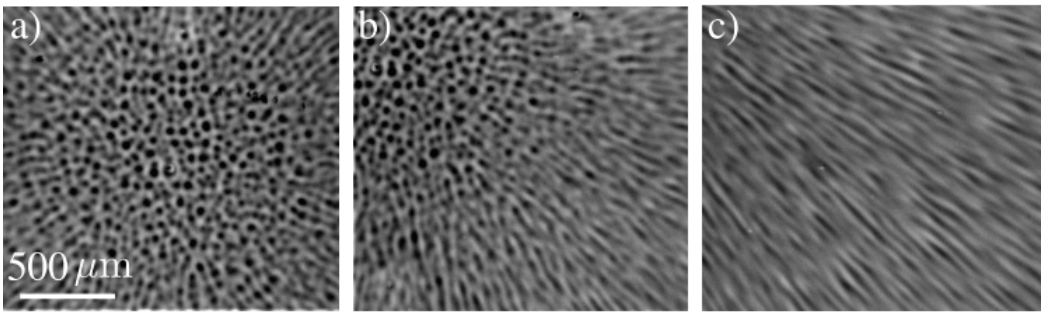

Figure 2.33: Optical microscope images at various radii of a striated film at a) the film centre, b) a small distance away from the centre of the film and c) the edge of the film. The radial striations are noticeable in b and more so c thus indicating greater prominence with radius. From P. D. Fowler et al, 2016 [16].

[15] as in figure 2.33.

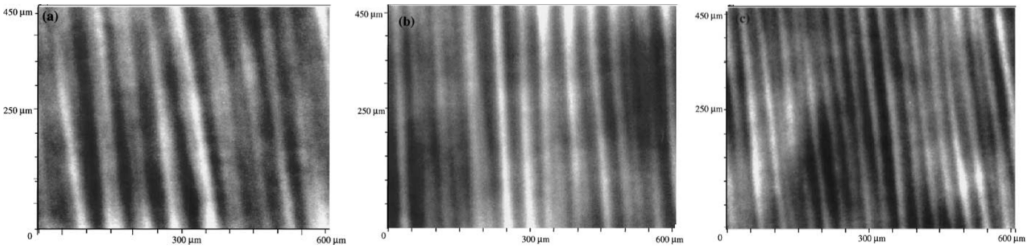

Figure 2.34: Optical microscope images of striated films spun at a) 2000rpm b) 3000rpm and c) 4000rpm. The striation spacing clearly decreases with increasing angular velocity indicating a relationship. From D. E. Haas et al, 2001 [14].

Striations and non-uniformities in thickness have been detected in spin coated sol-gel films [157] so the phenomena are due to spin coating and is not unique to polymer thin films.

Thermal fluctuations in the film cause certain regions to have more energy and so the solvent can evaporate more readily. This results in a non-uniform evaporation rate which causes convection within the solution [128]. The convection can also induce more separation of chemicals which causes a surface tension gradient between the polymers and the solvent.

The radial striations have been found to be eliminated from resultant films completely when the spin coating is performed at a lower than ambient temperature. Typically 15°C is sufficient to produce uniform films [16]. It had been suggested that the striations could be a surface tension effect caused by

the square substrates [158], but striations have been observed on films cast on circular substrates [157].

Periodic features similar to radial striations have been seen in polymer films that are caused by applying pulses to the films [159, 160]. Such features are called laser induced periodic surface structures or LIPSS and their size can be controlled by varying the pulse frequency.

3 Methods

This chapter shall detail the experimental methods used in the project and how data obtained are analysed, primarily from the optospinometer. In addition to this, the specifications for the materials used to produce the samples are given in this section.

3.1 Optospinometer

Using experimental equipment to obtain *in situ* data is well documented [161–164]. The primary piece of experimental equipment used in this thesis is the optospinometer. The instrument consists of a spin coater with a 633nm He-Ne laser incident on the spin coater platform at fixed angle of 45°. Emergent laser light is captured by a camera. The spin coater platform is connected to a vacuum pump to keep the substrate in position.

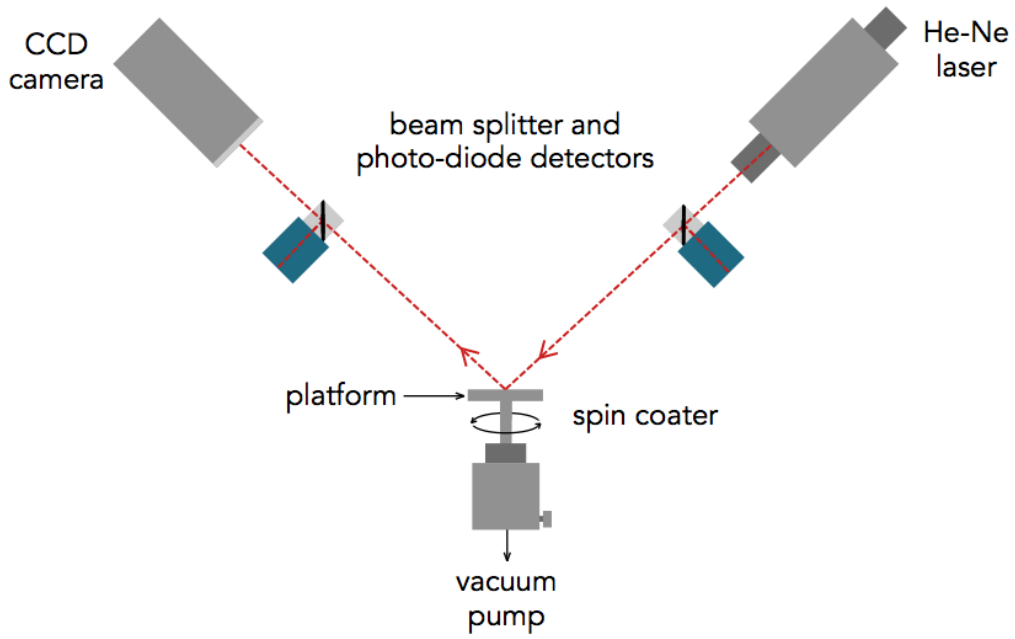

Figure 3.1: A diagram of the optospinometer.

For all experiments conducted, the centre of the substrate is always positioned at the centre of the platform and the film centre (0,0,0) is intersected

by the axis of rotation. A diagram and photograph of the optospinometer are shown in figures 3.1 and 3.2.

Figure 3.2: A photograph of the optospinometer.

The emergent light from an experimental run is recorded as both specular, numerical reflectivity and off-specular image capture.

The optospinometer can be adapted for a variety of spin coating experiments. As mentioned previously, it can be used to control the vapour pressure of a spin coating environment and consequentially the solvent evaporation rate by using a removable chamber. The height of the spin coater platform can be altered, moving the position of the laser to different radii of the film. The camera is large enough that data are not lost when this is done.

The solutions were added to the substrate before the spin was started. A minimum of two repeats were performed for all spin coatings to ensure the data obtained were reliable. If one of the three datasets looked drastically different to the others, a fourth would be done to check it was anomalous.

3.1.1 Specular Data

The final thickness of a film can be determined in numerous ways such as ellipsometry and atomic force microscopy. An *in situ* thickness is more difficult to determine as either of these experiments would not be possible

during a spin coating. The optospinometer yields information that would otherwise be extremely difficult to find from a regular spin coater.

The laser light is incident to the film and is refracted into the film and reflected off the film surface simultaneously. This is shown in figure 3.3. Whether the refracted light interferes constructively or destructively with the reflected light depends on the thickness of the film. The optospinometer records reflectivity as a function of time, resulting in a plot such as that in figure 3.4, which is called an optospinogram. The reflectivity oscillates due to constructive and destructive interference caused by the film thinning.

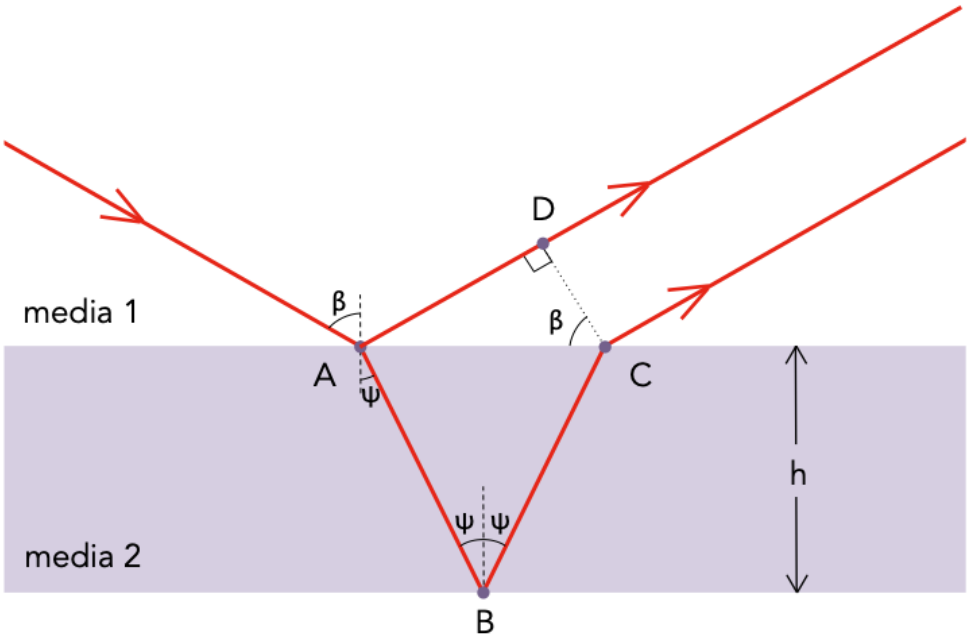

Figure 3.3: The refraction of light between two media.

The optical path difference Γ corresponds to the phase shift experienced by the two coherent sources. It is defined as

$$\Gamma = n\,(AB + BC) - AD, \tag{3.1}$$

where AB, BC and AD are distances defined in figure 3.3 and n is the refractive index of the media causing the phase shift, which in this case is the film, of thickness h. The distance AD is

$$AD = 2nh \tan\psi n \sin\psi. \tag{3.2}$$

The distances AB and BC are both

$$AB = BC = \frac{h}{\cos\psi} \tag{3.3}$$

so optical path difference Γ can be given as

$$\Gamma = n\left(\frac{h}{\cos\psi} + \frac{h}{\cos\psi}\right) - 2nh\tan\psi\sin\psi. \tag{3.4}$$

Simplified,

$$\Gamma = 2nh\cos\psi. \tag{3.5}$$

At each peak of an optospinogram, the interference is constructive and the optical path difference Γ is an integer multiple of the laser wavelength, λ. Mathematically, this is given by

$$\Gamma = 2nh\cos\psi = m\lambda. \tag{3.6}$$

The difference in thickness between two constructive, consecutive peaks m and $m+1$ is given by Δh which is defined as

$$\Delta h = h_{m+1} - h_m = \frac{\lambda\,(m+1)}{2n\cos\psi} - \frac{\lambda m}{2n\cos\psi} \tag{3.7}$$

and

$$\Delta h = \frac{\lambda}{2n\cos\psi} + \frac{\lambda m}{2n\cos\psi} - \frac{\lambda m}{2n\cos\psi}. \tag{3.8}$$

This change in thickness between two successive peaks can then be extrapolated back to get the thinning as a function of time using

$$h(t) = h_f + (m-1)\Delta h, \tag{3.9}$$

in which $h(t)$ is the thickness of the film at a given time t and h_f is the final thickness of the film, determined by a method such as ellipsometry. As

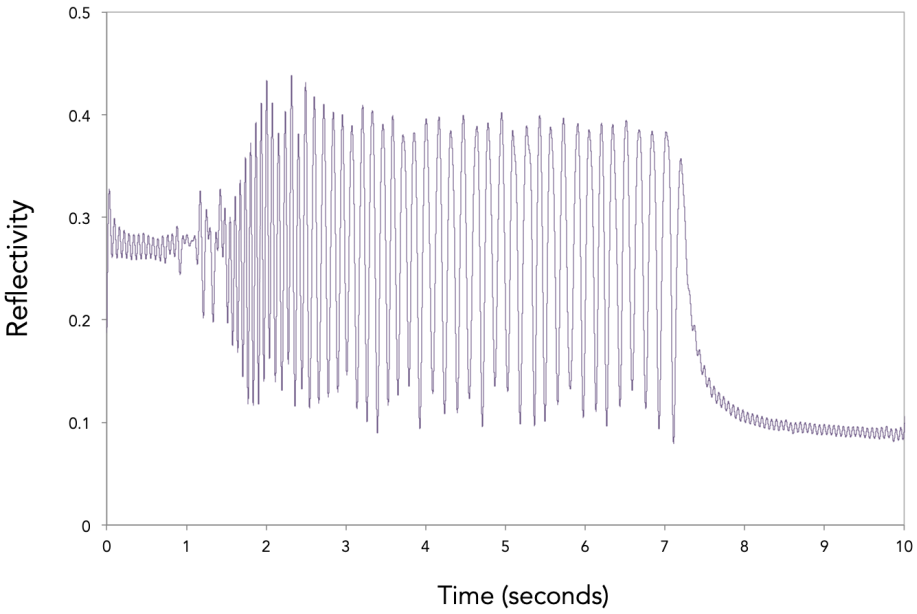

Figure 3.4: An optospinogram showing reflectivity as a function of time.

mentioned previously m is the peak number and $m = 1$ when the film is at its final thickness.

As the solvent evaporates, the refractive index of the film n and the internal angle ψ change. These must be modelled as changing with time. Snell's law is given by

$$n_{\text{air}} \sin \beta = n \sin \psi \tag{3.10}$$

which rearranged for ψ is

$$\psi(t) = \sin^{-1}\left(\frac{n_{\text{air}} \sin \beta}{n(t)}\right). \tag{3.11}$$

The time-dependent refractive index can be derived by firstly considering the initial refractive index, which can be calculated from the known volume fractions and refractive indices of A, B and S and the equation

$$n_i = n_A \phi_{Ai} + n_B \phi_{Bi} + n_S \phi_S, \tag{3.12}$$

where n_A, n_B and n_S are the refractive indices of polymer A, polymer B and solvent S respectively. ϕ_{Ai} and ϕ_{Bi} are the initial volume fractions of the polymers in the solution and ϕ_S is the volume fraction of the solvent within the solution. As the solvent evaporates during the spin coating the value of ϕ_S decreases and so the values of ϕ_{Ai} and ϕ_{Bi} increase until there is negligible solvent left in the film when coating has finished. At this point, the refractive index of the film is given by

$$n_f = n_A\phi_{Af} + n_B\phi_{Bf}. \tag{3.13}$$

For example in a solution that begins as 2% polymer concentration in a solution of 98% solvent in equal parts polymer A and polymer B would give the following values:

Volume Fraction	Value
ϕ_{Ai}	0.01
ϕ_{Bi}	0.01
ϕ_S	0.98
ϕ_{Af}	0.50
ϕ_{Bf}	0.50

By assuming that the refractive index of the polymer solution changes linearly with time, equation 3.14 holds true.

$$n(t) = n_i + g_n t \tag{3.14}$$

g_n is the gradient of this line and is expressed by equation 3.15.

$$g_n = \frac{1}{t_f}[n_f - n_i] \tag{3.15}$$

Combining equations 3.9, 3.11, 3.14 and 3.15 results equation 3.16 which can be used to calculate thickness as a function of time.

$$h(t) = h_f + \frac{(m-1)\lambda}{2\cos\psi\,(t)\left(n_i + \frac{t}{t_f}[n_f - n_i]\right)} \tag{3.16}$$

When the solvent has fully evaporated and the thinning has stopped, the value of $m = 1$ which causes the right hand side term in equation 3.16

to reduce to 0 and the thickness is that given experimentally by h_f, as is expected.

This method relies solely on the peaks which are caused by the cycle of constructive and destructive interference. The raw data taken by the optospinometer is actually subject to noise induced by the rotation of the spin coater. This noise results in extra peaks of a higher frequency which obscure the lower frequency peaks, especially at the first few seconds of spin coating, as can be seen in figure 3.5.

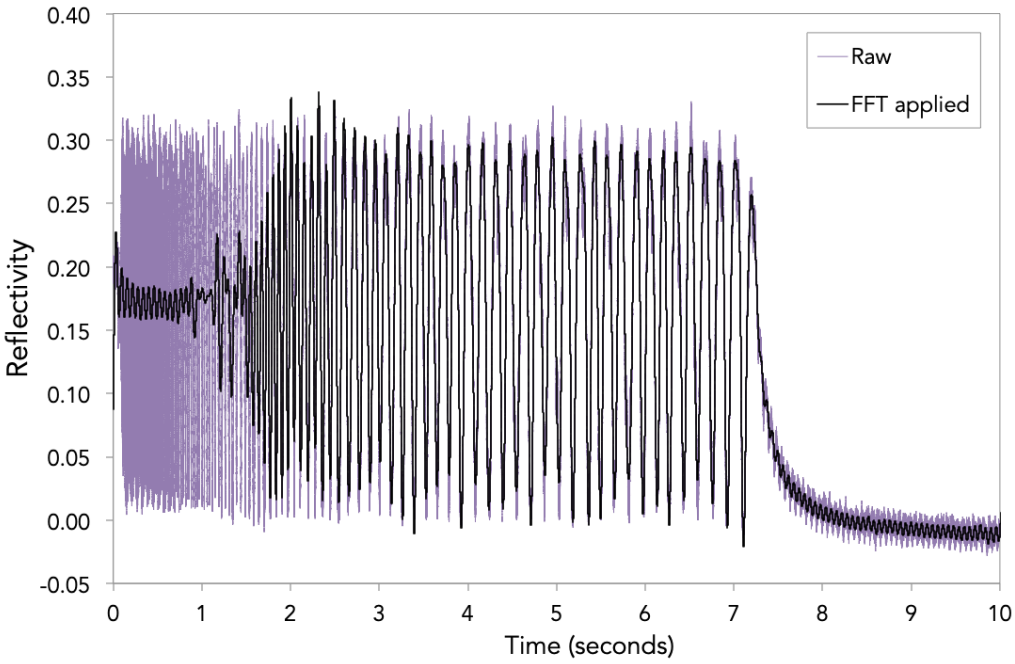

Figure 3.5: The raw data of the optospinometer has a lot of noise, especially in the first few seconds of spin coating (purple). After the FFT has been applied, the resultant optospinogram (black) can be used in analysis.

In order to extract only the Bragg peaks, a filter must be applied to remove the noise. A Fast Fourier Transform of the raw data optospinogram shows the frequencies at which there is periodicity, visible in figure 3.6.

For the example in figure 3.6, a number of noticeable frequencies are visible. The peak at approximately 16.$\dot{6}$ Hz is caused by the spin coater itself rotating at 1000rpm, or 16.$\dot{6}$rps. This peak of noise will always occur at the frequency of rotation.

By applying a low pass filter of 16 Hz to these raw data, all periodic noise

effects caused by the spin coater can be eliminated. The true peaks can then be detected clearly and used for equation 3.16. Any spin coatings done at 2000rpm require a low pass filter of 33 Hz to remove the noise at $33.\dot{3}$ Hz.

The angular acceleration of the optospinometer is approximately 560 rev/s^2, meaning the optospinometer reaches an angular velocity of 1000rpm in 0.03s and 2000rpm in 0.06s. The experimental runs conducted at each angular velocity did not exhibit a thinning peak during the acceleration period, so its affect on the data is discounted.

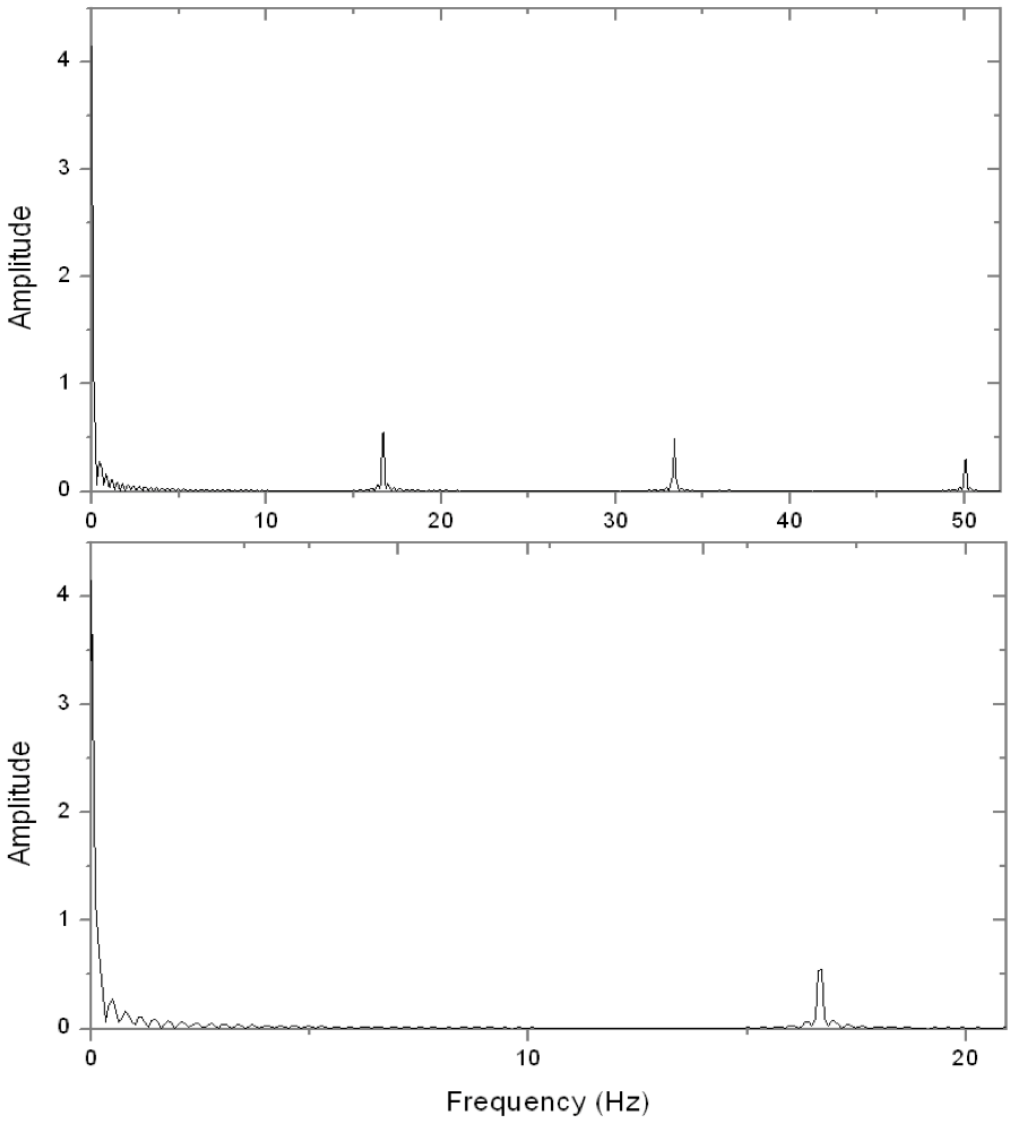

Figure 3.6: The FFT of an 1000rpm optospinogram (top) up to 50 Hz and (bottom) up to 21 Hz. At 16.7 Hz there are peaks due to the rotation of the optospinometer. This reverbs at 33.3 Hz and all higher frequencies that are multiples of 16.7.

3.1.2 Off-Specular Scattering

Off-specular light scattering is another non-invasive method of using light to infer information about a thin film. The roughness of a surface affects how the light is reflected and so images can be used to infer film structure,

especially the phase separation nature of films discussed in section 2.3.

Specular reflection occurs when the angles of the incident and reflected beam are equal, as is shown by figure 3.7a. This typically occurs when the reflective surface is smooth. In contrast off-specular scattering occurs when the angles of the incident and reflected beam are not equal, figure 3.7b. A rough surface acts like numerous reflective surfaces at different angles to the normal and is the cause of this. A higher roughness causes a larger off-specular reflection.

The resolution of laser off-specular scattering is limited by the area of the laser dot. If this is large, finer phase separated domains and small roughnesses will cause the specular and off-specular reflection to be indistinguishable. A similar case can occur when multiple length scales are present in the film, in which a laser with a low resolution will combine the results into one off-specular feature. The maximum value of q that can be recorded by the optospinometer is $0.4\mu\text{m}^{-1}$.

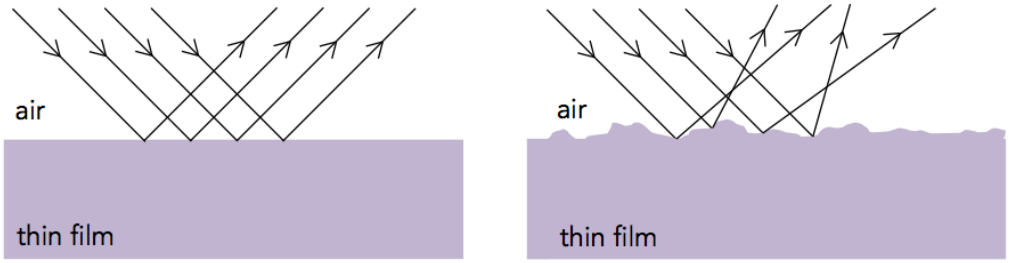

Figure 3.7: Left: The specular reflection due to light incident on a flat surface. Right: The off-specular reflection due to light incident on a textured surface.

Length scale features due to phase separation will cause the laser light to be reflected at a different angle to the specular reflection. The length scale d causing this off-specular reflection can be converted into reciprocal space, q-space using equation 3.17 [165]. As the structure changes with time, both d and q are time-dependent.

$$q\left(t\right) = \frac{2\pi}{d} \tag{3.17}$$

A camera images the film with a frame rate of 30 frames per second. For a typical 10 second spin, this results in 300 grey-scale intensity images. The image sequence is read in to a LabVIEW 8.5 script which performs the task illustrated and explained in figure 3.8. When the phase separation of the film

begins to exhibit a length scale within the film structure, this is indicated by the presence of a ring in the off-specular data.

An off-specular plot in which no ring develops is shown in figure 3.9a and an off-specular plot which does eventually display a ring is given in figure 3.9b. Time is plotted against q-space $q(t)$, which is given in $\mu.s^{-1}$. The LabVIEW programme gives three plots of the off specular in different dimensions: radial, horizontal and vertical. An off-specular feature could be seen in any of these three plots.

3.1.3 Position Calculations

The radius at which the laser is targeted can be calculated using the reflectivity data of a spin. A silicon wafer is marked with a strip of adhesive tape of constant width, as shown in figure 3.10. This wafer is referred to as the test wafer and is not reused with a polymer solution.

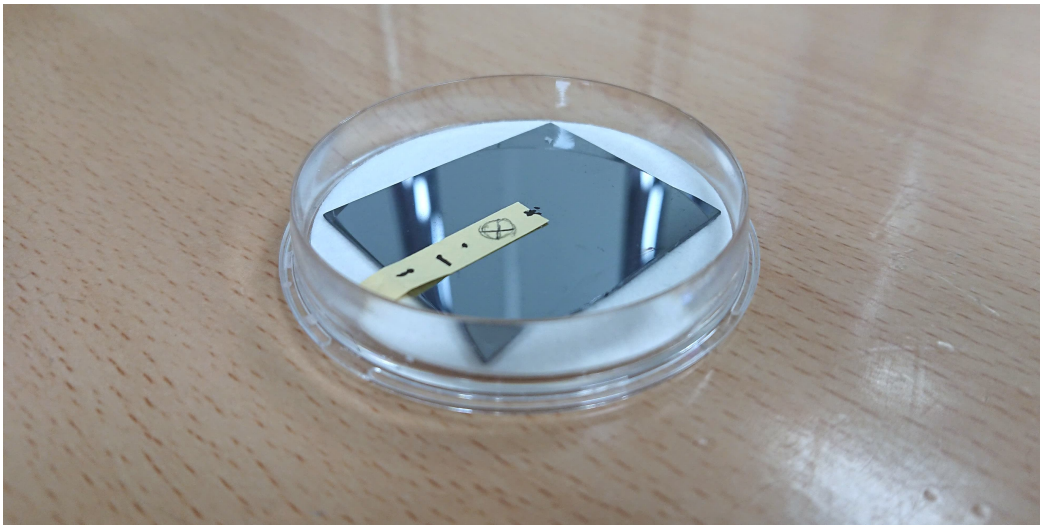

Figure 3.10: The silicon used as the test wafer is marked with opaque tape which in turn is marked with the multiple radii of interest.

As the platform spins, the off-centre laser traces a circumference around the centre of the test wafer which is reflected at all regions excluding the region obscured by the tape. The resultant reflectivity data is an oscillating function not dissimilar to a top-hat function. For a 10 second run at 1000rpm, there will be approximately 166 spins, two of which are shown below in figure 3.11. This process is repeated after each radial adjustment of the laser.

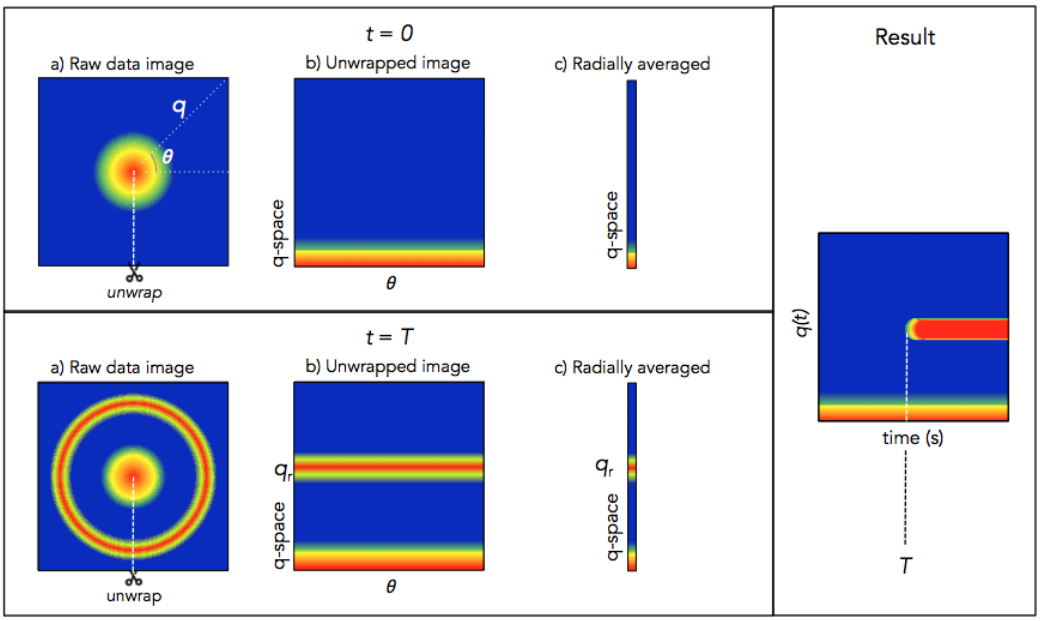

Figure 3.8: The a) raw data, b) unwrapped image and c) radially averaged images look different for both $t = 0$ and $t = T$. The highest intensity is red and the lowest intensity is blue. At $t = 0$, a) the raw data show that off-specular reflected laser light is concentrated at the centre of the image. An initial indicator such as this is typical for a film that has not begun to exhibit phase separation yet. For analysis, the centre of this image is selected using LabVIEW and taken as the centre of every image in the set. The image is cut from this point to the edge of the image. b) The resultant unwrapped image gives θ as a function of q-space q and intensity. c) This intensity is then radially averaged to produce a radially-averaged intensity 'slice' for a time $t = 0$. The process is repeated for each image obtained. At $t = T$ the film has begun to phase separate giving a feature length scale to the film. Because of this phase separation, a) the raw data show a ring around the centre of the image. Again in order to analyse this result, the image is cut from the edge to the previously defined central point. b) The resultant unwrapped image gives θ as a function of q-space q and intensity. c) This intensity is also radially averaged to produce a radially-averaged intensity 'slice' for a time $t = T$. The presence of a ring indicates that the film structure has a length scale which can be resolved by the laser. Such a feature is seen in all subsequent images. There will now be as many 'slices' as there are images in the sequence. These are consolidated to give a result similar to the one given here.

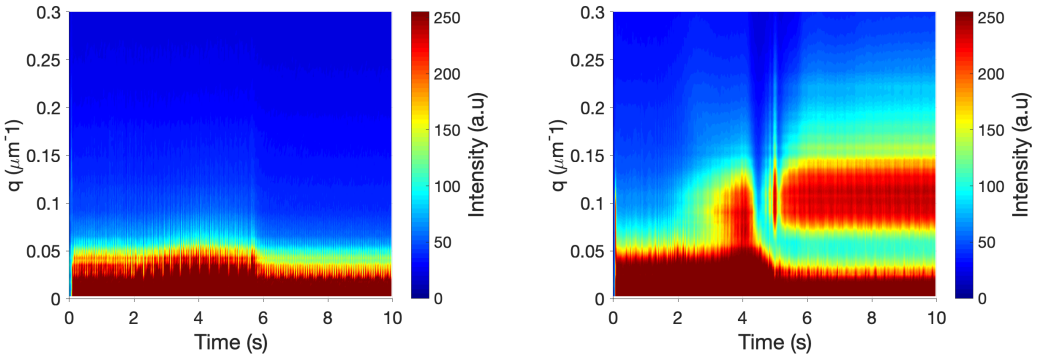

Figure 3.9: An off-specular plot from a 10 second spin coating (a) at the centre a film, at 1000rpm, using a 2% PS:PMMA solution of equal polymer ratio and (b) 8mm from the film centre, at 2000rpm, using a 8% PS:PMMA solution of equal polymer ratio.

A code was written in Python to find the sharp increase or decrease in reflectivity caused by the edges of the tape. When the change in intensity increased by more than 0.1, the time was recorded. The difference between these times was then sorted into two possible categories. The smaller time intervals were when the tape was obscuring the laser, t_d. The larger time intervals were when the reflectivity was at a maximum as nothing was obscuring the silicon reflecting, t_R. The total time for one rotation can therefore be expressed as $t_d + t_R = t_{\text{total}}$.

As the laser passes across the silicon it makes a circular path with a circumference of $2\pi R$. The arc of this circumference obstructed by the masking tape has a length approximately equal to the width of the tape. This assumption leads to a systematic error in the data which is the same for each set of radial data. From knowing the values of t_d and t_{total} the radius can be determined as

$$\frac{t_{\text{d}}}{t_{\text{total}}} = \frac{d_{\text{tape}}}{2\pi r}, \tag{3.18}$$

which rearranges to give r,

$$r = \frac{d_{\text{tape}}}{2\pi} \times \frac{t_{\text{total}}}{t_{\text{d}}}. \tag{3.19}$$

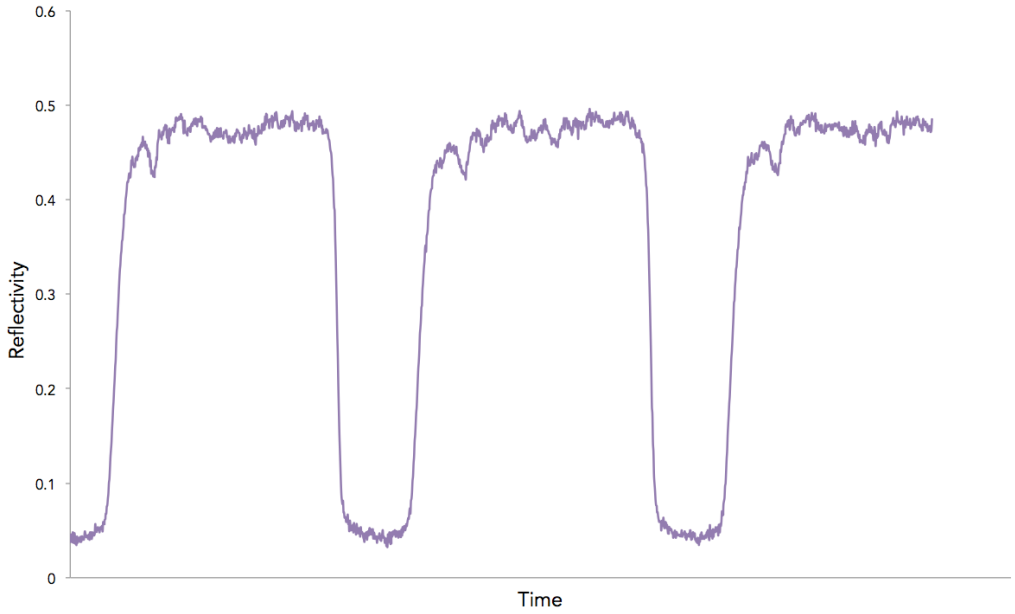

Figure 3.11: The resultant optospinogram for an observed spin of marked silicon. When the laser is incident on the tape, the reflectivity decreases. Knowing the diameter of the tape means such a plot can be used to determine the accurate radius that the laser is incident to.

As there are numerous rotations, a mean value of r can be calculated. If necessary this method can be altered in order to determine the accurate rotation of the optospinometer.

3.2 Equipment

3.2.1 Optical Microscope

An optical microscope utilises visible light and an arrangement of lenses in order to magnify a sample. The optical microscope used to image the structure of the phase separated blended polymer films was a Nikon Eclipse ME600 which was connected to a PixeLINK PL-A742 camera. A Reichert calibration grid was used to calibrate the length scales of the images.

3.2.2 Spectroscopic Ellipsometer

The spectroscopic ellipsometer used to measure the final thickness of the films was a J. A. Woollam alpha-SE Ellipsometer. A diagram of the ellipsometer is given in figure 3.12. Ellipsometry is an indirect method used to determine film thickness or in some cases, refractive index.

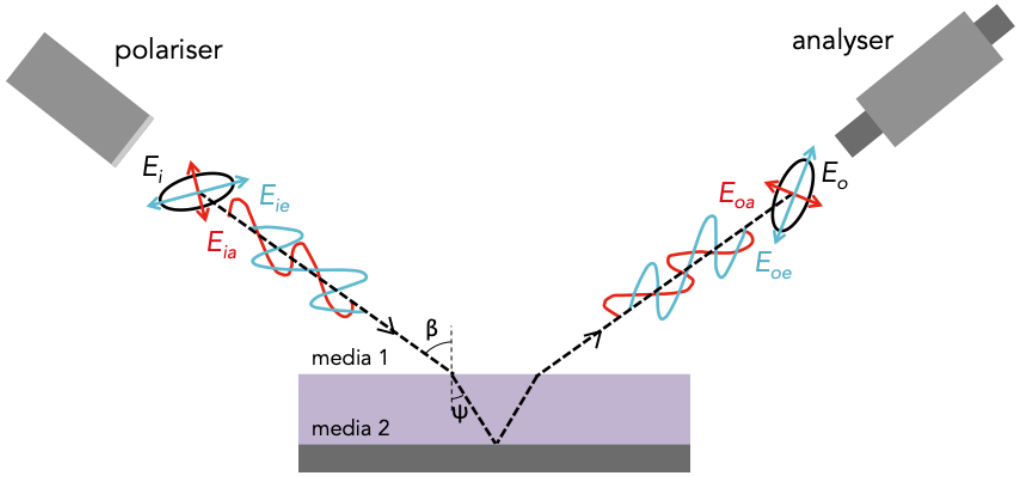

Figure 3.12: A diagram of the spectroscopic ellipsometer.

Elliptically polarised light is considered to be an electrical wave, which can be separated into two independent and orthogonal fields, each parallel or perpendicular to the plane of incidence. The incoming light is denoted as E_i and the outgoing light is E_o. Each has a parallel and perpendicular component, which for the incoming light are E_{ia} and E_{ie} respectively and for the outgoing light are similarly denoted as E_{oa} and E_{oe}.

The Fresnel reflection coefficients relate these two fields to one another in terms of incident angle β and refracted angle ψ and are given by

$$r_a = \frac{E_{oa}}{E_{ia}} = \frac{\widetilde{n}_1 \cos\beta - \widetilde{n}_2 \cos\psi}{\widetilde{n}_1 \cos\beta + \widetilde{n}_2 \cos\psi} \tag{3.20}$$

and

$$r_e = \frac{E_{oe}}{E_{ie}} = \frac{\widetilde{n}_1 \cos\beta - \widetilde{n}_2 \cos\psi}{\widetilde{n}_1 \cos\psi + \widetilde{n}_2 \cos\beta}, \tag{3.21}$$

where $\widetilde{n_1}$ and $\widetilde{n_2}$ are the complex refractive indices for medium 1, air, and medium 2, the film. They are also expressed as

$$\widetilde{n_1} = n_1 - iK_1 \tag{3.22}$$

and

$$\widetilde{n_2} = n_2 - iK_2, \tag{3.23}$$

where n_1 and n_1 are the real components of the complex refractive indices of the media and K_1 and K_2 are the imaginary components.

In ellipsometry, polychromatic, unpolarised light is elliptically polarised with known polarisation. As the light is reflected and refracted by the sample, the optical properties of the film affect the outgoing light. This change is recorded by an analyser, which characterises it in the complex reflectance ratio, given by

$$\delta = \frac{r_a}{r_e} = \tan(\Psi)e^{i\triangle}, \tag{3.24}$$

where Ψ is the amplitude component and Δ is the phase difference, which are calculated and given as a function of wavelength for the polychromatic light. A model is then used to determine the thickness from the experimental values Ψ and Δ. To quantify the refractive index of the film at all wavelengths, a dispersion equation was used. The Cauchy model was used, which is given by

$$n = A + \frac{B}{\lambda^2} + \frac{C}{\lambda^4}, \tag{3.25}$$

in which A, B and C are constants.

An example ellipsometry result is given in figure 3.13. The software that accompanies the ellipsometer is CompleteEASE, which produces the best film thickness fit, including the error in its measurement.

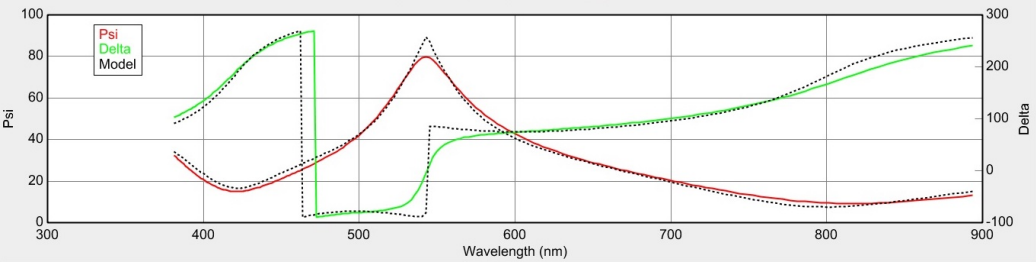

Figure 3.13: An example result from the spectroscopic ellipsometer in which the Cauchy model has been compared to the experimental results, Ψ and Δ. The film has a polymer concentration of 4% with equal ratio PS:PMMA and was spin coated at 1000rpm.

3.2.3 Atomic Force Microscope

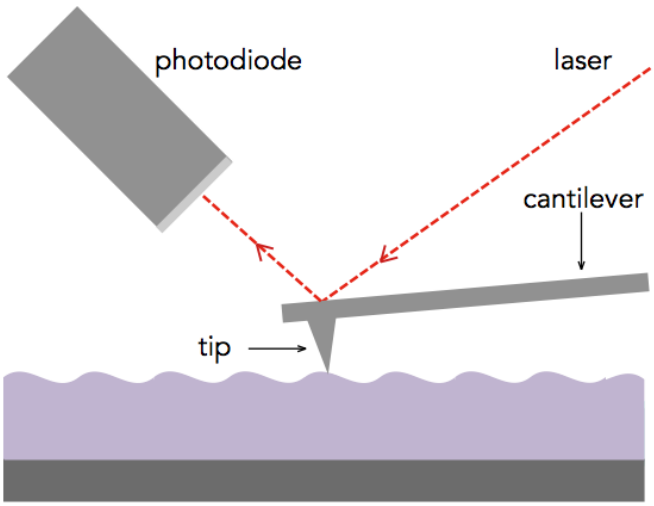

Figure 3.14: A diagram of an atomic force microscope.

Atomic force microscopy is a method of scanning probe microscopy that can be used to determine height variations in a sample. A cantilever tip is in contact with the sample and scanned across a set length. The height variations cause the cantilever to move. The peaks and troughs causing the cantilever movement are recorded using a laser incident on its surface which is reflected to a photodiode. A diagram is given in figure 3.14.

An AFM can also be used in tapping mode, where the cantilever tip is made to oscillate at its resonant frequency. When the tip is in near contact with

the sample, van der Waals forces are induced due to temporarily fluctuating dipoles between the cantilever and the sample. The forces are then recorded. Such a method is useful with phase separated polymer blends as each polymer will result in a different force which can be compared against known values.

The AFM used for these results was the Asylum Research MFP-3D AFM located in the Physics and Astronomy department at the University of Sheffield.

3.2.4 Surface Profiler

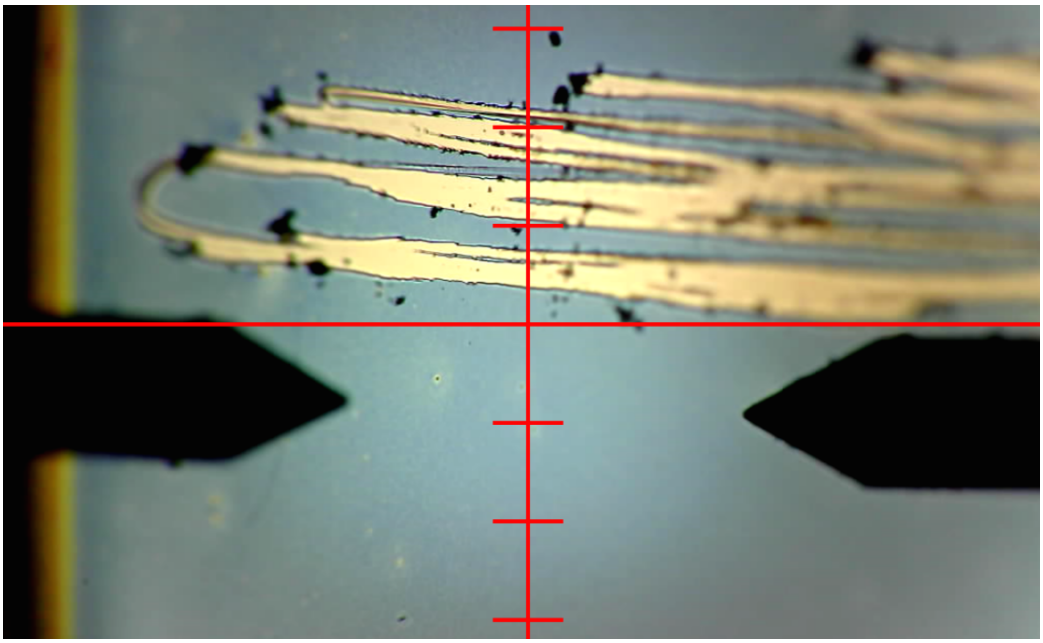

Figure 3.15: The edge of a 2% equal ratio PS:PMMA blend film cast at 1000rpm with scalpel scratches present in order to find the thickness of the film as seen from the surface profiling software. The film has been treated with nitrogen flow in order to remove the waste polymer film but as can be seen from the black marks, some remain.

The indirect thickness measurements obtained by ellipsometry were corroborated using a direct method. Surface profiling can be done using a scratched film. A scalpel is used to remove some of the film but so as to not damage the substrate. The tip of the surface profiler is then dragged across a set length for a given time and measures the peaks and troughs of the film and the scratch. A scratch will give a step in the data, and the height difference in the step is taken as the thickness of the film.

The surface profiler used for these experiments was a Bruker Dektak:XT, located in the Physics and Astronomy department at the University of Sheffield.

An image from the surface profilometer is given in figure 3.15 which shows a scratched film. An example of the output result is shown in figure 3.16.

The extremely high peaks in figure 3.16 are a result of dust on the film or waste polymer from the scratching. Smaller peaks and troughs are indicative of the roughness of the film but in measuring the thickness, these differences are averaged out.

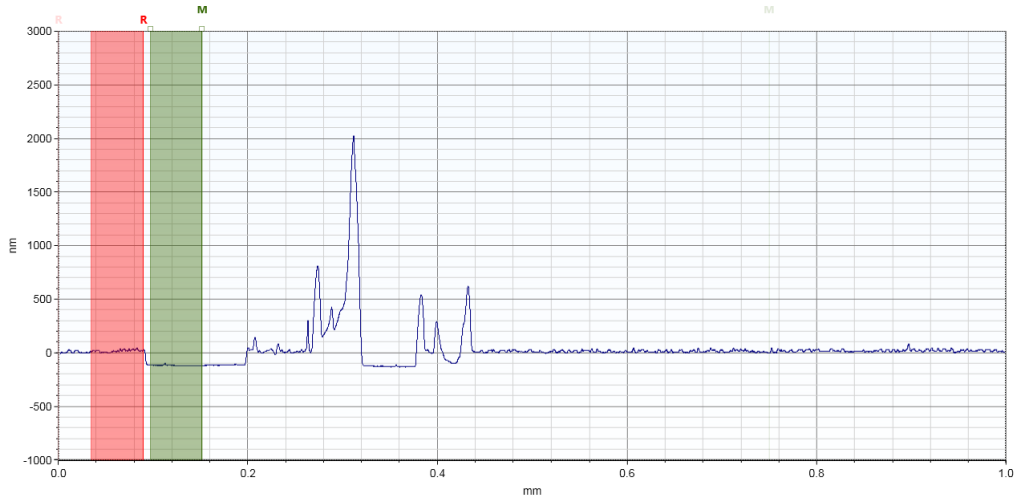

Figure 3.16: The surface profilometry result from the film in figure 3.15 at 12mm distance from the centre of the film. The profiler covered 1mm in 60 seconds. The red band is used to calculate the 'zero point' and when combined with the green band, the thickness is obtained.

3.3 Films

3.3.1 Substrate

Silicon wafers 28mm^2 in size were used as substrates for all spin coating experiments. The silicon was cleaned by immersion in toluene and then sonicated for a minimum of 1 hour and dried with a nitrogen flow. An O_2 plasma cleaner was used on each substrate to complete the final stage of cleaning.

The silicon wafers were made by Prolog Semicor LTD who report that, due to the silicon reacting with oxygen in the atmosphere, have a native oxide

layer SiO_2 approximately 2nm thick. This was supported by ellipsometry to determine the final film thicknesses, as modelled structures that included the SiO_2 had a better fit to the data. As the thickness of the films themselves are typically between 100 - 1100 nm the SiO_2 layer is considered to have a negligible effect but to be meticulous, its presence is stated here.

3.3.2 Solution

PS and PMMA were chosen for these experiments due their interaction parameters with toluene being similar, so one pair of chemicals would not dominate the interactions, but phase separating easily from each other as $\chi_{\mathrm{PS/PMMA}} = 0.04$ [59]. The interaction parameters for the polymers and toluene are $\chi_{\mathrm{PS/toluene}} = 0.44$ and $\chi_{\mathrm{PMMA/toluene}} = 0.41$ [71].

The masses of the polymers and toluene used to produce the solutions were measured using a scale which was accurate to 1×10^{-9}g. The solutions were mixed using magnetic stir bars for 24 hours before they were used to ensure the polymer was completely dissolved.

3.3.3 Toluene

The toluene used in these experiments was supplied by Sigma Aldrich and was used as a solvent for all the solutions used in spin coating. It has a chemical formula of $C_6H_5CH_3$. It was 99.9% pure and has a molecular weight of 92.12 g.mol^{-1}. When necessary in calculations, the refractive index of toluene is $n_{\mathrm{toluene}} = 1.4969$, the density is $\rho_{\mathrm{toluene}} = 867\mathrm{kg.m}^{-3}$ and its viscosity is $\eta_{\mathrm{toluene}} = 0.623$mPa.s at 19.3°C, as measured by rheometry.

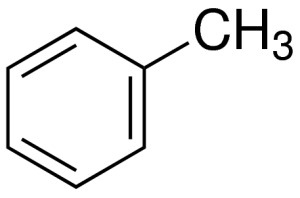

Figure 3.17: The structure of toluene.

3.3.4 Poly(styrene) PS

The PS used in these experiments was supplied by Kromatek. It has a chemical formula of $(C_8H_8)_n$. The PS used has a molecular weight of 184,000 g.mol^{-1}. When necessary in calculations, the refractive index of PS is $n_{PS} = 1.5894$ and the density is $\rho_{PS} = 1040$kg.m^{-3}. For simplicity poly(styrene) shall often be referred to as PS.

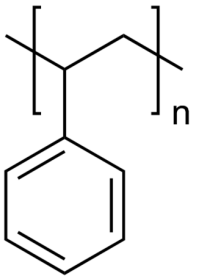

Figure 3.18: The structure of PS.

3.3.5 Poly(methyl methacrylate) PMMA

The PMMA used in these experiments was supplied by Kromatek. It has a chemical formula of $(C_5O_2H_8)_n$. The PMMA used has a molecular weight of 187,000 g.mol^{-1}. When necessary in calculations, the refractive index of PMMA is $n_{PMMA} = 1.4893$ and the density is $\rho_{PMMA} = 1180$kg.m^{-3}. For simplicity poly(methyl methacrylate) shall often be referred to as PMMA.

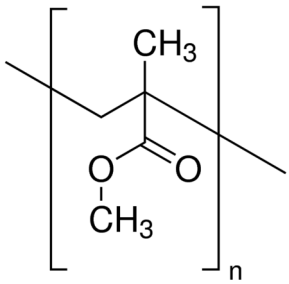

Figure 3.19: The structure of PMMA.

3.3.6 Deposition

Each spin coating was produced using the same deposition technique. Pure toluene is spin coated onto each film until it is dry to rid the surface of impurities. Enough solution to cover the substrate surface was deposited before the spinning started. The initial static stage in spin coating has been shown to not affect the thinning rate [21]. The films were not annealed after spin coating, which leaves trace solvent in the film that is accounted for by modelling.

4 Results I: Modelling

This chapter discusses the initialisation of the parameters in the Reisfeld, Bankoff and Davis model and the consequential results from using it to predict the time-dependent film thickness. The models are compared with experimental data obtained at radii of 0mm, 4mm, 8mm and 12mm from the centre of the film. As the RBD model does not have radial dependence, it was expected that the model would fit for the data taken at the centre of the film and any radial variations would be indicated by a diversion from the 0mm data or the model itself.

4.1 Radial Measurement

It was firstly necessary to determine that the optospinometer was capable of obtaining data when the laser was directed away from the centre of the film. Initial tests indicated that the camera capturing the off-specular light has a large enough aperture to not be affected by the change in position of the off-specularly reflected laser light.

The process detailed in section 3.1.3 in order to measure the radius at which the laser was incident was first conducted. Such a method was also be used in order to find the accurate spin speed of the optospinometer and to calibrate it.

The silicon test wafer approximately 28mm in diameter had a strip of masking tape attached to it. The tape had a width $d = 5$mm at all the various radii and was marked at the centre of the film and at 4mm, 8mm and 12mm. These values were measured with a ruler to gain approximate values when the wafers were placed at the centre of the spin coater.

The platform was then positioned so that the laser was on the 8mm mark. The test wafer was spun at 1000rpm for 10 seconds. This yielded an optospinogram with a roughly top hat function, from which an excerpt is given in figure 3.11. The minimum reflectivity ≈ 0.05 and the maximum reflectivity ≈ 0.5.

A code was then used to provide an accurate value for each radius of interest. The code can also be adapted to find an accurate angular velocity ω of the optospinometer. The target ω used for the initial test was 1000rpm, which is 16.667 revolutions per second. The time taken for one revolution should therefore be 0.060 seconds. The code gave the mean value for one rotation

as being 0.058 seconds. The more accurate ω for this test is therefore 17.233 revolutions per second or 1034rpm.

This was repeated for multiple spins with ω targeted to 1000rpm and all gave ω as being 1034rpm. Similarly when repeated multiple times for a target ω of 2000rpm, the angular velocity was found to be 2017rpm. This should be noted for any further works that depend on accurate angular velocities.

4.2 Polymer Solutions

A total of twelve solutions were made for the experiments, which were conducted in two stages. The solutions made for the first stage of experiments were:

- 2% equal blend
- 2% PS majority, PS:PMMA 3:1
- 2% PMMA majority, PS:PMMA 1:3
- 4% equal blend
- 4% PS majority, PS:PMMA 3:1
- 4% PMMA majority, PS:PMMA 1:3

The solutions made for the second stage of experiments were:

- 6% equal blend
- 6% PS homopolymer
- 6% PMMA homopolymer
- 8% equal blend
- 8% PS homopolymer
- 8% PMMA homopolymer

The first six solutions cast were of lower concentration, 2% and 4% polymer concentration by mass. These solutions were spun at either 1000rpm or 2000rpm for a total of 10 seconds at the four radii of interest: 0mm, 4mm, 8mm and 12mm. A total of 48 films were made for this initial analysis.

Once these experiments were completed, concentration was determined to be the variable of most interest and so polymer solutions of 6% and 8% concentration were then cast to further investigate the equal ratio blend

behaviour seen in the 2% and 4% films. Rather than use polymer blends in the ratio of PS:PMMA 1:3 and 3:1, homopolymer PS and PMMA films would be cast in order to be used as controls.

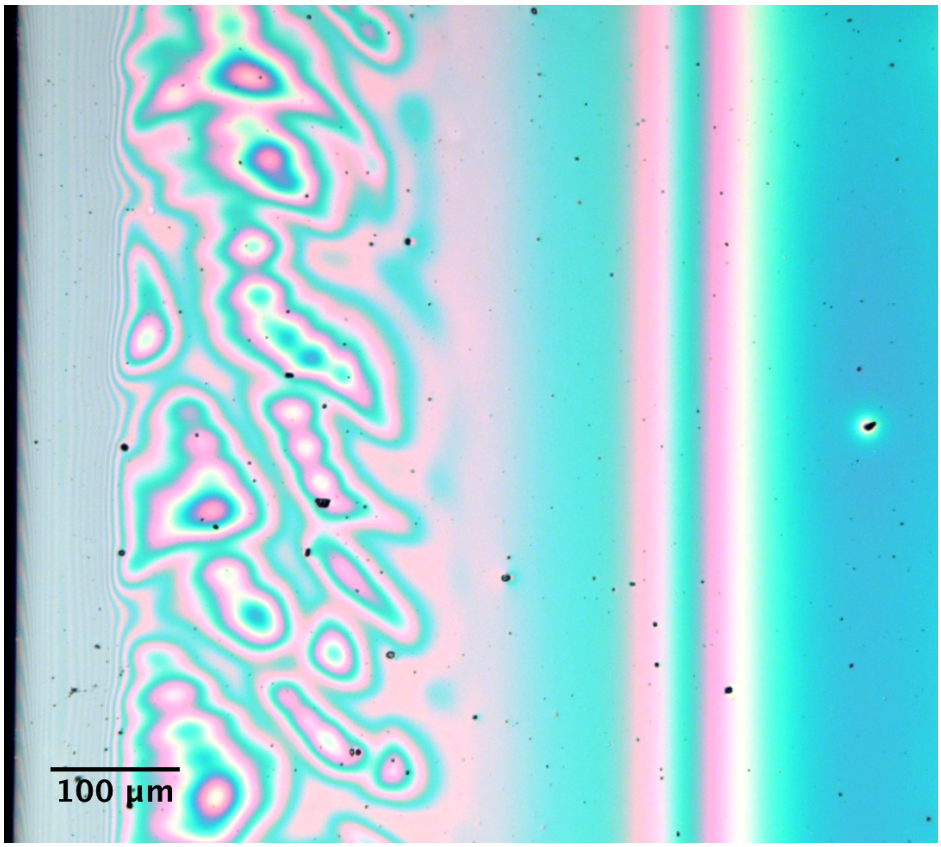

Figure 4.1: Edge morphology of an 6% PMMA film cast at 1000rpm.

These higher concentration solutions were also spun at either 1000rpm or 2000rpm. These spin coatings were conducted for 15 seconds as the 6% and 8% films took longer than 10 seconds to dry. Only data for 0mm, 4mm and 8mm could be obtained by the optospinometer because the 12mm data were seemingly subject to edge effects. The increased concentration of the solutions used caused interference to occur in the *in situ* data obtained with the laser. The ripples causing this effect can be seen in figure 4.1. 36 high concentration films were made in total.

For all experiments, solution was added to the substrate before the optospinometer had begun spinning. The atmospheric temperature and pressure were kept constant and ambient throughout.

4.3 Initialising the Model

$$\frac{\partial h^*}{\partial t^*} = -\frac{2e}{3} - \frac{h^{*3}}{3} - \frac{5\epsilon \mathtt{Re} h^{*4} e}{36} + \frac{34\epsilon \mathtt{Re} h^{*7}}{315} \tag{4.1}$$

The Reisfeld, Bankoff & Davis model given in equation 4.1 is given in terms of dimensionless thickness h^* and dimensionless time t^* and cannot be used until the dimensions have been restored.

The derivation used to obtain the model used dimensionless parameters such as length scale ϵ, Reynold's number $\mathtt{Re}$ and dimensionless thickness h^* in order to simplify the derivation and these terms must all be replaced.

The length scale of the system ϵ is given by equation 4.2 in which h_0 is the initial film thickness and R is the total radius of the system.

$$\epsilon = \frac{h_0}{R} \tag{4.2}$$

The Reynold's number $\mathtt{Re}$ is given by equation 4.3 in which U_0 is the radial velocity scale, ρ is the density of the solution and η is its viscosity.

$$\mathtt{Re} = \frac{U_0 h_0 \rho}{\eta} \tag{4.3}$$

The dimensionless evaporation rate e is given by equation 4.4 in which E is the true evaporation rate.

$$e = \frac{3E}{2\epsilon U_0} \tag{4.4}$$

The dimensionless time t^* is given in equation 4.5, in which t is the true time and T_0 is the time unit defined in equation 4.6, in which L is length of the system considered and the maximum value is the total radius $L = R$.

$$t^* = \frac{t}{T_0} \tag{4.5}$$

$$T_0 = \frac{L}{U_0} \tag{4.6}$$

The dimensionless thickness h^* is defined simply by equation 4.7 in terms of true thickness h and initial thickness h_0.

$$h^* = \frac{h}{h_0} \tag{4.7}$$

Equations 4.3, 4.4 and 4.6 depend on the radial velocity scale U_0 which is given in equation 4.8 in which ω represents the spin speed.

$$U_0 = \frac{h_0^2 \omega^2 R \rho}{\eta} \tag{4.8}$$

To simplify substituting the equations 4.2 - 4.8 into the RBD model, equation 4.1 is rearranged to

$$\frac{\partial h^*}{\partial t^*} = -\frac{2}{3}\left(e + h^{*3} + \epsilon \mathtt{Re}\left[\frac{5e}{12}h^{*4} - \frac{34}{105}h^{*7}\right]\right). \tag{4.9}$$

Substituting all the dimensioned variables into equation 4.9 gives

$$\frac{\partial h}{\partial t} = -\left(E + \frac{2\omega^2 \rho h^3}{3\eta} + \frac{5E\omega^2\rho^2 h^4}{12\eta^2} - \frac{68\omega^4\rho^3 h^7}{315\eta^3}\right), \tag{4.10}$$

in which $\partial h/\partial t$ is the thinning rate, E is the evaporation rate, ρ is the solution density, ω is the revolutions per second of the spin and h is the thickness. In order to obtain the thickness as a function of time or the thinning rate of the spin coating process, the unknown values must be quantified.

4.3.1 Evaporation Rate

The evaporation rate must be determined experimentally. The Meyerhofer model has been used by other research groups [166, 167] in order to find E by rearranging it to give 4.12 so that it follows the form of a straight line plot, equation 4.11.

$$y = m \times x + c \tag{4.11}$$

$$\frac{dh}{dt} = \frac{\rho\omega^2}{3\eta} \times 2h^3 + E \tag{4.12}$$

E is the y intercept on a plot of equation 4.12, as shown in figure 4.2. It is clear from figure 4.2 that this is not a straight line and thus this method is flawed, especially as there is not a clear value for the y intercept.

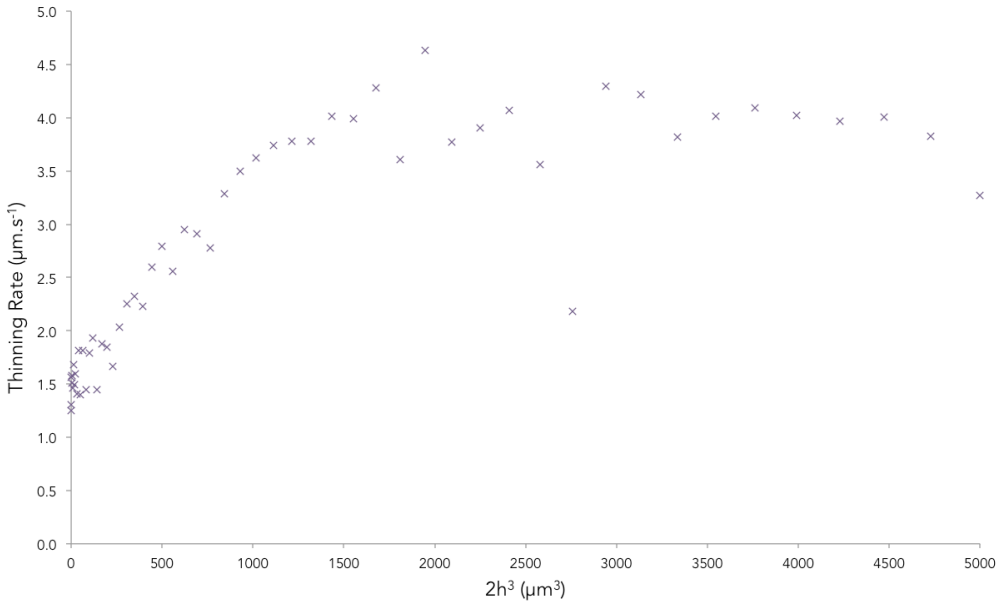

Figure 4.2: A plot of thinning rate against $2h^3$ for a spin coating of 2% equal ratio blend of PS:PMMA cast at 1000rpm.

Many factors affect the evaporation rate of a given solvent. Ambient temperature and vapour pressure are extremely influential but when these are kept constant, a notable variable in spin coating is the angular velocity ω. A larger ω causes the forces that contribute to turbulence to increase which then assists in evaporation by replenishing the surface with the solvent. Effectively, the solvent does not have to travel through the bulk to evaporate. In addition to this, the kinetic energy associated with the turbulence is transferred to the solvent molecules, giving them more energy and thus increases evaporation. This relationship is given mathematically by [166, 167]

$$E = C\sqrt{\omega}, \tag{4.13}$$

where the angular velocity is given by ω and C is a constant intrinsic to the solvent which considers the vapour pressure, boundary thickness, diffusion rate and viscosity of air. Finding a value of C experimentally and using equation 4.13 to obtain the evaporation rate requires many parameters to

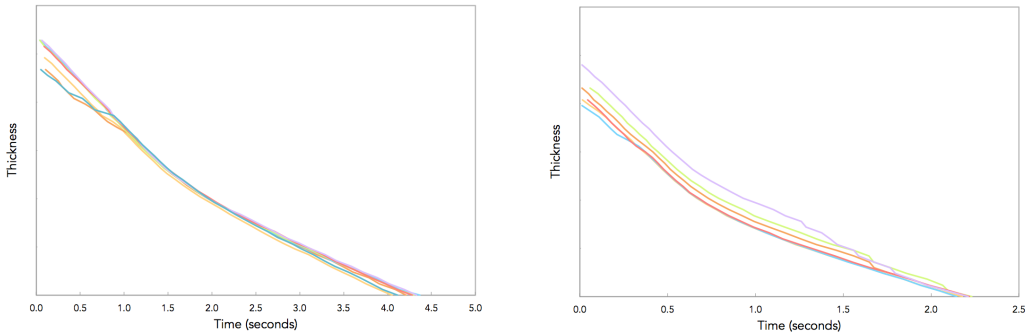

(a) 1000rpm (b) 2000rpm

Figure 4.3: The relative thickness as a function of time for toluene only spins.

be controlled. This is often not possible and so determining the evaporation rate using the straight line fit method has been used by groups [166, 167] in lieu of quantifying C.

Figure 4.2 gives an approximate value for the evaporation rate for an 1000rpm spin coating. If $E = 1.5\mu\text{m.s}^{-1}$ when $\omega = 1000\text{rpm}$, using equation 4.13, the constant C can be found for any spin speed [166, 167]. This method yields $E = 1.5\mu\text{m.s}^{-1}$ when $\omega = 1000\text{rpm}$ and $E = 2.1\mu\text{m.s}^{-1}$ when $\omega = 2000\text{rpm}$.

An alternative method is also possible. Pure toluene was spin coated numerous times at 1000rpm and 2000rpm. The relative thicknesses as a function of time are given in figure 4.3.

Both figures display a transition regime inflection, when inertial force thinning begins to become less significant. The evaporative dominant thinning in both figures is closer to a straight line than that of figure 4.2. After the thickness plot has fully undergone an inflection, it is assumed that only solvent evaporation contributes to the thinning and so this gradient is the evaporation rate. The gradient of a line is defined as

$$g = \frac{\Delta y}{\Delta x} \tag{4.14}$$

where Δy is the change in the y values and Δx is the change in the x values. At both spin speeds the toluene evaporated fully during the spin coating but a final thickness is necessary to generate figures 4.3a and 4.3b, h_f was set as 1×10^{-15}nm for all repeats. In this instance, change in thickness is

important rather than the thickness itself and so fixing the numerical value is not problematic.

The evaporation rate is calculated for all repeats and the standard error can also be found. Gaining the evaporation rate in this way is repeatable and more accurate and so the evaporation rates initially used for the RBD model were

$$E = 1.87 \pm 0.02 \mu\text{m.s}^{-1} \quad \text{when } \omega = 1000\text{rpm}$$

and

$$E = 2.71 \pm 0.13 \mu\text{m.s}^{-1} \quad \text{when } \omega = 2000\text{rpm}.$$

As the evaporation rate was determined, an interesting feature was observed during a pure toluene spin coating. The spin coatings must take place in a dark room in order to detect the laser light. When test spins were conducted in full light, an intense radial colour change was observed, shown in figures 4.4 and 4.5 which are a collection of chronological images from a recording. The 'toluene flash' was also seen in solution spin coatings conducted in light and the effect has been seen by others [168, 169].

The time at which this flash occurred changed for different angular velocities and solutions. As *in situ* laser experiments and recording optical images, such as those given in figure 4.4, are mutually exclusive, accurate times could not be obtained. The initial assumption is that the flash occurs during the regime change [168]; inertial force dominant thinning to evaporation dominant thinning.

4.3.2 Density

As the solvent evaporates during spin coating, the density of the solution changes as a result of the change in volume fraction of the polymer. A relationship for the time-dependent variations in the density must be found in order to use the RBD model. This can be done by considering a mixture consisting of two different types of molecules A and B which have densities ρ_A and ρ_B respectively. The mixture consists of A and B in measures that can be expressed with volume fractions, ϕ_A and ϕ_B. As a result, the density of the mixture is defined by [170]

$$\rho = \phi_\text{A}\rho_\text{A} + \phi_\text{B}\rho_\text{B}. \tag{4.15}$$

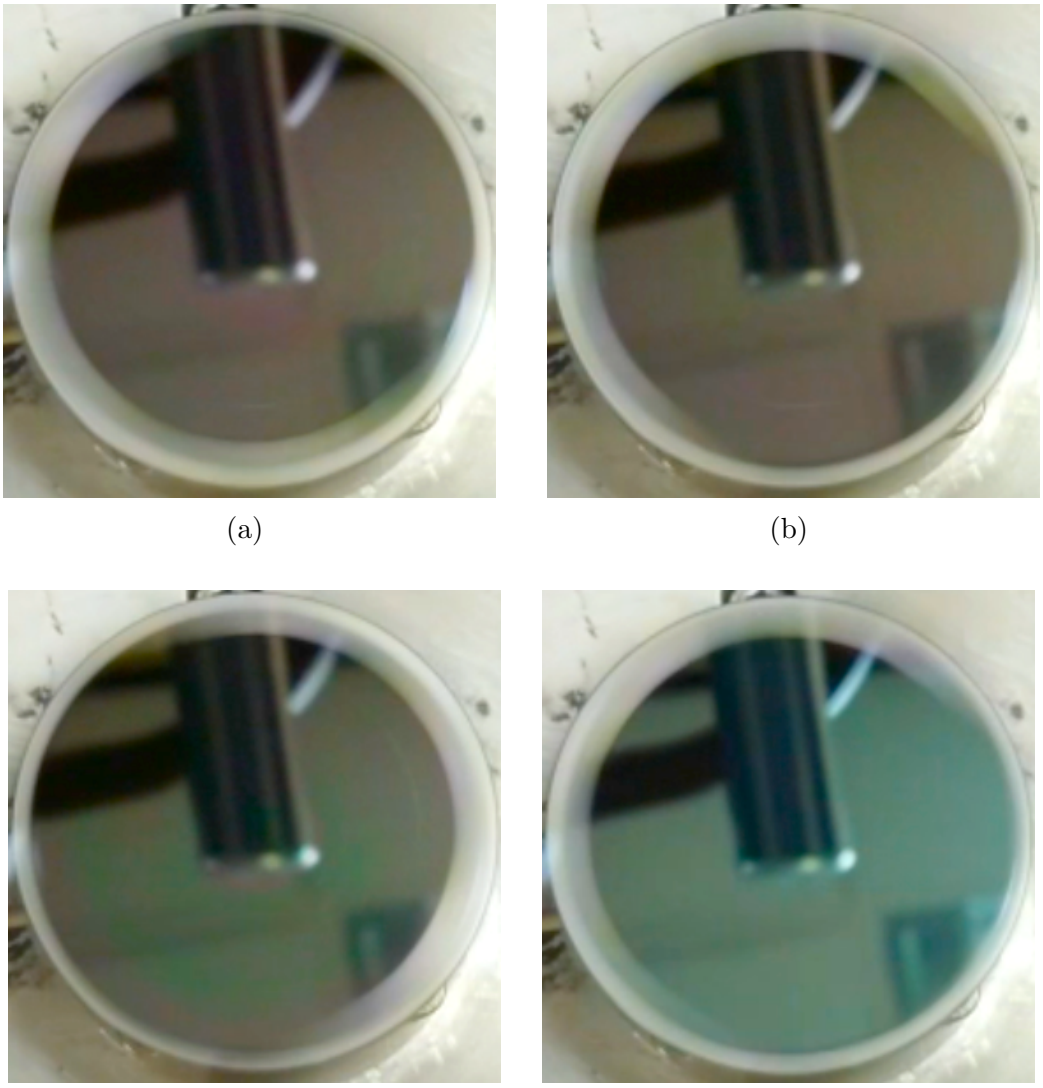

(a) (b)

(c) (d)

Figure 4.4: Four images taken in succession of the 'toluene flash'. The effect can particularly be seen on the edge of film in figures (c) and (d), indicating its radial behaviour.

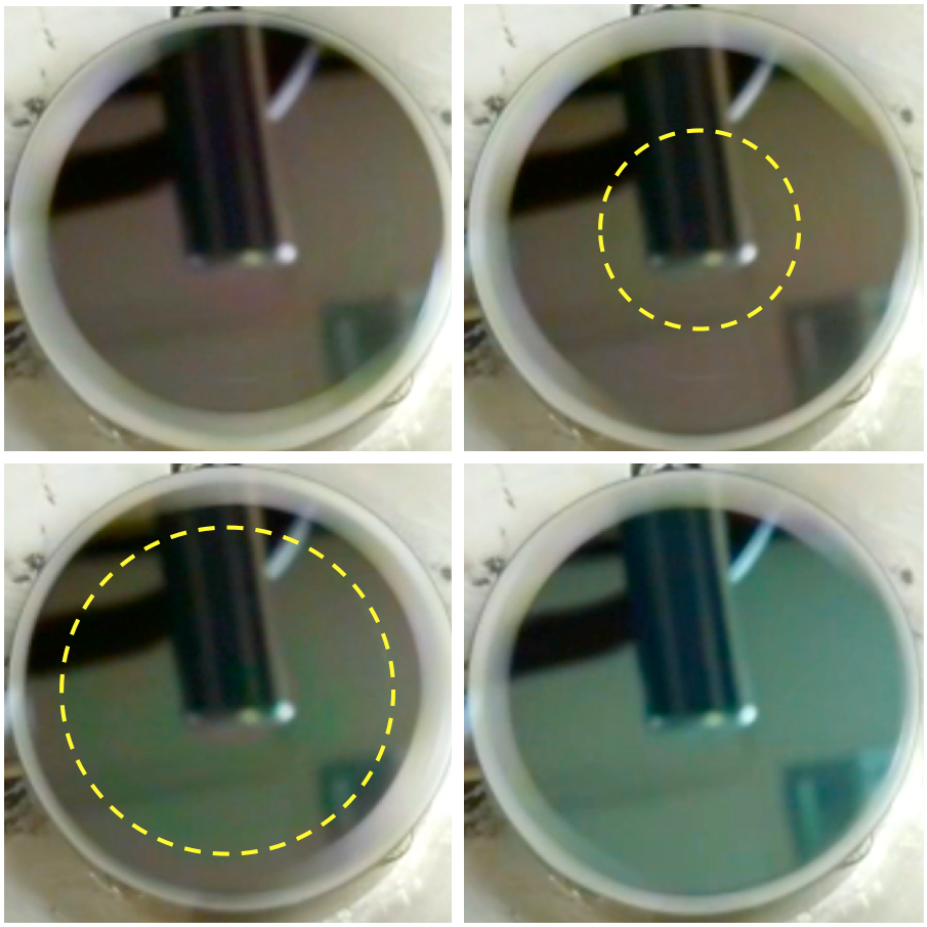

Figure 4.5: The radial flash exhibited in figure 4.4 has been highlighted.

In the solutions used in these experiments, the gradual evaporation of toluene causes a change in the volume fraction of the solvent. The volume fraction of the polymers rises as a result. This in turn causes a change in density which must be considered as toluene has a lower density than the polymers. This time-dependent relationship is given in equation 4.16.

$$\rho(t) = \rho_{\text{poly}}\phi(t) + \rho_{\text{solv}}\left(1 - \phi(t)\right) \tag{4.16}$$

Here $\rho(t)$ is the density of the solution as a function of time and ρ_{solv} is the toluene density, $\rho_{\text{solv}} = 867\text{kg.m}^{-3}$. The density of the polymers is given by ρ_{poly} and changes depending on the blend ratio. For equal blend solutions, $\rho_{\text{poly}} = 1110\text{kg.m}^{-3}$. For the PS majority solutions $\rho_{\text{poly}} = 1075\text{kg.m}^{-3}$ and for the PMMA majority solutions $\rho_{\text{poly}} = 1145\text{kg.m}^{-3}$. The volume fraction of the polymers is given by $\phi(t)$.

The volume fraction of the polymer $\phi(t)$ does not increase linearly with time. This must be estimated in the best possible method, which is done by relating the final film thickness h_{f} to the thickness as a function of time $h(t)$ in the relationship

$$\phi(t) = \frac{h_{\text{f}}}{h(t)}. \tag{4.17}$$

Hence the equation for solution density as a function of time is given by

$$\rho(t) = \rho_{\text{poly}}\left(\frac{h_{\text{f}}}{h(t)}\right) + \rho_{\text{solv}}\left(1 - \frac{h_{\text{f}}}{h(t)}\right). \tag{4.18}$$

The density of a solution depends on its temperature and pressure. All experiments and measurements were done at atmospheric pressure and the temperature was kept constant so this is not necessary to take into account.

4.3.3 Viscosity

As with density, the viscosity of the solution will also change with time due to the evaporation of the solvent. Initially the solution has a viscosity approximately equal to pure toluene, due to the low volume fraction of the polymers. As the solution evaporates, the volume fraction of the polymers increases and the solution becomes more viscous until the film is formed. A time-dependent value for viscosity is required.

The contribution of a solute to the viscosity of a solution can be found using the intrinsic viscosity, which is defined by

$$[\eta] = K {M_\mathrm{w}}^{\alpha}, \tag{4.19}$$

where K and α are the Mark-Houwink parameters, which are constants that determine the interactions of the molecules and M_w is the molecular weight of the solute. In some cases, the values of K and α have been found experimentally [93] but no data exist for the specific conditions of the solutions used. The intrinsic viscosity of a solution changes with solvent [171], the polymer molecular weight and the temperature, resulting in a different K and α for each solution. Measuring the Mark-Houwink parameters is convoluted and so another method is desired.

The viscosity η of a dilute solution is given by

$$\eta = \eta_\mathrm{solv} \left(1 + \eta_\mathrm{sp}\right), \tag{4.20}$$

in which the viscosity of the pure solvent is η_solv and the specific viscosity is η_sp [82]. The specific viscosity is related to the polymer volume fraction by

$$\frac{\eta_\mathrm{sp}}{\phi} = [\eta] + k_\mathrm{H} [\eta]^2 \phi, \tag{4.21}$$

where k_H is the Huggins constant [82]. Substituting equation 4.21 into equation 4.20 results in the solution viscosity as a function of volume fraction and intrinsic viscosity,

$$\eta = \eta_\mathrm{solv} \left(1 + [\eta]\, \phi + k_\mathrm{H} [\eta]^2 \phi^2\right). \tag{4.22}$$

If the solution is suitably dilute $\phi \to 0$, the final term is small enough to be ignored. Equation 4.22 then becomes [95],

$$\eta = \eta_\mathrm{solv} \left(1 + [\eta]\, \phi\right). \tag{4.23}$$

The intrinsic viscosity caused by the polymers is still unknown and it must be calculated. The solution viscosities are experimentally determined and as ϕ is known, equation 4.23 can be rearranged to find $[\eta]$.

Solution	η (mPa.s)
2% equal blend	1.60 ± 0.01
2% PS majority	1.75 ± 0.01
2% PMMA majority	1.42 ± 0.01
4% equal blend	3.12 ± 0.01
4% PS majority	3.53 ± 0.01
4% PMMA majority	2.95 ± 0.01
6% equal blend	5.36 ± 0.01
6% PS homopolymer	8.58 ± 0.01
6% PMMA homopolymer	4.61 ± 0.01
8% equal blend	11.07 ± 0.01
8% PS homopolymer	12.93 ± 0.01
8% PMMA homopolymer	8.43 ± 0.01

Table 3: The measured viscosities for the solutions at 19°C.

The initial viscosities of the solutions were measured using a rheometer. The values obtained at 19.3°C are given in table 3. The values obtained from the rheometer were corroborated by measuring the viscosity of pure water, which was found to be 1.000 mPa.s at 19.3°C, as is expected. The viscosity of toluene is known from literature, but was also measured using the rheometer and found to be 0.623 mPa.s at 19.3°C.

Equation 4.23 is valid for dilute solutions but as the toluene evaporates, the films become too viscous for this assumption to be always appropriate. The time-dependent viscosity for non-dilute films is given by [22]

$$\eta(t) = \eta_{\text{tol}} \left[\frac{h_0}{h(t)} \right]^{\alpha}, \tag{4.24}$$

where the viscosity of the toluene is η_{tol}, h_0 is the initial thickness of the film, $h\,(t)$ is the thickness of the film as a function of time, obtained by the optospinometer and α is a fitting parameter. This time-dependent viscosity has been used previously when in using the RBD model [46].

4.3.4 Thickness of Final Film

The final film thicknesses were found using ellipsometry. For blended films, the inhomogeneity in the film can lead to variations in thickness at different points due to phase separation. The beam of the ellipsometer used is has a

semi-major axis of 2mm and a semi-minor axis of 1mm. In order to corroborate the thicknesses obtained by the indirect method of ellipsometry, a direct thickness measurement was also taken for the equal ratio blended films using surface profilometry. The results are presented in figure 4.6 and can be seen for the films cast at 1000rpm and 2000rpm in tables 4 and 5 respectively.

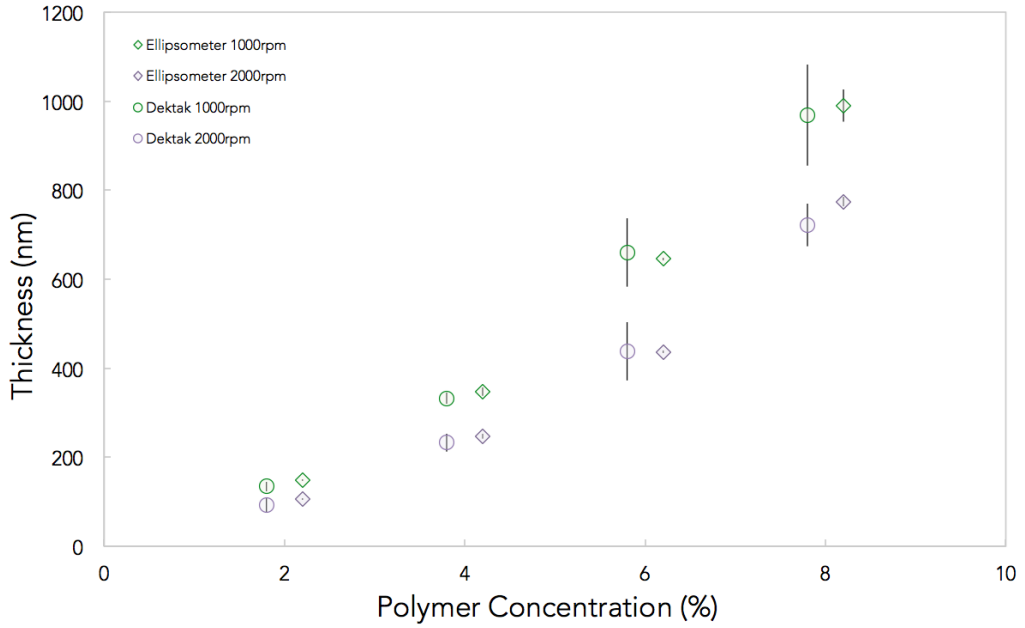

Figure 4.6: Comparing the thickness measurements of the ellipsometer and surface profiler for the equal ratio PS:PMMA blend films. The values for the error bars have been multiplied by 10 for clarity and the concentrations have been adjusted $\pm 0.2\%$ so that the data points for the ellipsometer and surface profiler do not overlap.

The results show that the error in the surface profilometry measurements is much larger than that of the ellipsometer. The ellipsometer beam measures thickness over a relatively large two-dimensional area whereas the measurement obtained by Dektak is reliant on a one-dimensional scan. Due to this, the surface profiler is subject to local fluctuations in thickness that would be averaged out by the ellipsometry measurement.

Film	Ellipsometer Thickness (nm)	Surface Profiler Thickness (nm)
2% blend	149±1	134±1
4% blend	347±1	332±1
6% blend	645±1	660±8
8% blend	990±3	970±10

Table 4: Comparing the thickness measurements of the ellipsometer and surface profiler for the equal ratio PS:PMMA blend films cast at 1000rpm.

Film	Ellipsometer Thickness (nm)	Dektak Thickness (nm)
2% blend	106±1	92±3
4% blend	247±1	233±3
6% blend	436±1	438±7
8% blend	774±1	720±11

Table 5: Comparing the thickness measurements of the ellipsometer and surface profiler for the equal ratio PS:PMMA blend films cast at 2000rpm

4.4 Results

4.4.1 Radial Distinctions

The thickness as a function of time for the films all displayed two 'regimes', as described by the two terms in the Meyerhofer model. Figures 4.7 and 4.9 display typical examples of thickness results from equal ratio blended films.

For the lower concentration solutions, the four data sets often converged at the critical time, t_c. This time indicates a regime change; the inertial forces become less important and the evaporation of the solvent begins to govern the thinning of the film. After this point, the evaporation of the toluene dominates the thinning of the film and the plots for each radii diverge with different gradients. The thinning ends when the film has dried and reached h_0. This radial diversion after t_c indicated that evaporation rate changes with radii even though it is generally considered to be constant with radius. This had an effect on the radial thinning of the low concentration films.

All films cast from 2% and 4% solutions showed a regular, radial drying order, regardless of angular velocity or the solution polymer ratio. The order can be seen in the example plots given, figure 4.7, which show the thickness as a function of time for the 4% equal ratio blended films at both 1000rpm and

2000rpm. This radial drying order could also be seen when the experiment was repeated, as is shown by figure 4.8.

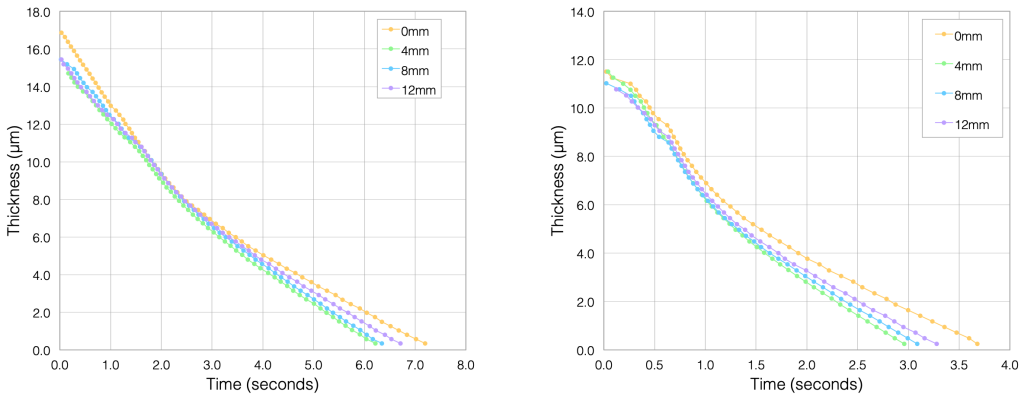

(a) 1000rpm (b) 2000rpm

Figure 4.7: The thickness as a function of time for the 4% equal ratio polymer blend, cast at (a) 1000rpm and (b) 2000rpm.

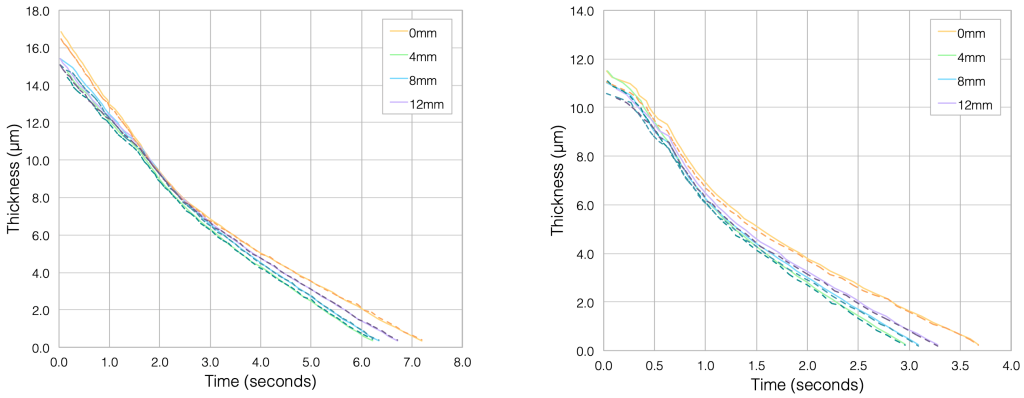

(a) 1000rpm (b) 2000rpm

Figure 4.8: The thickness as a function of time shown in figure 4.7, cast at (a) 1000rpm and (b) 2000rpm. A second, repeated data set is represented by the dashed lines and is in good agreement with the first experimental run.

The radial drying order, from fastest to slowest, was 4mm, 8mm, 12mm and 0mm. The effect is more noticeable in the films cast at 2000rpm than

1000rpm. As this diversion occurs when the solvent evaporation rate dominates the thinning, these results suggest that the solvent evaporation rate is varying with radius.

The thickness as a function of time plots for the 6% and 8% films however, did not show a drying order as the plots in figure 4.9 shows. This was the case for all higher concentration films regardless of spin parameters or solution composition, suggesting the radial drying order observed in the low concentration films is concentration dependent. Higher concentration solutions by definition have less solvent content and so would be less susceptible to an evaporation rate dependent phenomenon.

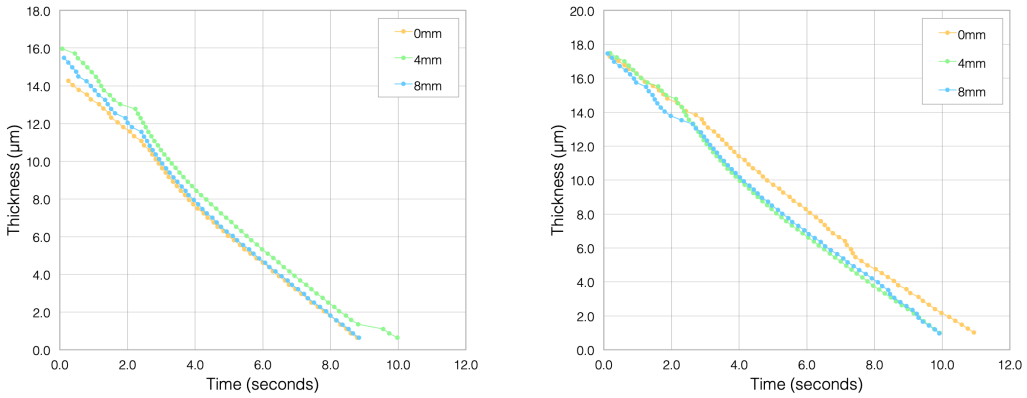

(a) 1000rpm (b) 2000rpm

Figure 4.9: The thickness as a function of time for the (a) 6% and (b) 8% equal ratio PS:PMMA polymer blend, cast at 1000rpm.

If the evaporation rate changes with radius, it is necessary to consider the factors that contribute to the value of E. As mentioned previously in equation 4.13, an evaporation rate depends on a constant C which is encompasses many factors. A system with a high vapour pressure will have a slow evaporation rate as the high concentration of solvent in the air hinders evaporation. This was kept constant throughout all film casting and previous experimentation with vapour pressure was not explored.

For a given volume, a larger surface area causes the evaporation rate to be faster due to more of the solvent being adjacent to air. A high temperature causes the solvent to have a greater amount of thermal energy and by extension, more kinetic energy. In contrast, strong inter-molecular forces can hinder evaporation. This also occurs if the air has a high viscosity. The

boundary thickness also contributes to the evaporation rate but shall be assumed to be negligible when considering a thin film.

The most significant contributor when considering the evaporation of a moving liquid is the flow rate. The literature most often only considers the flow rate of the air into which the solvent is evaporating, having a similar effect to vapour pressure: air unsaturated with solvent requires less energy for evaporation as in effect, the vapour pressure is lower. A high flow rate replenishes unsaturated air more quickly, which increases the evaporation rate. It is proposed here that the flow rate within the solution should not be ignored.

Convection is the means by which a liquid disperses energy so similarly, inertial forces within the film could act to replenish the film surface with solvent thus increasing the evaporation rate. As the radius of the film increases, different inertial forces are affecting the film. The idea of different forces acting upon different regions of the film with a radius dependency is not wholly novel.

The work of Bornside et al [152] explores the how photoresist films vary with radius as non-uniformities in film thickness can cause imperfections that propagate into the final film structure after photolithography. Bornside et al theorised from their data that as the radius changes, different physics governs the evaporation and mass transfer of the film. The boundaries for these physical regions are two radii r_1 and r_2 which are defined by equations 4.25 and 4.26, which are specific for their photoresist solution as at these radii, the Reynold's numbers are 1×10^5 and 3×10^5 respectively. To calculate r_1 and r_2, the kinematic viscosity ν of the solution at the start of the spin coating is used.

$$r_1 = \sqrt{\frac{1 \times 10^5 \nu}{\omega}} \tag{4.25}$$

$$r_2 = \sqrt{\frac{3 \times 10^5 \nu}{\omega}} \tag{4.26}$$

From the centre of the film to r_1, the flow of the solution is laminar, axisymmetric and steady state. In a ring, between r_1 and r_2, the flow becomes more disrupted as three-dimensional flow in the form of Ekman spirals occur. From r_2 to the edge of the film, the flow is turbulent and material is lost from the edge of the film.

The physics governing the film between radii r_1 and r_2 has a large effect on the thinning of this region. The Ekman vortices are a form of three-dimensional flow and so solution can flow upwards, hence replenishing the film surface with solvent and increasing evaporation rate. Furthermore any three-dimensional flow that carries the solution away from the centre will also contribute to thinning. The central region of the film is unaffected by the three-dimensional flow. A diagram detailing the different flow regimes proposed by Bornside et al can be seen in figure 4.10.

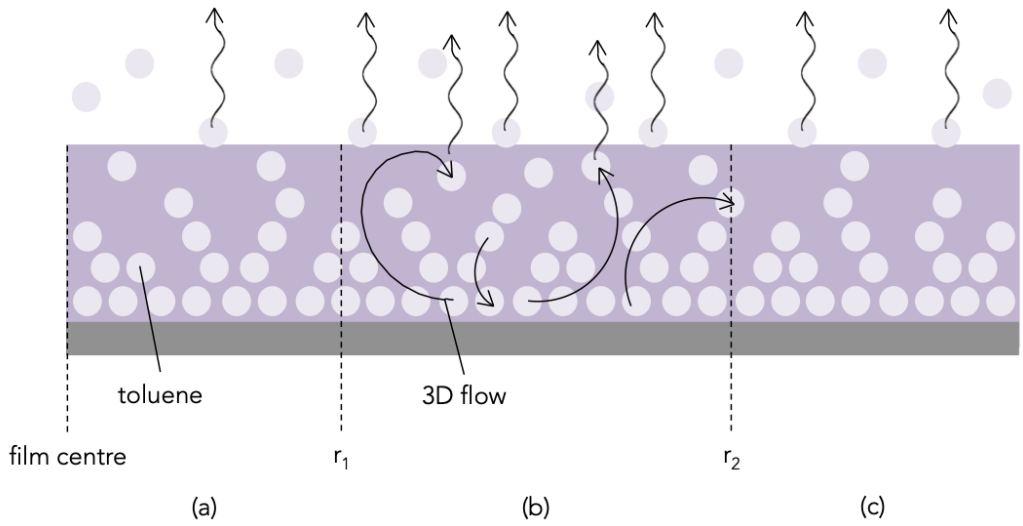

Figure 4.10: (a) The flow of the solution is laminar, axisymmetric and steady state. (b) The thinning is more rapid due to three-dimensional flow in the form of Ekman spirals causes the evaporative interface is replenished with solvent. (c) The flow is turbulent.

Using equations 4.25 and 4.26 to calculate r_1 and r_r for the films presented in this work results in values much larger than the substrate itself. This is because the Reynold's numbers used by Bornside et al are intrinsic to the photoresist films used in their experiments and are too large for these PS/PMMA films. Other research groups have found a more general case where films exhibit Ekman spirals when the solution has a Reynold's number between 2000 and 2500 [155] which are in accordance with the Reynold's numbers of solutions used in previous optospinometry experiments [46]. Using a new form of equations 4.25 and 4.26, the radius at which Ekman spirals begin to affect the film is given by

$$r_{\mathrm{e}} = \sqrt{\frac{2000\nu}{\omega}}. \tag{4.27}$$

Recalling that $\nu = \eta/\rho$ and using equation 4.27, the 4% films cast at 1000rpm have a calculated value of $r_{\mathrm{e}} \approx 1.8$cm, which is too large for these films, which would require a value of $0 > r_{\mathrm{e}} > 4$mm for this theory to be wholly correct. Conversely, equating equation 4.27 to a result that would be favourable such as 2mm and using the values $\mathtt{Re} = 2000$ and $\omega = 1000$rpm, the kinematic viscosity is $\nu = 3.3 \times 10^{-8}\mathrm{m}^2.\mathrm{s}^{-1}$. This is much smaller than possible for a spin coating system [20]. Evidently, the physics proposed by Bornside et al is an incomplete picture but the results of others can offer explanation and these calculations do not support Ekman spirals as a sole cause of the non-monotonic drying order.

Radial boundaries have been discussed by other research groups when considering the flow of a spin coating. Munekata et al determined the temperature distribution across films during their spin coating using an infra-red camera and found that certain points of the film were susceptible to a radial temperature gradient, especially when cast at higher angular velocities [172]. These infra-red experiments support the theory that a radial region of assisted drying is present. The radii affected by this depended on the flow rate of the solution and for a film cast at 3000rpm the region affected was between $0.55R$ and $0.75R$ of the film radii, where R is the total radius of the film. Furthermore Munekata et al found that the edge of the film had a higher temperature, and thus more evaporation, than the centre of the film. This would explain why the 12mm region dries before the 0mm data for all 2% and 4% films. Turbulent flow has been shown to induce a heat transfer between air and water [173] which could be causing this temperature gradient. This temperature gradient could also be inducing the Marangoni effect, recalling the Marangoni number Ma is defined by

$$\mathrm{Ma} = \left(\frac{\partial\sigma}{\partial T}\right)\frac{h^2\Delta T}{\eta\alpha_{\mathrm{T}}d}, \tag{4.28}$$

according to Birnie et al [128], in which h is the film thickness, η is the film viscosity and d is the penetration depth of the surface tension gradient. Most importantly, there are three temperature-dependent terms that contribute to the Marangoni number: $\frac{\partial\sigma}{\partial T}$, the change in surface tension with temperature; ΔT, the temperature gradient at the film surface; and α_{T}, the thermal diffusivity.

The temperature gradient proposed by Munekata et all could be causing r_e to be closer to the axis of rotation than predicted by equation 4.27. Considering that r_e increases with solution viscosity and none of the 6% and 8% films showed a non-monotonic drying order, it is proposed that for these solutions, the calculated r_e is larger than the film radius even after accounting for the temperature gradient effect proposed by Munekata.

While full Ekman spirals would be observed at $r_e > 18$mm, some semblance of three-dimensional flow could be affecting the film at smaller radii and the regions proposed by Bornside are not fully discrete. Regardless, when considered with the findings from the Bornside and Munekata groups, these results suggest that when lower concentration solutions are cast, at $r \geq$ 4mm, the films are susceptible to the effects of flow convection and increased temperature. Both groups attributed the radial differences to a non-constant flow rate, which has been assumed constant with radius previously [38, 174].

Munekata et al did not present an equation from which the radius at which the temperature gradient becomes significant to thinning for use with other cases, nor did they include results for 1000rpm or 2000rpm spin coatings. Despite this, the conclusions from Munekata et al can be extended to predict that a film cast at 3000rpm would have an accelerated evaporation between 7.7mm - 10.5mm from the film centre, as the total film radius was 14mm. The optospinometer has been primarily used for substrates 1cm^2 in size and larger wafers do not adhere securely to the spin coating platform at angular velocities larger than 2200rpm and so this result could not be verified.

As figure 4.9 shows, the 6% and 8% polymer concentration blend films did not exhibit radial divergence or dying order however, when the final thickness of the thickest film was found using ellipsometry, a radial variation in thickness was found. The 8% polymer blend film cast at 1000rpm decreased in thickness by 58±5.5nm from the centre of the film to 8mm away; this is a 5.7% decrease in thickness that was not seen in the thinner films and can be seen in figure can be seen in figure 4.11. This thickness variation can be seen by eye; a photograph of the film is shown in figure 4.12. Newtonian films have been shown to produce final films with uniform thickness regardless of the initial profile but this is not the case for non-Newtonian films [22]. This result shows that non-Newtonian effects must become significant for the 8% concentration film. A temperature gradient in the film [172] will result in viscosity changing with radius as fluids are less viscous at higher temperatures which could also be contributing to this affect.

Though high viscosity films are less susceptible to the temperature gradient, they are more prone to non-uniformities in thickness due resistance in iner-

tially induced thinning. The lower concentration films are more susceptible to evaporative effects due to the increased amount of toluene in the solution.

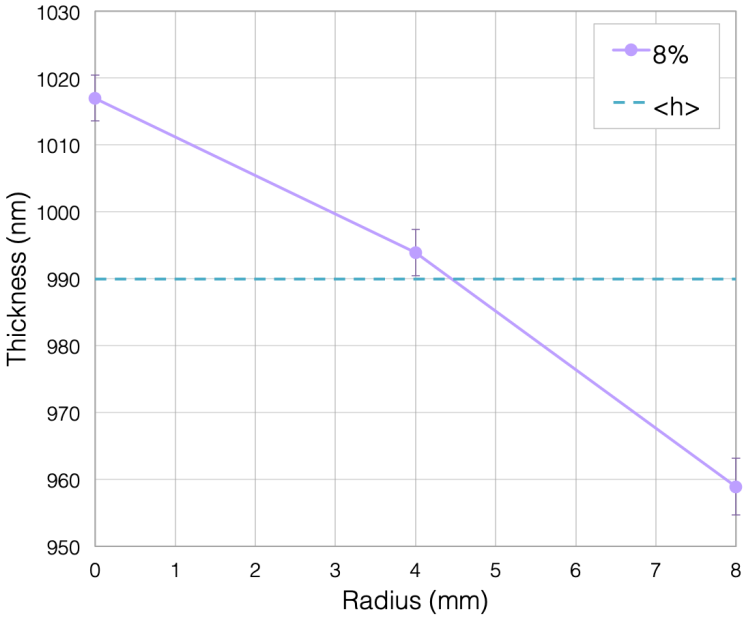

Figure 4.11: The thickest film produced, 8% blend spin coated at 1000rpm, showed a noticeable radial change in final thickness. The mean thickness of the film is plotted in blue $\langle h \rangle$.

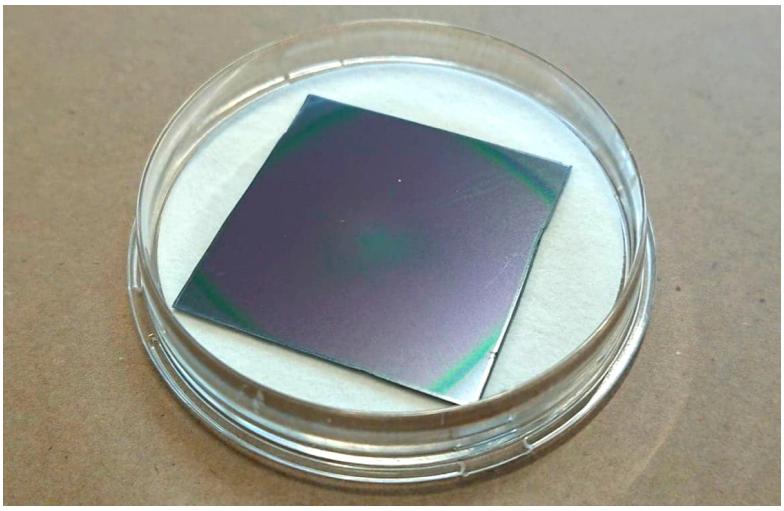

Figure 4.12: The thickest film produced, 8% blend spin coated at 1000rpm, showed a noticeable radial change in final thickness.

As the results discussed in this section cannot be explained by a single theory, it is presented here a combination of effects in one of two ways could be causing the non-monotonic drying order.

1. Whilst the values calculated for r_1 and r_2 are too large for whole Ekman spirals to be present in the film, small currents replenishing the film surface with toluene could still be present at smaller radii than 18mm. To use a hurricane analogy once more, this would not be dissimilar to how strong winds are felt outside of the cyclone itself. Equation 4.27 is the required radius for a full spiral to be observed but convectional flow could still be present in the film at radii $r < r_e$ and this these regions of the film would be in a catchment area for convectional flow affects. This is illustrated by figure 4.13.

2. Ekman spirals are present in the film but the radius at which they begin to form is reduced due to the temperature gradient observed by Munekata et al [172] inducing convectional flow and full vortices closer to the film centre than predicted by others [152, 155]. This is illustrated by figure 4.14.

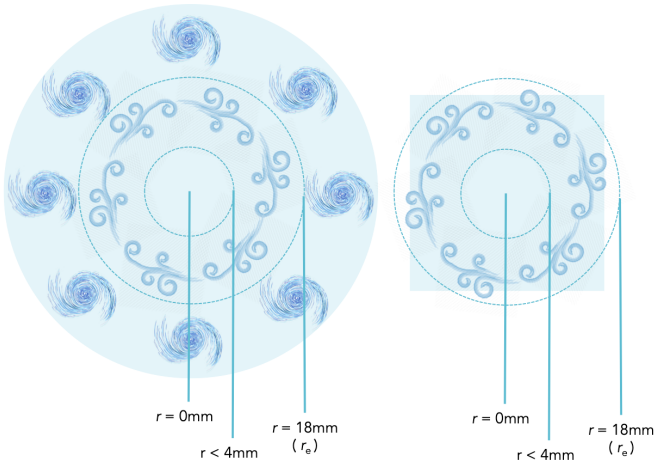

Figure 4.13: A diagram illustrating how Ekman spirals can induce convectional effect at radii smaller than r_e. The image to the left is of a film large enough to have full Ekman spirals present. This diagram is not to scale; the Ekman spirals and convectional currents are illustrative.

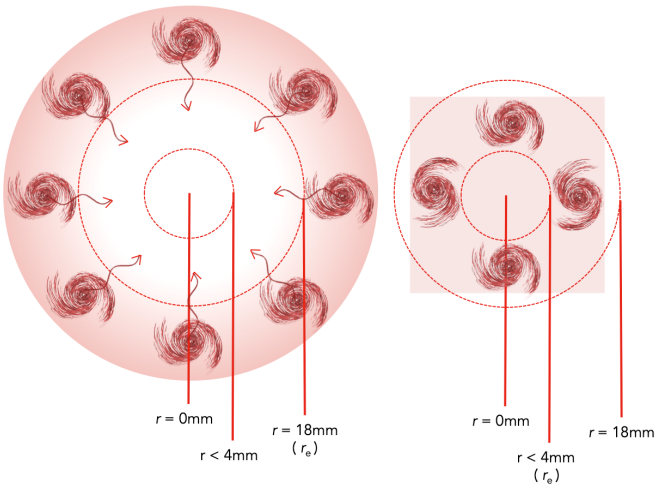

Figure 4.14: A diagram illustrating how the radius at which Ekman spirals begin can be decreased due to the Munekata temperature gradient. The image to the left is of a film large enough show how full Ekman spirals move closer to the film centre due to the temperature gradient. This diagram is not to scale; the Ekman spirals and temperature gradient are illustrative.

Regardless of which case occurs, convectional flow will reduce as the film viscosity increases during the spin coating. The film is its most viscous when evaporative dominant thinning has begun and so the inertial dominant stage must establish this radial dependent evaporative effect. To determine which case is occurring, films of a larger radius $R > 18mm$ must be cast in future experiments.

4.4.2 RBD model

The RBD model has varying success in modelling the thickness of the films depending on the experimental parameters. For the low concentration spin coatings at both 1000rpm and 2000rpm, the model is somewhat successful in predicting the thickness as a function of time for the 0mm data sets. Fundamentally, the model cannot predict the film thickness as a function of time for the radial data, which is indicated by the divergence of the 4mm, 8mm and 12mm data seen in figures 4.7- 4.9. If small films are cast, ignoring radial effects is a reasonable assumption due to r being less significant. However when the spin coating of large films is considered, this can no longer be the norm and more thorough models that consider radial effects are required.

Figure 4.15a shows the model for the 2% equal ratio polymer blend cast at 1000rpm alongside the corresponding data from the film centre. The divergence between the model and the data at the later times indicates that the evaporation rate experimentally found is too large. To explore this, the RBD [e] model is also plotted, in which the RBD model also fitted the evaporation rate E to the data. When this was done, the RBD calculation of $h(t)$ was accurate for the evaporative dominant thinning stage, but not at early times as the initial thickness is underestimated.

When comparing the RBD and RBD [e] model for each data set, it was observed that the films of higher concentration and spun at higher spin speeds fit the RBD [e] model much better than the RBD model, as is shown by figure 4.15b which shows the 8% equal ratio polymer blend cast at 2000rpm. At low concentrations and angular velocities, the opposite is true.

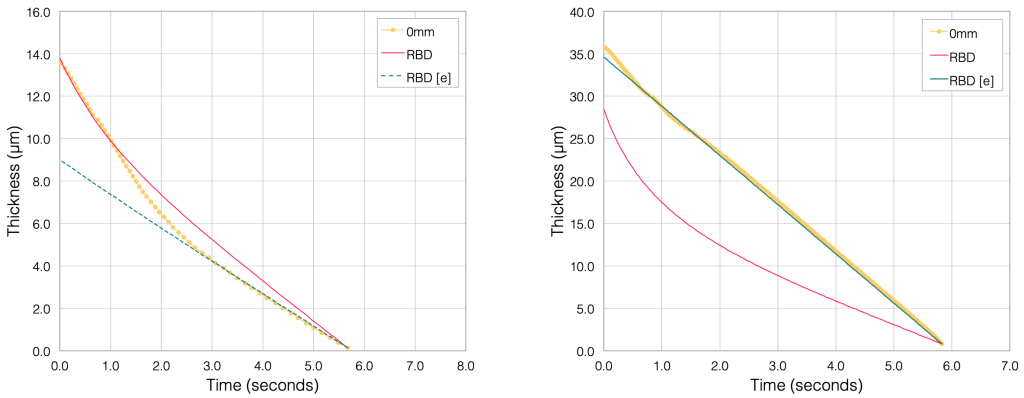

(a) 2%, 1000rpm

(b) 8%, 2000rpm

Figure 4.15: The RBD model, the modified RBD model RBD [e] and the corresponding data for equal ratio PS:PMMA polymer film (a) 2% concentration, cast at 1000rpm and (b) 8% concentration, cast at 2000rpm.

These results indicate that discrepancies exist between the RBD model and the true physics governing the thinning of the film. If the RBD [e] model is considered to be the more accurate model, inertial forces are greatly underestimated. Haas et al [167] explored how rapid evaporation rates could cause the surface of the film could form a skin that can hinder the evaporation rate. The disagreement between model and results could be due to skin formation at the surface of the film, hindering evaporation of toluene and the resultant thinning.

The derivation of the RBD model determines the Froude and Weber effects negligible at the centre of the film [20] as can be seen from equations 2.75 and 2.78, but further examination of these effects considers this assumption potentially invalid.

The Froude number depends on inertial forces, defined in equation 2.76, and the Weber number is quantified by the interface between more than one fluid, defined in equation 2.77. Inertial forces have been shown here to significantly affect the film thickness as a function of time, especially in the lower concentration solutions. The Froude effect may not be negligible for this reason. If the concentration gradient induced by a radially different evaporation rate causes the solution to behave as separate fluids due to surface tension gradients, the Weber number could also become significant. Perhaps ignoring these terms is inaccurate? Previous fittings of the RBD model have also exhibited similar discrepancies [46]. Reisfeld, Bankoff and Davis did acknowledge that the significance of the Froude and Weber effects may change when larger radii were considered [37, 175].

Figure 4.16 shows the RBD modelled thicknesses as a function of time for the equal ratio polymer blend films. As would be expected, the RBD model predicts that as solution concentration increases, h_0 and t_f are larger for both angular velocities. A concentration dependence study of the RBD has not been done so these results cannot be compared.

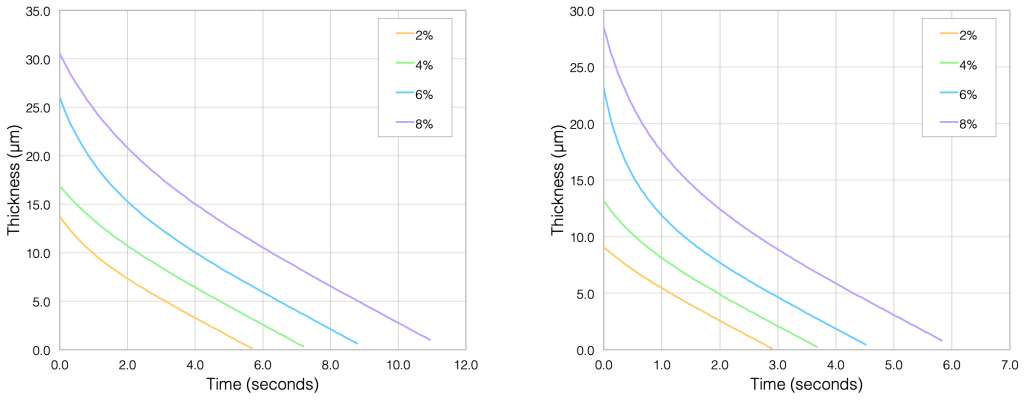

(a) 1000rpm (b) 2000rpm

Figure 4.16: The RBD models for the equal ratio PS:PMMA polymer films cast at (a) 1000rpm and (b) 2000rpm.

4.4.3 Viscosity

This section shall discuss the modelled viscosity of the solutions during the spin coating and use results from the 4% polymer concentration equal ratio PS:PMMA film cast at 1000rpm as an example. Previous work [23] has shown that the final data point in optospinometry is susceptible to an invalid assumption; the volume fraction of toluene is assumed to be 0 when the spin coating is completed and this is often not the case. In order to mitigate this problem, the volume fraction as a function of time is shown in figure 4.17a but the final data point is excluded.

The volume fraction and relative viscosity seen in figure 4.17 show that for inertially dominant thinning, there is little radial distinction as each curve is superimposed at this stage. This is due to this period of spin coating fulfilling the Huggins viscosity, equation 4.21, as the solution is suitably dilute.

When the evaporation rate dominates thinning, the curves begin to become distinct from one another. As would be expected on seeing the thickness plots in section 4.4, the difference in the plots is due to the radially different evaporation rates and the radial drying order is observed.

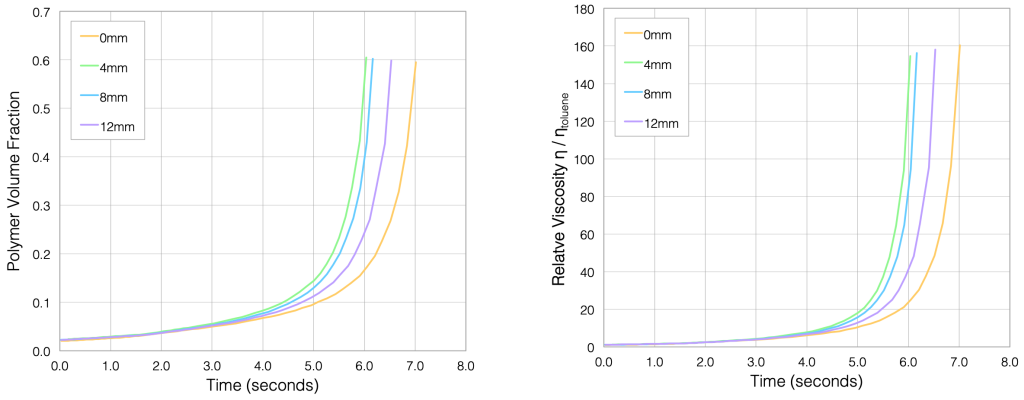

(a) volume fraction

(b) relative viscosity $\frac{\eta}{\eta_{\text{tol}}}$

Figure 4.17: The parameters for the 4% equal ratio PS:PMMA film cast at 1000rpm are (a) volume fraction and (b) relative viscosity.

The viscosities found for the initial solutions presented in table 3 are concurrent with the values obtained by others, around 3.6m Pa.s [46], but as the spin coating process progresses, the solution becomes increasingly viscous and non-Newtonian, more so than is quantified by the modelled viscosity used for

the RBD model. As a result of this underestimation, the final viscosities are modelled to be around 0.1 Pa.s which is many orders of magnitude too small: UVO treatment has been used to measure the effective viscosity of PS films with results varying between 10^6 and 10^7 Pa.s [176] for films 200nm thick.

Whilst equation 4.24 has been used to model spin coating viscosities in the past [46], it is clearly a poor model to use if a more accurate equation is possible. If the viscosity predicted for the RBD model is too small, the three terms dependent on η all have a greater significance at later times. The large powers of h for these terms do mitigate this effect somewhat, as at late times when $h << 1$, the η dependent terms are still much smaller than the dominant E term. Table 6 shows the magnitude differences between the terms in equation 4.29 at late times when viscosity is modelled inaccurately compared to effective viscosities of PS films.

$$\frac{\partial h}{\partial t} = -\left(E + \frac{2\omega^2\rho h^3}{3\eta} + \frac{5E\omega^2\rho^2h^4}{12\eta^2} - \frac{68\omega^4\rho^3h^7}{315\eta^3}\right), \tag{4.29}$$

Term	Order (m.s^{-1}) ($\eta = 0.1$ Pa.s)	Order (m.s^{-1}) ($\eta = 10^6$ Pa.s)
$-E$	10^{-6}	10^{-6}
$-\frac{2\omega^2\rho h^3}{3\eta}$	10^{-12}	10^{-20}
$-\frac{5E\omega^2\rho^2h^4}{12\eta^2}$	10^{-20}	10^{-33}
$+\frac{68\omega^4\rho^3h^7}{315\eta^3}$	10^{-26}	10^{-47}

Table 6: The difference in magnitude of the terms in the RBD model for a polymer film with polymer volume fraction $\phi = 0.6$ when viscosity is underestimated ($\eta = 0.1$ Pa.s) compared to experimental results ($\eta = 10^6$ Pa.s).

Modelling viscosity in this way has been justified previously [23] by assuming that viscosity predictions are only inaccurate when inertial forces no longer dominate thinning and are therefore insignificant. Whilst acceptable in some

regard as table 6 shows, this is clearly a disputable claim and future work should model viscosity more accurately.

4.5 Summary

This chapter addresses the primary hypothesis of this thesis; that a polymer film dries more quickly at regions further away from the film centre. Whilst this has been proven for low concentration films, indicating a radially differing evaporation rate, the relationship is non-monotonic and difficult to quantify. More viscous films appear to be less susceptible to this drying order, indicating it is established during the inertial dominant period of thinning.

The results presented thus far show that the film formation is not necessarily uniform at all regions of the film. Due to this, $h(t)$ spin coating models are inadequate and a model of the form $h(r,t)$ is necessary. This is a complicated feat, but potentially lies in exploring the Froude and Weber effects that were assumed negligible by Reisfeld, Bankoff and Davis. Most spin coating models focus heavily on the viscosity of a solution as being the parameter of most importance when predicting a film thinning. These results show that evaporation rate has a great effect on radial variations in film thickness and should be given due attention. Evaporation rate is dependent on many variables that are not only difficult to control, but are all consolidated by C in $E = C\sqrt{\omega}$ [128].

Problems also arise in fitting the RBD model for high concentration films or faster spins, as either the evaporation rate or the inertial forces are underestimated. Fitting a more appropriate evaporation rate does not help this, as the inertial forces are still underestimated. The disagreement could be due to skin formation at the surface of the film, hindering evaporation of toluene.

The next chapter discusses the film morphology, using off-specular reflection, optical microscopy and AFM results to probe the phase separation of the blended films. Important features to notice would be low concentration films indicating accelerated drying away from the film centre or isotropic phase separation features that could be used to replace top-down manufacturing of organic electronics.

5 Results II: Film Morphology

This chapter shall discuss the effect that spin coating has on the phase separation and general morphology of a film and whether a radial dependence is detected. Striations are a known radial effect, despite the assumption of many models that radius is not an important contributor to film formation. By varying the spin coating conditions, such as the solution concentration, angular velocity and polymer ratio in order to vary the film morphology, various experimental techniques can be used to observe any emergent radial relationships.

5.1 Off-Specular Images

The off-specular scattering data can give quantitative results for phase separation length scales observed in a polymer film. As discussed in section 3.1.2, the maximum value of q that can be recorded by the optospinometer is $0.4\mu m^{-1}$, which corresponds to a length scale of approximately 16μm and so only very large scale phase separation can be detected.

The off-specular results from the 2-6% films all looked similar to figure 5.1 and no distinct off-specular features were observed. Such a result suggests that phase separation does not occur, that any length scales are smaller than 16μm or that the films are too uniform in thickness to induce resolvable off-specular scattering. All films were imaged using optical microscopy to determine the cause of these results and the images are presented in section 5.2.

However the 8% concentration blend cast at 2000rpm did show an off-specular feature centred $0.1\mu m^{-1}$ at a radius of 8mm, as shown in figure 5.2. This indicated that at this point of the film, there was a phase separated structure with a length scale between 42-84μm with the most prominent length scale being 63μm. The resolution of the optospinometer could not distinguish if there were multiple length scales within this 42-84μm range.

The size of the structures detected in the 8% 2000rpm film is in agreement with those observed in similar polymer films with the same concentration, 50μm [138]. From the off-specular data alone, the 2%-6% films showing no phase separation with a length scale larger than 16μm is a somewhat ambiguous result, as length scales larger than 5μm were not detected in 2%-6% concentration films cast by others [138]. As the optospinometer resolution

does not reach 5μm, this result shall be considered with optical microscopy images.

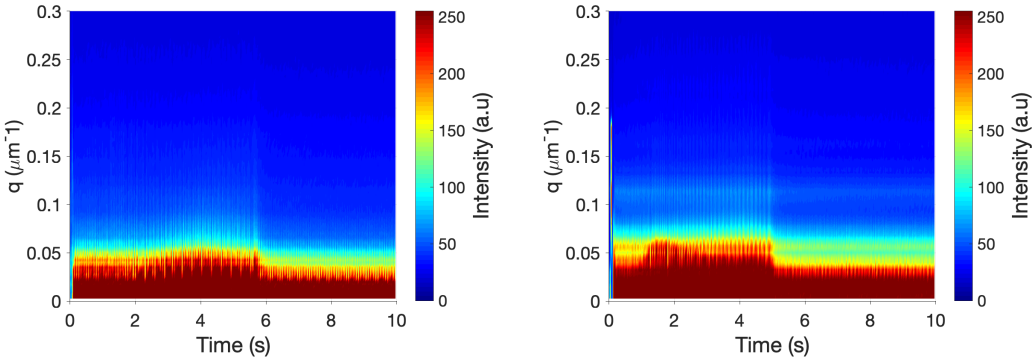

(a) 0mm (b) 4mm

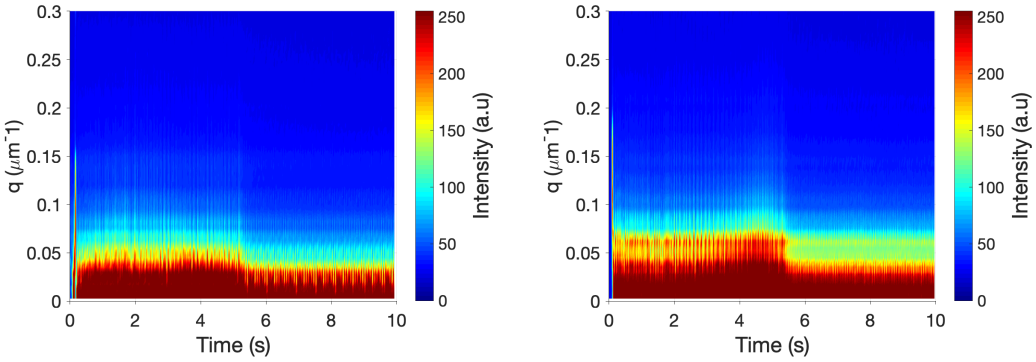

(c) 8mm (d) 12mm

Figure 5.1: Off-specular images for the equal ratio PS:PMMA 2% concentration cast at 1000rpm.

The free energy during the spin coating can be calculated in order to find the time t_{Gmin} at which the film reaches its minimum free energy, ΔG_{min}. In previous off-specular scattering profiles, the time at which ΔG_{min} was reached was defined as the transient bilayer becoming disrupted [21, 146, 162]. t_{Gmin} is indicated on the off-specular plot in figure 5.2c by a dashed black line. The effect that free energy and ΔG_{min} has on the film formation has been studied extensively.

The phase separation of a dry polymer film has previously been modelled to form flat bilayer which disrupts during the spin coating until lateral phase separation is reached [145]. This segregation is enhanced by concentration fluctuations on the film surface that become apparent at a time t_{on}. Experi-

mentally, an *in situ* spin coating has been observed which indicated that the onset of concentration fluctuations corresponded to instabilities observed in the off-specular data [163]. The concentration fluctuations are first observed at t_{on}, which is marked on figure 5.2c by a dashed pink line. When ΔG_{min} is reached, the bilayer has fully disrupted, therefore the time between t_{on} and t_{Gmin} is when the bilayer breaks [23]. The off-specular feature visible in figure 5.2c between t_{on} and t_{Gmin} is in agreement with the off-specular results of others [23].

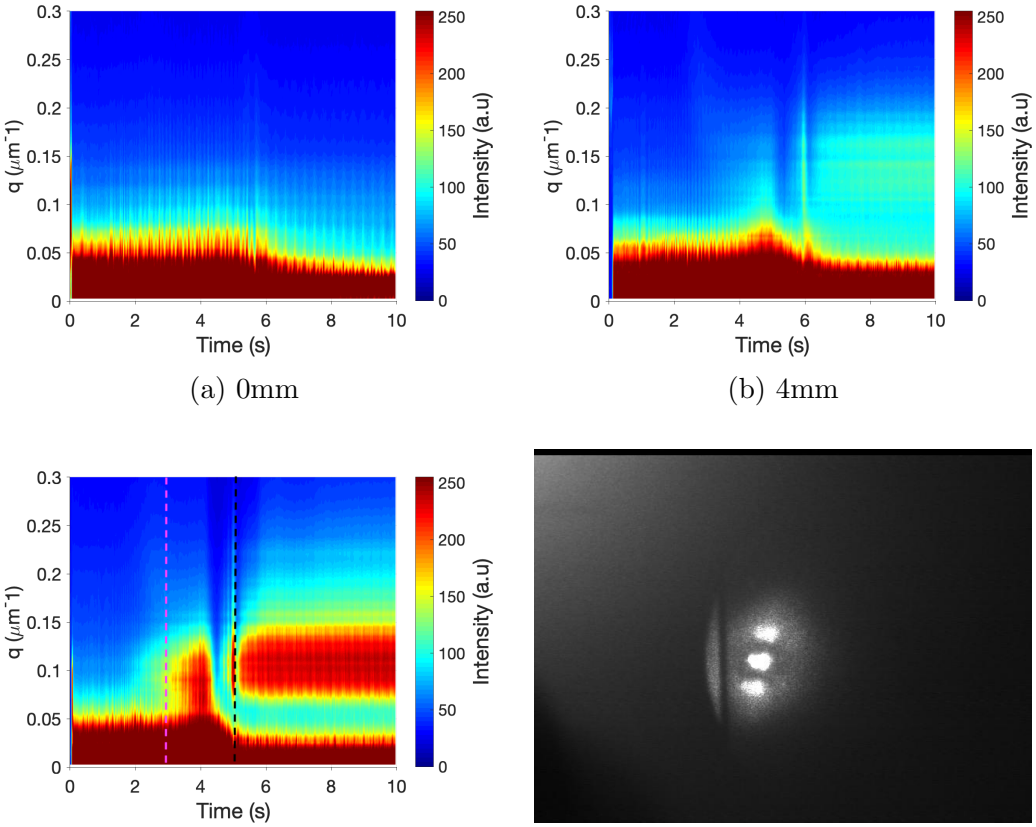

(a) 0mm (b) 4mm

(c) 8mm (d) Off-specular image at 8mm

Figure 5.2: Off-specular images of the 8% polymer blend concentration cast at 2000rpm, where (c) has t_{on} and t_{Gmin} indicated by the pink and black dashed lines, respectively, and where (d) is the raw off-specular at 8mm from the centre of the film.

In other optospinometry experiments [21] that varied the toluene evaporation rate, an off-specular ring was not present in PS:PMMA 10% films spin coated when $E = 0.42\mu\text{m.s}^{-1}$ despite clearly showing phase separating structures in

microscopy images. This was determined to be a result of the concentration gradient driving any Marangoni instabilities was most suppressed at low evaporation rates. This resulted in a layered structure with a small roughness which could not break the surface layer. When the evaporation rate was increased to $3.15\mu\text{m.s}^{-1}$, a clear off-specular ring was observed [21] as can be seen in figure 5.3a. This ring was present due to the isotropy of the film at this point. At the edge of the film, this feature changes due to the domains becoming elongated, as figure 5.3c shows. The results from the off-specular 8% film match are supported by this, as can be seen when comparing figure 5.2d with figure 5.3c.

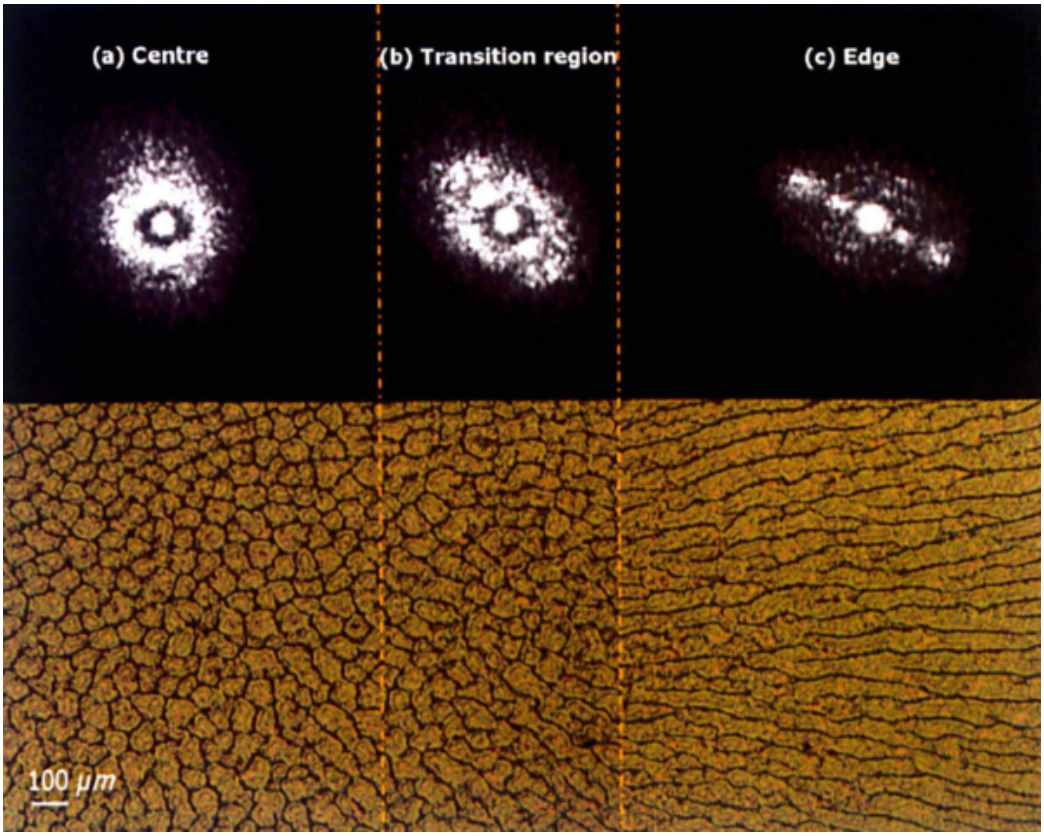

Figure 5.3: As the radius increases, the phase separated domains in the film become elongated. This is reflected in the off-specular data by the ring, observed at the centre of the film, not being present in the data taken at the edge of the film. This figure is from the thesis of Dr Parvaneh Mokarian-Tabari, 2009 [165].

When an off-specular feature is present, this is indicative that there are structures in the plane of the film that have a particular spatial wavelength. The causes of such structures are numerous but such rings have been seen

when the Marangoni effect in the film is large enough to induce laterally segregation due to the roughness of the film [146, 165]. It can therefore be concluded that the 8% blended film cast at 2000rpm had enough film instability to cause the roughness of the film to breach the surface.

In conclusion, the off-specular results show that by changing the concentration of the spin coating solution, radial distinctions in phase separation length scale can be induced. As the resolution of the optospinometer was not able to measure the length scale of more than one film, analysis and comparison of the structure of the films is presented with the optical microscopy images.

5.2 Optical Microscopy

As the phase separation in many of the blended films was too small to be detected by off-specular light scattering experiments, this subsection aims to explore the film morphology in more detail. Section 5.2.1 discusses the equal ratio PS:PMMA polymer blend films and section 5.2.2 discusses the effect on the films when the polymer ratio between the blend is altered.

5.2.1 Equal blends

The phase separation length scale $\bar{x}$ was defined as the mean distance between a phase separated region and the closest neighbours. Its calculation is given in equation 5.1, with reference to figure 5.4. The separated structure size $\bar{y}$ was defined as the mean diameter of a phase separated structure. Its calculation is given in equation 5.2, which also refers to figure 5.4. These two parameters were defined in order to compare the film structure numerically.

$$\bar{x} = \frac{1}{n}\sum_{i=1}^{n} x_i \tag{5.1}$$

$$\bar{y} = \frac{1}{n}\sum_{i=1}^{n} y_i \tag{5.2}$$

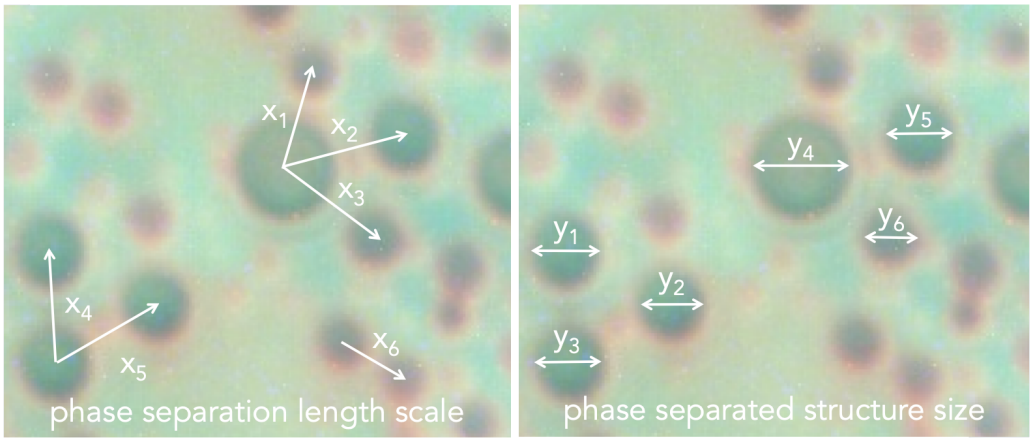

Figure 5.4: Defining the phase separation length scale and the phase separated structure size.

By increasing the concentration of the solution used to cast the film, figure 5.5 shows that the phase separation length scale $\bar{x}$ and structure size $\bar{y}$ generally increase with polymer concentration, but there is a decrease at 6% for the films cast at both angular velocities.

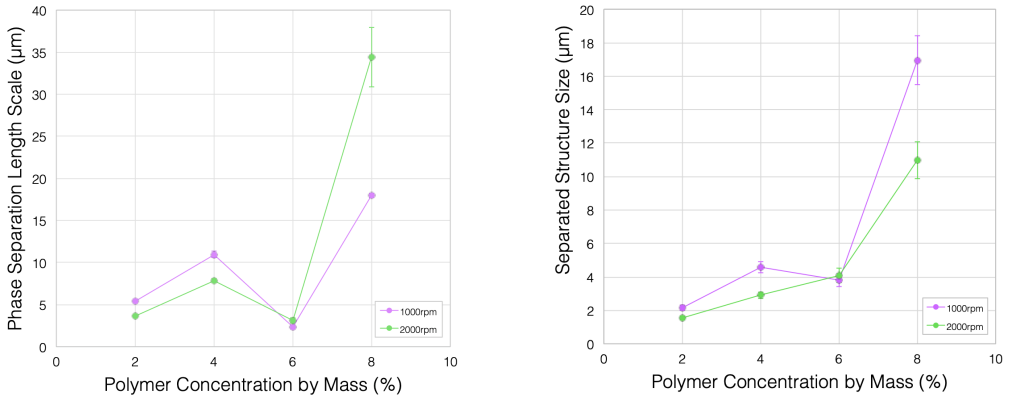

(a) (b)

Figure 5.5: The (a) mean phase separation length scale and (b) mean phase separated structure size as a function of solution polymer concentration. 1000rpm, purple. 2000rpm, green.

No clear radial results can be seen in the results presented in 5.6 and 5.7, but there is also a lack of pattern in the length scales with increasing concentration.

Film morphology has been shown to be concentration dependent [138] in experiments that studied the lateral film segregation in PS/d-PMMA films with solutions of various polymer concentrations. Low concentration solutions formed a bi-layer and are typically featureless. When intermediate concentration solutions were spin coated, a rippled bi-layered interface was formed, due to an instability within the film. High concentrations would cause the bi-layered interface to breech and laterally segregate [138].

Considering this, figure 5.5 suggest that the phase separation seen in the low concentration films (2% and 4%) is small scale phase separation instead of lateral segregation. As the concentration is increased to 6%, the instability of the bilayer increases and small regions of PS and PMMA migrate to the interface, reducing the overall interface at the surface. At 8%, the instability has breeched the film surface and larger length scale phase separation is observed due to lateral segregation.

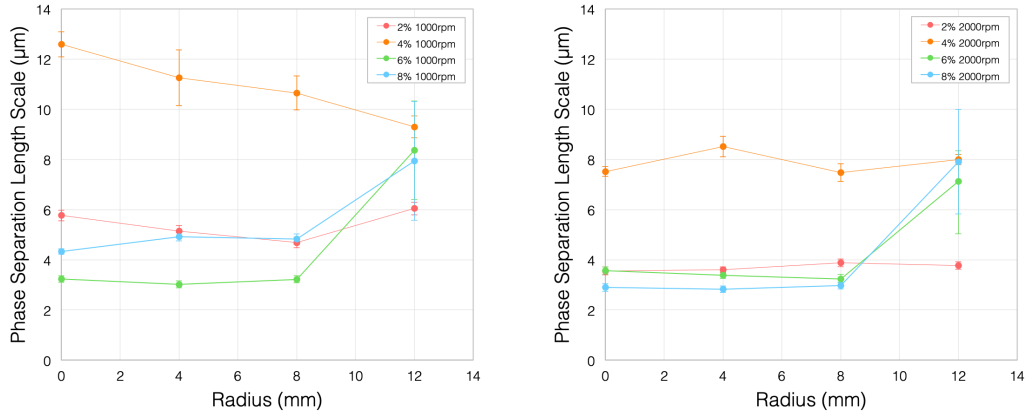

(a) 1000rpm (b) 2000rpm

Figure 5.6: The mean phase separation length scale of the film as a function of radius at (a) 1000rpm and (b) 2000rpm. 2% red, 4% orange, 6% green, 8% blue.

The radial results of figures 5.6 and 5.7 are marred by large errors and little radial distinctions are observed. When observed on the optical microscope images themselves, this radial effect is extremely clear in the images of the 6% and 8% blended films, figures 5.10, 5.14, 5.11 and 5.15.

Figure 5.8 shows the optical microscopy images for a 2% film cast at 1000rpm. There is very little radial distinctions in this film, and the phase separated structures have an average area of $11.2 \pm 0.7 \mu m^2$ at both the centre of the film and at the edge.

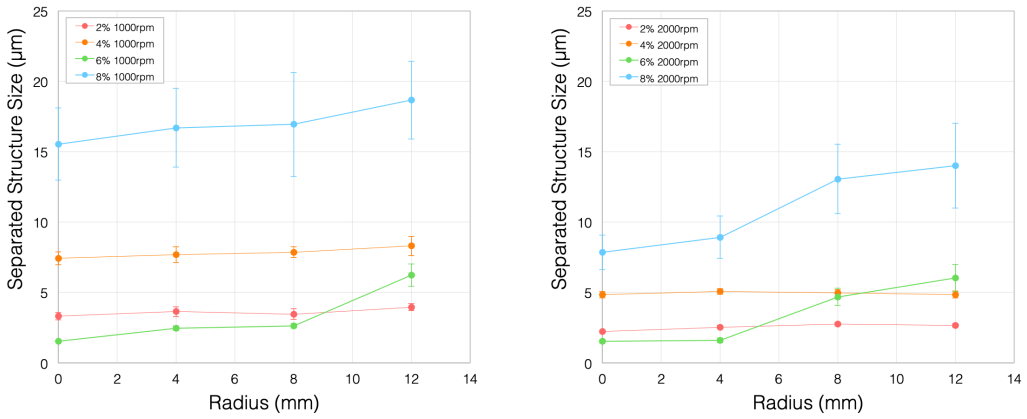

(a) 1000rpm (b) 2000rpm

Figure 5.7: The mean phase separated structure size of the film as a function of radius at (a) 1000rpm and (b) 2000rpm. 2% red, 4% orange, 6% green, 8% blue.

Figure 5.9 shows the optical microscopy images for a 4% film cast at 1000rpm. As with the 2% film, few radial distinctions are evident in this film. The phase separated structures have an average area of $5.2\pm0.9\mu m^2$ at the centre and $4.8\pm0.7\mu m^2$ at the film edge.

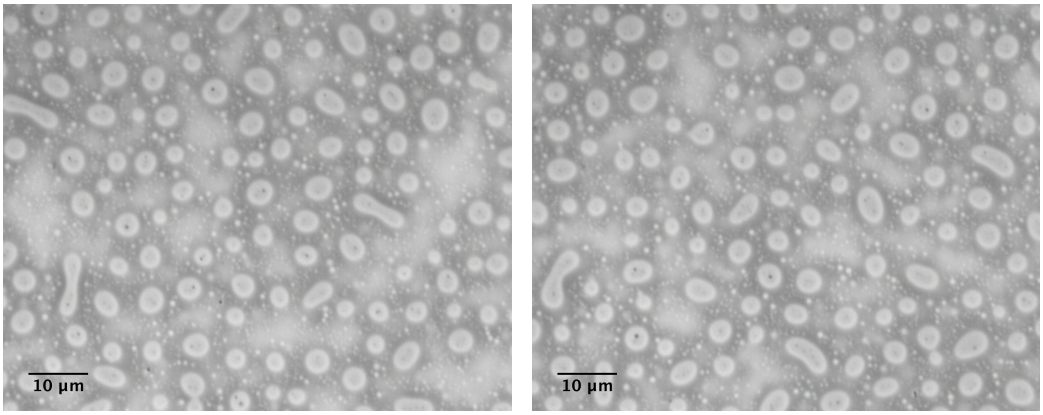

(a) 0mm (b) 12mm

Figure 5.8: 2% PS:PMMA polymer blend, 1000rpm.

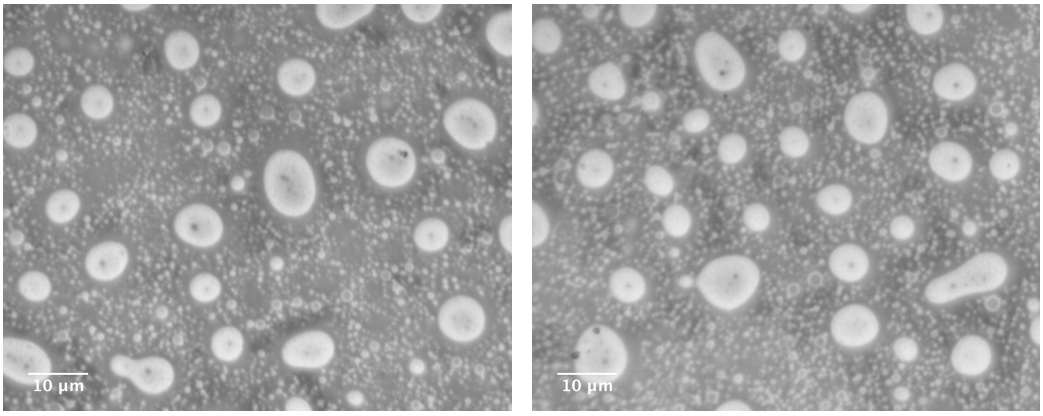

(a) 0mm (b) 12mm

Figure 5.9: 4% PS:PMMA polymer blend, 1000rpm.

The irregular drying order discussed in chapter 4 was more evident in low (2% and 4%) concentration films and so the lack of radial variations in the optical microscope images for these films is surprising. The length scales that result in the areas obtained are smaller than the minimum 16μm that can be detected by off-specular scattering.

Figure 5.10 shows the optical microscopy images for a 6% film cast at 1000rpm. There is noticeable radial distinctions in this film as the centre of the film, the phase separated structures all appear to be of similar area, 7.3$\pm$0.7μm^2. These structures are also observed at the film edge, in addition to much larger phase separated regions which affect the mean structure area, which is 10$\pm$ 1 μm^2. The off-specular result is explained as this film has a length scale smaller than the minimum of 16μm. This film has a significant differences with increasing radius.

Figure 5.11 shows the optical microscopy images for an 8% film cast at 1000rpm. In this film, radial striations have clearly formed at the edge of the film in the form of elongated phase separated domains. The film has two distinct length scales due to two distinct structure sizes being present in the film. The smaller of the two domain types has a mean area of 14$\pm$1μm^2 at the centre and 13$\pm$1μm^2 at the edge, which shows little indication of a radial difference. At the edge of the film, the larger structures have a different aspect ratio in addition to an increase in domain area: at the centre of the film, the large domains have a mean area of 1300$\pm$100μm^2 which increases to 3400$\pm$200μm^2 at the edge.

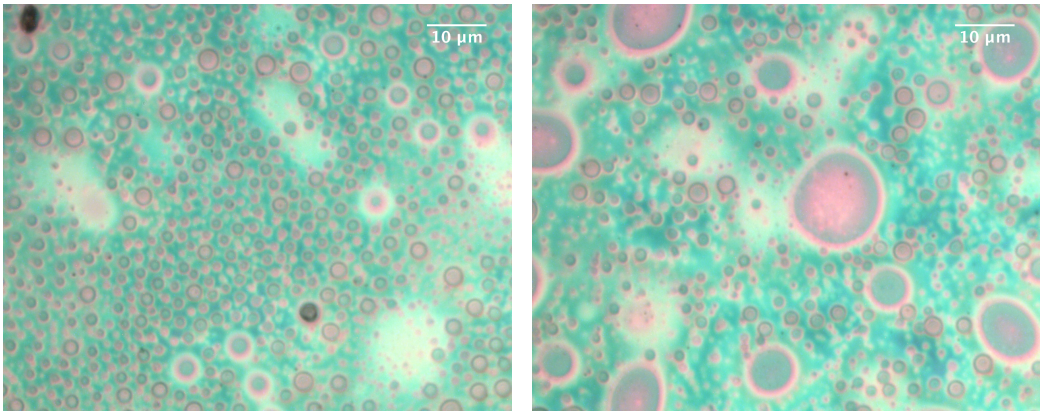

(a) 0mm (b) 12mm

Figure 5.10: 6% PS:PMMA polymer blend, 1000rpm.

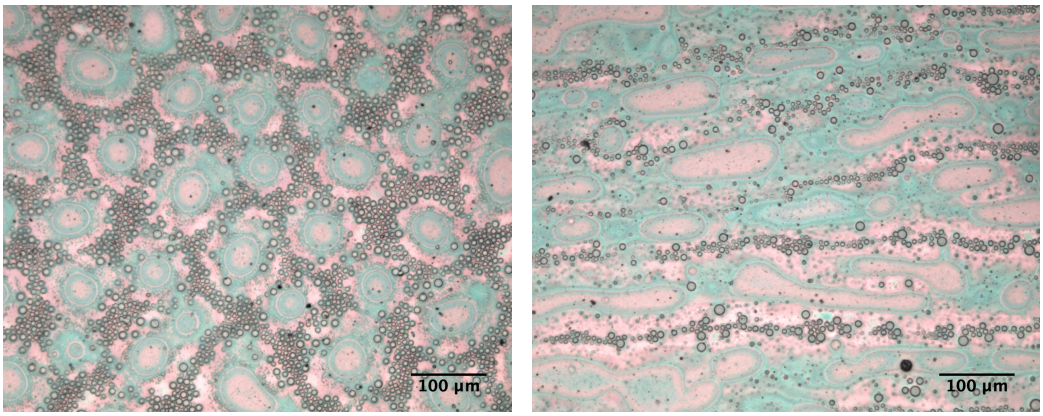

(a) 0mm (b) 12mm

Figure 5.11: 8% PS:PMMA polymer blend, 1000rpm.

The structures in the 8% film cast at 1000rpm are surprising as no length scale was detected by the off-specular scattering. This film has a length scale measured in Image-J of $57\pm3\mu m^2$ which makes it large enough to be detected by the optospinometer based on structure size alone. It is therefore speculated that the height difference between these structures is not large enough to cause off-specular scattering that can be resolved by the optospinometer laser.

Figure 5.12 shows the optical microscopy images for a 2% film cast at 2000rpm. There is no obvious difference morphology with radius for this film but the phase separated structure area is $6.7\pm0.3\mu m^2$ at the centre of the film and

7.7±0.4μm^2 at the edge. Similarly, no radial distinctions can be seen in the 4% film cast at 2000rpm, shown in figure 5.13. The structures have similar areas: 12±1μm^2 and 11±1μm^2.

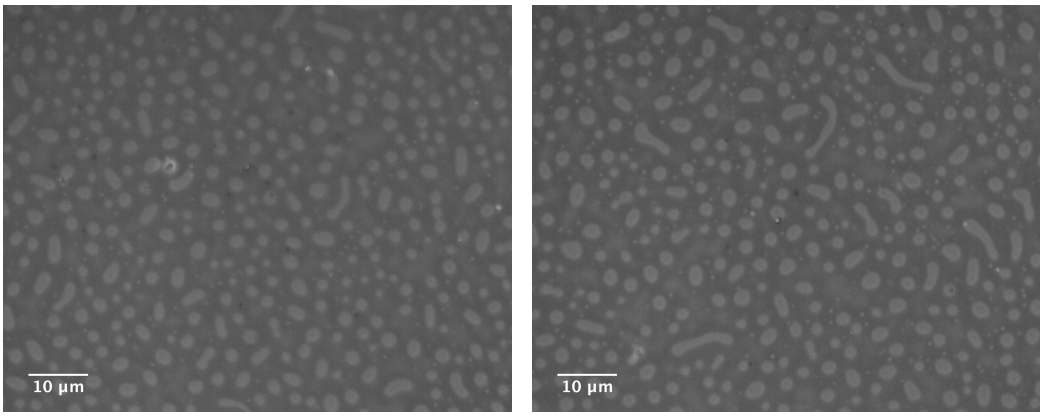

(a) 0mm (b) 12mm

Figure 5.12: 2% PS:PMMA polymer blend, 2000rpm.

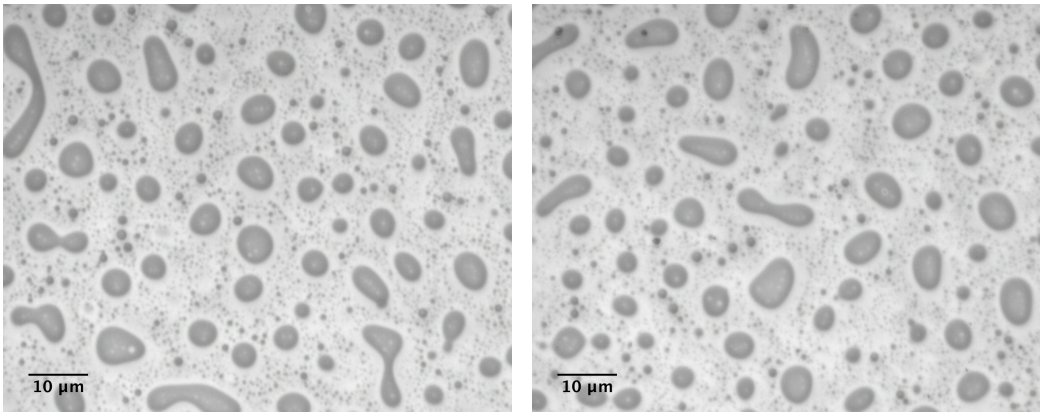

(a) 0mm (b) 12mm

Figure 5.13: 4% PS:PMMA polymer blend, 2000rpm.

The 6% film cast at 2000rpm is shown in the optical microscopy images in figure 5.14. There are significant differences in the morphology of the film with increasing radius for this film and this is reflected in the mean structure areas, which are 4.5±0.2μm^2 and 12±2μm^2 for the centre and edge of the film, respectively.

The optical microscopy images for the 8% film cast at 2000rpm are given in figure 5.15. The phase separated structures in this film have a much larger

area than in any other film, as would be expected from the off-specular data. At the centre of the film, the structures have a mean area of $11.9 \pm 0.4 \mu m^2$. This value increases to $80 \pm 10 \mu m^2$ at a radius 8mm from the centre of the film. The features at 8mm are elongated and this effect is more significant with increasing radius towards the edge of the film. The off-specular results indicated a phase separation length scale of approximately $63 \mu m$. When measured using Image-J, the mean phase separation was found to be $58 \pm 2 \mu m$, which is in agreement with the off-specular data.

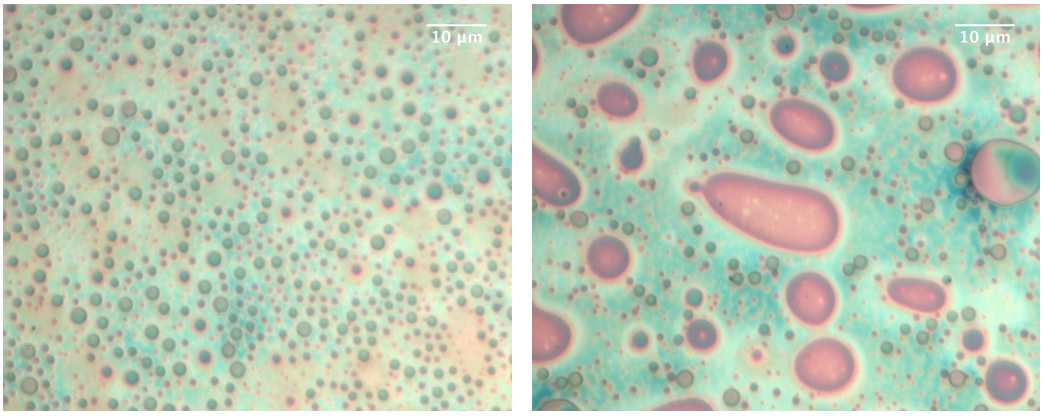

(a) 0mm (b) 12mm

Figure 5.14: 6% PS:PMMA polymer blend, 2000rpm.

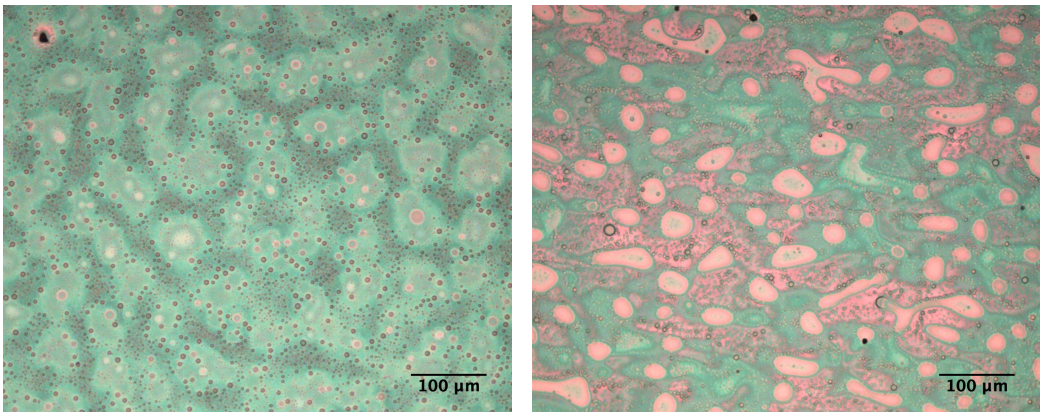

(a) 0mm (b) 8mm

Figure 5.15: 8% PS:PMMA polymer blend, 2000rpm.

How the structure of the 8% blended PS/PMMA film cast at 2000rpm changes with radius can be seen in figure 5.16. At the centre of the film,

the structures are axisymmetric and isotropic. With increasing radius, the phase separated features become larger and elongated in the radial dimension.

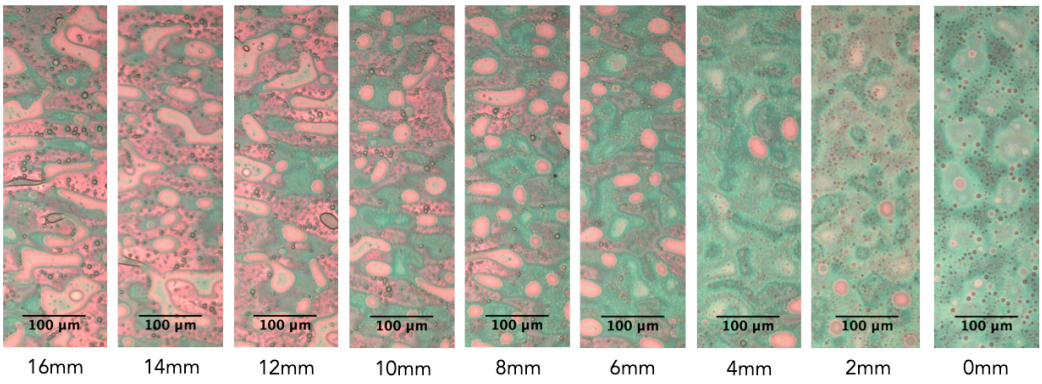

Figure 5.16: The morphology of the 8% equal blend film cast at 2000rpm changes with distance from radius.

The elongation with increasing radius can quantified by assuming the structures are ellipses, and calculating their eccentricity using a mean length/2, the semi-major axis b, and width/2, the semi-minor axis a, at each radius using the equation

$$e = \sqrt{1 - \left(\frac{b}{a}\right)^2}, \tag{5.3}$$

in which the eccentricity is e. The structure eccentricity as a function of radius is given in figure 5.17. The phase separated structures get more elongated with increasing radius and at 6mm and above, their eccentricity is greater than 0.9. Whilst the elongation of phase separated structures has not been numerically quantified in this way before, the increase in elongation with radius is in agreement with microscopy images of radial striations [16]. From figures 5.17 and 5.16, it is clear that film formation is different with increasing radii for a spin coated polymer blend. Similar results were found for the eccentricity of the structures observed in the 8% film cast at 1000rpm which increased from 0.22 to 0.97 from the film centre to and 12mm. As clear radial dependent striations were not observed for the lower concentration films, that exhibited the non-monotonic drying order discussed in section 4.4.1, the eccentricity radius could not be compared with optospinometer data. Regardless, eccentricity could be taken to be a quantitative measurement of the radial elongation effect on phase separated structures in future.

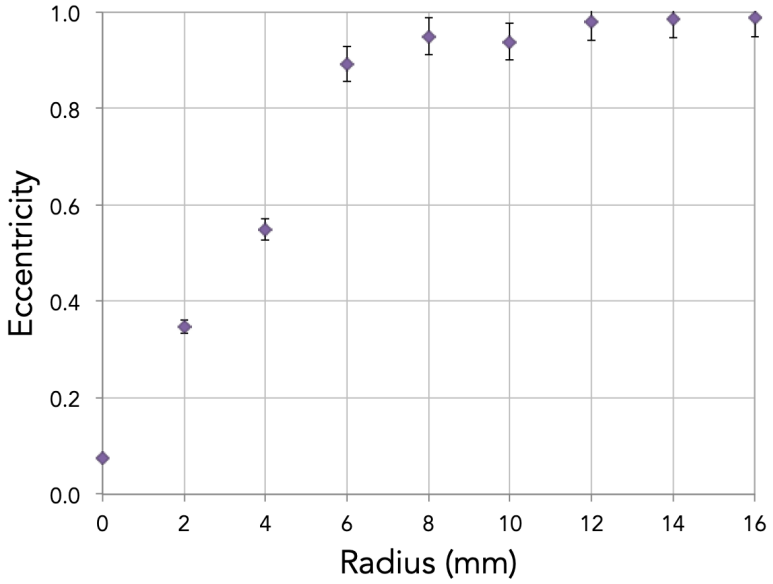

Figure 5.17: The eccentricity of the phase separated structures in the 8% film cast at 2000rpm increases with radius.

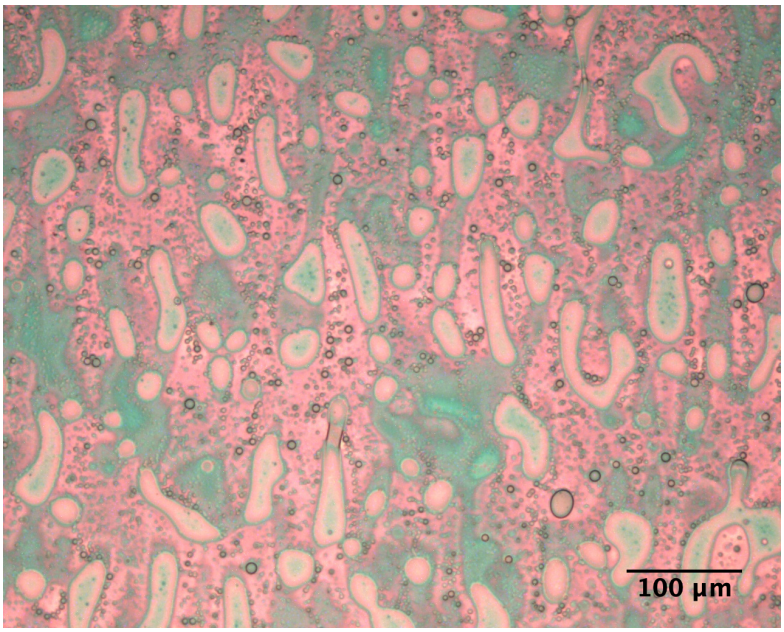

Figure 5.18: The phase separation in the 8% equal blend film cast at 2000rpm at 8mm from the film centre. The centre of the film, and thus the axis of rotation is located out of frame to the bottom of the image. The elongation of the structures is in the direction of increasing film radius.

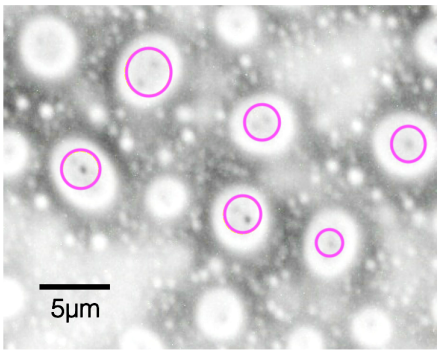

Figure 5.19: Small-scale phase separation in the 2% blended film, spin coated at 1000rpm, imaged near the centre of the film

8mm from the centre of the 8% 2000rpm film, the off-specular results indicated that length scales between 42-84μm were present. This optical microscopy images support the off-specular result, as can be seen in figure 5.18. Measuring the length of these features in Image-J gave a mean result of 75$\pm$5μm, which is in agreement with the off-specular results. Mokarian-Tabari et al measured phase separated structures at the edge of different polymer films that were 50μm in size, which is the smaller than mean feature size from figures 5.15b and 5.18 but are within the range of sizes detected in the off-specular results, 42-84μm.

An effect noticeable in all optical microscopy images is the small-scale phase separation in separated domains, illustrated by figure 5.19. This indicates that the regions of phase separation are not pure PS/PMMA. This is supported when the total area of the domains as a percentage of the image is calculated, which vary greatly between approximately 30-70%. In an ideal phase separated film, this value should equal the ratio between the polymers, 50%.

Previous experiments have shown that altering the concentration of a solution affects the phase separation [138]; low concentrations of a PS:d-PMMA solution are prone to form a bilayer whereas high concentrations of the solution will result in laterally segregated films. Furthermore, altering the vapour pressure of a spin coating environment can also control the phase separation length scale [21]. With increasing angular velocity, the phase separation length scale of PS:PMMA 1:4 was shown to decrease [163]. Similar effects seem to be occurring in the films presented in this section films as both concentration and angular velocity have affected the length scale of phase

separation.

The structure of these films indicates that nucleation and growth is the mechanism by which these films are phase separating [177]. At large film radii, the flow will be turbulent [7] which is accelerating the nucleation and growth for films of a suitably high concentration. This is shown by the large segregated structures, most notable in the 6% concentration film, figures 5.10 and 5.15. The lower concentration films however, show little radial variation but signs of small-scale phase separation [125], which is more prominent in films cast at 1000rpm, shown in figure 5.19.

5.2.2 Unequal blends

Varying the ratio between PS and PMMA in the polymer blend has an effect on the phase separation. Figure 5.20 shows the phase separation length scale and separated structure size as a function of PS mass fraction. The length scale for each concentration and spin speed was at a maximum for the equal ratio blend. PS majority films had the smallest length scales and structure sizes compared to the PS minority and equal ratio polymer blends.

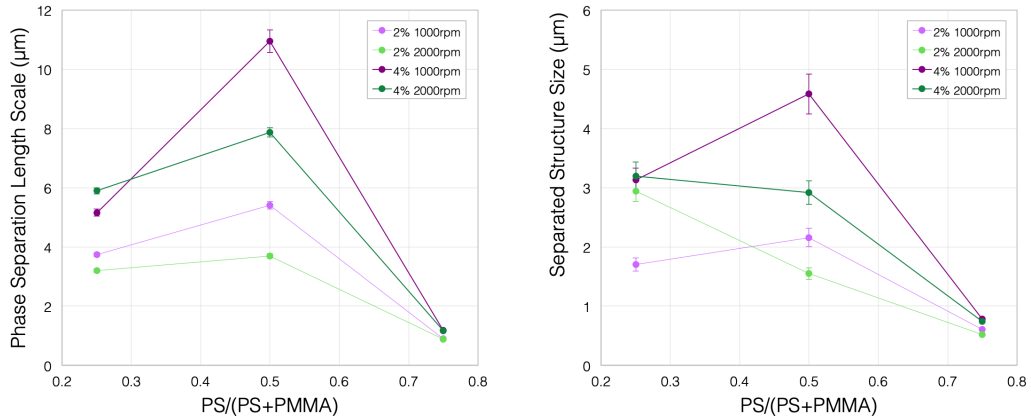

(a) (b)

Figure 5.20: The (a) mean phase separation length scale $\bar{x}$ and (b) mean phase separated structure size $\bar{y}$ as a function of PS content. 1000rpm purple, 2000rpm green, light 2%, dark 4%.

Figures 5.21 and 5.22 show phase separation length scale and separated structure size as a function of radius when varying both polymer concentration

of the solution and its PS content. Equal PS:PMMA ratio films generally yielded the largest $\bar{x}$ and $\bar{y}$ values, except for separated structure size of films cast at 2000rpm where $\bar{y}$ peaked at 0.25 PS content.

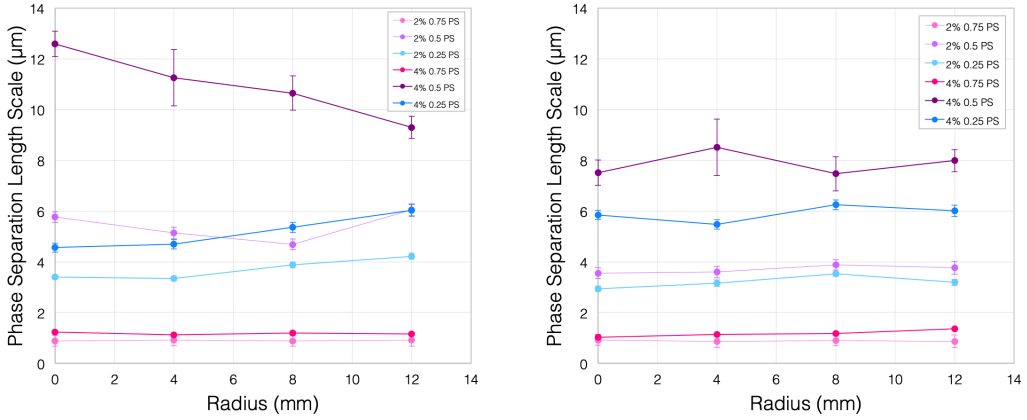

(a) 1000rpm (b) 2000rpm

Figure 5.21: The mean phase separation length scale of the film as a function of radius at (a) 1000rpm and (b) 2000rpm. 0.75 PS pink, 0.5 PS purple, 0.25 PS blue, light 2%, dark 4%.

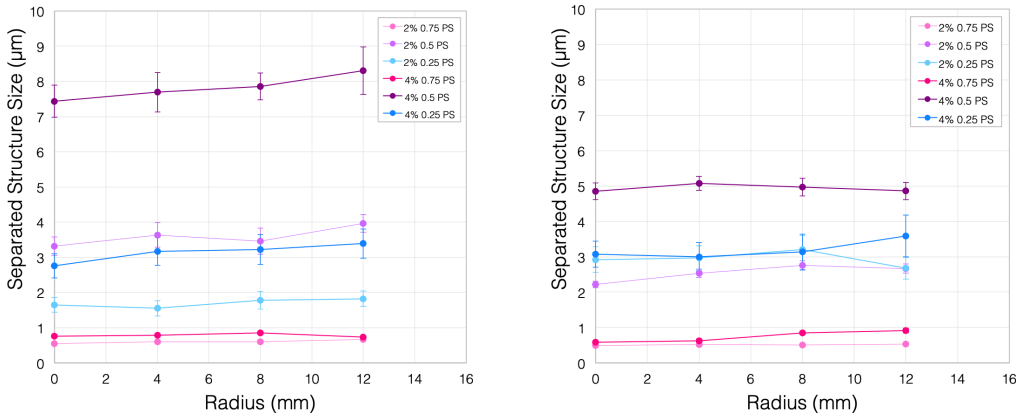

(a) 1000rpm (b) 2000rpm

Figure 5.22: The mean phase separated structure size of the film as a function of radius at (a) 1000rpm and (b) 2000rpm. 0.75 PS pink, 0.5 PS purple, 0.25 PS blue, light 2%, dark 4%.

Despite the small difference in molecular weight of the polymers, the equal ratio blend solution was found to be symmetric by calculating the critical volume fraction to be $\phi_{\text{crit}} = 0.49$. This should have should be highly immiscible, resulting in a short length scale and it is surprising that this is not the case.

Ternary blends of PS/PMMA/MEK and PS/PI/toluene have been studied in order to determine how varying PS content affects the final film morphology [139]. A film in which 0.4 of the polymer content was PS had larger values of both $\bar{x}$ and $\bar{y}$ than a PS majority 0.61 blend, which supports the results presented in figure 5.20.

The 0.5 PS solution has more time to phase separate in solvent as the cloud point is reached at a higher solvent concentration than either unsymmetrical solution. This allows the equal polymer ratio blend more opportunity to coarsen, therefore the length scale observed does not correspond to the spinodal phase separation length scale. Further coarsening processes occur in the film and this is the length scale that is obtained.

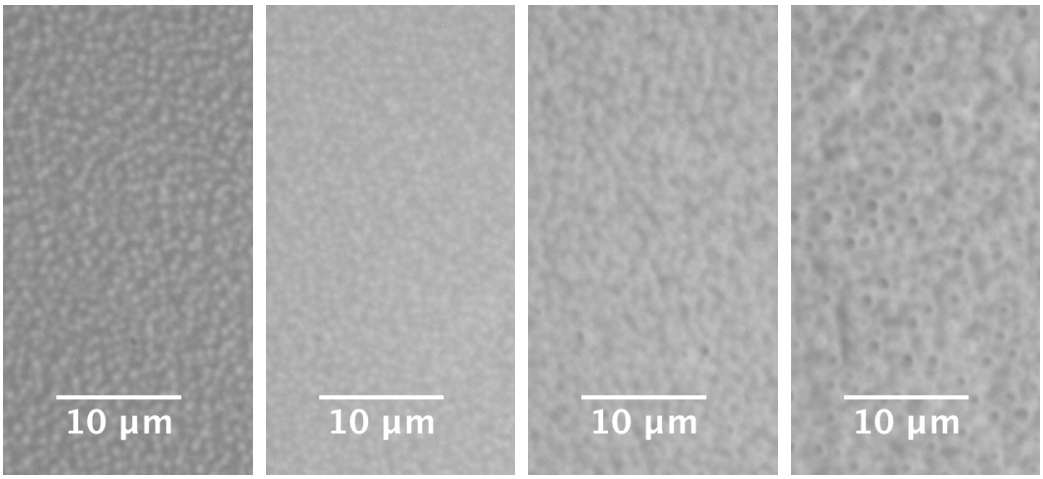

(a) 2%, 0mm (b) 2%, 12mm (c) 4%, 0mm (d) 4%, 12mm

Figure 5.23: The optical microscope images of the 2% and 4% PS:PMMA 3:1 polymer blends cast at 1000rpm.

The different solubilities of the polymers in toluene has clearly affected the unequal blended films. As toluene is a better solvent for PS than it is for PMMA [17], the PS majority films have very small phase separated length scales, structure sizes and structure areas, as is shown by figures 5.20, 5.21 and 5.22 in addition to the optical microscopy images themselves in figures

5.23 and 5.24. The area of these separated features could not accurately be determined by Image-J. The structures in the 0.75 PS films are much smaller than those recorded with a PS content of 0.61 [139] which is to be expected. As PS content increases, the length scale is observed to decrease.

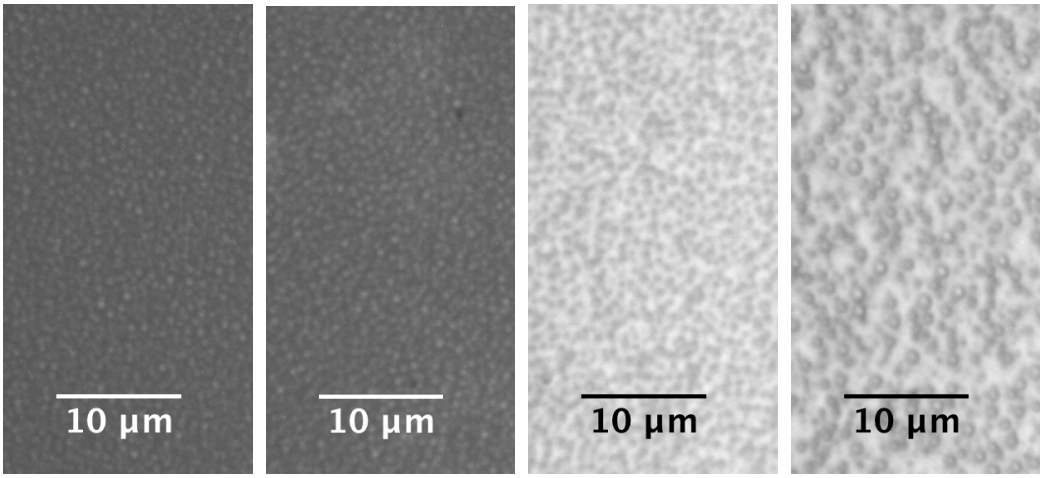

(a) 2%, 0mm (b) 2%, 12mm (c) 4%, 0mm (d) 4%, 12mm

Figure 5.24: The optical microscope images of the 2% and 4% PS:PMMA 3:1 polymer blends cast at 2000rpm.

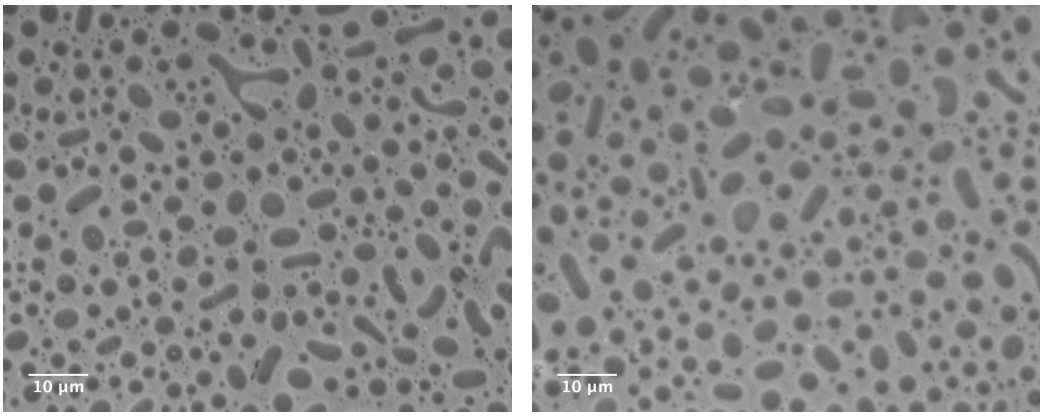

(a) 0mm (b) 12mm

Figure 5.25: 2% PS:PMMA 1:3 polymer blend, 1000rpm.

The PMMA majority films did have large enough phase separated structure areas for measurements to be taken with Image-J. Figure 5.25 shows the 2% PMMA majority film cast at 1000rpm. At the centre of the film, the

structures had a mean area of 2.0±0.1μm^2 which decreased at the edge of the film to 1.5±0.1μm^2.

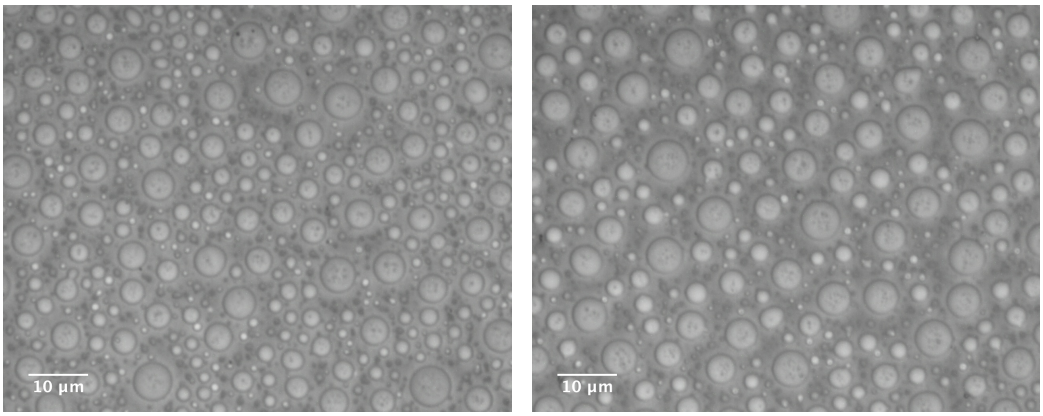

(a) 0mm (b) 12mm

Figure 5.26: 4% PS:PMMA 1:3 polymer blend, 1000rpm.

Figure 5.26 shows the 4% PMMA majority film cast at 1000rpm. The structures had a mean area of 1.8±0.1μm^2 at the film centre, which increased at the film edge to 2.4±0.2μm^2. Radial variance is therefore confirmed for this blend.

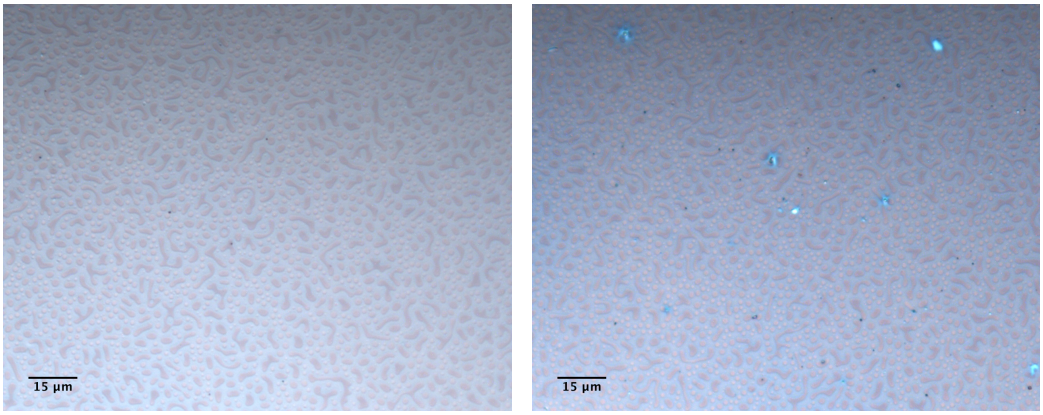

(a) 0mm (b) 12mm

Figure 5.27: 2% PS:PMMA 1:3 polymer blend, 2000rpm.

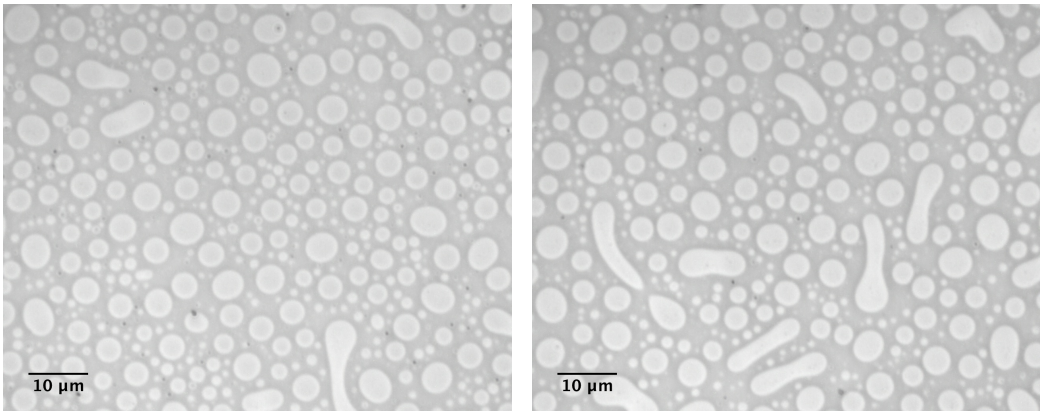

(a) 0mm (b) 12mm

Figure 5.28: 4% PS:PMMA 1:3 polymer blend, 2000rpm.

Figure 5.27 shows the 2% PMMA majority film cast at 2000rpm. This film had structures at the centre and edge of the film that had a mean area of $1.9\pm0.1\mu m^2$. The 4% PMMA majority film cast at 2000rpm is shown in figure 5.28. This film had more elongated structures at the edge of the film compared to the centre, which was represented in the difference in the mean areas of the structures, which were $2.7\pm0.2\mu m^2$ and $5.1\pm0.4\mu m^2$ respectively.

This subsection shows that a difference in polymer ratio has a great effect on the polymer film morphology due to the solubilities of the polymers but this effect is minimally noticeable with increasing radius. The change in the domain size of the blended films was again shown to be a strong function of angular velocity, which is supported by PS mass-fraction experiments [139]. Future work could consider using unequal blends with higher polymer concentrations or different solvents. However, minimal radial distinctions were found with changing the polymer ratio and as a result, the higher concentration solutions made for the second set of experiments consisted of equal ratio PS/PMMA blends and homopolymers.

5.3 Atomic Force Microscopy

The small scale structure of the films can be explored using atomic force microscopy. AFM nanoindentation can be performed on different regions that have occurred due to phase separation, thus determining with certainty which of these features are PMMA and PS [178]. The height differences between the regions can also be detected.

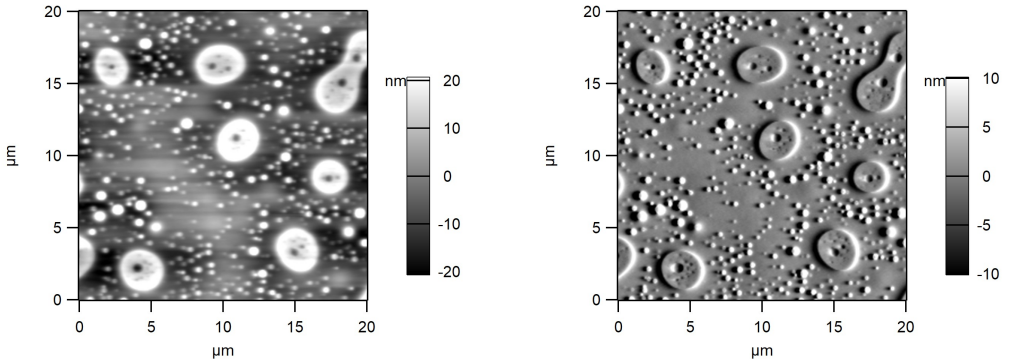

(a) Height (b) Deflection

Figure 5.29: An AFM image showing the height structure of a 6% blended film cast at 2000rpm. Figure 5.29a shows the height structure and figure 5.29b shows he deflection structure.

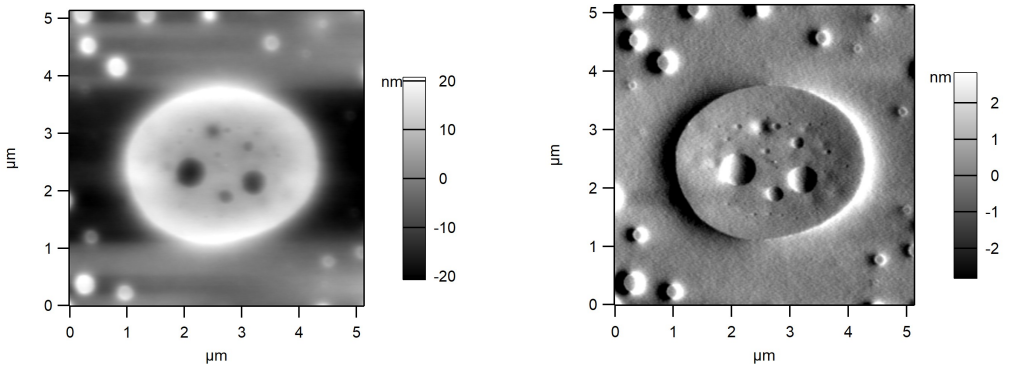

(a) Height (b) Deflection

Figure 5.30: An AFM image showing the height structure of a 6% blended film cast at 2000rpm.

Figure 5.29a shows the constant height plot of one of the 6% blended films cast at 2000rpm. In this figure, the height difference can be seen to vary by 40nm and the raised structures themselves are approximately 20nm thicker than the rest of the film. The corresponding deflection feedback image is given in figure 5.29b. In order to obtain this image, a constant force is applied to the film by the cantilever and the response of the sample can be used with known values to determine the composition of the film.

The nanoindentation on the blended films indicated that the raised structures have a slope gradient of -6.3×10^{-3}V.nm^{-1} and the thinner regions of the

film have a slope gradient of -5.6×10^{-3}V.nm^{-1}. The higher slope indicates that the material is stiffer, and considering the Young's modulus of PMMA is higher than that of PS at room temperature, it is concluded that the raised structures are PMMA. These domains are quite clear due to the different height difference which indicates that these films have breached the surface of the film to form fully-segregated lateral domains [146]. Despite this, the roughness and length scale of these domains must not be large enough to be detectable in off-specular scattering.

Similar PMMA-rich state 'islands' have been observed on a PS-rich 'sea' state previously [17] where the composition and height of the structures were found to be determined by both the solvent solubility of the polymers and the substrate preference of each polymer. Toluene is a better solvent for PS than PMMA, which has a higher surface tension than PS. As a result, a PS:PMMA film undergoing phase separation has a PS-rich state which is substrate preferential and a PMMA-rich state which is surface preferential [17].

5.4 Summary

This chapter has discussed the morphological differences seen in a film by varying the solution concentration, angular velocity and polymer ratio and if there is any radial distinction by using optical microscopy, off-specular reflection and atomic force microscope.

The only film with large enough phase separation length scales to be detected by off-specular scattering was the PS/PMMA blend cast from an 8% solution at 2000rpm. This phase separation length scale was radial dependent and only observed 8mm from the film centre. The length scale was approximately 62μm, and this was supported by results from the optical microscopy images.

The difference in phase separation length scales was concentration dependent, as would be expected [138]. The phase separation seen in the films cast from low concentration solution is small scale as the film forms a relatively uniform bilayer with preference for PMMA at the bottom and PS at the surface. At 4% solution concentration, Marangoni instabilities are believed to become significant [138].

When concentration is increased to 6%, the instability of the bilayer increases and small regions of PS and PMMA migrate to the interface. When the spin coating solution is increased to 8%, the instability is able to breech the film

surface and larger length scale phase separation is observed due to lateral segregation.

Radial distinctions were not clearly observed in the majority of these films, except those with a higher polymer concentration. Phase separated domain areas increased with radii which is a significant radial effect, as is the increasing eccentricity of structures observed in high concentration films.

The trigger for these features could be spiral vortices or three-dimensional flow causing the solution to mix, allowing like polymers to aggregate more readily. Bornside et al theorised [7] that when $r > r_2$, the film is subject to turbulence which in addition could encourage the phase separation. This is also supported by observations of a radial dependent temperature gradient [172] that could induce morphological features due to the Marangoni effect [169].

6 Results III: Immiscible Interfaces

This chapter details the theory, experimental methods and results from a project on immiscible interfaces conducted with the Free University of Brussels.

6.1 Introduction

Immiscibility of polymers is not limited to the phase separation of polymer blend films. The interfaces between a layered polymer film, such as a bilayer or a trilayer, can also exhibit unusual behaviour. Such a boundary is subject to effects from both the enthalpy of mixing and polymer chain entropy. These interfaces are not discrete and a volume fraction gradient exists across an interfacial width. The Helfand-Tagami theory quantifies the volume fraction gradient as a function of distance $\phi_{\mathrm{A}}(z)$ across the interface as

$$\phi_{\mathrm{A}}(z) = \frac{1}{2}\left(1 + \tanh\frac{z}{w}\right), \tag{6.1}$$

where z is the depth and w is the interfacial width, which is given by

$$w = \frac{2a}{\sqrt{6\chi}} \tag{6.2}$$

where a is the polymer segment size and χ is the interaction parameter between the polymers in the separate layers. Equations 6.1 and 6.2 were developed using mean field theory [179], but experimental results have proven that this is incomplete [180–182]; the interfacial width of PS and PMMA layers has been found to be 70% larger than those predicted by equation 6.2.

The discrepancy between the model and the experimental results has been attributed to surface roughening and capillary waves caused by thermal fluctuations in the structure [183]. These capillary waves travel along a phase boundary and are due to surface tension effects.

Capillary waves at a boundary between the horizontal layers of a polymer bilayer or trilayer display a vertical component, as shown by figure 6.1, which can be detected using neutron scattering experiments, which shall be discussed in section 6.2.

Figure 6.1: A capillary wave between the polymer-polymer interface of a bilayered film.

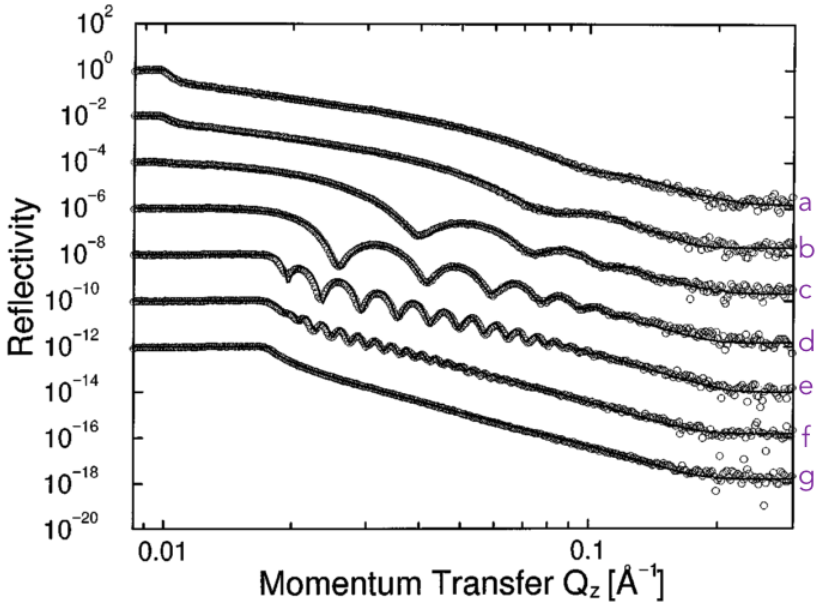

Figure 6.2: The neutron scattering results from a bilayer structure. The top layer was d-PS and varied in thickness from a) 6nm to g) 480nm. The PMMA layer was at least 400nm thick. From M. Sferrazza et al, 1997 [184].

Figure 6.2 displays the results from a neutron scattering experiment on numerous d-PS/PMMA polymer bilayers. Each sample had a PMMA base layer 400nm thick. The thickness of the d-PS surface layer was varied. The thinnest d-PS layer was 6nm and can be seen in figure 6.2a. The thickest d-PS layer was 480nm and can be seen in figure 6.2g.

The general trend of this relationship is that logarithmic reflectivity decreases with logarithmically increasing momentum transfer. Figure 6.2b-f show oscillations in reflectivity which have a smaller wavelength with in-

creasing thickness. The oscillations represent discrete layers in the sample and their roughness is obtained from the rate at which the reflectivity decreases when compared to an ideal sample with no roughness.

The bilayers with a 6nm and 480nm d-PS top layer did not show the oscillations in the reflectivity data. The 480nm d-PS layer is so thick that the capillary waves between the bilayer have such a small wavelength that the neutrons do not have a high enough resolution to detect it. The conclusion from the results was that thinner films have a smaller capillary wave contribution to interfacial width because for these films, capillary waves are suppressed and so the roughness is closer to the Helfand-Tagami value [184].

The effect of the multi-layer roughening has been seen in other experiments such as low molecular weight d-PS and PMMA layers [182] and high molecular weight d-PS and PMMA in which the d-PS layer was thick (>100nm) and thin (<20nm) [185]. Neutron refletometry indicated that capillary waves were present in unannealed d-PS/PMMA polymer bilayers of similar molecular weights but after annealing for an hour at 393K, the capillary waves were no longer detected.

The capillary dispersive length a_{dis} quantifies the degree at which the capillary waves affect the sample. It is given in equation 6.3 in terms of surface tension σ, the thickness of the top, often deuterated, layer h and Υ is the Hamaker constant [185].

$$a_{\text{dis}} = \sqrt{\frac{4\pi\sigma h^4}{\Upsilon}} \tag{6.3}$$

By conflating the theoretical predictions with experimental results, the effect of capillary waves can be quantified. As previous work has shown they can affect a variety of film thicknesses [184], the effects of capillary waves should not be ignored. Casting multi-layered organic films is vital to the photovoltaics industry and layer disruption can hinder their efficiency.

The aim of this project was to induce capillary waves across thin polymer films in the centre of a trilayer. It was hypothesised that as the samples were annealed for longer, eventually the capillary waves induced would cause the central layer to be fully disrupted. From this disruption, the contribution of capillary waves to the interfacial width could be calculated using a modified model of equation 6.2,

$$w = \frac{2a}{\sqrt{6\chi}} \left(1 + \ln 2 \left[\frac{1}{\chi N_{\mathrm{A}}} + \frac{1}{\chi N_{\mathrm{B}}} \right] \right), \tag{6.4}$$

where w is the interfacial width between two polymers A and B, a is the polymer segment size, χ is the interaction parameter between the polymers A and B and N is the degree of polymerisation of polymers A and B [186].

The mean-squared deviation of the interface from its average value can be used to quantify the interfacial width broadening caused by capillary waves. It is defined as

$$\langle \sigma_c^2 \rangle = \frac{k_{\mathrm{B}} T}{2\pi\sigma} \ln \left(\frac{\lambda_{\max}}{\lambda_{\min}} \right), \tag{6.5}$$

where k_{B} is Boltzmann's constant, T is temperature, σ is the surface tension between the polymers in each layer and $\lambda_{\max}$ $\lambda_{\min}$ are the maximum and minimum values possible for the capillary waves.

6.2 Neutron Reflectometry

When the neutrons make contact with the sample, they undergo a change in momentum which is indicative of the sample structure [187, 188]. The neutrons can be used in this manner because their de Broglie wavelength at ∼20 K is small enough (< 1nm) to be scattered by polymers in thin films.

Momentum transfer can be considered classically by first defining equation 6.6 in which $\vec{p}$ is used to define momentum.

$$\vec{p_{\mathrm{Ai}}} + \vec{p_{\mathrm{Bi}}} = \vec{p_{\mathrm{Af}}} + \vec{p_{\mathrm{Bf}}} \tag{6.6}$$

The sum of the momentum of particles A and B before the collision is equal to that of the sum of the momentum of particles A and B after the collision. The momentum transfer $\vec{p_{\mathrm{t}}}$ can then be defined by rearranging equation 6.6 to equation 6.7. A collision between a moving particle A and a free, stationary particle B is given in figure 6.3. Conservation of momentum is obeyed.

$$\vec{p_{\mathrm{t}}} = \vec{p_{\mathrm{Ai}}} - \vec{p_{\mathrm{Af}}} = \vec{p_{\mathrm{Bf}}} - \vec{p_{\mathrm{Bi}}} \tag{6.7}$$

At this point, real space can be converted to momentum space by using the reduced Plank constant $\hbar = \frac{h}{2\pi}$ in equation 6.8, as momentum $\vec{p}$ and wave-vector $\vec{k}$ are proportional to one another. This defines the unit of momentum space, the wave vector $\vec{k}$ which is given by

$$\vec{k} = \frac{\vec{p_{\mathrm{t}}}}{\hbar}, \tag{6.8}$$

which has a magnitude

$$|\vec{k}| = \frac{2\pi}{\lambda}. \tag{6.9}$$

The initial wave vector $\vec{k_{\mathrm{i}}}$ is incident to the sample at an angle of θ_{i}. The neutrons are reflected off the sample with a final wave vector $\vec{k_{\mathrm{f}}}$ at an angle θ_{f}. As the reflection is specular, $\theta_{\mathrm{i}} = \theta_{\mathrm{f}} = \theta$. The momentum has changed and so the wave vector has changed, $\vec{k_{\mathrm{i}}} \neq \vec{k_{\mathrm{i}}}$. This is seen in figure 6.4.

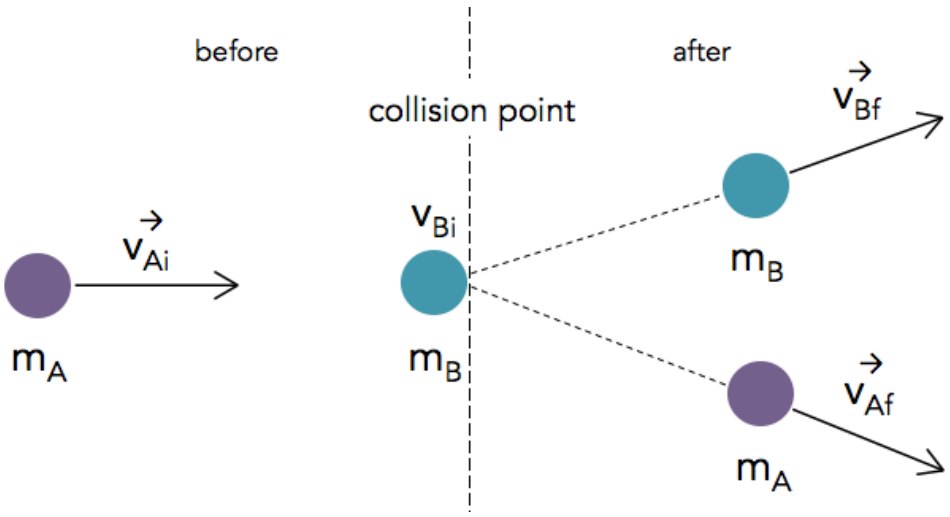

Figure 6.3: An elastic collision between two particles A and B.

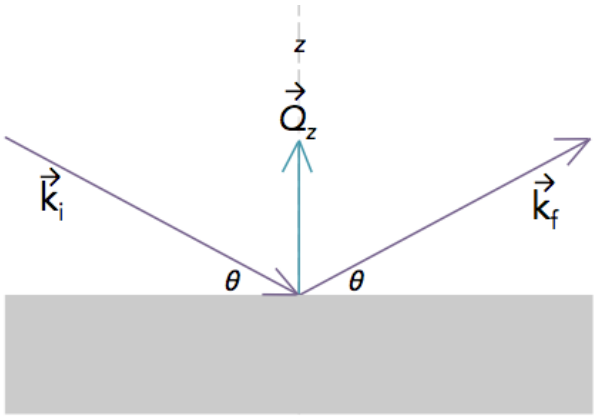

Figure 6.4: The neutron beam is incident to the sample at an angle θ_i. As it is a specular reflection technique, $\theta_\mathrm{i} = \theta_\mathrm{i}$.

This momentum transfer between the two wave vectors is $\vec{Q_z}$, which is given by

$$\vec{Q_z} = \vec{k_\mathrm{f}} - \vec{k_\mathrm{i}}. \tag{6.10}$$

This is more commonly in terms of its magnitude,

$$Q_z = \frac{4\pi}{\lambda} \sin\theta, \tag{6.11}$$

in which $\vec{k_{\mathrm{i}}}$ and $\vec{k_{\mathrm{f}}}$ are the initial and final wave vectors respectively, θ is the incident angle of the neutron beam and λ is the wavelength of the neutrons. Q_z has the units of inverse length. During neutron reflectometry at D17, the wavelength of the neutrons in the beam is varied, resulting in different values of Q_z. The reflectivity of the neutron beam is a function of Q_z this can be plotted, such as the result above in figure 6.2.

6.3 Method

PS/d-PMMA/PS polymer trilayers were subject to neutron scattering experiments in order to explore the interface morphology discussed.

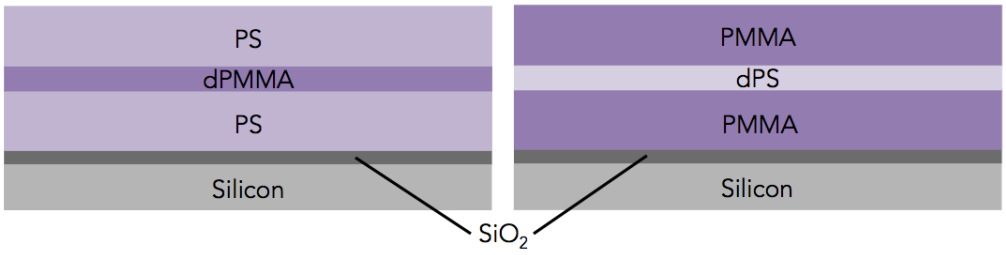

Figure 6.5: The trilayer structures.

Firstly, the PS base layer was spin coated onto silicon using a solution of 6% polymer concentration. The film was spun for 30 seconds at 3000rpm to make films approximately 300nm in thickness. The central d-PMMA layer was then coated onto glass from a polymer solution of concentration 2%. These were spun for 30 seconds at 3000rpm and the films were less than 20nm in thickness. The central film was adhered to the base layer by film floating. The final PS layer was then cast onto glass using the same conditions and solution as the foundation layer. This layer was then film floated onto bilayer atop the deuterated layer.

The silicon wafer typically reacts with the oxygen in the atmosphere to cause a native layer of silicon dioxide to be present on its surface. This layer was included in all models and has an approximate thickness of 2nm. Example structures are shown in figure 6.5.

The resultant trilayers had approximate central layer thicknesses of 60Å, 120Å, 150Åand 170Å. Multiple trilayers with these central thicknesses were made.

Beam time was granted at both D17 at the Institut Laue-Langevin (ILL) in Grenoble and OFFSPEC at the Rutherford Appleton Laboratory (RAL) in Didcot. Once at the site, each trilayer was annealed for 0, 5, 8, 10, 20, 60, 120, 300 and 480 minutes before being subject to neutron beam experiments.

Figure 6.6a shows the results from an unannealed PS-dPMMA-PS sample with a central layer thickness of 12nm. Figure 6.6b shows the results from

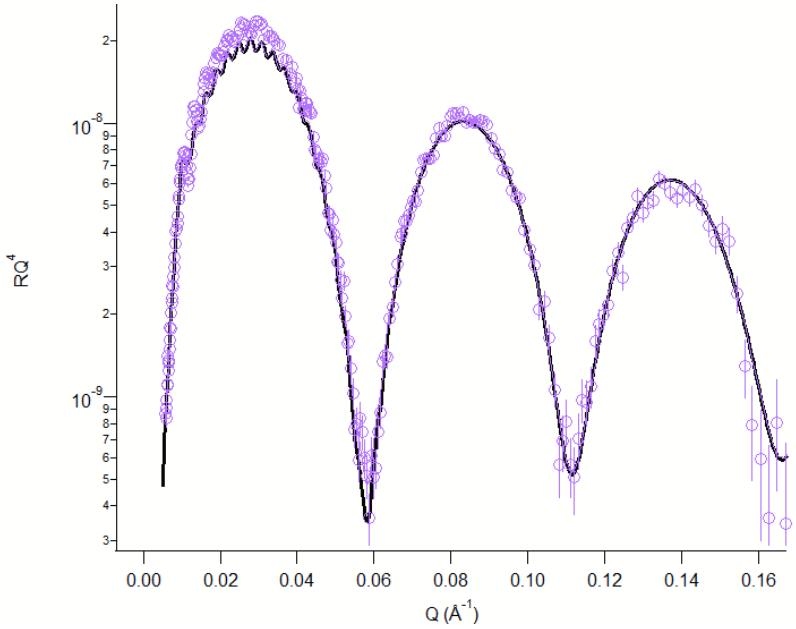

(a)

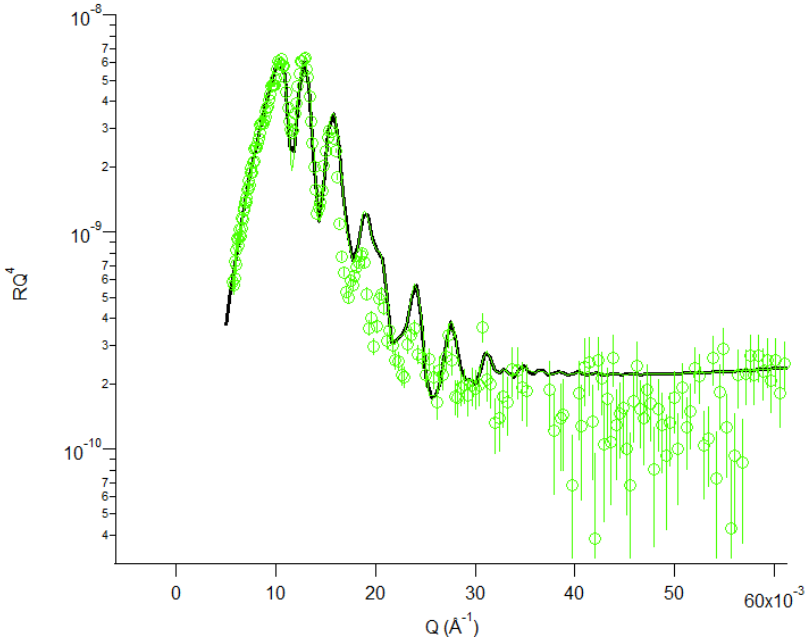

(b)

Figure 6.6: RQ^4 as a function of scattering vector Q_z for an (a) unannealed and (b) annealed for 120 minutes PS-dPMMA-PS trilayer, central thickness of 12nm. The model generated by IGOR Motofit is the black line. RQ^4 is given in units of $Å^{-4}$ and is used rather than reflectivity as the error bars can be seen more clearly.

the same film after annealing for 120 minutes. In these two figures, the y axis is in terms of RQ^4 in which R is the reflectance mentioned in figure 6.2 but a factor of Q^4 is included because this makes the peaks more noticeable.

Once the data were acquired, IGOR Motofit was used to build a model of the trilayer structures in order to determine the roughness of the central layer. The model is built by using known quantities, including the SLD, to gain an accurate thickness and roughness of each layer. The user interface is shown in figures 6.7a and 6.7b for the data obtained in figures 6.6a and 6.6b.

6.3.1 Films

Circular silicon wafers 5cm in diameter were used as the foundation substrate for the trilayers. These wafers were also made by Prolog Semicor LTD who report that, due to the silicon reacting with oxygen in the atmosphere, have a native oxide layer SiO_2 approximately 2nm thick. This was supported by the models produced in IGOR Motofit to determine the trilayer structures, as models that included the SiO_2 layer had a better fit to the data.

The central and surface layers of the trilayers were spin coated onto rectangular glass slides with a width of 7.5cm and height of 5cm. These slides were produced by Corning and supplied by Ted Pella, Inc.

The silicon wafers and glass slides were cleaned by immersion in toluene and then sonicated for a minimum of 1 hour and dried with a nitrogen flow. An O_2 plasma cleaner was used to complete the final stage of cleaning.

The toluene used in these experiments was the same as that described in Chapter 3, and supplied by Sigma Aldrich. The polymers used in these experiments were all supplied by Polymer Standards Service (PSS). The molecular weights are the following:

- PS: 560,000 g.mol^{-1}
- d-PMMA: 35,000 g.mol^{-1}

The central and top layers of the trilayer structures were applied by film-floating. The deposition technique was the same as that described in Chapter 3 and the films were not annealed after spin coating.

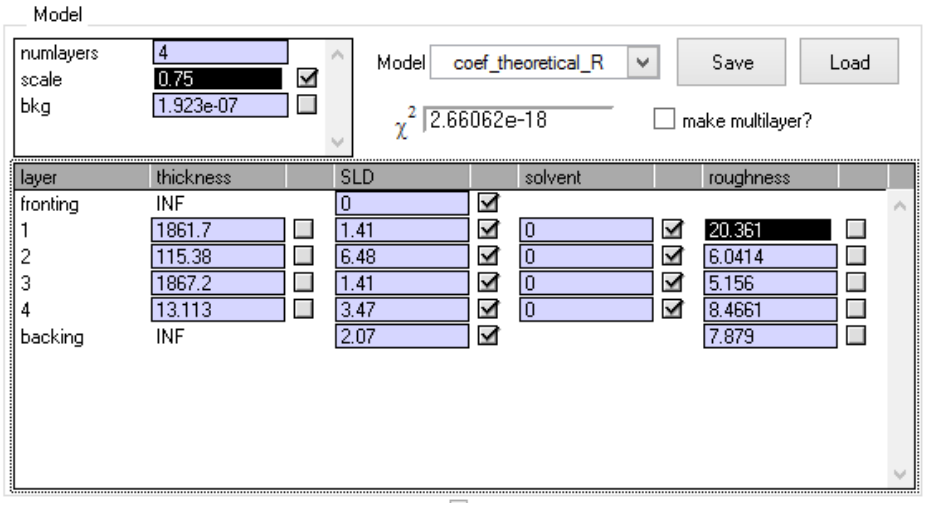

(a)

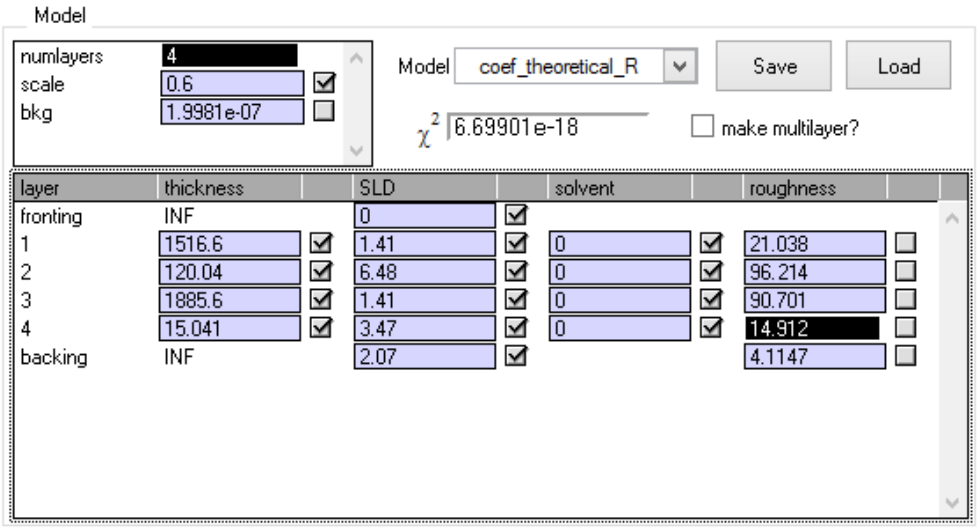

(b)

Figure 6.7: The model parameters input to and given by IGOR Motofit for a PS-dPMMA-PS trilayer (a) unannealed and (b) annealed for 120 minutes, both with a central thickness of 12nm. The values in (a) gave the plot in figure 6.6a and those in (b) gave the plot in figure 6.6b. Layer thickness and roughness are all given in Å.

6.4 Discussion

The experimental results from neutron spectrometry were compared to models made in IGOR Motofit. The thicknesses and roughnesses fitted by the model are shown in table 7 for the polymer layers and table 8 for substrate and its native oxide layer. The tables refer to individual layer roughnesses, which are defined by figure 6.8. Tables 7 and 8 refer to a singular roughness for each layer, when the majority of layers have two roughnesses. The boundary that each roughness measurement corresponds to is illustrated by figure 6.8.

The results in tables 7 and 8 were produced from known SLD values which are:

- PS 1.44 $\times 10^{-6}$Å^{-2}
- d-PMMA 6.48 $\times 10^{-6}$Å^{-2}
- SiO_2 3.47 $\times 10^{-6}$Å^{-2}
- silicon 2.08$\times 10^{-6}$Å^{-2}

Sample	Estimated dPMMA	Annealing time	Surface PS		Central d-PMMA		Foundation PS	
number	thickness (Å)	(mins)	Thickness (Å)	Roughness (Å)	Thickness (Å)	Roughness (Å)	Thickness (Å)	Roughness (Å)
1	60	0	1429.8	20.71	45.145	4.7985	1760.8	4.5223
1	60	0	1416	19.194	46.434	5.0171	1744.2	5.8861
1	60	5	1420	22.967	44.673	39.78	1761.3	39.982
1	60	5	1821.5	20.978	42.312	39.369	1773	39.901
1	60	300	1817.6	22.969	39.792	38.761	1777.8	39.681
2	120	8	1565.6	4.7062	114.17	12.081	1733.1	11.799
2	120	20	1575.1	20.3556	115.25	15.902	1775.3	13.059
2	120	60	1564.1	19.474	114.08	19.386	1751.6	18
2	120	60	1569.7	17.772	112.75	17.921	1757.7	17.987
2	120	60	1573.5	35.199	115.1	20.613	1754.2	19.353
2	120	120	1481.5	20.096	50.255	102.15	1855	103.55
2	120	120	1516.3	21.038	120.04	96.214	1885.6	90.701
3	120	0	1883.6	23.235	114.3	5.3639	1860.4	7.0665
3	120	0	1861.7	20.361	115.38	7.1084	1867.2	5.156
3	120	0	1821.2	22.087	114.76	6.489	1835.1	5.3919
3	120	20	1863.5	18.498	112.71	15.27	1852.9	15.189
4	150	8	1411.3	19.211	124.94	15.48	1800.9	10.817
4	150	20	1410.1	21.381	121.7	16.251	1778.9	14.44
4	150	20	1406.8	18.062	125.13	19.068	1785.6	10.573
4	150	60	1401	22.935	125.45	19.097	1777.8	11.142
4	150	300	1781.6	21.028	150.46	59.768	1846.1	58.791
4	150	300	1990.4	53.508	100.57	58.874	1943.7	58.673
5	170	8	1612.5	5.0026	149.99	14.325	1745.7	11.431
5	170	20	1635.3	22.308	148.07	19.26	1767.6	13.745
5	170	60	1617	18.982	150.44	18.452	1747.2	14.358
5	170	300	1655.9	15.993	150.14	24.897	1715.9	24.918
5	170	300	1703.6	21.943	150.01	23.846	1760.1	23.795
5	170	480	1554.3	20.453	150.76	57.693	1961.3	55.1
5	170	480	1628.6	5.7773	150.28	48.958	1853.8	49.463

Table 7: Polymer trilayer results.

Sample number	Estimated dPMMA thickness (Å)	Annealing time (mins)	SiO_2			Silicon Wafer	
			Thickness (Å)	SLD ($\times 10^{-6}$ Å^{-2})	Roughness (Å)	SLD ($\times 10^{-6}$ Å^{-2})	Roughness (Å)
1	60	0	25.722	3.47	5.6867	2.07	2.7071
1	60	0	19.27	3.47	5.2867	2.07	1.4332
1	60	5	18.178	3.47	7.3104	2.07	4.9651
1	60	5	14.258	3.47	15.219	2.07	6.8722
1	60	300	17.303	3.47	1.4159	2.07	5.9946
2	120	8	9.1433	3.47	2.5308	2.07	7.3601
2	120	20	15.932	3.47	7.2499	2.07	5.08
2	120	60	19.855	3.47	10.753	2.07	2.8147
2	120	60	19.944	3.47	18.84	2.07	0.53412
2	120	60	18.739	3.47	4.9688	2.07	3.5277
2	120	120	13.735	3.47	6.8936	2.07	4.0341
2	120	120	15.041	3.47	14.912	2.07	4.1147
3	120	0	0.80629	3.47	6.0084	2.07	25.238
3	120	0	13.113	3.47	8.4661	2.07	7.879
3	120	0	17.533	3.47	7.4052	2.07	5.5694
3	120	20	19.548	3.47	11.034	2.07	10.897
4	150	8	11.978	3.47	9.5464	2.07	1.9872
4	150	20	13.425	3.47	0.067459	2.07	5.3968
4	150	20	16.739	3.47	9.8941	2.07	6.1602
4	150	60	10.158	3.47	5.923	2.07	3.742
4	150	300	13.367	3.47	4.1013	2.07	6.5178
4	150	300	26.457	3.47	6.7147	2.07	0.47583
5	170	8	15.499	3.47	13.75	2.07	15.283
5	170	20	8.7719	3.47	1.506	2.07	2.6597
5	170	60	6.2178	3.47	3.347	2.07	10.996
5	170	300	15.325	3.47	8.4162	2.07	2.5699
5	170	300	15.929	3.47	3.5578	2.07	3.6997
5	170	480	24.82	3.47	0.38533	2.07	1.3043
5	170	480	18.814	3.47	5.6251	2.07	1.0816

Table 8: SiO_2 and silicon wafer results.

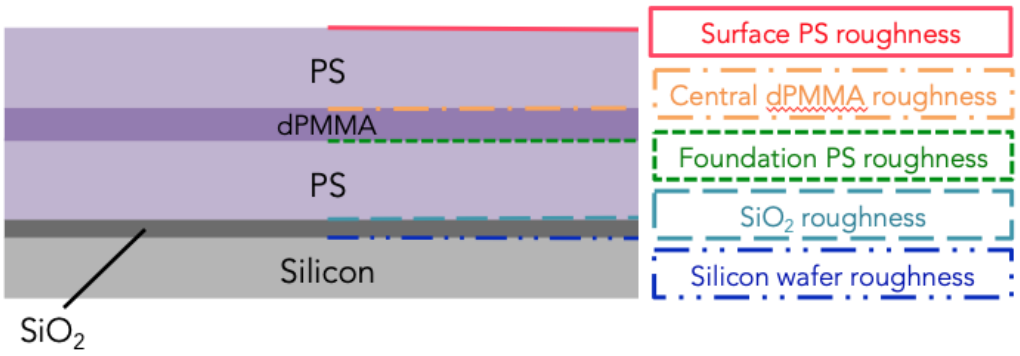

Figure 6.8: The roughness of each layer refers to the boundary of the layer closest to the surface of the structure, as labelled here.

Mean values and associated errors were found for the central layer thicknesses and roughnesses and these results are given in table 9 and presented in figure 6.9. When this data is collated, the increase in roughness with annealing time is more clear.

Expected thickness (Å)	Annealing time (minutes)	Mean central layer thickness (Å)	Mean central layer roughness (Å)
60	0	45.8±0.3	5.0±0.3
	5	43.5±0.2	39.6±0.2
120 [1] (Sample 2)	8	114±1	12.0±0.1
	20	115±2	14.5±1.4
	60	114±1	19.0±0.5
	120	85±5	96±4
120 [2] (Sample 3)	0	115±0.2	6.0±0.5
	20	113±1	15.23±0.04
150	8	125±2	13±2
	20	125±2	15±2
	60	126±3	15±4
	300	126±2	59.0±0.3
170	8	150±2	13±2
	20	148±3	16±3
	60	150±2	16±2
	300	150.1±0.3	24.4±0.3
	480	151±3	53±2

Table 9: The roughnesses of the films after their respective annealing times.

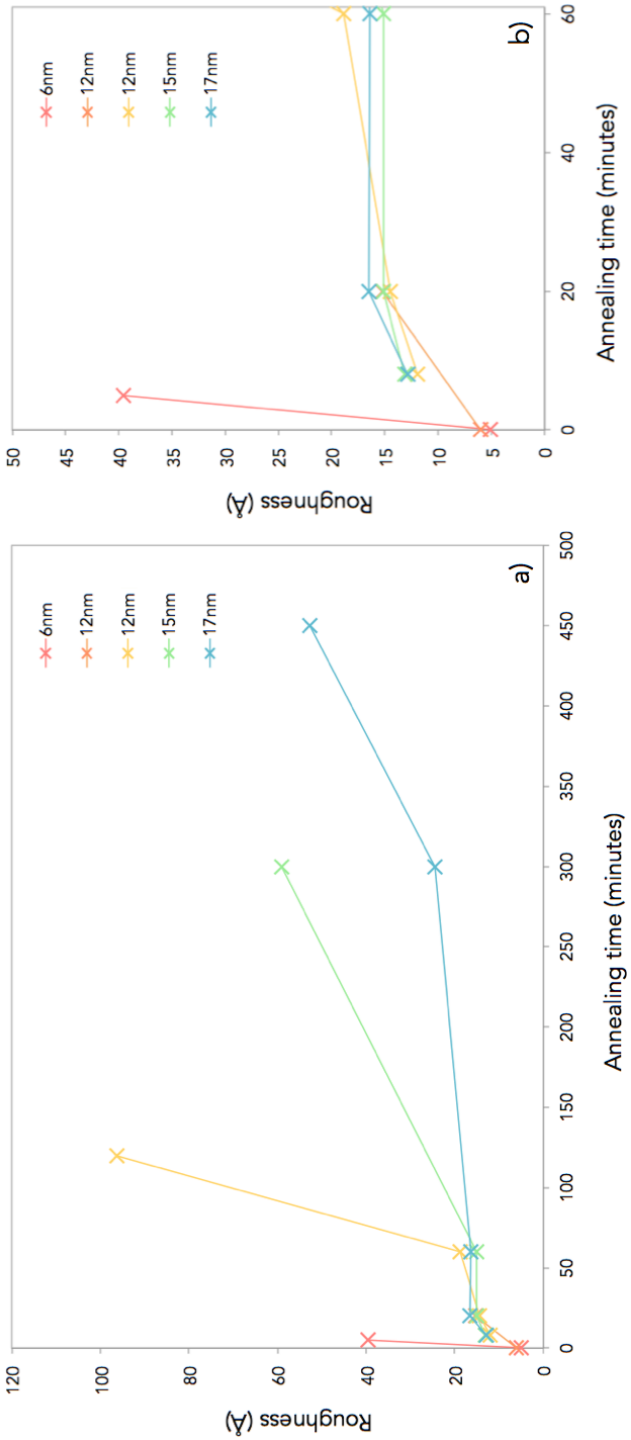

Figure 6.9: The central layer roughness after annealing for a) all the PS/d-PMMA/PS trilayers and for clarity b) the smallest annealing times.

These tables and plots show that the roughness of the d-PMMA layer increases with annealing time and this is in agreement with previous results [182, 184, 185]. The samples with a central layer thinner than 120Å were annealed until the central layer was no longer detected by applied models, indicating that the d-PMMA layer had ruptured. The samples with a central layer of predicted thickness of 120Å or above required an annealing time longer than possible with the allocated experiment time and so did not rupture. This is in agreement with the work of others, in which d-PS samples with different thicknesses were annealed for 8 hours or until the film ruptured [189]. The films that ruptured were all thinner than 110Å but d-PS layers 150Å and 300Å thick did not rupture in less than 8 hours [189].

The final data sets taken for trilayers with ruptured d-PMMA layers showed that the roughness of the d-PMMA layer was of similar value to the layer thickness; the estimated 60Å thick d-PMMA layers actually had a measured thickness of 44±3Åand after rupturing its roughness was 39±1Å. The roughness of d-PS layers with much lower molecular weights was found to be 29±3Åand 30±3Åwhen ruptured [182]. These values do not agree with those presented here but this can be attributed to the differences in molecular weight.

The d-PMMA layers that did not rupture had a high roughness after being annealed for 5-8 hours. After the second 120Å trilayer (sample 3) and 150Å trilayer were annealed for 300 and 480 minutes respectively, no central layer was detected by the neutron reflectivity indicating these layers had also broken apart since their previous beam data were taken. The roughness at each interface of the 170Å d-PMMA layer was approximately 35% of the central layer thickness after 8 hours of annealing and the roughness at each interface of the 150Å d-PMMA layer was approximately 47% of the central layer thickness after 5 hours of annealing.

Equation 6.5 can be used to calculate the effect of capillary waves on the interfacial width. The surface tension between the polymers is taken to be $\sigma = 1.5 \times 10^{-3}\text{N.m}^{-1}$ at $T = 140°\text{C}$ [190]. The values of λ_{min} and λ_{min} are unknown for PS/d-PMMA but are estimated. Assuming the smallest roughness measurement taken is $\lambda_{\text{min}} = 5$Å and the largest thickness of the PS layer is $\lambda_{\text{max}} = 2000$Å. The contribution of capillary waves is therefore predicted to be 19Å.

The neutron reflectometer can record the scattering length density (SLD) of the sample, which quantifies the ability of the sample to scatter the neutrons. Figure 6.10 is a result from a PS-dPMMA-PS trilayer and it shows how SLD can change with distance, which is the penetration depth into the

trilayer. The silicon oxide layer can be seen in this data as a sharp peak to 3.47×10^{-6}Å^{-2} at approximately 3500Å before the SLD decreases to the value for silicon, 2.08×10^{-6}Å^{-2}. As the annealing time for the film is increased, the SLD of the central layer decreases and the boundaries become less defined.

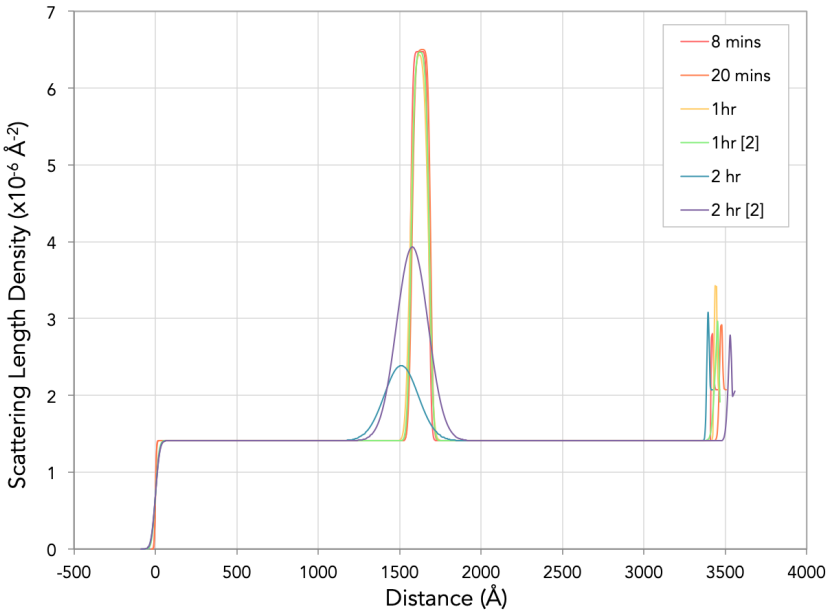

Figure 6.10: The measured SLD as a function of penetration depth into a PS-dPMMA-PS trilayer with a central layer thickness of 120Å [2], sample 3.

The results in figure 6.10 can be used to directly measure the interfacial width for the layers in each sample after every annealing time. This was done for the all the films and the interfacial width as a function of annealing time is given in figure 6.11.

In the example shown in figure 6.10, both of the data sets taken when the film had been annealed for two hours have interfacial widths so broad that the central film is no longer at its predicted SLD, as is indicated by their broad full width at half maximum (FWHM). From the increased roughness, interfacial width value and the knowledge that PS and PMMA are still immiscible, the decrease in SLD is a result of the central layer roughening and disrupting to the extent that the capillary waves induced by annealing eventually caused the layer to disrupt and separate into discrete regions and the foundation and surface polymer are able to interact and merge.

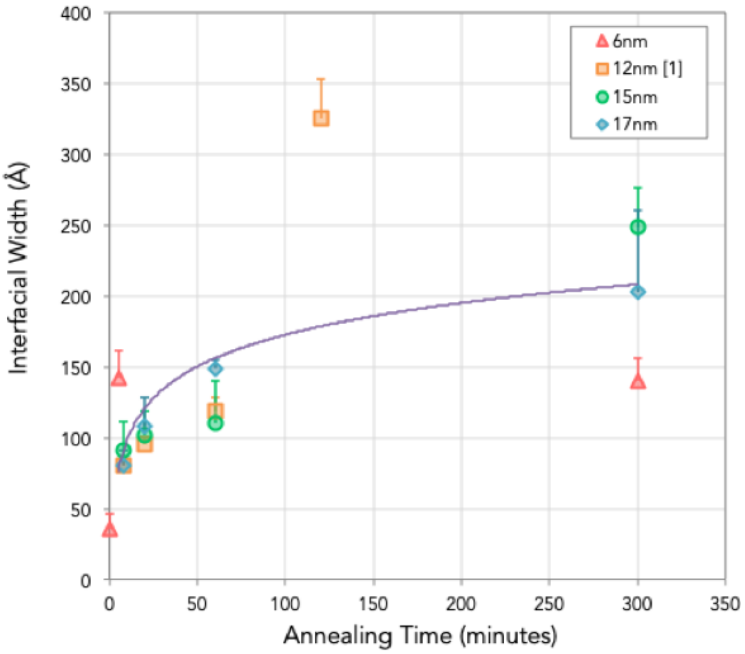

Figure 6.11: The interfacial widths as a function of annealing time. The errors are both positive and negative, but negative error bars are not included for clarity. The purple line is the best fit of w for the data and similar relationships have been seen by Sferrazza et al [182].

The aim of this project was to successfully detect a fully disrupted central layer in a polymer trilayer. This has been successfully accomplished by increasing the annealing time for a structure with a thin central layer, indicating the dependence of this affect on thermally induced capillary waves.

As this was a collaborative project, it is stated here for clarity that the author of this thesis made the following contributions:

- Made the PS/d-PMMA/PS trilayers.
- Annealed the samples at both sites.
- Loaded the samples into the neutron beam at both sites.
- Controlled the neutron reflectivity software at RAL.
- Fitted the models to the data using IGOR Motofit.
- Completed the interpretation of results presented in this thesis.

7 Closing Remarks

The results presented in this thesis show that polymer film drying time is susceptible to not only angular velocity, but is concentration and radial dependent. At regions further away from the centre of a low concentration film, there is a non-monotonic drying order. It has been shown quite clearly in section 4.4.1 that film formation is cannot be assumed constant with radius, especially for low concentration films.

The RBD model has been tested and has been proved to be insufficient in describing the thinning rate across the radius of a polymer spin coating due to this radially changing drying time. By fitting the model in section 4.4.2, and coupled with the results in section 4.4.1, it is evident that the evaporation rate of the solvent changes with radius. Solvent evaporation rate is not modelled to vary with radius by any theoretical models to date, which is something to consider. The film morphology data tenuously supports these conclusions. Larger phase separated structures were observed at larger radii in most of the phase separating films which look similar to Benard cells, which are a result of convection.

This thesis proposes that a polymer spin coating undergoes the following process:

The solution is deposited onto the stationary substrate and then the spin is initiated. As has been corroborated numerous times, the inertial forces cause the majority of thinning in the first few milliseconds. These inertial forces affect the different regions of the film to a varying degree, establishing radial regimes proposed by Bornside et al [7]. At the centre of the film, flow is laminar and moves towards the 'ring' resulting in a thinner centre. At the 'ring', material is subject to temperature gradient [172] which induces three-dimensional flow in the form of the Marangoni effect and Ekman spirals. This three-dimensional flow increases the evaporation rate away from the centre of the film. At the edge of the film, the convectional flow is at a maximum and material is lost from the edge of the film. Films with a low viscosity are more susceptible to these radial effects.

When these radial regimes have been established, the evaporation of the solvent becomes significant and dominates the thinning. It is at this point that the 'toluene flash' recorded by Birnie et al [168,169] can be observed. It is after this point, evaporation rate cannot be assumed constant with radius.

The experimental results presented in chapter 6 show that by increasing an-

nealing time, the interfacial widths in a multi-layered system are broadened by thermally induced capillary waves, which have the potential to fully disrupt a polymer layer. Such a disruption has been shown by multiple datasets due to large interfacial widths causing a drastic change in SLD for a region of trilayer where a layer was once detected. The annealing time required for full disruption increases with layer thickness: 150Å layers did not rupture even after 8 hours of annealing.

8 Future Work

8.1 Instrument Science

It was possible to obtain good data with the optospinometer but with time, failures were increasingly occurring. The end of this project is an ideal time to consider ways of modernising and perhaps overhauling the equipment, which is now approximately 15 years old.

It is my strong recommendation that before the optospinometer is used again, a PhD candidate with a background in software engineering or instrument science works with National Instruments and the workshop here at the University of Sheffield to update both the software and hardware. The optospinometer has a great amount of potential for numerous applications within the department and wider university community and this should be taken advantage of.

8.2 Theoretical Polymer Physics

The RBD model does not fully account for the film formation at different radii. Using fluid dynamics and modifying the techniques used by Reisfeld, Bonner and Peck, the model could be extended to consider radial variation and the imbalance between inertial and evaporative thinning. RBD ignore this by removing $\frac{\partial r}{\partial t}$ and $\frac{dr}{dt}$ terms. The results presented in this thesis show that evaporation rate is not constant with radius and any future model should take this into consideration. Furthermore, any future derivation should consider the flow regimes discussed by Bornside et al, the temperature gradient suggested by Munekata et al and the experimental results this thesis presents.

8.3 Experimental Polymer Physics

There are a number of avenues that can be explored experimentally after the consideration of these results. Repeating the experiments with 6% and 8% concentration blends of PS:PMMA in ratios of 1:3 and 3:1 would be the natural continuation of this work. How the relationships seen in the equal ratio blends of concentrations 2%, 4%, 6% and 8% are affected by a shift in the polymer ratio, and in regards to one another, gives the potential for seeing different morphological patterns emerge. In the equal blended films

at higher concentrations, certain conditions resulted in the phase separation becoming noticeable in the off-specular images.

If the concentration of a polymer blend is increased, the phase separation should be observable in resultant off-specular data. Polymer blend concentrations of 10%, 12% and 14% cast when the optospinometer is targeted at numerous radii could give a deeper insight into how phase separation varies with radius. The small differences seen at 6% and 8% could become more noticeable when the concentration is increased.

The region of the film surrounding 4mm and 8mm proved the most interesting. Targeting the laser at a greater number of radii of the film, such as in increments of 2mm or 3mm, would give a more precise indication of what is occurring at this region of the film. An extension of this radial investigation would be using the full-sized silicon wafers that are circular and 10cm in diameter and extending the radial investigation to as many radii as possible. Is the 'ring' a noticeably affected part of the film due to this region being in the radial half point to the edge? Increasing the radius further was not viable during the experiments undertaken for this thesis due to the high fail rate of the optospinometer but it is worth consideration. Measuring the eccentricity of separated domains as a function of radius for higher concentrated films would also be an interesting experimental result.

9 Terms

Latin Symbols

a monomer size

a_{dis} capillary dispersive length

a_{s} sphere size

b_n constant

c concentration

c_* overlap concentration

d depth

d_{tape} tape width

e dimensionless evaporation rate

f force

g gravitational constant

g_n gradient

h film thickness

h_0 initial film thickness

h_{c} critical film thickness

h_{f} final film thickness

h^* dimensionless film thickness

Δh thickness difference

i lattice position

j mass transfer coefficient

k wave vector

k_{B} Boltzmann's constant

k_{H} Huggins coefficient

m peak number

n power index

n_{A} refractive index of polymer A

n_{B} refractive index of polymer B

n_{f} final refractive index

n_{i} initial refractive index

n_{PMMA} refractive index of PMMA

n_{PS} refractive index of PS

n_{S} refractive index of solvent

n_{toluene} refractive index of toluene

$\widetilde{n_1}$ complex refractive index of medium 1

$\widetilde{n_2}$ complex refractive index of medium 2

p pressure

$\vec{p}$ momentum

p_i probability of lattice occupancy

q q-space

q_{f} radial flow per unit length of circumference

$\vec{q}$ momentum transfer in regular space

r radius, the r dimension

r^* critical size

s inter sphere distance

t time

t_0 initial time

t_{c} critical time

t_{d} obscure time

t_{f} spin coating time

t_{total} time for one revolution

u velocity

u_r velocity in the r dimension

u_x displacement in the x dimension

u_z velocity in the z dimension

u_θ velocity in the θ dimension

v excluded volume

v_x velocity in x dimension

w mixture weight fractions

x the x dimension

y the y dimension

z the z dimension

z_n number of nearest neighbours on lattice

A polymer A, surface area

B polymer B

C concentration

D diffusion rate

D_0 diffusion coefficient

D_{solv} solvent diffusivity in air

D_{mu} mutual diffusion

E evaporation rate

E_i incoming light wave

E_{ia} incoming light wave, parallel component

E_{ie} incoming light wave, perpendicular component

E_o outgoing light wave

E_{oa} outgoing light wave, parallel component

E_{oe} outgoing light wave, perpendicular component

F Helmholtz free energy

F_{mix} free energy of Mixing

F_{sep} free energy of Separating

F_{site} free energy per lattice site

ΔF^* free energy needed to reach critical size r^*

ΔF_v free energy per unit volume

G Gibbs free energy

ΔG_{mix} Flory-Huggins free energy

H Bragg thickness

J diffusion flux

K Mark-Houwink parameter

K_0 Ostwald law constant

K_1 imaginary component of refractive index of medium 1

K_2 imaginary component of refractive index of medium 2

L interface length

Ma Marangoni number

M_{w} molecular weight

N degree of polymerisation

N_{A} Avogadro's Number

O momentum

P probability

Q momentum transfer in momentum space

R total film radius

R_{g} radius of gyration

$< R >$ end-to-end polymer distance

`Re` Reynolds Number

S entropy

S_{mix} entropy of mixing

T temperature

T_c critical temperature

T_g glass transition temperature

T_W wetting temperature

$\mathbb{T}$ viscous stress tensor

ΔT temperature difference

U internal energy

U_0 radial velocity scale

U_{mix} internal energy of mixing

V volume

W work done

X solute volume

Y solvent volume

Z^* polymer segregation excess

Greek Symbols

α Mark-Houwink parameter

α_T thermal diffusivity

α_1 substitution V_1/V_0

α_2 substitution V_2/V_0

β incident angle

γ strain

$\dot{\gamma}$ strain rate

δ complex reflectance ratio

ϵ length scale

ϵ_{AA} interaction energy between A and A

ϵ_{BB} interaction energy between B and B

ϵ_{AB} interaction energy between A and B

ζ surface energy

η dynamic viscosity

η_0 initial dynamic viscosity

η_{00} dynamic viscosity with no shear

η_{f} final dynamic viscosity

η_{r} relative viscosity

η_{solv} pure solvent viscosity

η_{sp} specific viscosity

η_{toluene} viscosity of toluene

$[\eta]$ intrinsic viscosity

θ angle, the θ dimension

ι inverse power law index

κ substitution for $\rho\omega^2/3\eta$

λ wavelength

μ chemical potential

$\Delta\mu_\infty$ chemical potential of the bulk

ν kinematic viscosity

ν_0 initial kinematic viscosity

π 3.14159265... etc

ρ density

ρ_{PMMA} density of PMMA

ρ_{PS} density of PS

ρ_{toluene} density of toluene

σ surface tension

τ stress

ϕ volume fraction

ϕ_{pen} penultimate volume fraction

χ interaction parameter

ψ internal angle of refraction

ω angular velocity

Δ Laplacian operator, ellipsometry phase difference

Θ angle

Λ system relaxation time

Ξ square gradient term

Σ sum

Υ Hamaker constant

Ψ ellipsometry amplitude component

Ω rotation rate

Chemicals

PB poly(butadiene)

PCDTBT poly[N-9'-heptadecanyl-2,7-carbazole-alt-5,5-(4',7'-di-2-thienyl-2',1',3'-benzothiadiazole)]

PEDOT:PSS poly(3,4-ethylenedioxythiophene) polystyrene sulfonate

PEMA poly(ethyl methacrylate)

PEP poly(ethyl propylene)

PI poly(isoprene)

PMMA poly(methyl methacrylate)

PS polystyrene

THF tetrahydrofuran

MEK methyl ethyl ketone

Vectors

$\overrightarrow{f_{\mathrm{I}}}$ centripetal force vector

$\overrightarrow{f_{\mathrm{V}}}$ viscous force vector

$\overrightarrow{g}$ gravitational vector

$\overrightarrow{n}$ outward normal vector

$\overrightarrow{r}$ radial velocity vector

$\overrightarrow{r_{\mathrm{i}}}$ vector from 0 to initial monomer

$\overrightarrow{r_{\mathrm{j}}}$ vector from 0 to final monomer

$\overrightarrow{t}$ tangent normal vector

$\overrightarrow{u}$ velocity vector

$\overrightarrow{u}$ fluid velocity vector

$\overrightarrow{\omega}$ angular velocity vector

10 List of Figures

11 References

[1] F. C. Krebs, "Fabrication and processing of polymer solar cells: A review of printing and coating techniques," *Solar Energy Materials and Solar Cells*, vol. 93, pp. 394–412, 2009.

[2] V. Pensabene, L. Costa, A. Y. Terekhov, J. S. Gnecco, J. P. Wikswo, and W. H. Hofmeister, "Ultrathin Polymer Membranes with Patterned, Micrometric Pores for Organs-on-Chips," *ACS Applied Materials and Interfaces*, vol. 8, no. 34, pp. 22629–22636, 2016.

[3] J. Park, V. A. Dao, S. Kim, D. P. Pham, S. Kim, A. Huy, and T. Le, "High Efficiency Inorganic / Inorganic Amorphous Silicon / Heterojunction Silicon Tandem Solar Cells," *Scientific Reports*, no. June, pp. 1–11, 2018.

[4] M. Wong-Stringer, J. E. Bishop, J. A. Smith, D. K. Mohamad, A. J. Parnell, V. Kumar, and D. G. Lidzey, "Efficient perovskite photovoltaic devices using chemically doped PCDTBT as a hole-transport material," *Journal of Materials Chemistry*, vol. 5, pp. 15714–15723, 2017.

[5] L. Wengeler, M. Schmitt, K. Peters, P. Scharfer, and W. Schabel, "Chemical Engineering and Processing : Process Intensification Comparison of large scale coating techniques for organic and hybrid films in polymer based solar cells," *Chemical Engineering & Processing: Process Intensification*, vol. 68, pp. 38–44, 2013.

[6] D. B. Mitzi, *Solution Processing of Inorganic Materials*. New Jersey, USA: John Wiley & Sons, Inc., first ed., 2009.

[7] D. E. Bornside, C. W. Macosko, and L. E. Scriven, "Spin coating: One-dimensional model," *Journal of Applied Physics*, vol. 66, no. 11, pp. 5185–5193, 1989.

[8] D. B. Hall, P. Underhill, and J. M. Torkelson, "Spin Coating of Thin and Ultrathin Polymer Films," *Polymer Engineering and Science*, vol. 38, no. 12, pp. 2039–2045, 1998.

[9] J. A. Reinspach, Y. Diao, G. Giri, T. Sachse, K. England, Y. Zhou, C. Tassone, B. J. Worfolk, M. Presselt, M. F. Toney, S. Mannsfeld, and Z. Bao, "Tuning the Morphology of Solution-Sheared P3HT:PCBM Films," *ACS Applied Materials and Interfaces*, vol. 8, no. 3, pp. 1742–1751, 2016.

[10] B. K. Daniels, C. R. Szmanda, M. K. Templeton, and P. Trefonas III, "Surface Tension Effects In Microlithography - Striations," *1986 Microlithography Conferences*, no. July 1986, pp. 192–201, 1986.

[11] H. Kozuka, Y. Ishikawa, and N. Ashibe, "Radiative striations of spin-coating films: Surface roughness measurement and in-situ observation," *Journal of Sol-Gel Science and Technology*, vol. 31, no. 1-3 SPEC.ISS., pp. 245–248, 2004.

[12] D. E. Haas and D. P. Birnie III, "Real-time monitoring of striation development during spin-on-glass deposition," *SPIE Proceedings, Sol-Gel Optics*, no. May, pp. 1–6, 2000.

[13] D. E. Haas and D. P. Birnie III, "Nondestructive measurement of striation defect spacing using laser diffraction," *Journal of Materials Research*, vol. 16, no. 12, pp. 3355–3360, 2001.

[14] D. E. Haas, D. P. Birnie III, M. J. Zecchino, and J. T. Figueroa, "The effect of radial position and spin speed on striation spacing in spin on glass coatings," *Journal of Materials Science Letters*, vol. 20, no. 19, pp. 1763–1766, 2001.

[15] D. E. Haas and D. P. Birnie III, "Evaluation of thermocapillary driving forces in the development of striations during the spin coating process," *Journal of Materials Science*, vol. 37, pp. 2109–2116, 2002.

[16] P. D. Fowler, C. Ruscher, J. D. McGraw, J. A. Forrest, and K. Dalnoki-Veress, "Controlling Marangoni-induced instabilities in spin-cast polymer films: How to prepare uniform films," *European Physical Journal E*, vol. 39, no. 9, 2016.

[17] S. Walheim, M. Böltau, J. Mlynek, G. Krausch, and U. Steiner, "Structure Formation via Polymer Demixing in Spin-Cast Films," *Macromolecules*, vol. 30, no. 96, pp. 4995–5003, 1997.

[18] A. G. Emslie, F. T. Bonner, and L. G. Peck, "Flow of a viscous liquid on a rotating disk," *Journal of Applied Physics*, vol. 29, no. 1958, pp. 858–862, 1958.

[19] D. Meyerhofer, "Characteristics of resist films produced by spinning," *Journal of Applied Physics*, vol. 49, no. 1978, pp. 3993–3997, 1978.

[20] B. Reisfeld, S. G. Bankoff, and S. H. Davis, "The dynamics and stability of thin liquid films during spin coating. I. Films with con-

stant rates of evaporation or absorption," *Journal of Applied Physics*, vol. 70, no. 1991, pp. 5258–5266, 1991.

[21] P. Mokarian-Tabari, M. Geoghegan, J. R. Howse, S. Y. Heriot, R. L. Thompson, and R. A. L. Jones, "Quantitative evaluation of evaporation rate during spin-coating of polymer blend films: Control of film structure through defined-atmosphere solvent-casting," *European Physical Journal E*, vol. 33, pp. 283–289, 2010.

[22] S. A. Jenekhe, "Effects of Solvent Mass Transfer on Flow of Polymer Solutions on a Flat Rotating Disk," *Industrial and Engineering Chemistry Fundamentals*, vol. 23, no. 4, pp. 425–432, 1984.

[23] Y. Mouhamad, *Dynamics and phase separation during spin casting of polymer film*. PhD thesis, The University of Sheffield, 2014.

[24] E. Stephens, I. L. Ross, J. H. Mussgnug, L. D. Wagner, M. A. Borowitzka, C. Posten, O. Kruse, and B. Hankamer, "Future prospects of microalgal biofuel production systems," *Trends in Plant Science*, vol. 15, no. 10, pp. 554–564, 2010.

[25] S. Solomon, G.-k. Plattner, R. Knutti, and P. Friedlingstein, "Irreversible climate change due to carbon dioxide emissions," *PNAS*, vol. 106, no. 6, pp. 1704–1709, 2009.

[26] B. Burger, K. Kiefer, C. Kost, S. Nold, S. Philipps, R. Preu, J. Rentsch, T. Schlegl, G. Stryi-Hipp, G. Willeke, H. Wirth, and W. Werner, "Photovoltaics report," in *Photovoltaics Report*, no. August, p. 5, Fraunhofer ISE, 2018.

[27] B. T. Ellison and I. Cornet, "Mass Transfer to a Rotating Disk," *Journal of The Electrochemical Society*, vol. 118, no. 1, pp. 68–72, 1971.

[28] B. D. Washo, "Rheology and Modeling of the Spin Coating Process," *IBM Journal of Research and Development*, vol. 21, no. 2, pp. 190–198, 1977.

[29] M. H. Clarkson, S. C. Chin, and P. Shacter, "Flow visualization of inflexional instabilities on a rotating disk," *AIAA Paper*, vol. 18, no. 12, pp. 1541–1543, 1980.

[30] W. J. Daughton and F. L. Givens, "An Investigation of the Thickness Variation of Spun-on Thin Films Commonly Associated with the Semiconductor Industry," *Journal of The Electrochemical Society*, vol. 129, no. 1, p. 173, 1982.

[31] W. W. Flack, D. S. Soong, A. T. Bell, and D. W. Hess, "A mathematical model for spin coating of polymer resists," *Journal of Applied Physics*, vol. 56, no. 4, pp. 1199–1206, 1984.

[32] S. A. Jenekhe and S. B. Scheldt, "Coating Flow of Non-Newtonian Fluids on a Flat Rotating Disk," *Industrial and Engineering Chemistry Fundamentals*, vol. 23, no. 4, pp. 432–436, 1984.

[33] M. R. Malik, "The neutral curve for stationary disturbances in rotating-disk flow," *Journal of Fluid Mechanics*, vol. 164, pp. 275–287, 1986.

[34] S. Middleman, "The effect of induced airflow on the spin coating of viscous liquids," *Journal of Applied Physics*, vol. 62, no. 6, pp. 2530–2532, 1987.

[35] C. J. Lawrence, "The Mechanics of Spin Coating of Polymer-Films," *Physics of Fluids*, vol. 31, no. 10, pp. 2786–2795, 1988.

[36] T. J. Rehg and B. G. Higgins, "The effects of inertia and interfacial shear on film flow on a rotating disk," *Physics of Fluids*, vol. 31, no. 6, p. 1360, 1988.

[37] J. H. Hwang and F. Ma, "On the flow of a thin liquid film over a rough rotating disk," *Journal of Applied Physics*, vol. 66, no. 1, pp. 388–394, 1989.

[38] T. Ohara, Y. Matsumoto, and O. Hideo, "The film formation dynamics in spin coating," *Physics of Fluids A*, vol. 1, no. 12, pp. 1949–1959, 1989.

[39] C. J. Lawrence and W. Zhou, "Spin coating of non-Newtonian fluids," *Journal of Non-Newtonian Fluid Mechanics*, vol. 39, pp. 137–187, 1991.

[40] L. M. Peurrung, "Film Thickness Profiles over Topography in Spin Coating," *Journal of The Electrochemical Society*, vol. 138, no. 7, pp. 2115–2124, 1991.

[41] R. K. Yonkoski and D. S. Soane, "Model for spin coating in microelectronic applications," *Journal of Applied Physics*, vol. 72, no. 2, pp. 725–740, 1992.

[42] J. Gu, M. D. Bullwinkel, and G. A. Campbell, "Measurement and modeling of solvent removal for spin coating," *Polymer Engineering and Science*, vol. 36, no. 7, pp. 1019–1026, 1996.

[43] N. Sahu, B. Parija, and S. Panigrahi, "Fundamental understanding and modeling of spin coating process: A review," *Indian Journal of Physics*, vol. 83, no. 4, pp. 493–502, 2009.

[44] A. Münch, C. P. Please, and B. Wagner, "Spin coating of an evaporating polymer solution," *Physics of Fluids*, vol. 23, no. 10, 2011.

[45] V. Cregan and S. B. G. O'Brien, "Extended asymptotic solutions to the spin-coating model with small evaporation," *Applied Mathematics and Computation*, vol. 223, pp. 76–87, 2013.

[46] Y. Mouhamad, P. Mokarian-Tabari, N. Clarke, R. A. L. Jones, and M. Geoghegan, "Dynamics of polymer film formation during spin coating," *Journal of Applied Physics*, vol. 116, p. 123513, sep 2014.

[47] S. Karpitschka, C. M. Weber, and H. Riegler, "Spin casting of dilute solutions: Vertical composition profile during hydrodynamic-evaporative film thinning," *Chemical Engineering Science*, vol. 129, pp. 243–248, 2015.

[48] J. J. van Franeker, D. Westhoff, M. Turbiez, M. M. Wienk, V. Schmidt, and R. A. J. Janssen, "Controlling the Dominant Length Scale of Liquid-Liquid Phase Separation in Spin-coated Organic Semiconductor Films," *Advanced Functional Materials*, vol. 25, pp. 855–863, 2015.

[49] J. Danglad-Flores, S. Eickelmann, and H. Riegler, "Deposition of polymer films by spin casting: A quantitative analysis," *Chemical Engineering Science*, vol. 179, pp. 257–264, 2018.

[50] G. R. Brannock and D. R. Paul, "Phase Behavior of Ternary Polymer Blends Composed of Three Misciblebinaries," *Macromolecules*, vol. 23, no. 25, pp. 5240–5250, 1990.

[51] W.-h. Luo and N.-q. Zhou, "Rheology-morphology relationship in polystyrene/poly(methyl methacrylate) blends," *Journal of Central South University*, vol. 15, no. 1, pp. 72–75, 2008.

[52] K. Tanaka, A. Takahara, and T. Kajiyama, "Film Thickness Dependence of the Surface Structure of Immiscible Polystyrene/Poly(methyl methacrylate) Blends," *Macromolecules*, vol. 29, no. 9, pp. 3232–3239, 1996.

[53] G. Krausch, "Surface induced self assembly in thin polymer films," *Materials Science and Engineering: R: Reports*, vol. 14, no. 1, pp. v–94, 1995.

[54] P. W. K. Rothemund, "Folding DNA to create nanoscale shapes and patterns.," *Nature*, vol. 440, no. March, pp. 297–302, 2006.

[55] H. Uchiyama, Y. Mantani, and H. Kozuka, "Spontaneous formation of linearly arranged microcraters on sol-gel-derived silica-poly(vinylpyrrolidone) hybrid films induced by Bénard-Marangoni convection," *Langmuir*, vol. 28, no. 27, pp. 10177–10182, 2012.

[56] H. Uchiyama, Y. Miki, Y. Mantani, and H. Kozuka, "Spontaneous formation of micrometer-scaled cell-like patterns on alkoxide-derived silica gels induced by Benard-Marangoni convections," *Journal of Physical Chemistry C*, vol. 116, no. 1, pp. 939–946, 2012.

[57] K. H. Lee, J. Hong, S. J. Kwak, M. Park, and J. G. Son, "Spin self-assembly of highly ordered multilayers of graphene-oxide sheets for improving oxygen barrier performance of polyolefin films," *Carbon*, vol. 83, pp. 40–47, 2015.

[58] J. Kressler, N. Higashida, K. Shimomai, T. Inoue, and T. Ougizawa, "Temperature Dependence of the Interaction Parameter between Polystyrene and Poly(methyl methacrylate)," *Macromolecules*, vol. 27, no. 9, pp. 2448–2453, 1994.

[59] T. P. Russell, R. P. Hjelm, and P. A. Seeger, "Temperature Dependence of the Interaction Parameter between Polystyrene and Poly(methyl methacrylate)," *Macromolecules*, vol. 23, no. 0, pp. 890–893, 1990.

[60] P. J. Flory and H. Daoust, "Osmotic Pressures of Moderately Concentrated Polymer Solutions," *Journal of Polymer Science*, vol. 25, pp. 429–440, 1957.

[61] B. E. Eichinger and P. J. Flory, "Thermodynamics of polymer solutions. Part 1 - Natural rubber and benzene," *Transactions of the Faraday Society*, vol. 64, pp. 2035–2052, 1968.

[62] B. E. Eichinger and P. J. Flory, "Thermodynamics of polymer solutions Part 3 - Polyisobutylene and Cyclohexan," *Transactions of the Faraday Society*, vol. 64, pp. 2061–2065, 1968.

[63] R. Koningsveld, L. A. Kleintjens, and A. R. Shultz, "Liquid-liquid phase separation in multicomponent polymer solutions. IX. Concentration-dependent pair interaction parameter from critical miscibility data on the system polystyrene-cyclohexane," *Journal of*

Polymer Science Part A-2: Polymer Physics, vol. 8, no. 8, pp. 1261–1278, 1970.

[64] R. Koningsveld and L. A. Kleintjens, "Liquid-Liquid Phase Separation in Multicomponent Polymer Systems. X. Concentration Dependence of the Pair Interaction Parameter in the System Cyclohexane-Polystyrene," *Macromolecules*, vol. 4, no. 5, pp. 637–641, 1971.

[65] I. Noda, Y. Higo, N. Ueno, and T. Fujimoto, "Semidilute Region for Linear Polymers in Good Solvents," *Macromolecules*, vol. 17, no. 5, pp. 1055–1059, 1984.

[66] N. Schuld and B. A. Wolf, "Solvent quality as reflected in concentration and temperature-dependent Flory-Huggins interaction parameters," *Journal of Polymer Science, Part B: Polymer Physics*, vol. 39, no. 6, pp. 651–662, 2001.

[67] B. E. Eichinger and P. J. Flory, "Thermodynamics of Polymer Solutions. Part 2 - Polyisobutylene and Benzene," *Transactions of the Faraday Society*, vol. 64, no. 1, pp. 2053–2060, 1968.

[68] R. D. Newman and J. M. Prausnitz, "Thermodynamics of concentrated polymer solutions containing polyethylene, polyisobutylene, and copolymers of ethylene with vinyl acetate and propylene," *AIChE Journal*, vol. 19, no. 4, pp. 704–710, 1973.

[69] T. G. Fox and H. W. Schnecko, "The effect of temperature, conversion and solvent on the stereospecificity of the free radical polymerization of methyl methacrylate," *Polymer*, vol. 3, pp. 575–584, 1962.

[70] M. Nawaz, M. K. Baloch, and W. Rehman, "Investigating the compatibility of polymers in common solvent," *Journal of the Chilean Chemical Society*, vol. 55, no. 1, pp. 90–93, 2010.

[71] W. W. Y. Lau and R. Y. M. Huang, "Interaction parameters in mixtures of polystyrene-poly(methyl methacrylate)-toluene," *European Polymer Journal*, vol. 23, no. I, pp. 37–39, 1987.

[72] C. B. Walsh and E. I. Franses, "Ultrathin PMMA films spin-coated from toluene solutions," *Thin Solid Films*, vol. 429, no. 1-2, pp. 71–76, 2003.

[73] Y. Yao, J. Hou, Z. Xu, G. Li, and Y. Yang, "Effects of solvent mixtures on the nanoscale phase separation in polymer solar cells," *Advanced Functional Materials*, vol. 18, pp. 1783–1789, 2008.

[74] Y. Li, Y. Yang, F. Yu, and L. Dong, "Surface and interface morphology of polystyrene/ poly(methyl methacrylate) thin-film blends and bilayers," *Journal of Polymer Science, Part B: Polymer Physics*, vol. 44, no. 1, pp. 9–21, 2006.

[75] G. Allen, G. Gee, and J. P. Nicholson, "The Miscibility of Polymers: I. Phase Equilibria in Systems containing two Polymers and a Mutual Solvent," *Polymer*, vol. 1, no. c, pp. 56–62, 1960.

[76] T. H. G. Scholte, "Determination of Thermodynamic Parameters of Polymer-Solvent Systems by Light Scattering," *European Polymer Journal*, vol. 6, pp. 1063–1074, 1970.

[77] V. Narasimhan, R. Y. M. Huang, and C. M. Burns, "Determination Of Polymer-Polymer Interaction Parameters Of Incompatible Monodisperse And Polydisperse Polymers In Solution," *Journal of Polymer Science: Polymer Symposium*, vol. 284, no. 74, pp. 265–284, 1969.

[78] X. Li, Y. Han, and L. An, "Inhibition of thin polystyrene film dewetting via phase separation," *Polymer*, vol. 44, no. 19, pp. 5833–5841, 2003.

[79] R. J. Fort and W. R. Moore, "Viscosities of binary liquid mixtures," *Transactions of the Faraday Society*, vol. 62, pp. 1112–1119, 1966.

[80] C. Aust, M. Kröger, and S. Hess, "Structure and dynamics of dilute polymer solutions under shear flow via nonequilibrium molecular dynamics," *Macromolecules*, vol. 32, no. 17, pp. 5660–5672, 1999.

[81] A. Calleja, S. Ricart, M. Aklalouch, N. Mestres, T. Puig, and X. Obradors, "Thickness-concentration-viscosity relationships in spin-coated metalorganic ceria films containing polyvinylpyrrolidone," *Journal of Sol-Gel Science and Technology*, vol. 72, no. 1, pp. 21–29, 2014.

[82] M. L. Huggins, "The Viscosity of Dilute Solutions of Long-chain Molecules. IV. Dependence on Concentration," *Journal of the American Chemical Society*, vol. 64, no. 11, pp. 2716–2718, 1942.

[83] B. M. Haines and A. L. Mazzucato, "A Proof of Einstein's Effective Viscosity for a Dilute Suspension of Spheres," *SIAM Journal on Mathematical Analysis*, vol. 44, no. 3, pp. 2120–2145, 2012.

[84] J. H. Baxendale, S. Bywater, and M. G. Evans, "Relation between molecular weight and intrinsic viscosity for polymethyl methacrylate," *Journal of Polymer Science*, vol. 1, no. 4, pp. 237–244, 1946.

[85] J. G. Kirkwood and J. Riseman, "The Intrinsic Viscosities and Diffusion Constants of Flexible Macromolecules in Solution," *The Journal of Chemical Physics*, vol. 16, no. 6, pp. 565–573, 1948.

[86] S. N. Chinai, J. D. Matlack, and A. L. Resnick, "Polymethyl Methacrylate : Dilute Solution Properties by Viscosity and Light Scattering," *Science*, vol. XVII, pp. 391–401, 1955.

[87] S. Krause, "Dilute Solution Properties of Tactic Poly-methyl Methacrylates I-Intrinsic Viscosities of Isotactic Fractions," *Polymer*, vol. 3, pp. 565–573, 1961.

[88] E. Casassa and W. Stockmayer, "Thermodynamic properties of dilute solutions of polymethyl methacrylate in butanone and in nitroethane," *Polymer*, vol. 3, pp. 53–69, 1962.

[89] E. Cohn-Ginsberg, T. G. Fox, J. B. Kinsinger, H. F. Mason, and E. M. Schuele, "Properties of dilute polymer solutions IILight scattering and viscometric properties of solutions of conventional polymethyl methacrylate," *Polymer*, vol. 3, no. 1, pp. 71–95, 1962.

[90] R. Moore and R. J. Fort, "Viscosities of Dilute Solutions of PMMA," *Journal of Polymer Science: Part A*, vol. 1, pp. 929–942, 1963.

[91] I. Kössler, M. Netopilik, G. Schulz, and R. Gnauck, "The Mark-Houwink Constants for Poly (Methyl Methacrylate)," *Polymer Bulletin*, vol. 598, pp. 597–598, 1982.

[92] H. L. Wagner, "The Mark-Houwink-Sakurada Equation for the Viscosity of Linear Polyethylene," *Journal of Physical and Chemical Reference Data*, vol. 14, no. 2, pp. 611–617, 1985.

[93] H. L. Wagner, "The Mark-Houwink-Sakurada Relation for Poly(Methyl Methacrylate)," *Journal of Physical and Chemical Reference Data*, vol. 16, no. 2, pp. 165–173, 1987.

[94] Y. Song, P. M. Mathias, D. Tremblay, and C.-c. Chen, "Liquid Viscosity Model for Polymer Solutions and Mixtures," *Industrial and Engineering Chemistry Research*, vol. 42, pp. 2415–2422, 2003.

[95] R. Dell'erba, "Measurement of the Mark-Houwink constant of ultra high molecular mass poly(methyl methacrylate) in toluene," *Journal of Materials Science Letters*, vol. 20, pp. 371–373, 2001.

[96] T. G. Fox, J. B. Kinsinger, H. F. Mason, and E. M. Schuele, "Properties of dilute polymer solutions IILight scattering and viscometric properties of solutions of conventional polymethyl methacrylate," *Polymer*, vol. 3, no. 1, pp. 71–95, 1962.

[97] T. G. Fox, "Properties of dilute polymer solutions IIIIntrinsic viscosity/temperature relationships for conventional polymethyl methacrylate," *Polymer*, vol. 3, pp. 111–128, 1962.

[98] M. Bouldin, W. M. Kulicke, and H. Kehler, "Prediction of the non-Newtonian viscosity and shear stability of polymer solutions," *Colloid & Polymer Science*, vol. 266, no. 9, pp. 793–805, 1988.

[99] P. J. Carreau, "Rheological Equations from Molecular Network Theories," *Transactions of the Society of Rheology*, vol. 16, no. 1, pp. 99–127, 1972.

[100] M. Clausi, M. G. Santonicola, and S. Laurenzi, "Fabrication of carbon-based nanocomposite films by spin-coating process: An experimental and modeling study of the film thickness," *Composites Part A: Applied Science and Manufacturing*, vol. 88, pp. 86–97, 2016.

[101] V. N. Tsvetkov and S. I. Klekin, "A Study of Diffusion in Polymer Solutions by the Use of the Polarization Interferometer," *Journal of Polymer Science*, vol. 30, no. 121, pp. 187–200, 1958.

[102] A. Acrivos, M. J. Shah, and E. E. Petersen, "Momentum and heat transfer in laminar boundary layer flows of non-Newtonian fluids past external surfaces," *AIChE Journal*, vol. 6, no. 2, pp. 312–317, 1960.

[103] W. Ostwald, "Ueber die rechnerische Darstellung des Strukturgebietes der Viskosit??t," *Kolloid-Zeitschrift*, vol. 47, no. 2, pp. 176–187, 1929.

[104] A. Onuki, "Domain growth and rheology in phase-separating binary mixtures with viscosity difference," *Europhysics Letters (EPL)*, vol. 28, no. 3, pp. 175–179, 1994.

[105] S. R. Vashishtha, N. Chand, and S. A. R. Hashmi, "Morphology of PS/PMMA blends and their solution rheology," *Indian Journal of Chemical Technology*, vol. 9, no. 4, pp. 316–323, 2002.

[106] V. E. Dreval', A. A. Tager, E. I. Sycheva, and Z. P. Vzvadskaya, "Effect of the molecular weight of polystyrene on the viscosity of concentrated solutions," *Polymer Mechanics*, vol. 6, no. 5, pp. 795–800, 1973.

[107] B. I. Fedorov, G. Z. Plavnik, I. V. Prokhorov, and G. Zhukhovitskii, L, "Transitional Flow Conditions on a Rotating Disk," *Journal of Engineering Physics*, vol. 31, pp. 1448–1453, 1976.

[108] R. Kobayashi, Y. Kohama, and C. Takamadate, "Spiral vortices in boundary layer transition regime on a rotating disk," *Acta Mechanica*, vol. 35, no. 1-2, pp. 71–82, 1980.

[109] Y. Kohama, "Study on boundary layer transition of a rotating disk," *Acta Mechanica*, vol. 199, pp. 193–199, 1984.

[110] X. Rui, Z. Song, S. Jing, and T. Decheng, "Phase Separation and Dewetting Induced Surface Pattern in PS/PMMA Blend Films," *Polymer Journal*, vol. 37, no. 8, pp. 560–564, 2005.

[111] M. Böltau, S. Walheim, S. Mlynek, G. Krausch, and U. Steiner, "Surface-Induced Structure Formation of Polymer Blends on Patterned Substrates," *Nature*, vol. 391, no. October 1997, pp. 877–879, 1998.

[112] L. Makkonen, "Young's equation revisited," *Journal of Physics Condensed Matter*, vol. 28, no. 13, 2016.

[113] J. Thomson, "XLII. On certain curious motions observable at the surfaces of wine and other alcoholic liquors," *Philosophical Magazine*, vol. 10, pp. 330–333, 1855.

[114] C. Marangoni, "1. Ueber die Ausbreitung der Tropfen einer Flussigkeit auf der Oberflache einer anderen," *Annalen der Physik*, pp. 337–354, 1871.

[115] J. E. Wesfreid, *2 Scientific Biography of Henri Bernard (1874 - 1939).* 2006.

[116] L. Rayleigh, "59. On convection currents in a horizontal layer of fluid, when the higher temperature is on the under side," *Philosophical Magazine Series 6*, vol. 32, no. 192, pp. 529–546, 1916.

[117] J. R. A. Pearson, "On convection cells induced by surface tension," *Journal of Fluid Mechanics*, vol. 4, no. 5, pp. 489–500, 1958.

[118] M. K. Smith and S. H. Davis, "Instabilities of dynamic thermocapillary liquid layers. Part 2. Surface-wave instabilities," *Journal of Fluid Mechanics*, vol. 132, pp. 145–162, 1983.

[119] M. K. Smith and S. H. Davis, "Instabilities of dynamic thermocapillary liquid layer. Part 1. Convective instabilities," *Journal of Fluid Mechanics*, vol. 132, pp. 119–144, 1983.

[120] A. Zebib, G. M. Homsy, and E. Meiburg, "High Marangoni number convection in a square cavity," *Physics of Fluids*, vol. 28, no. 12, pp. 3467–3476, 1985.

[121] D. P. Birnie III and M. Manley, "Combined flow and evaporation of fluid on a spinning disk," *Physics of Fluids*, vol. 9, no. 4, pp. 870–875, 1997.

[122] M. Geoghegan, "Wetting at polymer surfaces and interfaces," *Progress in Polymer Science*, vol. 28, pp. 261–302, 2003.

[123] S.-C. Luo, V. Craciun, and E. P. Douglas, "Instabilities during the formation of electroactive polymer thin films," *Langmuir*, vol. 21, no. 7, pp. 2881–2886, 2005.

[124] G. A. Buxton and N. Clarke, "Ordering polymer blend morphologies via solvent evaporation," *Europhysics Letters (EPL)*, vol. 78, no. 5, p. 56006, 2007.

[125] S. Ebbens, R. Hodgkinson, A. J. Parnell, A. D. F. Dunbar, S. J. Martin, P. D. Topham, N. Clarke, and J. R. Howse, "In situ imaging and height reconstruction of phase separation processes in polymer blends during spin coating," *ACS Nano*, vol. 5, no. 6, pp. 5124–5131, 2011.

[126] N. J. Cira, A. Benusiglio, and M. Prakash, "Vapour-mediated sensing and motility in two-component droplets," *Nature*, vol. 519, pp. 446–450, 2015.

[127] D. T. W. Toolan, A. Isakova, R. Hodgkinson, N. Reeves-Mclaren, O. S. Hammond, K. J. Edler, W. H. Briscoe, T. Arnold, T. Gough, P. D. Topham, and J. R. Howse, "Insights into the influence of solvent polarity on the crystallization of poly(ethylene oxide) spin-coated thin films via in situ grazing incidence wide-angle X-ray scattering," *Macromolecules*, vol. 49, no. 12, pp. 4579–4586, 2016.

[128] D. P. Birnie III, "Rational solvent selection strategies to combat striation formation during spin coating of thin films," *Journal of Materials Research*, vol. 16, pp. 1145–1154, 2001.

[129] A. Vidal and A. Acrivos, "Effect of nonlinear temperature profiles on the onset of convection driven by surface tension gradients," *Industrial and Engineering Chemistry Fundamentals*, vol. 7, no. 1, pp. 53–58, 1968.

[130] D. P. Birnie III, "A model for drying control cosolvent selection for spin-coating uniformity: The thin film," *Langmuir*, vol. 29, pp. 9072–9078, 2013.

[131] D. Schwabe and A. Scharmann, "Some evidence for the existence and magnitude of a critical marangoni number for the onset of oscillatory flow in crystal growth melts," *Journal of Crystal Growth*, vol. 46, pp. 125–131, 1979.

[132] H. Uchiyama, W. Namba, and H. Kozuka, "Spontaneous formation of linear striations and cell-like patterns on dip-coating titania films prepared from alkoxide solutions," *Langmuir*, vol. 26, no. 13, pp. 11479–11484, 2010.

[133] F. Bruder and R. Brenn, "Spinodal decomposition in thin films of a polymer blend," *Physical Review Letters*, vol. 69, no. 4, pp. 624–627, 1992.

[134] S. Reich and Y. Cohen, "Phase separation of polymer blends in thin films," *Journal of Polymer Science: Polymer Physics Edition*, vol. 19, no. 8, pp. 1255–1267, 1981.

[135] R. A. L. Jones, E. J. Kramer, M. H. Rafailovich, J. Sokolov, and S. A. Schwarz, "Surface enrichment in an isotopic polymer blend," *Physical Review Letters*, vol. 62, no. 3, pp. 280–283, 1989.

[136] J. W. Cahn and J. E. Hilliard, "Free energy of a nonuniform system. I. Interfacial free energy," *Journal of Chemical Physics*, vol. 28, no. 1958, p. 258, 1958.

[137] S. Puri and K. Binder, "Surface-directed spinodal decomposition: Phenomenology and numerical results," *Physical Review A*, vol. 46, no. 8, pp. 4487–4489, 1992.

[138] A. D. F. Dunbar, P. Mokarian-Tabari, A. J. Parnell, S. J. Martin, M. W. A. Skoda, and R. A. L. Jones, "A solution concentration dependent transition from self-stratification to lateral phase separation

in spin-cast PS:d-PMMA thin films," *European Physical Journal E*, vol. 31, no. 4, pp. 369–375, 2010.

[139] K. Dalnoki-Veress, J. A. Forrest, J. R. Stevens, and J. R. Dutcher, "Phase separation morphology of spin-coated polymer blend thin films," *Physica A*, vol. 239, pp. 87–94, 1997.

[140] R. C. Ball and R. L. H. Essery, "Spinodal decomposition and pattern formation near surfaces," *Journal of Physics: Condensed Matter*, vol. 2, pp. 10303–10320, 1990.

[141] P. Lambooy, K. C. Phelan, O. Haugg, and G. Krausch, "Dewetting at the liquid-liquid interface," *Physical Review Letters*, vol. 76, no. 7, pp. 1110–1113, 1996.

[142] C. Wang, G. Krausch, and M. Geoghegan, "Dewetting at a Polymer - Polymer Interface : Film Thickness Dependence," *Langmuir*, vol. 17, no. 20, pp. 6269–6274, 2001.

[143] N. Clarke, "Instabilities in thin-film binary mixtures," *European Physical Journal E*, vol. 14, no. 3, pp. 207–210, 2004.

[144] N. Clarke, "Toward a model for pattern formation in ultrathin-film binary mixtures," *Macromolecules*, vol. 38, no. 16, pp. 6775–6778, 2005.

[145] S. Coveney and N. Clarke, "Breakup of a transient wetting layer in polymer blend thin films: Unification with 1D phase equilibria," *Physical Review Letters*, vol. 111, no. 12, pp. 1–5, 2013.

[146] S. Y. Heriot and R. A. L. Jones, "An interfacial instability in a transient wetting layer leads to lateral phase separation in thin spin-cast polymer-blend films.," *Nature Materials*, vol. 4, no. October, pp. 782–786, 2005.

[147] M. Souche and N. Clarke, "Interfacial instability in bilayer films due to solvent evaporation," *European Physical Journal E*, vol. 28, no. 1, pp. 47–55, 2009.

[148] M. Habibi, A. Rahimzadeh, and M. Eslamian, "On dewetting of thin films due to crystallization (crystallization dewetting)," *European Physical Journal E*, vol. 39, no. 3, 2016.

[149] M. Souche and N. Clarke, "Phase equilibria in polymer blend thin films: A Hamiltonian approach," *Journal of Chemical Physics*, vol. 131, no. 24, 2009.

[150] M. Souche and N. Clarke, "Equilibrium phases for thin films of polymer blend solutions," *Macromolecules*, vol. 43, no. 12, pp. 5433–5441, 2010.

[151] P. C. Sukanek, "Dependence of Film Thickness on Speed in Spin Coating," *Journal of The Electrochemical Society*, vol. 138, no. 6, pp. 1712–1719, 1991.

[152] D. E. Bornside, R. A. Brown, P. W. Ackmann, J. R. Frank, A. A. Tryba, and F. T. Geyling, "The effects of gas phase convection on mass transfer in spin coating," *Applied Physics*, vol. 73, no. 2, pp. 585–600, 1993.

[153] T. V. Kármán, "On the mechanism of the drag a moving body experiences in a fluid," *Progress in Aerospace Sciences*, vol. 59, pp. 16–19, 2013.

[154] B. Y. N. Gregory, J. T. Stuart, and W. S. Walker, "On the Stability of Three-Dimensional Boundary Layers with Application to the Flow Due to a Rotating Disk Author (s): N . Gregory , J . T . Stuart and W . S . Walker Source : Philosophical Transactions of the Royal Society of London . Series A , Mathema," *Mathematical and Physical Sciences*, vol. 248, no. 943, pp. 155–199, 1955.

[155] A. Öztekin, D. E. Bornside, R. A. Brown, and P. K. Seidel, "The connection between hydrodynamic stability of gas flow in spin coating and coated film uniformity," *Journal of Applied Physics*, vol. 77, no. 6, pp. 2297–2308, 1995.

[156] A. Acrivos, J. J. Shah, and E. E. Petersen, "On the flow of a non-Newtonian liquid on a rotating disk," *J. Appl. Phys.1*, vol. 31, no. (6), pp. 963–968, 1960.

[157] X. M. Du, X. Orignac, and R. M. Almeida, "Striation-Free, Spin-Coated Sol-Gel Optical Films," *Journal of the American Ceramic Society*, vol. 78, no. 8, pp. 2254–2256, 1995.

[158] Y. Haruvy, A. Heller, and S. E. Webber, "Supported sol-gel thin-film glasses embodying laser dyes. II: Three-layered waveguide assemblies," *Proceedings of SPIE - The International Society for Optical Engineering*, vol. 1590, no. Submol. Glass Chem. Phys., pp. 59–70, 1991.

[159] I. Martín-Fabiani, E. Rebollar, M. C. García-Gutiérrez, D. R. Rueda, M. Castillejo, and T. A. Ezquerra, "Mapping the structural order

of laser-induced periodic surface structures in thin polymer films by microfocus beam grazing incidence small-angle x-ray scattering," *ACS Applied Materials and Interfaces*, vol. 7, no. 5, pp. 3162–3169, 2015.

[160] E. Rebollar, D. R. Rueda, I. Martín-Fabiani, M. C. García-Gutiérrez, G. Portale, M. Castillejo, and T. A. Ezquerra, "In situ monitoring of laser-induced periodic surface structures formation on polymer films by grazing incidence small-angle X-ray scattering," *Langmuir*, vol. 31, no. 13, pp. 3973–3981, 2015.

[161] F. Horowitz, E. Yeatman, E. Dawnay, and A. Fardad, "Real-time optical monitoring of spin coating," *Journal de Physique III*, vol. 3, no. 11, pp. 2059–2063, 1993.

[162] P. C. Jukes, S. Y. Heriot, J. S. Sharp, and R. A. L. Jones, "Time-Resolved Light Scattering Studies of Phase Separation in Thin Film Semiconducting Polymer Blends during Spin-Coating," *Macromolecules*, vol. 38, pp. 2030–2032, 2005.

[163] D. T. W. Toolan, E.-U. Haq, A. D. F. Dunbar, S. Ebbens, N. Clarke, P. D. Topham, and J. R. Howse, "Direct observation of morphological development during the spin-coating of polystyrene-poly(methyl methacrylate) polymer blends," *Journal of Polymer Science, Part B: Polymer Physics*, vol. 51, no. 11, pp. 875–881, 2013.

[164] D. T. W. Toolan, N. Pullan, M. J. Harvey, P. D. Topham, and J. R. Howse, "In situ studies of phase separation and crystallization directed by Marangoni instabilities during spin-coating," *Advanced Materials*, vol. 25, no. 48, pp. 7033–7037, 2013.

[165] P. Mokarian-Tabari, "Controlling the Morphology of Spin coated Polymer Blend Films," *(Doctoral Thesis)*, 2009.

[166] D. P. Birnie III, "Combined flow and evaporation during spin coating of complex solutions," *Journal of Non-Crystalline Solids*, vol. 218, pp. 174–178, 1997.

[167] D. E. Haas, J. N. Quijada, S. J. Picone, and D. P. Birnie III, "Effect of solvent evaporation rate on "skin" formation during spin coating of complex solutions," *SPIE Proceedings, Sol-Gel Optics*, pp. 280–284, 2000.

[168] D. P. Birnie III, "Optical video interpretation of interference colors from thin transparent films on silicon," *Materials Letters*, vol. 58, no. 22-23, pp. 2795–2800, 2004.

[169] D. P. Birnie III, D. E. Haas, and C. M. Hernandez, "Laser interferometric calibration for real-time video color interpretation of thin fluid layers during spin coating," *Optics and Lasers in Engineering*, vol. 48, no. 5, pp. 533–537, 2010.

[170] J. A. R. Renuncio and J. M. Prausnitz, "Densities of Polymer Solutions to 1 kbar," *Macromolecules*, vol. 9, no. 2, pp. 324–328, 1976.

[171] E. Hamori, L. R. Prusinowski, P. G. Sparks, and R. E. Hughes, "Intrinsic Viscosity Studies of Stereoregular Poly (methyl methacrylate) in 2, 2, 3, 3-Tetrafluoropropanol1a," *The Journal of Physical Chemistry*, vol. 69, no. 4, pp. 1101–1105, 1965.

[172] M. Munekata, J. Nishiyama, A. Noguchi, H. Kurishima, H. Yoshikawa, and H. Ohba, "Drying of flowing liquid film on rotating disk," *Journal of Thermal Science*, vol. 19, no. 3, pp. 234–238, 2010.

[173] F. Kreith and D. Margolis, "Heat transfer and friction in turbulent vortex flow," *Applied Scientific Research*, vol. 8, pp. 457–473, 1959.

[174] H. Schlichting, "Boundary Layer Theory," *McGraw-Hill, New York*, pp. 83–89, 1955.

[175] L. E. Stillwagon, R. G. Larson, and G. N. Taylor, "Planarization of Substrate Topography by Spin Coating," *Journal of The Electrochemical Society*, vol. 134, no. 8, pp. 2030–2037, 1987.

[176] X. Yu, A. Beharaj, M. W. Grinstaff, and O. K. C. Tsui, "Modulation of the effective viscosity of polymerfilms by ultravioletozone treatment," *Polymer*, vol. 116, pp. 498–505, 2017.

[177] J. Berry, C. P. Brangwynne, and M. Haataja, "Physical principles of intracellular organization via active and passive phase transitions," *Reports on Progress in Physics*, vol. 81, no. 4, 2018.

[178] P. Achalla, J. McCormick, T. Hodge, C. Moreland, P. Esnault, A. Karim, and D. Raghavan, "Characterization of elastomeric blends by atomic force microscopy," *Journal of Polymer Science, Part B: Polymer Physics*, vol. 44, no. 3, pp. 492–503, 2006.

[179] E. Helfand and Y. Tagami, "Theory of the interface between immiscible polymers. II," *The Journal of Chemical Physics*, vol. 56, no. 7, pp. 3592–3601, 1972.

[180] M. L. Fernandez, J. S. Higgins, J. Penfold, R. C. Ward, C. Shackleton, and D. J. Walsh, "Neutron reflection investigation of the interface between an immiscible polymer pair," *Polymer*, vol. 29, no. 11, pp. 1923–1928, 1988.

[181] S. H. Anastasiadis, T. P. Russell, S. K. Satija, and C. F. Majkrzak, "The morphology of symmetric diblock copolymers as revealed by neutron reflectivity," *The Journal of Chemical Physics*, vol. 92, no. 9, pp. 5677–5691, 1990.

[182] M. Sferrazza, C. Xiao, D. G. Bucknall, and R. A. Jones, "Interface width of low-molecular-weight immiscible polymers," *Journal of Physics Condensed Matter*, vol. 13, no. 46, pp. 10269–10277, 2001.

[183] K. R. Shull, A. M. Mayes, and T. P. Russell, "Segment Distributions in Lamellar Diblock Copolymers," *Macromolecules*, vol. 26, no. 15, pp. 3929–3936, 1993.

[184] M. Sferrazza, C. Xiao, R. A. Jones, D. G. Bucknall, J. Webster, and J. Penfold, "Evidence for capillary waves at immiscible polymer/polymer interfaces," *Physical Review Letters*, vol. 78, no. 19, pp. 3693–3696, 1997.

[185] M. Sferrazza, R. A. Jones, J. Penfold, D. B. Bucknall, and J. R. Webster, "Neutron reflectivity studies of the structure of polymer/polymer and polymer/substrate interfaces at the nanometer level," *Journal of Materials Chemistry*, vol. 10, no. 1, pp. 127–132, 2000.

[186] D. Brosetav, T. B. Laborarories, M. Hill, T. B. Laboratories, and M. Hill, "Molecular Weight and Polydispersity Effects at Polymer-Polymer Interfaces," *Macromolecules*, vol. 139, no. 12, pp. 132–139, 1990.

[187] J. Penfold and R. K. Thomas, "The application of the specular reflection of neutrons to the study of surfaces and interfaces," *Journal of Physics: Condensed Matter*, vol. 2, no. 6, pp. 1369–1412, 1999.

[188] T. Nylander, R. A. Campbell, P. Vandoolaeghe, M. Cárdenas, P. Linse, and A. R. Rennie, "Neutron reflectometry to investigate

the delivery of lipids and DNA to interfaces (Review)," *Biointerphases*, vol. 3, no. 2, pp. FB64–FB82, 2008.

[189] J. P. De Silva, S. J. Martin, R. Cubitt, and M. Geoghegan, "Observation of the complete rupture of a buried polymer layer by off-specular neutron reflectometry," *European Polymer Journal*, vol. 86, no. 36005, pp. 1–6, 2009.

[190] C. J. Carriere, G. Biresaw, and R. L. Sammler, "Temperature dependence of the interfacial tension of PS/PMMA, PS/PE, and PMMA/PE blends," *Rheologica Acta*, vol. 39, no. 5, pp. 476–482, 2000.